Phase-Shifting Full-Field Interferometric Methods for In-Plane Tensorial Stress Determination for Fracture Studies

Thesis by

Sharlotte Lorraine Bolyard Kramer

In Partial Fulfillment of the Requirements

for the Degree of

Doctor of Philosophy

California Institute of Technology

Pasadena, California

2009

(Defended April 15, 2009)

To my family, friends, and Heavenly Father who give me strength.

Acknowledgments

I would like to begin my acknowledgements with my two advisors, Guruswami (Ravi) Ravichandran and Kaushik Bhattacharya, for their practical and moral support during my five years at Caltech. This dynamic advising duo helped me navigate the sometimes treacherous waters of the Ph.D. thesis, always with some form of encouragement or useful prodding to get me to the finish. Ravi's advice to "just do it" and to "go for it" was not always easy for me, but usually proved to be the best medicine for a problem. Kaushik's enthusiasm for my progress kept my spirits up. They gave me the freedom to work through problems without letting me lose track of the goals of my thesis.

I must acknowledge Ares Rosakis for his enthusiasm for my research that combines two of his pet experimental methods and for this professional encouragement towards the end of my time at Caltech. I would like to acknowledge the remaining members of my thesis committee, Nadia Lapusta, Chiara Daraio, and Sergio Pellegrino, for their patience with schedules and for reading through my thesis that at first appears long, but is quite full of figures. I thank Eann Patterson of Michigan State University for his helpful discussions on photoelasticity. I would also like to thank my undergraduate advisor, Iaonnis Chasiotis, who still is a big professional support.

I must acknowledge the practical support of the National Defense Science and Engineering Graduate Fellowship program and the National Science Foundation Graduate Research Fellowship program. I would also like to acknowledge the National Science Foundation Center for the Science and Engineering of Materials at Caltech for their support of my research.

I also must acknowledge my friend and colleague, Michael Mello. He was responsible for teaching me the practical side of optics and has been a wonderful person to discuss theory with. He is a tremendous person to work with and be friends with. I would also like to acknowledge the members of my research group who have been with me during the development of my research, providing helpful comments and camaraderie. I would like to acknowledge Linda Miranda for help with administrative issues and for her friendship. I must acknowledge the gentlemen of the Aeronautics Machine Shop for their practical help in making my parts and specimens, always with a smile.

In addition to the friends and colleagues I have already mentioned, I would like to acknowledge my many friends at Caltech that have been a great source of joy and strength, with special thanks to Sally Bane, Shannon Kao, Lydia Ruiz, Nathalie Vriend, and Sam Daly. I must also acknowledge my friends from afar, Emily Swafford and Crystal Cronan, who have helped me through it all over the phone and by email.

I must acknowledge my family: Mom, Dad, Philip, and Deborah. They have always encouraged me to work hard, strive to do well, and be a good person. Their love has been constant and unwavering. I also must thank my new family by marriage, Pat, Mike, Jason, Granny, and Grandpa, for their abundant enthusiasm and encouragement from across the globe in New Zealand.

I would like to state some special words of acknowledgement of my fabulous husband, Richard. He has been a constant rock to lean on during our entire time at Caltech, from homework sets to thesis writing. I can always trust in him for love, encouragement, practical help, a kind ear, and a hug. Even if I had not gained anything from my experience at Caltech other than him as a husband, I would still be eternally enriched and fortunate. The most important acknowledgement of them all is to God, my Lord and Savior. He has been the true foundation and source of strength of all that I do and all that I am. He has blessed me with many gifts. He presents me with challenges to teach me perseverance and hope in Him. All the glory must ultimately be given to Him.

Abstract

Fracture criteria of anisotropic materials can be established with understanding of full-field stresses near a crack. The anisotropy of the stresses implies that the full in-plane tensorial stress is required, but current experimental optical techniques only give the sum or difference of principal stresses, motivating the development of an experimental method that combines two experimental techniques to determine all of the stress components. The proposed hybrid experimental method of phase-shifting photoelasticity and transmission Coherent Gradient Sensing (CGS) can determine the full-field in-plane tensorial stress around a crack. This thesis establishes this method for stress determination around cracks in photoelastic materials, the foundation for future studies extending this method to anisotropic materials.

The first step in developing this experimental method requires a new theory for the use of CGS, a wavefront shearing interferometry technique, for photoelastic materials. The first analysis and experimental verification of transmission wavefront shearing interferometry for photoelastic materials are presented. These interferometers applied to optically isotropic materials produce a single interference pattern related to one phase term, but when applied to photoelastic materials, they produce the sum of two different interference patterns with phase terms that are the sum and difference, respectively, of two stress-related phase terms. The two stress-related phase terms may be separated using phase shifting and polarization optics. These concepts are experimentally demonstrated using CGS in full field for a compressed polycarbonate plate with a side V-shaped notch with good agreement with theoretical data derived from Williams' solution for a thin plate with an angular corner. The analysis may be applied to any wavefront shearing interferometer by modifying parameters describing the wavefront shearing distance.

The new method that combines phase-shifting photoelasticity and transmission CGS is first developed to determine the tensorial stress field in thin plates of photoelastic materials. A six-step phase-shifting photoelasticity method determines principal stress directions and the difference of principal stresses. The transmission CGS method utilizes a standard four-step phase-shifting method to measure the x and y first derivatives of the sum of principal stresses. These stress derivatives are numerically integrated using a weighted preconditioned conjugate gradient (PCG) algorithm, which is also used for the phase unwrapping of the photoelastic and CGS phases. With full-field measurement of the sum and difference of principal stresses, the principal stresses may be separated, followed by the Cartesian and polar coordinate stresses using the principal stress directions and the polar angle. The method is demonstrated for in-plane tensorial stress determination for a compressed polycarbonate plate with a side V-shaped notch with good comparison to theoretical stress fields.

The CGS-photoelasticity experimental method is applied to determine stresses around Mode I-dominant cracks in Homalite-100. The cases presented here range in Mode I stress intensity factor, K_I, from about one-quarter to just below the fracture toughness and have small mode-mixity ratios K_{II}/K_I. This experimental method demonstrates the calculation of mode-mixity ratios as small as 0.0043 with a range of -0.010 to 0.020. The experimental stress fields have excellent agreement with the full-field 2D asymptotic crack solution using the K_I and K_{II} values calculated from the experimental data. With this foundation of stress determination around cracks in photoelastic materials and with some future analysis, this experimental method can be extended to determine stresses in anisotropic crystals for fracture studies.

Contents

List of Figures

List of Tables

Nomenclature

Greek symbols

α	isoclinic angle; angle of linear retardation of photoelastic material; angle between Cartesian and principal coordinate systems, Equation (3.3), Page 40	radian
β	angle of polarization axis of the second polarizer in the polariscope, Page 39	radian
Δh	thickness variation, Equation (2.5), Page 12	m
Δn_i	change in refractive index in the i-th direction, Equation (2.4), Page 12	
$\Delta S_{1,2}$	optical path difference along principal directions, Equation (2.6), Page 12	
ΔS_a	general optical path difference along the a axis, Equation (2.3), Page 11	
δ	photoelastic isochromatic phase, Equation (3.1), Page 39	radian
$\Delta\psi$	wrapped phase difference between neighboring pixels, Equation (2.28), Page 32	radian
ϵ	error associated with assumption relating CGS phases to derivatives of $\sigma_1 + \sigma_2$, Equation (4.7), Page 112	
ϵ^{δ}	error between experimental and theoretical δ for mixed-mode fracture, Equation (4.4), Page 84	
$\epsilon^{\partial x}$	error between experimental and theoretical $\varphi_{sum}^{\partial x}$ for mixed-mode fracture, Equation (4.4), Page 84	
$\epsilon^{\partial y}$	error between experimental and theoretical $\varphi_{sum}^{\partial y}$ for mixed-mode fracture, Equation (4.4), Page 84	

γ	angle of ± 1 diffraction relative to z axis, Page 10	radian
λ	wavelength, Page 11	m
$\lambda/2$ plate	half-wave plate	
$\lambda/4$ plate	quarter-wave plate	
λ_o	exponent of r in Williams asymptotic stress field, Page 23	
μ_{SIF}	stress intensity factor ratio, Page 87	
ν	Poisson's ratio	
ω	angular frequency of the electric field, Page 11	
ϕ	angle of fast axis of the second $\lambda/4$ plate in the polariscope, Page 39	radian
$\phi_{x,y}$	arbitrary constant phase terms of x and y amplitudes of electric field, Page 11	radian/s
ρ	angle of polarization axis of first polarizer, Page 20	radian
$\sigma_{\alpha\beta}$	2D stress components for Carteisian $\alpha, \beta = \{x, y\}$ or polar $\alpha, \beta = \{r, \theta\}$	Pa
$\sigma_{\theta\theta}$	hoop stress, Page 1	Pa
σ_{app}	far-field applied stress, Page 23	
σ_i	principal stress for $i = \{1, 2, 3\}$	Pa
θ	polar coordinate for polar angle	
$\tilde{\Delta}$	Ronchi grating separation, Page 10	m
φ	general phase of interference term, Equation (2.19), Page 17	radian
$\varphi_{1,2}$	phase of interference term for $I_{1,2}^{image}$, Equation (2.14), Page 15	radian
$\varphi_{\alpha d}$	compound phase related to α and ϕ_{diff}, Equation (2.22), Page 18	radian
φ_c	phase of compound interference, Equation (2.17), Page 16	radian

φ_{diff}	CGS phase related to $\sigma_1 - \sigma_2$, Equation (2.16), Page 16	radian
φ_{Ex}	phase of compound interference from pure $E_x\hat{\imath}$ input, Equation (2.22), Page 18	radian
φ_{Ey}	phase of compound interference from pure $E_y\hat{\jmath}$ input, Equation (2.23), Page 19	radian
φ_{sum}	CGS phase related to $\sigma_1 + \sigma_2$, Equation (2.16), Page 16	radian
$\varphi_{sum}^{\partial x}$	CGS phase related to the x derivative of $\sigma_1 + \sigma_2$, Equation (4.3), Page 83	radian
$\varphi_{sum}^{\partial y}$	CGS phase related to the y derivative of $\sigma_1 + \sigma_2$, Equation (4.3), Page 83	radian
ξ	angle of fast axis of first wave plate, Page 20	radian
ζ	material remaining after angular corner removed, Page 23	radian
C_f	fitting coefficient for Williams asymptotic stress field, Page 23	

Roman characters

A	absolute photoelastic constant, Equation (2.4), Page 12	
a	length of the side of the square base in a tetragonal crystal, Page 184	Å
$A_o^{\pm 1}$	nominal magnitude of pure x or pure y electric field amplitude after ± 1 diffraction, Page 18	
a_1	length of straight notch in fracture specimens, Page 86	m
a_2	length of straight crack in fracture specimens, Page 86	m
A_o	nominal magnitude of pure x or pure y electric field amplitude, Page 18	
A_x	magnitude of E_x, Page 11	
$A_x^{\pm 1}$	magnitude of x amplitude of $\boldsymbol{E}^{\pm 1}$, Page 14	
A_y	magnitude of E_y, Page 11	
$A_y^{\pm 1}$	magnitude of y amplitude of $\boldsymbol{E}^{\pm 1}$, Page 14	
B	absolute photoelastic constant, Equation (2.4), Page 12	

C	constant related to photoelasticity used in $\Delta S_{1,2}$, Equation (2.7), Page 13	m^2/N
c	length of the long side of a tetragonal crystal, Page 184	Å
c_o	relative photoelastic (stress-optic) constant, Equation (3.1), Page 39	m^2/N
d	depth of V-notch, Page 21	
d_{shear}	lateral shearing distance, Page 10	m
E	Young's (elastic) modulus	Pa
$E_1^{\pm 1}$	amplitude in $\hat{p}_1$ direction of $\boldsymbol{E}^{\pm 1}$, Equation (2.11), Page 14	
$E_2^{\pm 1}$	amplitude in $\hat{p}_2$ direction of $\boldsymbol{E}^{\pm 1}$, Equation (2.11), Page 14	
E_1	amplitude for $\hat{p}_1$ direction of input electric field, Equation (2.9), Page 13	
e_1	rotational misalignment of input $\lambda/4$ plate, Page 43	radian
E_1^{image}	electric field amplitude in $\hat{p}_1$ direction at the image plane, Equation (2.11), Page 14	
E_2	amplitude for $\hat{p}_2$ direction of input electric field, Equation (2.9), Page 13	
e_2	rotational misalignment of output $\lambda/4$ plate, Page 43	radian
E_2^{image}	electric field amplitude in $\hat{p}_2$ direction at the image plane, Equation (2.11), Page 14	
e_3	rotational misalignment of output polarizer, Page 43	radian
E_x	x amplitude of input electric field, Equation (2.1), Page 11	
$E_x^{specimen}$	x amplitude of electric field after specimen, Equation (2.2), Page 11	
E_y	y amplitude of input electric field, Equation (2.1), Page 11	
$E_y^{specimen}$	y amplitude of electric field after specimen, Equation (2.2), Page 11	
g	constant related to photoelasticity used in $\Delta S_{1,2}$, Equation (2.7), Page 13	
$G_{1,2}$	Ronchi grating $1, 2$, Page 10	

h	nominal specimen thickness, Page 11	m
h_d	height of wrapped phase discontinuities, Page 17	radian
I	intensity (irradiance) of an interference pattern	
I^{circ}	irradiance (intensity) at the image plane from circularly polarized electric field input, Equation (2.24), Page 19	
I_c^{circ}	constant for compound interference pattern from circularly polarized electric field input depending on I_o^{circ} and φ_{diff}, Equation (2.24), Page 19	
I_o^{circ}	constant for compound interference pattern from circularly polarized electric field input, Equation (2.24), Page 19	
I^{Ex}	irradiance (intensity) at the image plane from pure $E_x\hat{\imath}$ input, Equation (2.22), Page 18	
I_c^{Ex}	constant for compound interference term for pure $E_x\hat{\imath}$ input depending on I_o^{Ex}, α, and φ_{diff}, Equation (2.22), Page 18	
I_o^{Ex}	constant for compound interference pattern for pure $E_x\hat{\imath}$ input, Equation (2.22), Page 18	
I^{Ey}	irradiance (intensity) at the image plane from pure $E_y\hat{\jmath}$ input, Equation (2.23), Page 19	
I_c^{Ey}	constant for compound interference term for pure $E_y\hat{\jmath}$ input depending on I_o^{Ey}, α, and φ_{diff}, Equation (2.23), Page 19	
I_o^{Ey}	constant for compound interference pattern for pure $E_y\hat{\jmath}$ input, Equation (2.23), Page 19	
I^{image}	irradiance (intensity) of electric field at the image plane, Equation (2.12), Page 14	
I_1^{image}	irradiance (intensity) of E_1^{image}, Equation (2.12), Page 14	
I_2^{image}	irradiance (intensity) of E_2^{image}, Equation (2.12), Page 14	
$I^{isotropic}$	irradiance (intensity) of CGS image for an isotropic material, Page 17	
I_{1o}	constant in I_1^{image} depending on $A_{x,y}^{\pm 1}$, α and $\phi_{x,y}$, Equation (2.16), Page 16	

I_{2o}	constant in I_2^{image} depending on $A_{x,y}^{\pm 1}$, α and $\phi_{x,y}$, Equation (2.16), Page 16	
I_c	constant for compound interference term depending on I_{1o}, I_{2o}, and φ_{diff}, Equation (2.17), Page 16	
I_i	i-th phase-shifted image ($i = 1$–6 for photoelasticity, $i = 1$–4 for CGS)	
I_o	constant in I^{image}, Equation (2.16), Page 16	
I_o	intensity (irradiance) of a photoelastic interference pattern, Equation (3.2), Page 39	
k	wave number, Page 11	radian/m
K_{Ic}	fracture toughness, Page 88	MPa/$\sqrt{\text{m}}$
K_{II}	Mode II stress intensity factor, Equation (4.1), Page 82	MPa$\sqrt{\text{m}}$
K_I	Mode I stress intensity factor, Equation (4.1), Page 82	MPa$\sqrt{\text{m}}$
L	half of the CGS shearing distance, Page 181	pixel
L^f	height of image field of view, Page 15	
M_i	coefficients in intensity for polariscope with non-polarizing beamsplitter, $i = 1$–4, Equation (3.5), Page 42	
N	photoelastic fringe order, Equation (3.1), Page 39	
n_o	refractive index, Page 11	
p	pitch, i.e., line density of Ronchi grating, Page 10	1/m
r	polar coordinate for radius	
$R_{x,y}$	reflectance coefficients along the $\{x, y\}$ directions for a non-polarizing beamsplitter, Page 41	
s	sum of the in-plane principal stresses, Page 51	
t	time	s

$T_{x,y}$ transmission coefficients along the $\{x, y\}$ directions for a non-polarizing beamsplitter, Page 41

$thresh$ user-defined threshold value used in correction of the wrapped isoclinic angle, Page 49

w opening width of V-notch, Page 21

W_i^{δ} quality-driven weight function for PCG algorithm for the isochromatic phase for mixed-mode fracture at point i, Page 84

$W_i^{\partial x}$ quality-driven weight function for PCG algorithm for the CGS phase related to the x derivative of $\sigma_1 + \sigma_2$ for mixed-mode fracture at point i, Page 84

$W_i^{\partial y}$ quality-driven weight function for PCG algorithm for the CGS phase related to the y derivative of $\sigma_1 + \sigma_2$ for mixed-mode fracture at point i, Page 84

W^f width of image field of view, Page 15

x Cartesian coordinate

y Cartesian coordinate

z Cartesian coordinate

CGS Coherent Gradient Sensing, Page 10

FCT fast cosine transform, Page 29

G energy release rate, Page 1 N/m

NRMSD RMSD normalized by range of data, Page 32

PCG preconditioned conjugate gradient, Page 29

RMSD root mean square deviation, Page 32

Sub-scripts and Super-scripts

$()^{circ}$ related to circularly polarized electric field input

$()^{Ex}$ related to pure $E_x\hat{\imath}$ input

$()^{Ey}$ related to pure $E_y\hat{\jmath}$ input

$()^{image}$ refers to image plane

$()^{in}$ refers to input plane prior to specimen

$()^{resid}$ refers to residual stresses

$()^{specimen}$ refers to plane immediately after specimen

$()_c$ refers to a compound quantity

$()_p$ written in principal coordinate system

Vectors and Matrices

$\hat{\imath}$ x direction unit vector

$\hat{\jmath}$ y direction unit vector

$\hat{p}_i$ principal unit vectors for $i = \{1, 2, 3\}$, Equation (2.9), Page 13

$\mathbf{W}$ quality-driven weight function for PCG algorithm, Equation (2.28), Page 32

$\boldsymbol{E}_{(\mathbf{0},\pm\mathbf{1})}$ transmitted, then ± 1 diffracted wavefront, Page 10

$\boldsymbol{E}_{(\pm\mathbf{1},\mathbf{0})}$ ± 1 diffracted, then transmitted wavefront, Page 10

$\boldsymbol{E}^{\pm 1}$ once diffracted electric field vector after Ronchi gratings, Page 14

$\boldsymbol{E}_p^{image}$ electric field vector at the image plane, Equation (2.11), Page 14

$\boldsymbol{E}^{in}$ input electric field vector, Equation (2.1), Page 11

$\boldsymbol{E}_p^{in}$ input electric field vector in principal coordinates, Equation (2.9), Page 13

$\boldsymbol{E}_p^{specimen}$ electric field vector after the specimen in principal coordinates, Equation (2.10), Page 14

$\boldsymbol{f}(K_I, K_{II})$ function to be minimized by nonlinear least-squares fitting algorithm to determine K_I and K_{II}, Equation (4.5), Page 85

Chapter 1

Introduction

Active materials that have coupled responses to external stimuli, such as ferroelectric crystals that exhibit electromechanical actuation and nonlinear optical properties, are advantageously used in applications such as actuators, microdevices, and photonics. In order to improve fabrication techniques that focus on making flat surfaces for these applications and to characterize device failure, their fracture properties need to be determined. Such materials undergo anisotropic fracture, but the criteria for anisotropic fracture are not well established. The commonly used fracture criteria from isotropic fracture mechanics of maximum Mode I stress intensity factor (max-K_I), zero Mode II stress intensity factor ($K_{II} = 0$), maximum hoop stress (max-$\sigma_{\theta\theta}$), and maximum energy release rate (max-G) lead to the same prediction of crack propagation path in isotropic materials, but not in anisotropic materials (Goldstein and Salganik, 1974; Cotterell and Rice, 1980; Hodgdon and Sethna, 1993; Azhdari and Nemat-Nasser, 1998). A set of theoretical numerical, and experimental studies of fracture in sapphire, a brittle anisotropic crystal, by Azhdari and Nemat-Nasser (1996, 1998) and Azhdari et al. (1998) determined that a stress-based fracture criterion best determines the crack kinking properties for this material. Such studies motivate determining anisotropic fracture criteria by knowledge of the anisotropic stress field around a crack tip, allowing for calculation of quantities such as K_I, K_{II}, $\sigma_{\theta\theta}$, and G, which may be compared to determine what best predicts the crack path and the critical conditions for crack initiation and propagation for a given anisotropic material.

In plane-stress problems for these materials, the anisotropy of the stress field implies that the sum or difference of the in-plane principal stresses is not sufficient to determine fracture properties, as it is for linearly elastic isotropic materials. Therefore, the study of aniostropic fracture motivates the development of experimental methods employing full-field techniques to determine the full-field tensorial stress (i.e., σ_{xx}, σ_{yy}, and σ_{xy}) for fracture studies. This thesis presents the development and experimental validation of a hybrid experimental method of phase-shifting photoelasticity and transmission Coherent Gradient Sensing (CGS), a wavefront shearing interferometry technique, for full-field in-plane tensorial stress determination around cracks in photoelastic materials, which serves as the foundation for future work in extending this method for fracture studies in anisotropic crystalline materials.

1.1 Transmission Wavefront Shearing Interferometry for Photoelastic Materials

Wavefront shearing interferometry is a well-established optical technique for measuring many optical, material, and mechanical properties such as wavefront slope characterization (Murty, 1964), surface deformation (Park et al., 2003), and even fracture of materials (Tippur et al., 1991a,b; Rosakis, 1993; Krishnaswamy, 2000). Shearing interferometry essentially is the interference of a coherent wavefront with a copy of itself "sheared" or translated by a lateral distance d_{shear}; this technique is self-referencing and hence is insensitive to rigid body motion (Park et al., 2003; Tippur et al., 1991a,b; Rosakis, 1993). The general analysis of the interference pattern for standard wavefront shearing interferometers depends only on the wavefront characteristics and the distance d_{shear}. Once the parameters for producing the sheared wavefront and interfering the two wavefronts are characterized for a particular shearing method, then the analysis may be specified for that particular method. With several methods to produce the wavefront shearing, the choice of shearing interferometer depends on the requirements of the application, such as measurement sensitivity or compactness.

An important consideration to the analysis is how the wavefront is formed. For techniques that involve transmission through a material of interest, the shape and optical properties of the material are considered (e.g., spherical wavefront emanating from an optically isotropic plano-convex lens.) In the case of a deformed material that is originally planar, thickness and refractive index variations in the material result in optical path differences that may be related to stresses. A general analysis of the optical path difference in this case has previously been completed for the method of caustics (Papdopoulos, 1993; Kobayashi, 1993; Shimizu et al., 1998). Though not a wavefront shearing interferometry technique, the method of caustics, which has been used for large stress gradient applications, does consider optical path differences due to a deformed material, resulting in a shadow spot in the far field. The method of caustics only gives a point measurement, which motivated the development of CGS that is capable of measuring full-field stress or displacement gradients when used in transmission or in reflection, respectively (Tippur et al., 1991a,b). CGS is a wavefront lateral shearing interferometer that achieves shearing by a pair of amplitude gratings; sensitivity adjustment is achievable through choice of grating line density, separation between the gratings, and light wavelength. Previously, CGS in transmission has been used only for optically isotropic materials (Tippur et al., 1991a,b; Krishnaswamy, 2000). CGS in reflection has been used for opaque isotropic materials (Tippur et al., 1991a,b), for materials with reflective coatings (Tippur et al., 1991a,b; Lee et al., 2001), and for composite materials (Rosakis, 1993; Liu et al., 1998). No previous studies have considered CGS in transmission for optically anisotropic materials.

Taking inspiration from the method of caustics applied to photoelastic materials, this study presents the first general analysis of an initially planar wavefront transmitted through a photoelastic material, in terms of electric field and optical path difference, for a general wavefront shearing interferometer; the analysis is then specifically applied to CGS. The analysis may easily be modified for any wavefront shearing interferometer by changing the experimental parameters related to the distance d_{shear}.

This study demonstrates that the resultant interference pattern is no longer a simple function of a single phase term related to the sum of principal stresses, denoted φ_{sum}, as in the case of optically isotropic materials. Due to the optical anisotropy from the stress birefringence, the interference patterns from the x and y coordinates of the electric field, E_x and E_y, are no longer equivalent. Considering the interference patterns along the orthogonal principal axes of the photoelastic specimen, denoted I_1^{image} and I_2^{image}, the phase terms of these distinct interference patterns, φ_1 and φ_2, are $\varphi_{sum} + \varphi_{diff}$ and $\varphi_{sum} - \varphi_{diff}$, respectively, where φ_{diff} is related to the difference of principal stresses. Thus, φ_{diff} obscures the desired phase information, φ_{sum}, due to the optical anisotropy of the material. φ_{diff} is zero for an optically isotropic material, and therefore is not an issue for isotropic materials. For a general incident electric field, wavefront shearing interferometry for photoelastic materials results in an image that is the superposition of I_1^{image} and I_2^{image}, which is too complicated to analyze by itself. The desired phase φ_{sum} may be recovered by using phase shifting and polarization optics. These concepts are demonstrated using CGS for a compressed polycarbonate thin plate with a V-shaped side notch with good agreement between experimental and theoretical data.

1.2 Experimental In-Plane Tensorial Stress Determination

The analysis of various complex geometries and materials requires the full-field measurement of the in-plane tensorial stress, but full-field optical interference techniques generally provide a linear combination of stress or strain components. For example, standard photoelasticity yields the difference of the principal stresses $(\sigma_1 - \sigma_2)$ and the principal directions, meaning the angle between the Cartesian and principal coordinate systems known as the isoclinic angle (Patterson et al., 1997; Siegmann et al., 2005). Coherent Gradient Sensing (CGS) in transmission, on the other hand, provides a spatial derivative of the sum of the principal stresses $(\sigma_1 + \sigma_2)$ when applied to thin plate specimens (Tippur et al., 1991a; Rosakis, 1993). Methods for the determination of the in-plane stress tensor often combine either one experimental technique with a theoretical or numerical analysis component or two experimental techniques. Among the single experimental and theoretical/numerical hybrid methods are photoelasticity and a shear difference method, which calculates stress components on a raster scan from initial values of stress determined by photoelastic parameters at the boundary points (Haake et al., 1996; Greene et al., 2007), a hybrid photoelasticity and finite element method technique (Berghaus, 1991), and a hybrid technique combining thermoelasticity, which relates to the change in the sum of principal stresses with surface temperature, and both theoretical and numerical methods (Huang et al., 1990a,b). A double experimental hybrid technique utilizes reflection photoelasticity as a strain witness and thermoelasticity (Barone and Patterson, 1996; Sakagami et al., 2004); the opaque nature of photoelastic coatings in the infrared spectrum allows these techniques to investigate the same surface of the specimen (Greene et al., 2007; Barone and Patterson, 1998). Interferometric photoelasticity gives both the isochromatic phase, related to the difference of principal stresses, and the isopachic phase, related to the sum of principal stresses; these two fields may be separated using a Mach-Zehnder interferometer combined with a circular polariscope (Yoneyama et al., 2005).

In this study, the proposed technique combines two full-field optical techniques, CGS in transmission and photoelasticity, used simultaneously with the aid of phase-shifting diagnostics. The x and y derivatives from the CGS data are numerically integrated to provide the sum of principal stresses, which, when combined with the difference of principal stresses and principal stress directions derived from photoelasticity, yield full-field in-plane stresses in principal, Cartesian, or polar coordinate systems. This method is the most similar to interferometric photoelasticity, given that the sum and difference of principal stress fields both require phase shifting to extract phase information and that both techniques are used in transmission. The proposed technique differs from interferometric photoelasticity in that the sum of the principal stresses comes from stress gradient measurements. Additionally, the CGS optic parameters, as described in Chapter 2, may be varied to adjust the measurement sensitivity to optimize the fringe density. This study concentrates on the hybrid technique in transmission; further analysis would be required to determine if this method could be used in reflection, where the separation of the principal strains are considered. The use of this method in reflection would be similar to the combined reflection photoelasticity/thermoelasticity (Greene et al., 2007; Barone and Patterson, 1998), but in this case, a photoelastic coating would affect the displacement derivative measurement on the same surface using reflection CGS.

This study demonstrates the combined experimental techniques for polycarbonate, a linear elastic photoelastic material. The test configuration is a plate with a side V-shaped notch along the $-x$ axis, compressed uniformly along the y axis. A six-step phase-shifting photoelastic method based on

Patterson et al. (1997) and Siegmann et al. (2005) utilizes a circular polariscope, except here a non-polarizing beamsplitter is positioned after the specimen to split the light such that the transmitted light travels through the remaining polariscope optics and the reflected light travels through the CGS optics. The photoelastic data involve two phases, the isoclinic angle α and isochromatic phase δ, related to the principal stress directions and the difference of principal stresses, respectively. Phase shifting allows for the separation of these two phases, but produces "wrapped" data with a limited range due to inverse trigonometric functions. The wrapped isoclinic angle and isochromatic phase are both unwrapped using a global least square integration phase unwrapping algorithm called weighted preconditioned conjugate gradient (PCG) method (Ghiglia and Romero, 1994; Baldi et al., 2002). This robust method allows for discrete jumps in phase that may arise due to a free surface, imperative to studying specimens with cracks or cutouts.

Since a transmission CGS interference pattern for a photoelastic material is a superposition of two interference patterns, phase-shifting techniques combined with appropriate control of the input polarization state prior to the specimen, achieved by the first two optics of the circular polariscope, lead to the elimination of φ_{diff}, leaving the desired phase φ_{sum}. The remaining phase is unwrapped using the weighted PCG algorithm. The x and y derivatives of $\sigma_1 + \sigma_2$ from the CGS data from the vertical and horizontal shearing directions are integrated using the PCG algorithm as well. With the constant of integration identified by a boundary condition, the full-field sum and difference of principal stresses allow for separation of the principal stresses, which may be transformed into Cartesian or polar coordinate systems utilizing the isoclinic angle. Experimental data of the test problem shows good agreement with theoretical data generated from an asymptotic solution derived from Williams' (1952) solution for a thin plate with an angular corner.

1.3 Full-Field Experimental Methods for Fracture Studies

Having established the use of the proposed hybrid experimental method for full-field tensorial stress determination around a V-notch stress concentration in polycarbonate, the next stage in this study is to demonstrate the method for full-field tensorial stress determination around a crack in a photoelastic material. To the author's knowledge, the only study of full-field tensorial stress determination in a cracked material is by Sakagami et al. (2004), who used thermoelasticity and reflection-photoelasticity applied to a mechanically loaded plate with a small central crack-like slit. This study determines the full-field stresses for an aluminum alloy plate 450 mm $\times$ 80 mm $\times$ 6 mm in dimension with a central crack-like slit through the thickness, 16mm in length and 0.2 mm in width. Their field of view is 200 mm $\times$ 80 mm centered around the slit. Although qualitative comparison of their full-field experimental tensorial stresses to their boundary element method simulation appears poor, they report less than 5% error in their K_I calculation as compared to theory. The study by Sakagami et al. (2004) does demonstrate the capability for tensorial stress determination using their hybrid method for this situation, but for a large field of view, for a crack-like slit, and for an opaque isotropic material.

This thesis is intended to demonstrate full-field tensorial stress determination using the proposed hybrid transmission optical methods in photoelastic materials with an actual crack and for small fields of view around 4.6 mm$\times$4.6 mm, zoomed in very close around the crack. This study is the first to use a hybrid experimental method for full-field tensorial stress determination around cracks in photoelastic materials. The photoelastic material used here is Homalite-100, a brittle thermosetting polyester, often used as a model material for dynamic linear elastic fracture studies (Bradley and Kobayashi, 1971; Irwin et al., 1979; Dally, 1979; RaviChandar, 1982). Straight pre-cracks in the Homalite-100 specimens are loaded via a wedge opening load, which simulates Mode I loading. Four different load cases are presented, with calculated K_I values ranging from about one-quarter to just below the fracture toughness, the critical value of K_I for crack propagation, of Homalite-100. The experimental stress fields exhibit K-dominant stress behavior and show excellent comparison with the 2D asymptotic crack solution for mixed-mode fracture using the calculated K_I and K_{II} values from the experimental σ_{xx} and σ_{yy}. The experimental stresses indicate that the wedge loading is not purely Mode I, but can have a slight Mode II component, with measured mode-mixity K_{II}/K_I ranging from -0.010 to 0.020, demonstrating that this experimental method is sensitive enough to capture slight mixed-mode fracture. Since these cases are for small fields of view, these experimental stress fields are for the local crack behavior, an important asset in studying small-scale specimens. The current method does have some known local error sources that can be improved, as will be discussed. This study of full-field tensorial stress determination around cracks in a photoelastic material lays the foundation for future research in extending this hybrid experimental method for determining fracture criteria in anisotropic crystals and in active materials like ferroelectric crystals.

1.4 Thesis Outline

This thesis is divided into four main chapters with a chapter for conclusions and three appendices of supporting derivations. Chapter 2 presents the first analytical derivation of transmission wavefront shearing interferometry applied to photoelastic materials and provides experimental verification of the theory using CGS as the specific wavefront shearing interferometry technique, based on Kramer et al. (2009a). Chapter 3 introduces six-step phase-shifting photoelasticity, describes how CGS and photoelasticity are combined experimentally and how the data is analyzed, and demonstrates the proposed phase-shifting full-field CGS-photoelasticty experimental method for in-plane tensorial stress determination in a compressed polycarbonate plate with a side V-notch, based on Kramer et al. (2009b). Chapter 4 demonstrates the proposed experimental method for in-plane tensorial stress determination around Mode I–dominant cracks in Homalite-100. Chapter 5 describes future improvements to the experimental method and possible extension of this method for fracture studies in anisotropic materials. Chapter 6 provides concluding remarks for the thesis. Appendix A presents the relationships between the principal, Cartesian, and polar in-plane tensorial stress components, as well as relevant derivatives of stresses. Appendix B derives the 2D stress field for a plate with a side V-notch under uniform normal loading used for the theoretical solution in the experimental verification studies in Chapters 2 and 3. Appendix C presents details on the theory of phase-shifting photoelasticity.

Chapter 2

Transmission Wavefront Shearing Interferometry for Photoelastic Materials

2.1 Introduction

This chapter presents the first analysis of transmission wavefront shearing interferometry for photoelastic materials and experimental verification of the theory. Section 2.2 describes the experimental method and derives the interference pattern first for a general transmission wavefront shearing interferometer, and then specifically for Coherent Gradient Sensing (CGS), from a photoelastic material. Section 2.2.3 describes how phase shifting and polarization optics allow for the determination of the phase related to $\sigma_1 + \sigma_2$. Section 2.3 presents the experimental verification of the analysis for a compressed polycarbonate plate with a side V-notch with good agreement with theoretical data based on a 2D asymptotic solution derived from Williams (1952). The content of this chapter is based on Kramer et al. (2009b), but with more details on the experimental verification.

2.2 Experimental Method and Full-Field Phase Analysis

2.2.1 Experimental Method

The CGS method starts with an incident plane wave of a collimated laser beam that transmits through a transparent specimen or that reflects off an opaque specimen. The working principle of

CGS to laterally shear an incident wavefront, shown in Figure 2.1 for horizontal shear, is the same for both transmission and reflection. Tippur et al. (1991a,b) give a full description of the CGS working principle. The main concept of CGS is that the d_{shear} of the interfered wavefronts is due to diffraction through a pair of Ronchi gratings, G_1 and G_2, each with pitch p, separated by distance $\tilde{\Delta}$ such that the desired wavefronts $\boldsymbol{E_{(0,\pm1)}}$ and $\boldsymbol{E_{(\pm1,0)}}$ are separated by a lateral shearing distance $d_{shear} = \gamma\tilde{\Delta}$ in the x–z or y–z plane and propagate at the same angle γ relative to the z axis upon leaving grating G_2. The diffracted waves transmit through a filtering lens, which separate the corresponding diffraction orders into horizontal diffraction spots at the focal plane of the filtering lens. An aperture at this focal plane selects either the $+1$ or -1 diffraction order, meaning only the wavefronts $\boldsymbol{E_{(0,\pm1)}}$ and $\boldsymbol{E_{(\pm1,0)}}$ propagate to the image plane. In Section 2.2.2, analysis of the first-order diffraction shows how the interference pattern may be related to first x and y derivatives of principal stresses based on assumption of a small d_{shear}.

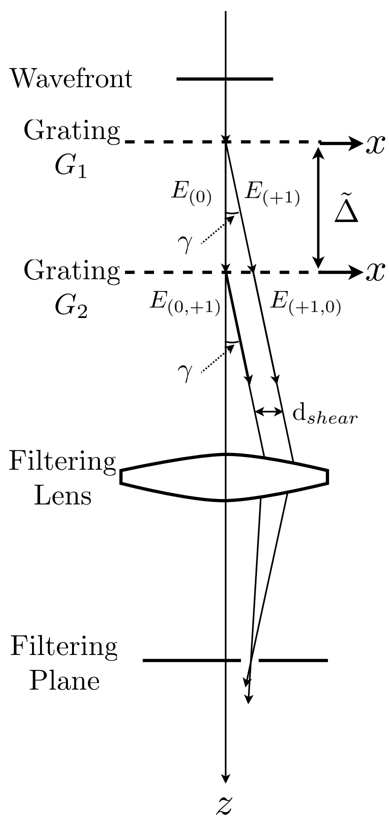

Figure 2.1: Working principle for horizontal shearing transmission CGS

2.2.2 Analysis

2.2.2.1 Electric Field Description of the Transmitted Wavefront

Assuming a coherent plane wave of monochromatic light propagating along the z axis, the electric field of the wavefront at $z = z_o$ is given by

$$\boldsymbol{E}^{in}(x,y,t) = E_x(x,y,t)\hat{\imath} + E_y(x,y,t)\hat{\jmath} \tag{2.1a}$$

$$E_x(x,y,t) = A_x \exp[j(kz_o - \omega t + \phi_x)] \tag{2.1b}$$

$$E_y(x,y,t) = A_y \exp[j(kz_o - \omega t + \phi_y)] \tag{2.1c}$$

where E_x and E_y are the amplitudes, A_x and A_y are constants, λ is the wavelength, $k = 2\pi/\lambda$ is the wave number, ω is the angular frequency, and ϕ_x and ϕ_y are arbitrary constant phase terms. If the plane wave propagates through a transparent material with refractive index n_o and nominal thickness h, then the resulting electric field magnitudes of this perturbed wavefront in the x and y directions after the specimen material at z are

$$E_x^{specimen}(x,y,t) = A_x \exp[j(kz - \omega t + \phi_x + k(n_o - 1)h + k\Delta S_x(x,y))] \tag{2.2a}$$

$$E_y^{specimen}(x,y,t) = A_y \exp[j(kz - \omega t + \phi_y + k(n_o - 1)h + k\Delta S_y(x,y))] \tag{2.2b}$$

where $\Delta S_x(x,y)$ and $\Delta S_y(x,y)$ are the optical path differences at each point (x,y) along the x and y directions, as further described in Section 2.2.2.2.

2.2.2.2 Photoelastic Effect in Transparent Materials

In general, a plane wave transmitted through a material experiences some change in optical path length due to both variation in refractive index, $\Delta n(x,y)$, and variation in thickness, $\Delta h(x,y)$, in the transmitting media. Along a given axis a, the optical path difference is expressed as

$$\Delta S_a(x,y) = h\Delta n_a(x,y) + (n_o - 1)\Delta h(x,y). \tag{2.3}$$

A full explanation of the optical path difference may be found in Papdopoulos (1993). These variations from an initially uniform material can be related to stresses in the material. First, a transparent material that experiences stress-induced birefringence, also known as the photoelastic effect, has variations in refractive index along the three principal optical axes such that

$$\Delta n_1 = n_1 - n_o = A\sigma_1 + B(\sigma_2 + \sigma_3) \tag{2.4a}$$

$$\Delta n_2 = n_2 - n_o = A\sigma_2 + B(\sigma_1 + \sigma_3) \tag{2.4b}$$

$$\Delta n_3 = n_3 - n_o = A\sigma_3 + B(\sigma_1 + \sigma_2) \tag{2.4c}$$

where σ_i, $i = \{1, 2, 3\}$, are the principal stresses and A and B are the two absolute photoelastic constants of the transparent material. These equations are known as the Neumann-Maxwell stress optic law (Coker and Filon, 1993; Frocht, 1941; Narasimhamurty, 1981). In this analysis, the $\hat{p_3}$ principal direction is assumed to be along the z axis. Second, the thickness change in a linear elastic material is related to the principal stresses by Hooke's Law:

$$\Delta h = \left[\frac{\sigma_3}{E} - \frac{\nu}{E}(\sigma_1 + \sigma_2)\right]h, \tag{2.5}$$

where E is the Young's modulus, ν is the Poisson's ratio, $\sigma_3 = 0$ for plane stress, and $\Delta h = 0$ for plane strain.

Substituting Equations (2.4a), (2.4b), and (2.5) into Equation (2.3) results in the following two equations for optical path length difference in along the $\hat{p_1}$ and $\hat{p_2}$ principal directions in terms of the sum and difference of principal stresses:

$$\Delta S_1(x, y) = Ch[(\sigma_1 + \sigma_2) + g(\sigma_1 - \sigma_2)] \tag{2.6a}$$

$$\Delta S_2(x, y) = Ch[(\sigma_1 + \sigma_2) - g(\sigma_1 - \sigma_2)] \tag{2.6b}$$

such that

$$C = \frac{A+B}{2} - \frac{\nu}{E}(n_o - 1) \tag{2.7a}$$

$$g = \frac{A-B}{A+B-2\nu(n_o-1)/E} \tag{2.7b}$$

for plane stress, and

$$C = \frac{A+B}{2} + \nu B \tag{2.8a}$$

$$g = \frac{A-B}{A+B+2\nu B} \tag{2.8b}$$

for plane strain. For optically isotropic (nonbirefringent) materials, $A = B$, resulting in $g = 0$; thus, in this case, $\Delta S_1(x,y) = \Delta S_2(x,y) = \Delta S(x,y)$. For optically anistropic (birefringent) materials, $A \neq B$; thus, $\Delta S_1(x,y) \neq \Delta S_2(x,y)$ in general.

2.2.2.3 Electric Field of the Transmitted Wavefront

The incident wavefront given in Equation (2.1) may be written in the orthogonal principal coordinate system at each point (x,y), such that

$$\boldsymbol{E}_p^{in}(x,y,t) = E_1(x,y,t)\hat{p_1} + E_2(x,y,t)\hat{p_2} \tag{2.9a}$$

$$E_1(x,y,t) = E_x(x,y,t)\cos(\alpha) + E_y(x,y,t)\sin(\alpha) \tag{2.9b}$$

$$E_2(x,y,t) = -E_x(x,y,t)\sin(\alpha) + E_y(x,y,t)\cos(\alpha) \tag{2.9c}$$

$$\hat{p_1} = \cos(\alpha)\hat{\imath} + \sin(\alpha)\hat{\jmath} \tag{2.9d}$$

$$\hat{p_2} = -\sin(\alpha)\hat{\imath} + \cos(\alpha)\hat{\jmath}, \tag{2.9e}$$

where α is the angle between the Cartesian and principal coordinate systems. The effect of transmission through a birefringent plate is the gain of a phase of $k\Delta S_{1,2}$ along the principal directions, resulting in a transmitted wavefront in the principal coordinate system of

$$\boldsymbol{E}_p^{specimen}(x,y,t) = E_1(x,y,t)\exp[jk\Delta S_1(x,y)]\hat{p_1} + E_2(x,y,t)\exp[jk\Delta S_2(x,y)]\hat{p_2}. \tag{2.10}$$

2.2.2.4 Analysis of Interference Pattern

As described in Section 2.2.1, the interference of wavefronts $\boldsymbol{E_{(0,\pm1)}}$ and $\boldsymbol{E_{(\pm1,0)}}$ is the interference of two identical wavefronts $\boldsymbol{E}^{\pm1}$ that are separated by distance d_{shear}, as written in Equation (2.11) for the lateral shearing of the electric field in the x direction with the electric field in the principal coordinate system:

$$\boldsymbol{E}_p^{image}(x,y) = E_1^{image}(x,y)\hat{p_1} + E_2^{image}(x,y)\hat{p_2} \tag{2.11a}$$

$$E_1^{image}(x,y) = E_1^{\pm1}(x,y) + E_1^{\pm1}(x+d_{shear},y) \tag{2.11b}$$

$$E_2^{image}(x,y) = E_2^{\pm1}(x,y) + E_2^{\pm1}(x+d_{shear},y) \tag{2.11c}$$

$$\begin{aligned} E_1^{\pm1}(x,y) = {} & A_x^{\pm1}\cos(\alpha)\exp[j(kz-\omega t+\phi_x+k\Delta S_1(x,y))] \\ & + A_y^{\pm1}\sin(\alpha)\exp[j(kz-\omega t+\phi_y+k\Delta S_1(x,y))] \end{aligned} \tag{2.11d}$$

$$\begin{aligned} E_2^{\pm1}(x,y) = {} & -A_x^{\pm1}\sin(\alpha)\exp[j(kz-\omega t+\phi_x+k\Delta S_2(x,y))] \\ & + A_y^{\pm1}\cos(\alpha)\exp[j(kz-\omega t+\phi_y+k\Delta S_2(x,y))], \end{aligned} \tag{2.11e}$$

where constants $A_x^{\pm1} < A_x$ and $A_y^{\pm1} < A_y$ due to diffraction. The resulting irradiance (intensity) of the interfered wavefronts, I^{image}, in Equation (2.12), is the superposition of the irradiance of the E_1 component, I_1^{image}, and the irradiance of the E_2 component, I_2^{image}, since the principal directions are orthogonal:

$$I^{image} = \langle E_1^{image}E_1^{image*}\rangle_t + \langle E_2^{image}E_2^{image*}\rangle_t = I_1^{image} + I_2^{image} \tag{2.12a}$$

$$
\begin{aligned}
I_1^{image} &= 2(A_x^{\pm 1})^2\cos^2(\alpha) + 2(A_y^{\pm 1})^2\sin^2(\alpha) + 4A_x^{\pm 1}A_y^{\pm 1}\cos(\alpha)\sin(\alpha)\cos(\phi_x - \phi_y) \\
&\quad + \{2(A_x^{\pm 1})^2\cos^2(\alpha) + 2(A_y^{\pm 1})^2\sin^2(\alpha)\}\cos[k\Delta S_1(x,y) - k\Delta S_1(x + d_{shear}, y)] \\
&\quad + 2A_x^{\pm 1}A_y^{\pm 1}\cos(\alpha)\sin(\alpha)\{\cos[\phi_x - \phi_y + k\Delta S_1(x,y) - k\Delta S_1(x + d_{shear}, y)] \\
&\qquad + \cos[\phi_y - \phi_x + k\Delta S_1(x,y) - k\Delta S_1(x + d_{shear}, y)]\} \qquad (2.12b)
\end{aligned}
$$

$$
\begin{aligned}
I_2^{image} &= 2(A_x^{\pm 1})^2\sin^2(\alpha) + 2(A_y^{\pm 1})^2\cos^2(\alpha) - 4A_x^{\pm 1}A_y^{\pm 1}\cos(\alpha)\sin(\alpha)\cos(\phi_x - \phi_y) \\
&\quad + \{2(A_x^{\pm 1})^2\sin^2(\alpha) + 2(A_y^{\pm 1})^2\cos^2(\alpha)\}\cos[k\Delta S_2(x,y) - k\Delta S_2(x + d_{shear}, y)] \\
&\quad - 2A_x^{\pm 1}A_y^{\pm 1}\cos(\alpha)\sin(\alpha)\{\cos[\phi_x - \phi_y + k\Delta S_2(x,y) - k\Delta S_2(x + d_{shear}, y)] \\
&\qquad + \cos[\phi_y - \phi_x + k\Delta S_2(x,y) - k\Delta S_2(x + d_{shear}, y)]\}. \qquad (2.12c)
\end{aligned}
$$

Therefore, the resultant image is the following:

$$
\begin{aligned}
I^{image} &= 2(A_x^{\pm 1})^2 + 2(A_y^{\pm 1})^2 \\
&\quad + \{2(A_x^{\pm 1})^2\cos^2(\alpha) + 2(A_y^{\pm 1})^2\sin^2(\alpha) + 4A_x^{\pm 1}A_y^{\pm 1}\cos(\alpha)\sin(\alpha)\cos(\phi_x - \phi_y)\} \\
&\qquad \cos[k(\Delta S_1(x,y) - \Delta S_1(x + d_{shear}, y))] \\
&\quad + \{2(A_x^{\pm 1})^2\sin^2(\alpha) + 2(A_y^{\pm 1})^2\cos^2(\alpha) - 4A_x^{\pm 1}A_y^{\pm 1}\cos(\alpha)\sin(\alpha)\cos(\phi_x - \phi_y)\} \\
&\qquad \cos[k(\Delta S_2(x,y) - \Delta S_2(x + d_{shear}, y))]. \qquad (2.13)
\end{aligned}
$$

The shearing distance is usually small compared to the field of view of the image ($L^f \times W^f$), so the phase terms of I_1^{image} and I_2^{image}, denoted $\varphi_{1,2}(x,y)$, can be related to the derivatives of $\Delta S_{1,2}$. For $(d_{shear}/\{L^f, W^f\}) \ll 1$,

$$
\varphi_{1,2} = k(\Delta S_{1,2}(x,y) - \Delta S_{1,2}(x + \Delta x, y)) \approx k d_{shear}\frac{\partial \Delta S_{1,2}(x,y)}{\partial x}. \qquad (2.14)
$$

Substituting $\Delta S_{1,2}$ from Equations (2.6a) and (2.6b) into Equation (2.14) connects the phase terms of the interference patterns to stresses:

$$\varphi_{1,2} = kd_{shear}Ch\Big[\frac{\partial(\sigma_1+\sigma_2)}{\partial x} \pm g\frac{\partial(\sigma_1-\sigma_2)}{\partial x}\Big]. \tag{2.15}$$

The equation for the image may be written in terms of two phases, one related to $\sigma_1+\sigma_2$ and the other related to $\sigma_1-\sigma_2$ as follows:

$$I^{image} = I_o + I_{1o}\cos[\varphi_{sum}+\varphi_{diff}] + I_{2o}\cos[\varphi_{sum}-\varphi_{diff}] \tag{2.16a}$$

$$I_o = 2(A_x^{\pm 1})^2 + 2(A_y^{\pm 1})^2 \tag{2.16b}$$

$$I_{1o} = 2(A_x^{\pm 1})^2\cos^2(\alpha) + 2(A_y^{\pm 1})^2\sin^2(\alpha) + 4A_x^{\pm 1}A_y^{\pm 1}\cos(\alpha)\sin(\alpha)\cos(\phi_x-\phi_y) \tag{2.16c}$$

$$I_{2o} = 2(A_x^{\pm 1})^2\sin^2(\alpha) + 2(A_y^{\pm 1})^2\cos^2(\alpha) - 4A_x^{\pm 1}A_y^{\pm 1}\cos(\alpha)\sin(\alpha)\cos(\phi_x-\phi_y) \tag{2.16d}$$

$$\varphi_{sum} = kd_{shear}Ch\frac{\partial(\sigma_1+\sigma_2)}{\partial x} \tag{2.16e}$$

$$\varphi_{diff} = kd_{shear}Chg\frac{\partial(\sigma_1-\sigma_2)}{\partial x}. \tag{2.16f}$$

Since the intensity contains a sum of two sinusoids with the same frequency k, then Equation (2.16a) may be written as a single interference pattern with a phase that is the sum of φ_{sum} and a compound phase φ_c:

$$I^{image} = I_o + I_c\cos[\varphi_{sum}+\varphi_c] \tag{2.17a}$$

$$I_c = \sqrt{I_{1o}^2 + I_{2o}^2 + 2I_{1o}I_{2o}\cos(2\varphi_{diff})} \tag{2.17b}$$

$$\varphi_c = \arctan\Big[\frac{(I_{1o}-I_{2o})\sin(\varphi_{diff})}{(I_{1o}+I_{2o})\cos(\varphi_{diff})}\Big]. \tag{2.17c}$$

A similar result for the y direction shearing may be obtained from the previous analysis, except the derivatives are with respect to y instead of x.

For the specific case of CGS, d_{shear} is $\tilde{\Delta}\lambda/p$, with $k = 2\pi/\lambda$, such that Equations (2.16e) and

(2.16f) become the following:

$$\varphi_{sum} = \frac{2\pi\tilde{\Delta}Ch}{p}\frac{\partial(\sigma_1+\sigma_2)}{\partial x} \tag{2.18a}$$

$$\varphi_{diff} = \frac{2\pi\tilde{\Delta}Chg}{p}\frac{\partial(\sigma_1-\sigma_2)}{\partial x}. \tag{2.18b}$$

For linearly elastic, optically isotropic materials with $g = 0$, then $\varphi_{diff} = 0$, which leads to the classic result for the image irradiance, $I^{isotropic} = I_o\{1 + \cos[\varphi_{sum}]\}$, where the phase term of the interference pattern is related only to the derivative of the sum of principal stresses (Tippur et al., 1991b). As shown above, unlike optically isotropic materials, photoelastic materials produce complicated interference patterns that are difficult to interpret. Fortunately, phase shifting methods in conjunction with incident polarized light allow for the recovery of φ_{sum}, and thus the x or y derivative of $\sigma_1 + \sigma_2$, in full field.

2.2.3 Phase Separation and Interpretation

2.2.3.1 Four-Step Phase Shifting

The phase-shifting interferometry technique used for CGS in this study is a four-step technique with $\pi/2$ phase steps, induced by a lateral shift of $p/4$ in one Ronchi grating in the direction of the dominant lateral shearing, resulting in four phase-shifted interference patterns. For an optically isotropic material, the resultant intensities, which are functions of a single phase term φ, are $I_1 = I_o(1 + \cos(\varphi))$, $I_2 = I_o(1 + \cos(\varphi + \pi/2))$, $I_3 = I_o(1 + \cos(\varphi + \pi))$, and $I_4 = I_o(1 + \cos(\varphi + 3\pi/2))$. The original phase map, φ, is related to these intensities by

$$\varphi = \arctan\left[\frac{I_4 - I_2}{I_1 - I_3}\right] = \arctan\left[\frac{\sin(\varphi)}{\cos(\varphi)}\right]. \tag{2.19}$$

This equation yields a "wrapped" phase map with discontinuities of height $h_d = 2\pi$ since the range of an arctan() formula is 2π when the signs of the numerator and denominator are known. The full range of φ is determined by unwrapping the phase term from the arctan() formula, as described in

Section 2.3.

For optically anisotropic materials for a general initial electric field, from Equation (2.17), the four phase-shifted images are

$$I_1 = I_o + I_c \cos[\varphi_{sum} + \varphi_c] \tag{2.20a}$$

$$I_2 = I_o + I_c \cos[\varphi_{sum} + \varphi_c + \tfrac{\pi}{2}] \tag{2.20b}$$

$$I_3 = I_o + I_c \cos[\varphi_{sum} + \varphi_c + \pi] \tag{2.20c}$$

$$I_4 = I_o + I_c \cos[\varphi_{sum} + \varphi_c + \tfrac{3\pi}{2}]. \tag{2.20d}$$

The phase map of $\varphi_{sum} + \varphi_c$ may be recovered using the typical arctan() formula similar to Equation (2.19) such that

$$\varphi_{sum} + \varphi_c = \arctan\left[\frac{I_4 - I_2}{I_1 - I_3}\right] = \arctan\left[\frac{I_c \sin(\varphi_{sum} + \varphi_c)}{I_c \cos(\varphi_{sum} + \varphi_c)}\right], \tag{2.21}$$

but Equation (2.21) is indeterminate when $I_c = 0$, so this equation is only true for $I_c \neq 0$. Specifically polarized input electric fields allow for separation of φ_{sum} from φ_c, as discussed below.

2.2.3.2 Two Methods for Determination of the First Derivative of $\sigma_1 + \sigma_2$

The first method to recover φ_{sum} involves capturing images from a pure $E_x\hat{\imath}$ input electric field and from a pure $E_y\hat{\jmath}$ input electric field. From Equation (2.17), for $A_x = A_o$ and $A_y = 0$, and thus $A_x^{\pm 1} = A_o^{\pm 1}$ and $A_y^{\pm 1} = 0$, the image is

$$I^{Ex} = I_o^{Ex} + I_c^{Ex} \cos[\varphi^{Ex}] \tag{2.22a}$$

$$\varphi^{Ex} = \varphi_{sum} + \varphi_{\alpha d} \tag{2.22b}$$

$$I_o^{Ex} = 2(A_o^{\pm 1})^2 \tag{2.22c}$$

$$I_c^{Ex} = I_o^{Ex}\sqrt{1 - \sin^2(2\alpha)\sin^2(\phi_{diff})} \tag{2.22d}$$

$$\varphi_{\alpha d} = \arctan[\cos(2\alpha)\tan(\phi_{diff})] \tag{2.22e}$$

where $\varphi_{\alpha d}$ is a compound phase related to α and φ_{diff}. Similarly, for $A_x = 0$ and $A_y = A_o$, and thus $A_x^{\pm 1} = 0$ and $A_y^{\pm 1} = A_o^{\pm 1}$ from Equation (2.17), the image is

$$I^{Ey} = I_o^{Ey} + I_c^{Ey} \cos[\varphi^{Ey}] \tag{2.23a}$$

$$\varphi^{Ey} = \varphi_{sum} - \varphi_{\alpha d} \tag{2.23b}$$

$$I_o^{Ey} = 2(A_o^{\pm 1})^2 \tag{2.23c}$$

$$I_c^{Ey} = I_o^{Ey}\sqrt{1 - \sin^2(2\alpha)\sin^2(\phi_{diff})}. \tag{2.23d}$$

If phase-shifted images for these two configurations are taken for the same field of view for the same deformation state in the specimen, then the φ^{Ex} and φ^{Ey} fields are calculated by Equation (2.21). For both of these fields, Equation (2.21) does not hold for $\sqrt{1 - \sin^2(2\alpha)\sin^2(\phi_{diff})} = 0$, but this is likely true for only a few points in the field of view. Since I_c^{Ex} and I_c^{Ey} are always nonnegative, then Equation (2.21) can express the absolute signs of the numerator and denomiator separately for each configuration, and the height discontinuity of the wrapped phases are $h_d = 2\pi$, as explained in Section 2.2.3.1. After unwrapping these fields, φ_{sum} may be separated from the other phase, meaning $\varphi_{sum} = (\varphi^{Ex} + \varphi^{Ey})/2$. Additionally, $\varphi_{\alpha d} = (\varphi^{Ex} - \varphi^{Ey})/2 = \arctan[\cos(2\alpha)\tan(\phi_{diff})]$. Section 2.2.3.3 describes possible configurations of polarization optics to achieve this case.

Another possible method for determining φ_{sum} only requires one set of phase-shifted images. If the input electric field is circularly polarized such that $A_x = A_y = A_o/\sqrt{2}$, $\phi_x = \phi_y \pm \pi/2$, and consequently $A_x^{\pm 1} = A_y^{\pm 1} = A_o^{\pm 1}/\sqrt{2}$ using polarization optics, then the image given in Equation (2.17) may be simplified to

$$I^{circ} = I_o^{circ} + I_c^{circ} \cos[\varphi_{sum}] \tag{2.24a}$$

$$I_o^{circ} = 2(A_o^{\pm 1})^2 \tag{2.24b}$$

$$I_c^{circ} = I_o^{circ} \cos[\varphi_{diff}]. \tag{2.24c}$$

If phase-shifted images for this configuration are analyzed using Equation (2.21), then φ_{sum} is determined by

$$\varphi_{sum} = \arctan\left[\frac{I_4 - I_2}{I_1 - I_3}\right] = \arctan\left[\frac{\sin(\varphi_{sum})\cos(\varphi_{diff})}{\cos(\varphi_{sum})\cos(\varphi_{diff})}\right]. \tag{2.25}$$

This equation is only true for (x, y) coordinates where $\cos(\varphi_{diff}) \neq 0$, since the argument of the arctan() is indeterminate where $\cos(\varphi_{diff}) = 0$. Since $\cos(\varphi_{diff})$ is in the numerator and the denominator, the argument to the arctan() formula in Equation (2.25) cannot express the absolute signs of the numerator and denominator separately, so an arctan() algorithm that gives values from $-\pi/2$ to $\pi/2$ should be used. Thus, the wrapped phase term from this formula should have discontinuities of height $h_d = \pi$ instead of 2π. If the other arctan() algorithm that gives values from $-\pi$ to π is used, then the wrapped phase term is incorrect. After unwrapping, with the full range of φ_{sum} from wavefront shearing in the x direction and Equation (2.18a), the full-field x-derivative of $\sigma_1 + \sigma_2$ may be determined by

$$\frac{\partial(\sigma_1 + \sigma_2)}{\partial x} = \frac{p}{2\pi\tilde{\Delta}Ch}\varphi_{sum}. \tag{2.26}$$

2.2.3.3 Polarization Optics

Polarization optics, such as a linear polarizer, $\lambda/2$ plate, and $\lambda/4$ plate, allow for manipulation of the input electric field. A general schematic of configurations useful here is shown in Figure 2.2. To obtain pure $E_x\hat{\imath}$ or $E_y\hat{\jmath}$ fields with only a simple change required to switch between the two inputs, a polarizer and a $\lambda/2$ plate are used; this combination of optics also gives the same range of intensity for both input types, allowing for optimization of the intensity for the experimental equipment, helping to prevent camera saturation. The objective is to start with either pure $E_x\hat{\imath}$ or $E_y\hat{\jmath}$ after the polarizer at $\rho = m\pi/2$, m integer, then maintain that field through the $\lambda/2$ plate with $\xi = \rho$ for the first image, and then obtain the opposite field by setting the $\lambda/2$ to $\xi = \rho \pm (2n+1)\pi/4$, n integer.

To create circularly polarized light, the collimated laser beam passes through a polarizer with polarization axis at angle ρ to the x axis and then through a $\lambda/4$ plate with fast axis at angle ξ to the x axis with $\rho - \xi = \pm\pi/4$. Other combinations of optics can produce the desired equal amplitudes

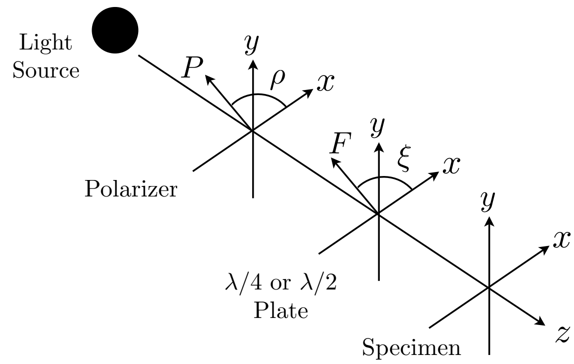

Figure 2.2: Polarization optics before the transparent specimen: two configurations with either a $\lambda/4$ or $\lambda/2$ plate before the specimen

of the E_x and E_y fields, but for clarity and simplicity, these two configurations are considered here. Table 2.1 gives the specific polarization optic configurations used in this study, stating the angles of the optics, the amplitudes of the electric field components, and the resultant phase term of the interference pattern in Equation (2.17).

ρ of Polarizer	ξ of $\lambda/4$ Plate	ξ of $\lambda/2$ Plate	$\lvert E_x \rvert$	$\lvert E_y \rvert$	Phase Determined
0	$\pi/4$	-	$A_x/\sqrt{2}$	$A_x/\sqrt{2}$	φ_{sum}
0	-	0	A_x	0	$\varphi_{sum} + \varphi_{\alpha d}$
0	-	$\pi/4$	0	A_x	$\varphi_{sum} - \varphi_{\alpha d}$

Table 2.1: Polarization optic configurations used in this study

2.3 Experimental Verification

The experimental verification was performed on a 12.7 mm $\times$ 12.7 mm square plate with thickness h = 1.0 mm and with a 60^o V-notch cut out of the side of the plate, as shown in Figure 2.3. The depth of the V-notch, d, is 6.35 mm, and the V-notch opening width, w, is 7.34 mm. The plate is polycarbonate, which is a thermoplastic polymer that is highly photoelastic, with absolute photoelastic constants $A = -2.45\times10^{-11}$ m^2/N and $B = -9.38\times10^{-11}$ m^2/N (Shimizu et al., 1998). This plastic has a Young's modulus of $E = 2.3$ GPa, Poisson's ratio of $\nu = 0.36$, and refractive index of $n_o = 1.586$. The photoelasticity-related constants used in calculating φ_{sum} and φ_{diff} are therefore $C = 1.51 \times 10^{-10}$ m^2/N and $g = 0.23$. The specimen is from a polycarbonate sheet with residual stress due to forming; for this specimen in the field of view, the through-thickness average residual stresses are determined to be $\sigma_{xx}^{resid} \approx 1.59$ MPa, $\sigma_{yy}^{resid} \approx -1.9$ MPa, and $\sigma_{xy}^{resid} \approx -0.1$ MPa. This residual stress is assumed to be constant throughout the field of view. The procedure for determining these residual stresses is explained in Section 3.3.

In the following example, the specimen is compressed by 14.5 N (1.14 MPa) along the y axis. The experimental optical parameters are the following: the monochromatic CCD camera is the IMPERX IPX-1M48-L with a 1000×1000 pixel chip; the field of view is 3.77 mm $\times$ 3.77 mm; the image resolution is 3.8 μm; the Ronchi grating pitch, p, is 1 mm/40; the grating separation, $\tilde{\Delta}$, is 12.48 mm; the wavelength of light from the linearly polarized HeNe laser is 632. nm; and the lateral shearing distance, d_{shear}, is 313 μm.

Williams (1952) presented a derivation of the stress fields of a thin plate with an "angular corner" cut out of it under uniaxial tensile load with various boundary conditions. This derivation most commonly utilized for the derivation of the stress field of a Mode I crack, which is a corner of angle 0^o, in a plate. Here, the derivation is applied to a thin plate with a 60^o V-shaped notch under uniaxial compression, as shown in Figure 2.3, and is detailed in Appendix B. The 2D stress solution in polar coordinates is as follows:

$$\begin{aligned}
\sigma_{rr}(r,\theta) = \frac{C_f \sigma_{app} d^{1-\lambda_o}}{(r)^{1-\lambda_o}} \Big\{ &- \lambda_o(\lambda_o+1)\cos[(\lambda_o+1)\theta] \\
&+ \lambda_o(\lambda_o-3)\frac{\cos[(\lambda_o+1)\frac{\zeta}{2}]}{\cos[(\lambda_o-1)\frac{\zeta}{2}]}\cos[(\lambda_o-1)\theta]\Big\}, \qquad (2.27a)\\
\sigma_{\theta\theta}(r,\theta) = \frac{C_f \sigma_{app} d^{1-\lambda_o}\lambda_o(\lambda_o+1)}{(r)^{1-\lambda_o}} \Big\{ &\cos[(\lambda_o+1)\theta] \\
&- \frac{\cos[(\lambda_o+1)\frac{\zeta}{2}]}{\cos[(\lambda_o-1)\frac{\zeta}{2}]}\cos[(\lambda_o-1)\theta]\Big\}, \qquad (2.27b)\\
\sigma_{r\theta}(r,\theta) = \frac{C_f \sigma_{app} d^{1-\lambda_o}\lambda_o}{(r)^{1-\lambda_o}} \Big\{ &(\lambda_o+1)\sin[(\lambda_o+1)\theta] \\
&- (\lambda_o-1)\frac{\cos[(\lambda_o+1)\frac{\zeta}{2}]}{\cos[(\lambda_o-1)\frac{\zeta}{2}]}\sin[(\lambda_o-1)\theta]\Big\}, \qquad (2.27c)
\end{aligned}$$

where σ_{app} is the far-field applied stress, $\lambda_o = 0.512221$ for a 60^o V-notch, C_f is a fitting parameter depending on specimen geometry, $\zeta = 5\pi/3$ is material remaining after V-notch is cut out, and d is the depth of the V-notch. A constant residual stress, as given above for this specimen, is added to this theoretical stress field solution in Equations (2.27a)–(2.27c). For this particular example, the applied stress σ_{app} is -1.39MPa, and the fitting parameter C_f is 0.57, as determined by comparing the experimental and theoretical in-plane stress fields. The equations for the x derivatives of $\sigma_1 + \sigma_2$ and of $\sigma_1 - \sigma_2$ in terms of the polar stresses, α and θ is provided in Appendix A.

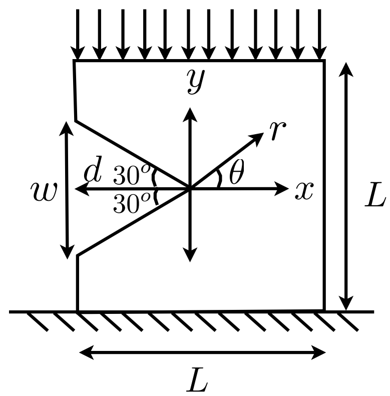

Figure 2.3: Schematic of a compressed polycarbonate plate with a side V-notch

2.3.1 Images for Compressed Polycarbonate Specimen

Figure 2.4 shows the experimental and theoretical images of I_1 for horizontal shear of the configuration shown in Figure 2.3. In Figures 2.4(a) and 2.4(c), the images for the pure $E_x\hat{\imath}$ and pure $E_y\hat{\jmath}$ fields, respectively, have interference fringes with good fringe contrast because I_c^{Ex} and I_c^{Ey} vary little in the field of view. The image in Figure 2.4(e) of the $|E_x| = |E_y|$ fields using the $\lambda/4$ plate method shows discontinuous fringes, evidence of $I_c^{circ} = I_o^{circ}\cos(\varphi_{diff})$ modulating $\cos(\varphi_{sum})$. Clearly, these interference patterns cannot yield the desired phase terms as they are, but require phase shifting. Figures 2.4(b), 2.4(d), and 2.4(f) are the theoretical images for the pure $E_x\hat{\imath}$, pure $E_y\hat{\jmath}$, and $|E_x| = |E_y|$ input fields, which compare well to the experimental fields in shape and fringe density. The residual stress may not be uniform near the V-notch cut-out because some of the residual stress may be relieved during specimen preparation; since the theoretical field is based on a uniform residual stress assumption, then the theoretical and experimental α have slight differences for $|\theta| > \pi/2$, resulting in slight shape differences in comparing theoretical and experimental images for $|\theta| > \pi/2$. The slightly larger lobes near $\theta = 0$ are mostly likely due to slightly higher applied stress on this side because of nonuniform compressive loading. Despite these slight differences due to experimental error and residual stress in the material, near $\theta = 0$, the experimental image from the pure $E_x\hat{\imath}$ input has the expected wider lobe, the experimental image from the $E_y\hat{\jmath}$ input has the expected narrower lobe, and the experimental image from the $|E_x| = |E_y|$ input field indicates the same interference beading as the theoretical image. Figures 2.5, 2.6, and 2.7 show the sets of four experimental phase-shifted images for pure $E_x\hat{\imath}$ input, pure $E_y\hat{\imath}$ input, and circularly polarized electric field input, respectively. The interference patterns within a set of phase-shifted images clearly are slightly different, though they have the same fringe density and shape, indicating a constant phase shift added to the interference pattern over the entire field between each subsequent phase-shifted image. The part of the image with the V-notch cut-out clearly shows a uniform $\pi/2$ phase shift in the intensity between the images since this part of the image comes from light passing through air, which does not change with load like the intensity from the specimen does.

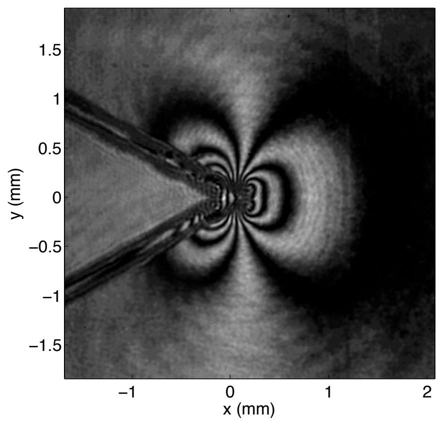

(a) Experimental I^{Ex}

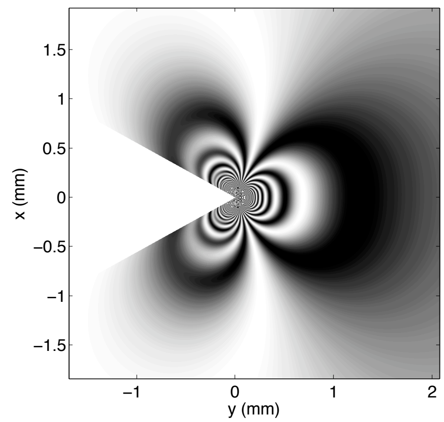

(b) Theoretical I^{Ex}

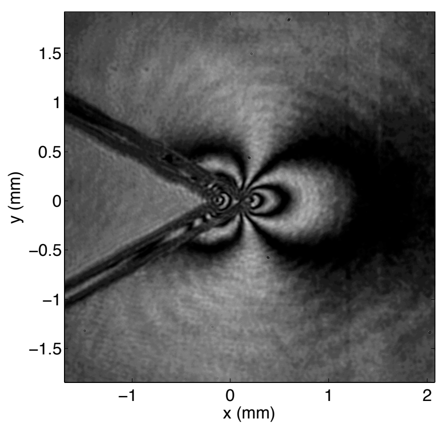

(c) Experimental I^{Ey}

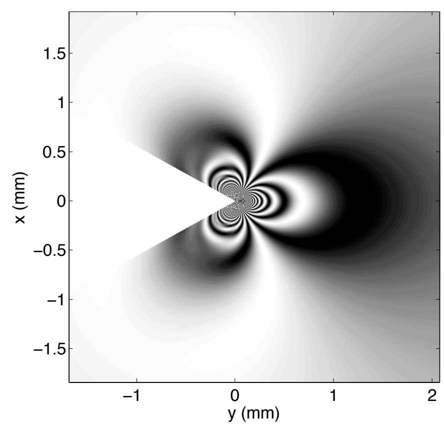

(d) Theoretical I^{Ey}

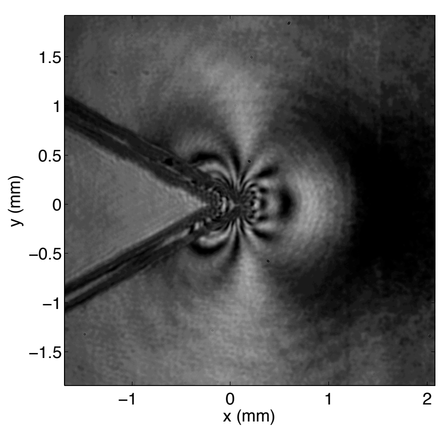

(e) Experimental I^{circ}

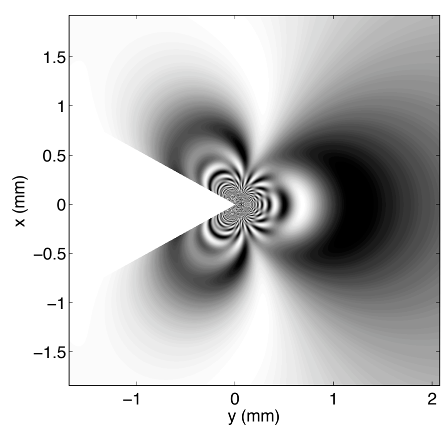

(f) Theoretical I^{circ}

Figure 2.4: Experimental and theoretical images for horizontal shear with good comparison: (a) experimental $I^{Ex} = I_o^{Ex} + I_c^{Ex} \cos[\varphi_{sum} + \varphi_{\alpha d}]$; (b) theoretical $I^{Ex} = I_o^{Ex} + I_c^{Ex} \cos[\varphi_{sum} + \varphi_{\alpha d}]$; (c) experimental $I^{Ey} = I_o^{Ey} + I_c^{Ey} \cos[\varphi_{sum} - \varphi_{\alpha d}]$; (d) theoretical $I^{Ey} = I_o^{Ey} + I_c^{Ey} \cos[\varphi_{sum} - \varphi_{\alpha d}]$; (e) experimental $I^{circ} = I_o^{circ} + I_o^{circ} \cos[\varphi_{diff}] \cos[\varphi_{sum}]$; and (f) theoretical $I^{circ} = I_o^{circ} + I_o^{circ} \cos[\varphi_{diff}] \cos[\varphi_{sum}]$ [Note: V-notch region masked in white in theoretical images]

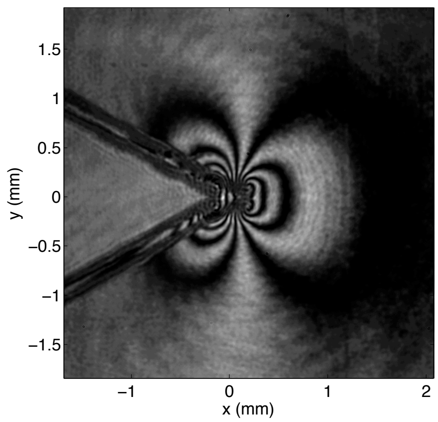

(a) I_1^{Ex}

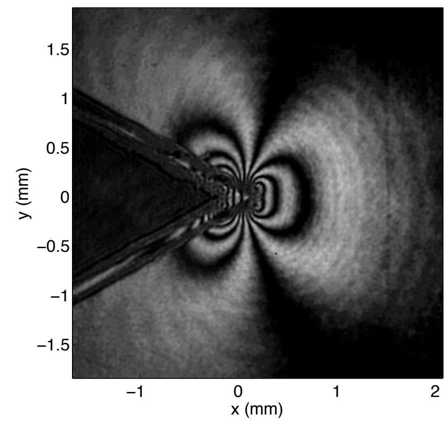

(b) I_2^{Ex}

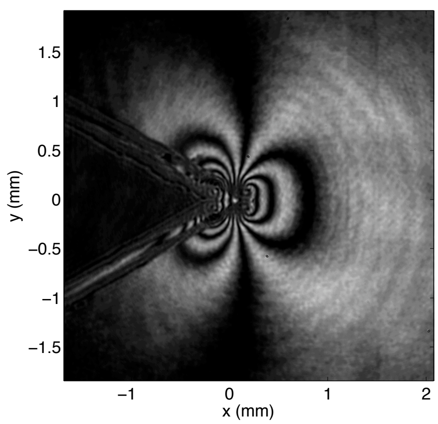

(c) I_3^{Ex}

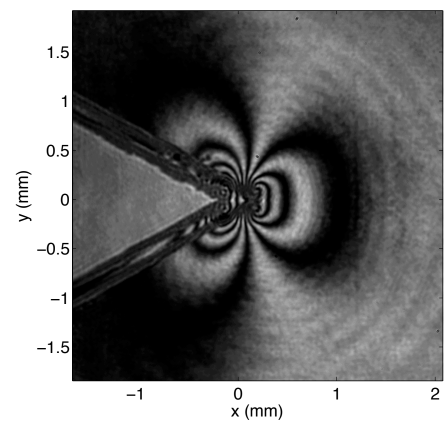

(d) I_4^{Ex}

Figure 2.5: Experimental phase-shifted images from horizontal shearing CGS using pure $E_x\hat{\imath}$ input for compressed polycarbonate V-notch plate

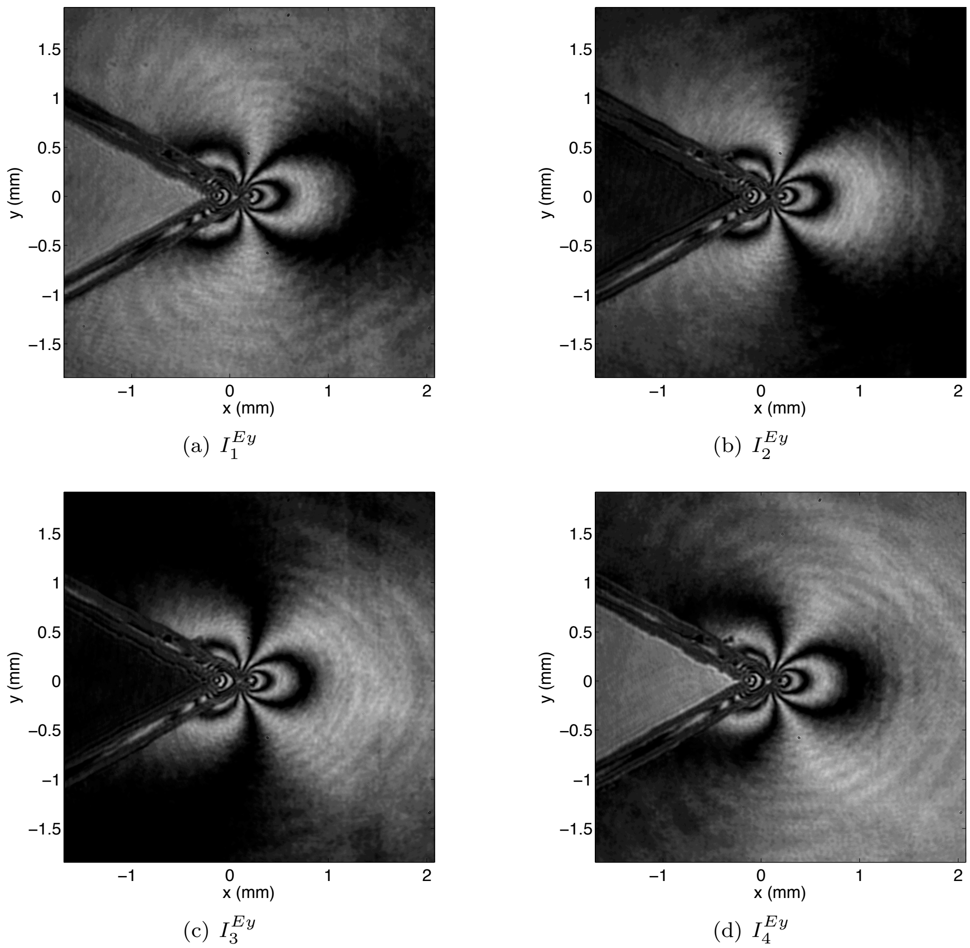

(a) I_1^{Ey}

(b) I_2^{Ey}

(c) I_3^{Ey}

(d) I_4^{Ey}

Figure 2.6: Experimental phase-shifted images from horizontal shearing CGS using pure $E_y\hat{\jmath}$ input for compressed polycarbonate V-notch plate

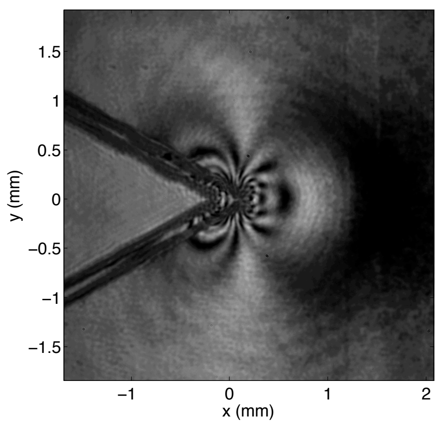

(a) I_1^{circ}

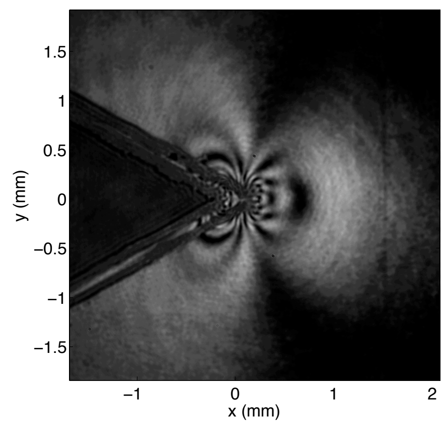

(b) I_2^{circ}

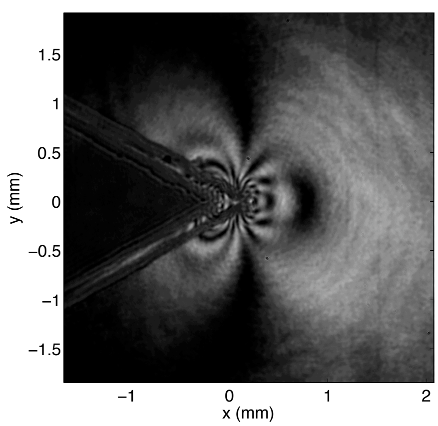

(c) I_3^{circ}

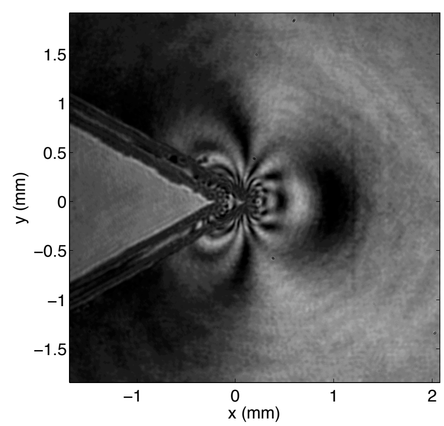

(d) I_4^{circ}

Figure 2.7: Experimental phase-shifted images from horizontal shearing CGS using the $\lambda/4$ polarization method for compressed polycarbonate V-notch plate

2.3.2 Image Analysis

Figure 2.8 includes the experimental and theoretical wrapped phase fields for φ^{Ex} and φ^{Ey}. The general three-lobed shape in each experimental field compares well with the theoretical fields, though the differences between the theoretical and experimental are most likely due to slightly nonuniform compressive loading of the specimen. The experimental and theoretical wrapped phase field for the φ_{sum} from Equation (2.25) from the $\lambda/4$ plate method and the theoretical $\cos(\varphi_{diff})$ field are shown in Figure 2.9. In Figure 2.9(a), the fringes have regions in a four-lobed clover leaf pattern with greater noise and scatter, which corresponds to regions near $\cos(\varphi_{diff}) = 0$ boundaries found in Figure 2.9(c); the noise and scatter are expected since Equation (2.25) is indeterminate for $\cos(\varphi_{diff}) = 0$ and since the experimental data would be dominated by the division of small numbers from $\cos(\varphi_{diff})$ in the numerator and denominator. The theoretical wrapped φ_{sum} field in Figure 2.9(b) does not have these poor contrast regions because the theoretical data has exact cancellation of the $\cos(\varphi_{diff})$ in the arctan() formula.

Ghiglia and Romero (1994) developed robust 2D phase unwrapping methods for interferometric fringes with noise. The general phase unwrapping problem is equivalent to the solution to the Poisson's equation with Neumann boundary conditions, which may be solved by fast cosine transform (FCT) methods. With experimental data that may contain noise and measurement errors, the reliability of the wrapped phase information at each pixel should be considered. Since the FCT method cannot incorporate a weight function, a weighted phase unwrapping method based on preconditioned conjugate gradient (PCG) numerical methods was developed. The PCG unwrapping method falls under the category of global minimization, meaning the method attempts to minimize discontinuities globally based on the assumption of a continuous function. If a discontinuity or isolated region is physically allowed in the field as in the case of a regional boundary, then those regions may be weighted such that the PCG algorithm is not required to meet the phase continuity constraint across that region. PCG methods have the added benefit of robust convergence.

The weight function used in this study begins with a quality condition where phase jumps in the wrapped phase of size h_d or nearly zero are considered very reliable with weight of close to one,

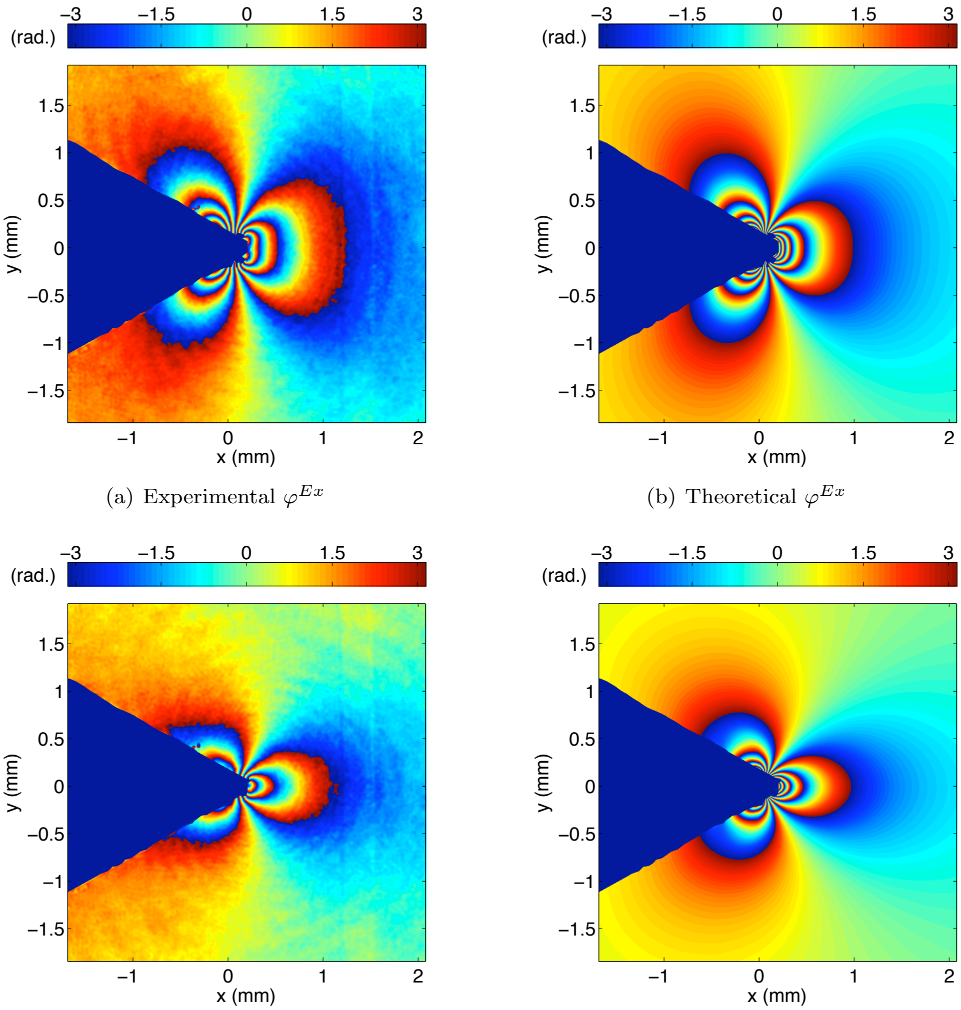

(a) Experimental φ^{Ex}

(b) Theoretical φ^{Ex}

(c) Experimental φ^{Ey}

(d) Theoretical φ^{Ey}

Figure 2.8: Experimental and theoretical wrapped phase maps (in radians) from horizontal shearing CGS with V-notch masked in white: (a) experimental $\varphi^{Ex} = \varphi_{sum} + \varphi_{\alpha d}$; (b) theoretical $\varphi^{Ex} = \varphi_{sum} + \varphi_{\alpha d}$; (c) experimental $\varphi^{Ey} = \varphi_{sum} - \varphi_{\alpha d}$; and (d) theoretical $\varphi^{Ey} = \varphi_{sum} - \varphi_{\alpha d}$

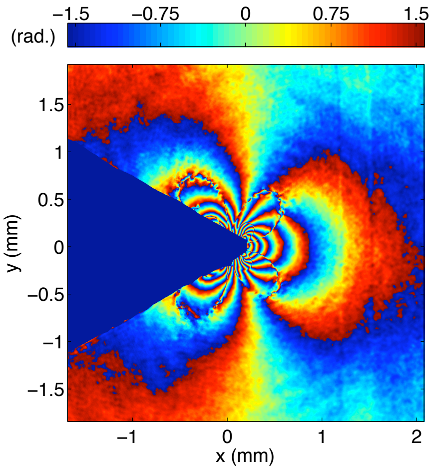

(a) Experimental φ_{sum}

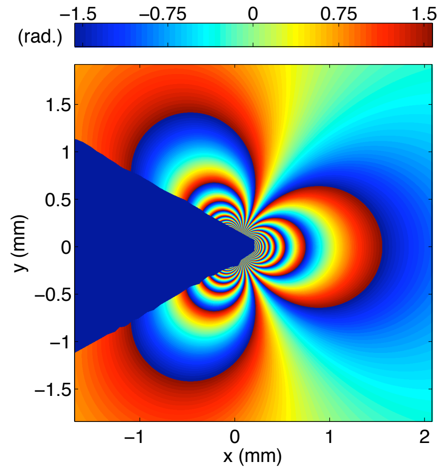

(b) Theoretical φ_{sum}

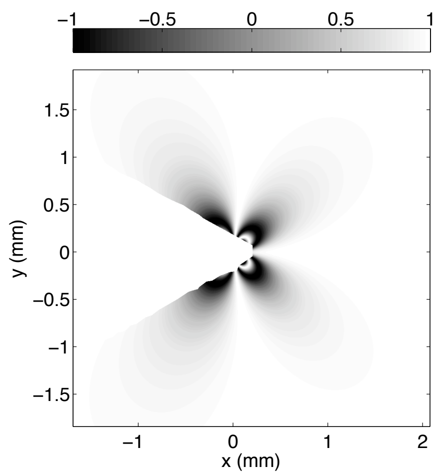

(c) Theoretical $\cos(\varphi_{diff})$

Figure 2.9: Wrapped phase maps from $\lambda/4$ plate method (in radians) with V-notch masked in white: (a) experimental φ_{sum} for $\cos(\varphi_{diff}) \neq 0$; (b) theoretical φ_{sum}; and (c) theoretical $\cos(\varphi_{diff})$ field with its four-lobed clover leaf pattern

while jumps of $h_d/2$ are considered unreliable with weight of zero. The following formula is applied to each pixel to develop the weight function $\mathbf{W}$, where $\Delta\psi_k$ is the wrapped phase difference between the k-th nearest neighbor of the (i, j) pixel (Baldi et al., 2002):

$$W_{i,j} = \prod_{k=1}^{8} \frac{1}{2}\{\cos(2\pi\frac{\Delta\psi_k}{h_d}) + 1\}. \tag{2.28}$$

Additionally, physical boundaries and regions in the field with no photoelastic material, as with the V-notch in the example, are given a weight of zero. Based on *a priori* knowledge of the experiment, the weight of regions with high concentrations of fringes that cannot be resolved with the given pixel resolution are also set to zero to reduce unwrapping errors near these regions.

Figure 2.10 shows the unwrapped φ^{Ex} and φ^{Ey} fields for experimental and theoretical data. The PCG method successfully unwraps the phase discontinuities in these fields; the data from the air in the V-notch region does not propagate into the polycarbonate data due to the weight function; the unwrapped φ^{Ex} and φ^{Ey}, like the theoretical fields, have the general monotonic increase or decrease as $r \to 0$ towards the notch tip.

Figure 2.11(a) is the experimental φ_{sum} determined by the $(\varphi^{Ex} + \varphi^{Ey})/2$, and Figure 2.11(b) is the unwrapped experimental φ_{sum} from the $\lambda/4$ plate method. In comparison, qualitatively, the φ_{sum} field from the $\lambda/4$ plate method does not agree with the theoretical field in Figure 2.11(c) as well as the φ_{sum} from the pure $E_x\hat{\imath}$ and pure $E_y\hat{\jmath}$ fields agrees with the theoretical field; some minor unwrapping errors are evident in Figure 2.11(b) near the $\cos(\varphi_{diff}) = 0$ regions in the four-lobed clover leaf pattern seen in Figure 2.9(c). Additionally, the experimental $\varphi_{\alpha d}$ in Figure 2.11(d) from the $(\varphi^{Ex} - \varphi^{Ey})/2$ has a four-lobed clover leaf pattern like the theoretical $\varphi_{\alpha d}$ field in Figure 2.11(e).

One measure of the global error is the root mean square deviation (RMSD) normalized by the range of experimental data, denoted NRMSD. Only data points not masked by notch mask are considered here. Table 2.2 reports the error analysis of several fields. The NRMSD is low for each of the fields, with the largest error in the φ^{Ey} at only 2.1%. As is evident in Figure 2.12(a) and (b), which show the difference between the theoretical and the two experimental φ_{sum} fields,

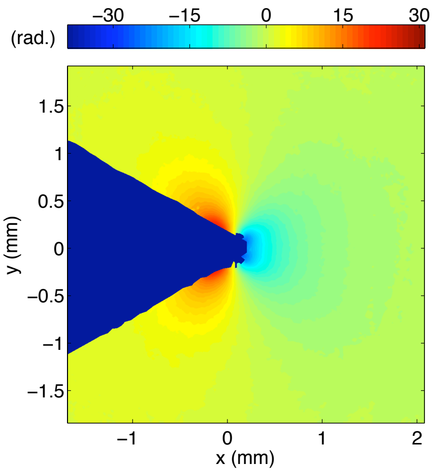

(a) Experimental φ^{Ex}

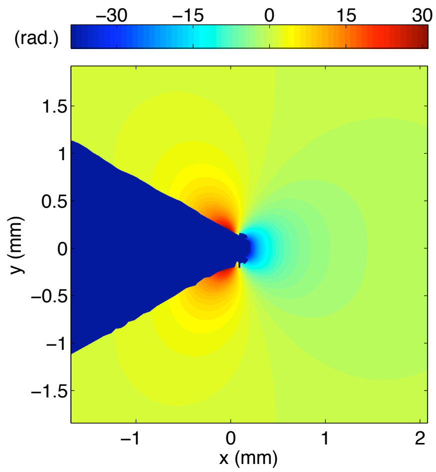

(b) Theoretical φ^{Ex}

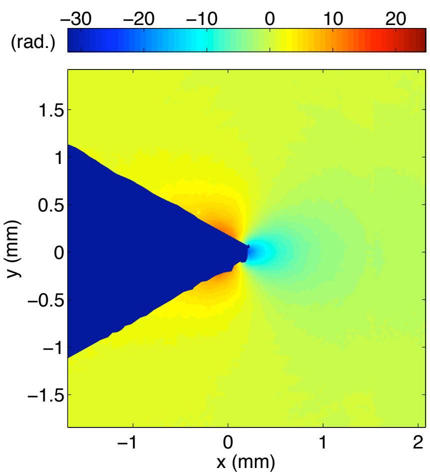

(c) Experimental φ^{Ey}

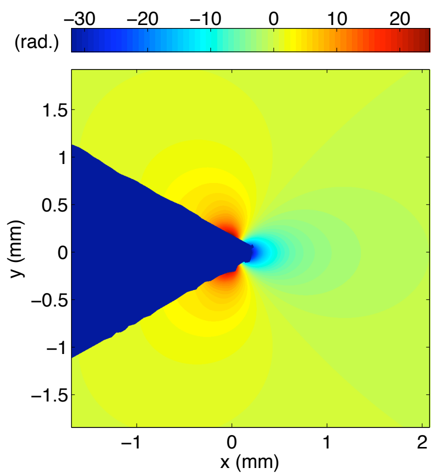

(d) Theoretical φ^{Ey}

Figure 2.10: Experimental and theoretical unwrapped phase term from the pure $E_x\hat{\imath}$ and pure $E_y\hat{\jmath}$ fields (in radians) from horizontal shearing CGS with V-notch masked in white

the greatest errors are close to the notch tip, which is understandable since the stress derivative changes so rapidly near the notch tip that the small d_{shear} assumption, which allows the phase to be related to stress derivatives in Equation (2.15), breaks down. The unwrapping errors due to the $\cos(\varphi_{sum}) = 0$ regions are in the four-lobed clover leaf pattern in Figure 2.12(b), leading to a slightly higher NRMSD for the φ_{sum} from the $\lambda/4$ plate method than for the φ_{sum} from the pure $E_x\hat{\imath}$ and pure $E_y\hat{\jmath}$ fields data. Both methods of determining φ_{sum} give reasonable global error, though the pure $E_x\hat{\imath}$ and pure $E_y\hat{\jmath}$ fields method does seem to better confine the error to near the notch tip and is not affected by the $\cos(\varphi_{diff})$ issue. Another benefit of the the pure $E_x\hat{\imath}$ and pure $E_y\hat{\jmath}$ fields method is the determination of $\varphi_{\alpha d}$, which has low error as well; the difference between the theoretical and experimental $\varphi_{\alpha d}$ is shown in Figure 2.12(c), confining the error to near the notch tip. The excellent agreement of the experimental data with theoretical data in this example demonstrates that the use of polarization optics and phase shifting can successfully extract phase data from complicated interference images that have physical meaning in terms of stress in the photoelastic material, as explained in the previous analysis in Section 2.2.2.

Phase	RMSD (in rad.)	Data Range (in rad.)	NRMSD (No units)
φ^{Ex}	0.73	49.14	0.015
φ^{Ey}	0.52	34.05	0.015
φ_{sum} from $\lambda/4$ method	0.72	34.57	0.021
$\varphi_{sum} = (\varphi^{Ex} + \varphi^{Ey})/2$ method	0.57	38.94	0.015
$\varphi_{\alpha d} = (\varphi^{Ex} - \varphi^{Ey})/2$ method	0.26	17.85	0.015

Table 2.2: Error analysis for various experimental fields for horizontal shear

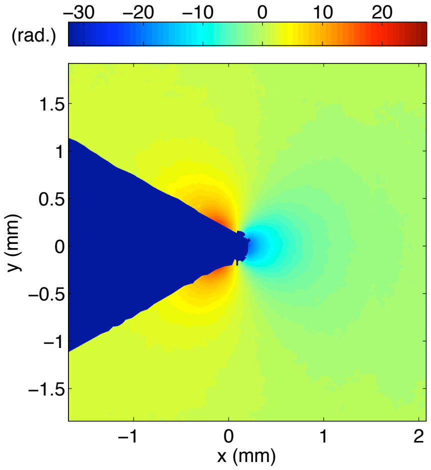

(a)

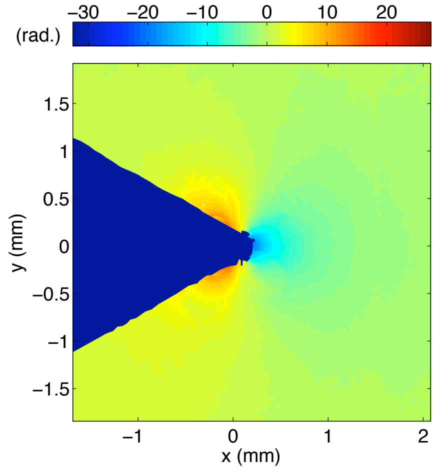

(b)

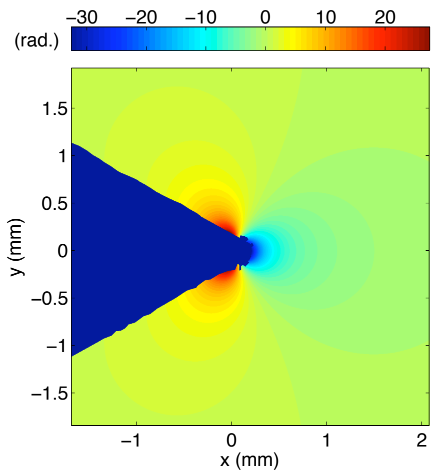

(c)

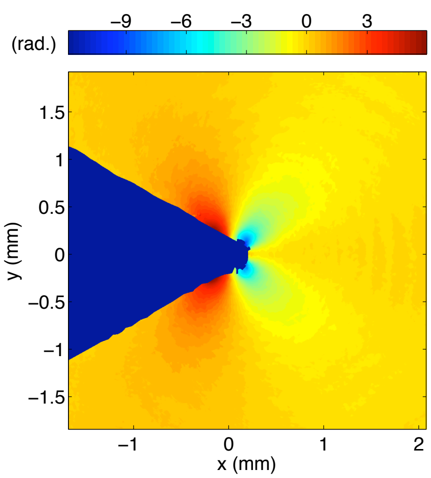

(d)

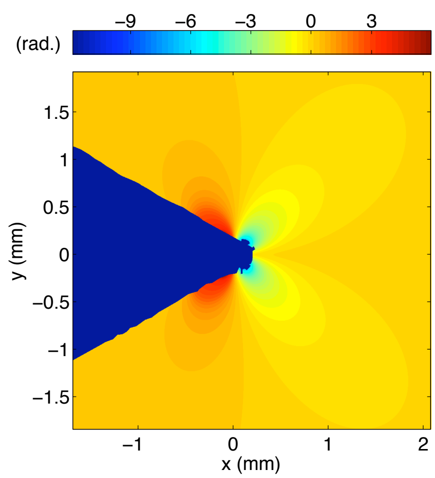

(e)

Figure 2.11: Experimental and theoretical phase maps of φ_{sum} and φ_{diff} (in radians) from horizontal shearing CGS with V-notch masked in white: (a) experimental $\varphi_{sum} = (\varphi^{Ex} + \varphi^{Ey})/2$; (b) experimental φ_{sum} from the $\lambda/4$ method (c) theoretical φ_{sum}; (d) experimental $\varphi_{\alpha d} = (\varphi^{Ex} - \varphi^{Ey})/2$; and (e) theoretical $\varphi_{\alpha d}$

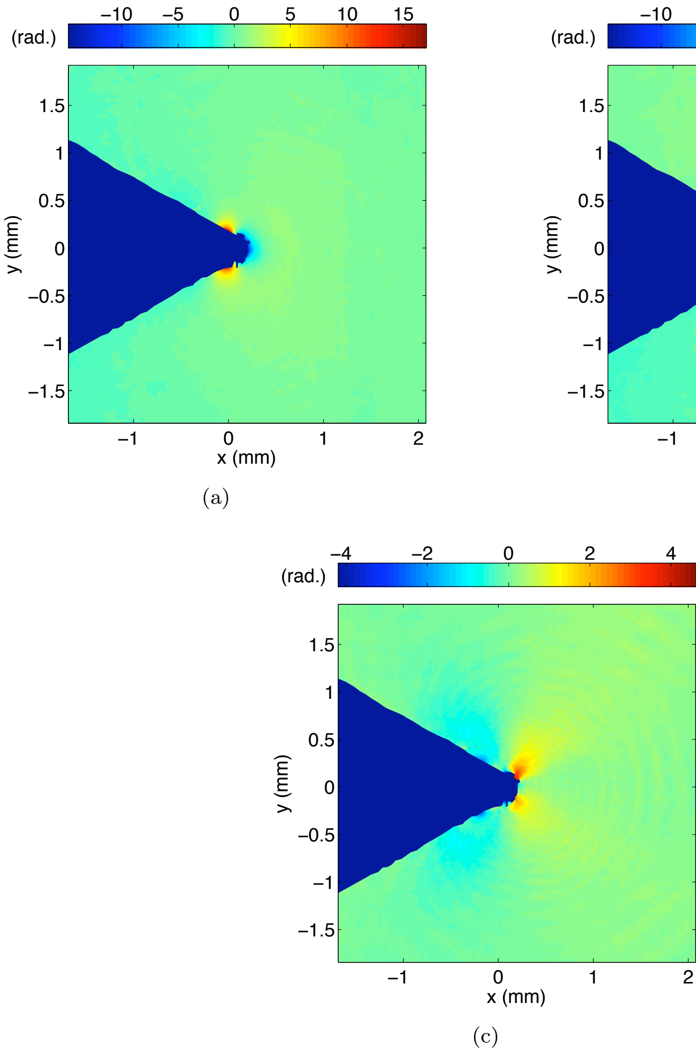

Figure 2.12: Difference between theoretical and experimental φ_{sum} and $\varphi_{\alpha d}$ (in radians) from horizontal shearing CGS with V-notch masked in white: (a) comparison for $\varphi_{sum} = (\varphi^{Ex} + \varphi^{Ey})/2$; (b) comparison for φ_{sum} from the $\lambda/4$ method; and (c) comparison for $\varphi_{\alpha d} = (\varphi^{Ex} - \varphi^{Ey})/2$

2.4 Conclusions

Wavefront shearing interferometry, specifically coherent gradient sensing (CGS), is used to analyze a wavefront transmitted through a photoelastic material. A detailed analysis of the transmitted wavefront properties, of the lateral shearing, and of the resulting interference patterns depending on the polarization of the electric field input to the photoelastic material is provided for a general wavefront shearing interferometer, with some specialization for CGS. Phase information related to stress gradients in a deformed photoelastic material may be extracted from the complicated interference pattern by the use of polarization optics and phase shifting. This is experimentally verified using CGS on a compressed polycarbonate plate with a V-notch. Using this general analysis, stress information may be obtained in full field for photoelastic materials with input electric field polarization control and any phase-shifting transmission wavefront shearing interferometry.

Chapter 3

Phase-Shifting Interferometry and Combined Methods

3.1 Introduction

The chapter describes the hybrid phase-shifting full-field experimental CGS-photoelasticity method for in-plane tensorial stress determination and the experimental verification of the method. Section 3.2 presents the two experimental methods and how these are combined to determine the stress fields, detailing phase-shifting photoelasticity, the hybrid optical setup, and phase analysis methods. Section 3.3 describes the experimental verification of this method for stress determination in a compressed polycarbonate plate with a side V-notch and provides comparison with theoretical stress fields. This chapter is based on Kramer et al. (2009a), but provides more details of potential error sources and of the experimental analysis. Also, the comparison of experimental and theoretical stress fields has improved agreement upon further analysis after publication of the paper.

3.2 Phase-Shifting Interferometric Methods

3.2.1 Photoelasticity

Photoelasticity utilizes the stress-optic effect in certain materials that have a stress-induced birefringence proportional to the difference of the in-plane principal stresses: $n_1 - n_2 = c_o(\sigma_1 - \sigma_2)$, where c_o is the relative stress-optic coefficient. A detailed derivation of this equation may be found in Appendix C. A photoelastic plate under stress acts as a linear retarder plate for polarized light with linear retardation δ with a fast axis at angle α relative to the x axis. The change in refractive index in the plane perpendicular to the optical axis is related to δ by the thickness of the plate h and the wavelength λ: $n_1 - n_2 = \delta\lambda/(2\pi h)$. Therefore, the governing equation, the Stress-Optic Law, may be written as the following (Kobayashi, 1993; Narasimhamurty, 1981):

$$\sigma_1 - \sigma_2 = \frac{\delta\lambda}{2\pi c_o h} = \frac{N\lambda}{c_o h}, \tag{3.1}$$

where $N = \delta/2\pi$ is the "fringe order".

A circular polariscope used to view the photoelastic effect includes a polarizer with axis at angle ρ, a $\lambda/4$ plate with fast axis at angle ξ, the photoelastic material, another $\lambda/4$ plate with fast axis at angle ϕ, and a final polarizer with axis at angle β as shown in Figure 3.1.

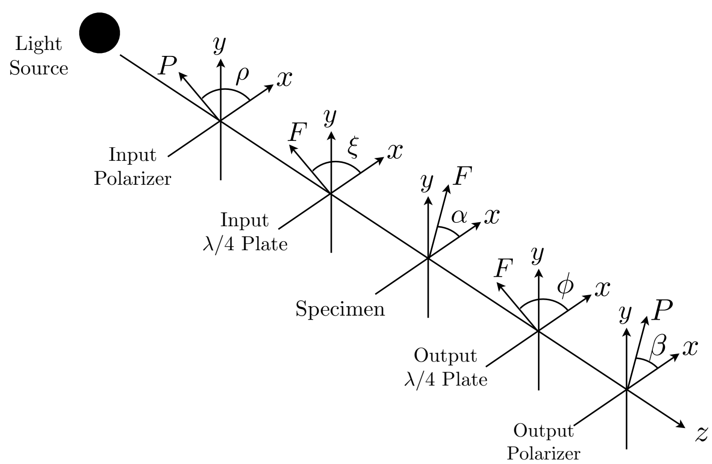

Figure 3.1: Schematic of circular polariscope with fast axes of optics labeled

The six-step method either has the input polarizer set to $\rho = \pi/2$ and the input $\lambda/4$ plate set to $\xi = 3\pi/4$ or has the input polarizer set to $\rho = 0$ and the input $\lambda/4$ plate set to $\xi = \pi/4$. The intensity for this general polariscope, calculated using Mueller Calculus as explained in Appendix C, is

$$I = I_o[1 + \cos(\delta)\sin(2(\beta - \phi)) - \sin(\delta)\sin(2(\alpha - \phi))\cos(2(\beta - \phi))]. \tag{3.2}$$

Image	Intensity	ϕ	β
I_1	$I_o[1+\cos(\delta)]$	$\pi/2$	$3\pi/4$
I_2	$I_o[1-\cos(\delta)]$	$\pi/2$	$\pi/4$
I_3	$I_o[1-\sin(\delta)\sin(2\alpha)]$	π	π
I_4	$I_o[1+\sin(\delta)\cos(2\alpha)]$	$\pi/4$	$\pi/4$
I_5	$I_o[1+\sin(\delta)\sin(2\alpha)]$	$\pi/2$	$\pi/2$
I_6	$I_o[1-\sin(\delta)\cos(2\alpha)]$	$3\pi/4$	$3\pi/4$

Table 3.1: Photoelasticity phase shifting: Angles refer to fast axes of optics

With six combinations of the ϕ and β, the six-step method produces two images including only δ and four images including both δ and α, given in Table 3.1.

The isoclinic angle emerges from I_3 through 1_6 in Equation (3.3) with wrapped phase range of $-\pi/4 \leq \alpha < \pi/4$:

$$\alpha = \frac{1}{2}\arctan\Big(\frac{I_5 - I_3}{I_4 - I_6}\Big) = \frac{1}{2}\arctan\Big(\frac{\sin(2\alpha)\sin(\delta)}{\cos(2\alpha)\sin(\delta)}\Big). \tag{3.3}$$

This wrapped α is only true for $\sin(\delta) \neq 0$; regions near $\sin(\delta) = 0$ will falsely appear to have α close to $\pm\pi/4$ since the argument to the arctan() in Equation (3.3) will grow very large as $\sin(\delta) \to 0$, as will be discussed in Section 3.3.1. By definition, the isoclinic angle may represent the angle between the reference axis and either σ_1 direction or σ_2 direction, a fact known as the isoclinic ambiguity (Siegmann et al., 2005). From the arctan() function in Equation (3.3), the wrapped isoclinic angle has $\pi/2$ discontinuities that are the boundaries between regions referring to σ_1 and σ_2. Unwrapping the isoclinic angle by removing the $\pi/2$ discontinuities by adding $\pm\pi/2$ to appropriate regions produces a field that refers to only one of the principal stresses. These unwrapped isoclinic angles are allowed to contain π discontinuities since these are consistent with a reference to only one principal stress.

The isochromatic phase in Equation (3.4) uses all six images and the unwrapped isoclinic angle, producing a wrapped phase with range $-\pi \leq \delta < \pi$:

$$\delta = \arctan\Big(\frac{(I_5 - I_3)\sin(2\alpha) + (I_4 - I_6)\cos(2\alpha)}{I_1 - I_2}\Big). \tag{3.4}$$

If the wrapped isoclinic angle is used in Equation (3.4), then the resulting isochromatic phase may be modulated (i.e., ambiguous), meaning some regions are related to $\sigma_1 - \sigma_2$ and other regions are related to $\sigma_2 - \sigma_1$, evident in the wrapped phase by poor fringe contrast and a sudden change in sign. This modulated/ambiguous isochromatic data is due to the isoclinic ambiguity such that α relative to σ_1 produces the $\sigma_1 - \sigma_2$ isochromatic regions and α relative to σ_2 produces the $\sigma_2 - \sigma_1$ isochromatic regions. The isochromatic phase may be demodulated by a load stepping method, which takes advantage of the change in δ at each point over three successive incremental loads (Ekman and Nurse, 1998; Ramesh and Tamrakar, 2000), by an automated digital technique that identifies and corrects the ambiguous zones before analysis (Ashokan and Ramesh, 2006), or by unwrapping the isoclinic angle (Siegmann et al., 2005). The load stepping method is not useful in an experiment that is sensitive to incremental loads as is the case with fracture, so it is not pursued for this proposed hybrid experimental method. The automated digital technique can be prone to error when poor quality data pixels are near the boundaries of the ambiguous zones, and this technique does not unwrap the isoclinic angle. Unwrapping the isoclinic angle can be complicated by the $\sin(\delta) \approx 0$ regions and by the allowance of π discontinuities such that careful choice in unwrapping algorithms is required, as will be discussed in Section 3.2.4.1.

For the combined CGS-photoelasticity method, a non-polarizing beamsplitter is positioned after the specimen to split the light for the two techniques, as further explained in Section 3.3. The incident face of the beamsplitter is aligned to be perpendicular to the light, resulting in a transmitted wavefront and a reflected wavefront that is perpendicular to the original propagation direction. The effect of a beamsplitter on polarized light can be modeled as a partial linear polarizer with transmission coefficients, T_x and T_y, and reflection coefficients, R_x and R_y, assuming the principal axes of the beamsplitter are aligned with the Cartesian axes; a similar model is used in a simultaneous capture phase-shifting photoelasticity technique developed by Patterson and Wang (1998). The transmitted beam is used for photoelasticity, and, thus, T_x and T_y affect the intensity of the modified circular polariscope, calculated using Mueller calculus, as follows:

$$I = \frac{I_o}{2}[M_1 + M_2\cos(\delta) - M_3\sin(\delta)\sin(2\alpha) + M_4\sin(\delta)\cos(2\alpha)] \tag{3.5a}$$

$$M_1 = (T_x + T_y) + (T_x - T_y)\cos(2\phi)\cos(2(\beta - \phi)) \tag{3.5b}$$

$$M_2 = 2\sqrt{T_x T_y}\sin(2(\beta - \phi)) \tag{3.5c}$$

$$M_3 = (T_x - T_y) + (T_x + T_y)\cos(2\phi)\cos(2(\beta - \phi)) \tag{3.5d}$$

$$M_4 = 2\sqrt{T_x T_y}\sin(2\phi)\cos(2(\beta - \phi)). \tag{3.5e}$$

With the prescribed angles for the output $\lambda/4$ plate and polarizer given in Table 3.1, the six-step phase-shifted images have intensities shown in Table 3.2.

Image	Intensity
I_1	$(I_o/2)[(T_x + T_y) + 2\sqrt{T_x T_y}\cos(\delta) - (T_x - T_y)\sin(\delta)\sin(2\alpha)]$
I_2	$(I_o/2)[(T_x + T_y) - 2\sqrt{T_x T_y}\cos(\delta) - (T_x - T_y)\sin(\delta)\sin(2\alpha)]$
I_3	$I_o T_x[1 - \sin(\delta)\sin(2\alpha)]$
I_4	$(I_o/2)[(T_x + T_y) + 2\sqrt{T_x T_y}\sin(\delta)\cos(2\alpha) - (T_x - T_y)\sin(\delta)\sin(2\alpha)]$
I_5	$I_o T_y[1 + \sin(\delta)\sin(2\alpha)]$
I_6	$(I_o/2)[(T_x + T_y) - 2\sqrt{T_x T_y}\sin(\delta)\cos(2\alpha)) - (T_x - T_y)\sin(\delta)\sin(2\alpha)]$

Table 3.2: Photoelasticity phase-shifted images for a field transmitted through a beamsplitter placed inbetween the specimen and the output $\lambda/4$ plate

Considering images I_3 through I_6 to obtain α, the argument of the arctan() function from Equation (3.3) becomes

$$\Big(\frac{I_5 - I_3}{I_4 - I_6}\Big) = \Big(\frac{-(T_x - T_y) + (T_x + T_y)\sin(\delta)\sin(2\alpha)}{2\sqrt{T_x T_y}\sin(\delta)\cos(2\alpha)}\Big). \tag{3.6}$$

If $T_x = T_y$, then $(T_x + T_y) = 2\sqrt{T_x T_y}$, which implies the images from the modified circular polariscope in Table 3.2 give the same argument of the arctan() function as in Equation (3.3) for calculating the isoclinic angle. With the isoclinic angle and the six images, the argument of the arctan() function in Equation (3.4) becomes

$$\Big(\frac{(I_5 - I_3)\sin(2\alpha) + (I_4 - I_6)\cos(2\alpha)}{I_1 - I_2}\Big) = \Big(\frac{[(T_x + T_y)sin^2(2\alpha) + 2\sqrt{T_xT_y}\cos^2(2\alpha)]\sin(\delta)}{2\sqrt{T_xT_y}\cos(\delta)}\Big) - \Big(\frac{(T_x - T_y)\sin(2\alpha)}{2\sqrt{T_xT_y}\cos(\delta)}\Big). \tag{3.7}$$

Assuming $T_x = T_y$ and $(T_x + T_y) = 2\sqrt{T_xT_y}$, the calculation for the isochromatic phase simplifies to Equation (3.4). Perfectly aligned non-polarizing beamsplitters ideally have $T_x = T_y$, but usually have a tolerance on $(T_x - T_y)$, such that $(T_x + T_y) \approx 2\sqrt{T_xT_y}$. Manageable error may occur where $\sin(\delta)$ is close to zero in the isoclinic angle since the numerator in Equation (3.6) will be a discrete number larger than the small denominator, such that a false $\pi/2$ discontinuity may appear. These regions are considered carefully to eliminate these false discontinuities, as explained in Section 3.2.4.1. The potential for error in the isochromatic phase is smaller than in the isoclinic angle since the $(T_x - T_y)$ term in Equation (3.7) does not dominate the other term for the range of δ.

Another possible source of error is the rotational misalignment of the polarization optics in the rotation optical mounts. If (i) the first polarizer is correctly aligned with the specimen coordinate system, (ii) the misalignments of the first $\lambda/4$ plate, the second $\lambda/4$ plate, and the second polarizer are e_1, e_2, and e_3 in radians, respectively, and (iii) the beamsplitter is not in the polariscope, then the general intensity for the polariscope with $\rho = \pi/2$ and $\xi = 3\pi/4 + e_1$ (or $\rho = 0$ and $\xi = \pi/4 + e_1$) is

$$\begin{aligned} I = I_o\big(1 + &\sin(2e_1)\{\sin(\delta)\sin[2(\beta - \phi) + 2(e_3 - e_2)]\sin(2\alpha - 2e_1) \\ &+ \cos(\delta)\sin[2(\beta - \phi) + 2(e_3 - e_2)]\cos[2(\beta - \phi) + 2(e_3 - e_2)]\sin(2\alpha - 2e_1) \\ &+ \cos[2(\beta - \phi) + 2(e_3 - e_2)]\cos[2(\alpha - \phi) - 2e_2]\cos(2\alpha - 2e_1)\} \\ &+ \cos(2e_1)\{\cos(\delta)\sin[2(\beta - \phi) + 2(e_3 - e_2)] \\ &- \sin(\delta)\cos[2(\beta - \phi) + 2(e_3 - e_2)]\sin[2(\alpha - \phi) - 2e_2]\}\big). \end{aligned} \tag{3.8}$$

With the prescribed angles for the output $\lambda/4$ plate and polarizer given in Table 3.1 and considering images I_3 through I_6 to obtain α, the argument of the arctan() function from Equation (3.3) becomes

$$\left(\frac{I_5 - I_3}{I_4 - I_6}\right) = \left(\frac{\cos(2e_1)\sin(\delta)\sin(2\alpha - 2e_2) + \sin(2e_1)\sin(2\alpha - 2e_1)\cos(2\alpha - 2e_2)}{\cos(2e_1)\sin(\delta)\cos(2\alpha - 2e_2) - \sin(2e_1)\sin(2\alpha - 2e_1)\sin(2\alpha - 2e_2)}\right). \tag{3.9}$$

The argument to the wrapped α equation does not depend on e_3, the error of the output polarizer, but only on the misalignment of the $\lambda/4$ plates. As will be demonstrated in the theoretical data in the example in Section 3.3.2.2, the isoclinic angle is more sensitive to e_1 than to e_2 in terms of development of false phase discontinuities near $\sin(\delta) = 0$, while error due to e_2 results in a shift in the values of α by e_2. When $\sin(\delta) = 0$, Equation (3.9) should be indeterminate with $0/0$, leading to a value of zero for $\arctan[(I_5 - I_3)/(I_4 - I_6)]$ in MATLAB®, but if $e_1 \neq 0$, then Equation (3.9) is a small number divided by a different small number, leading to values close to $\pm\pi/2$ for $\arctan[(I_5 - I_3)/(I_4 - I_6)]$. When $\sin(\delta)$ is close to zero and $e_1 \neq 0$, then Equation (3.9) will likely be a small number divided by a different small number or $0/0$ depending on the values for α and e_2, leading to a combination of false phase discontinuities and false zero-crossings in the wrapped α field, which require correction before unwrapping. Methods for this correction are described in Section 3.2.4.1. Without correction, the unwrapping algorithm will incorrectly determine α, which will be apparent in phase ambiguities in the wrapped δ data. Since the isoclinic angle is more sensitive to e_1 than e_2, then e_2 is assumed to be zero and e_1 is a small number on the order of $\pm\pi/90$ radians.

With the correction methods for the wrapped isoclinic angle, the resulting isoclinic angle data appears to propagate only modest global error, as shown in the error analysis in Section 3.3.2, indicating that the correction methods are successful and that assuming $T_x \approx T_y$, $e_1 \approx \pm\pi/90$, and $e_2 \approx 0$ are reasonable assumptions.

3.2.2 Coherent Gradient Sensing

As described in Chapter 2, CGS in transmission applied to photoelastic materials is different from CGS applied to optically isotropic materials, leading to interference patterns related to two phases φ_{sum} and φ_{diff}, not just one phase. Controlling the input electric field polarization and adding phase shifting allows determination of the desired phase φ_{sum} related to the spatial derivative of $\sigma_1 + \sigma_2$. Using the same polarization optics for both control of the polarization input for CGS and for the photoelasticity polariscope demonstrates how these two techniques may be combined to investigate the same field of view of the specimen. Additionally, the same input optics for both techniques simplifies the experimental setup. Therefore, using a polarizer and $\lambda/4$ plate prior to the specimen allows for the circularly polarized light necessary for photoelasticity and for determining φ_{sum} with only four phase-shifted CGS images per shearing direction.

Since the combined technique includes a non-polarizing beamsplitter after the specimen, then the reflectance coefficients, R_x and R_y, should be considered in the CGS analysis. The intensity of the image given in Equation (2.16a) is derived without consideration of R_x and R_y; the intensity is the sum of the intensities from the E_1 field and from the E_2 field, and this sum advantageously cancels several terms present in the individual intensities. With R_x and R_y modulating the amplitudes of terms in these two orthogonal fields, many terms will not exactly cancel if $R_x \neq R_y$; but, the relative amplitudes of these uncanceled terms are small, on the order of $(R_x - R_y)$, compared to that of the terms given in Equation (2.16a). Assuming $R_x \approx R_y$ is reasonable since the global error is small, as is evident in Section 3.3.2.

Another possible source of error in the CGS data is the misalignment of the first two polarization optics. Since the photoelastic data is sensitive to the alignment of the first $\lambda/4$ plate, determining the sensitivity of the CGS data to this misalignment is important as well. A misalignment of e_1 radians for the first $\lambda/4$ plate leads to slightly elliptically polarized light as opposed to circularly polarized light. Depending on which pair of angles used for the circularly polarized light from the photoelasticity setup, whether $\rho = 0$ and $\xi = \pi/4 + e_1$ or $\rho = \pi/2$ and $\xi = 3\pi/4 + e_1$, the general equation for the CGS images in Equation (2.16) becomes the following, where A_o is the amplitude of the electric field after the first polarizer:

$$I^{image} = I_o + I_{1o}\cos[\varphi_{sum} + \varphi_{diff}] + I_{2o}\cos[\varphi_{sum} - \varphi_{diff}] \tag{3.10a}$$

$$I_o = 2(A_o^{\pm 1})^2 \tag{3.10b}$$

for $\rho = 0$ and $\xi = \dfrac{\pi}{4} + e_1$:

$$I_{1o} = I_o\Big\{\frac{1}{2}\cos^2(\alpha)[1+\sin^2(2e_1)] + \frac{1}{2}\sin^2(\alpha)\cos^2(2e_2)$$

$$+ \cos(\alpha)\sin(\alpha)\cos\Big[\arctan\Big[\frac{1-sin(2e_1)}{1+sin(2e_1)}\Big] + \frac{\pi}{4}\Big]\Big\} \tag{3.10c}$$

$$I_{2o} = I_o\Big\{\frac{1}{2}\sin^2(\alpha)[1+\sin^2(2e_1)] + \frac{1}{2}\cos^2(\alpha)\cos^2(2e_2)$$

$$- \cos(\alpha)\sin(\alpha)\cos\Big[\arctan\Big[\frac{1-sin(2e_1)}{1+sin(2e_1)}\Big] + \frac{\pi}{4}\Big]\Big\}, \tag{3.10d}$$

and for $\rho = \dfrac{\pi}{2}$ and $\xi = \dfrac{3\pi}{4} + e_1$:

$$I_{1o} = I_o\Big\{\frac{1}{2}\cos^2(\alpha)\cos^2(2e_2) + \frac{1}{2}\sin^2(\alpha)[1+\sin^2(2e_1)]$$

$$+ \cos(\alpha)\sin(\alpha)\cos\Big[\frac{3\pi}{4} - \arctan\Big[\frac{1+sin(2e_1)}{1-sin(2e_1)}\Big]\Big]\Big\} \tag{3.10e}$$

$$I_{2o} = I_o\Big\{\frac{1}{2}\sin^2(\alpha)\cos^2(2e_2) + \frac{1}{2}\cos^2(\alpha)[1+\sin^2(2e_1)]$$

$$- \cos(\alpha)\sin(\alpha)\cos\Big[\arctan\Big[\frac{3\pi}{4} - \arctan\Big[\frac{1+sin(2e_1)}{1-sin(2e_1)}\Big]\Big]\Big\}. \tag{3.10f}$$

When rewriting this as a single interference pattern using Equation (2.17), the equation is not as simple as that for the exactly circularly polarized electric field such that

$$I^{image} = I_o + I_c\cos[\varphi_{sum} + \varphi_c] \tag{3.11a}$$

$$I_c = \sqrt{I_{1o}^2 + I_{2o}^2 + 2I_{1o}I_{2o}\cos(2\varphi_{diff})} \neq \cos(\varphi_{diff}) \tag{3.11b}$$

$$\varphi_c = \arctan\Big[\frac{(I_{1o} - I_{2o})\sin(\varphi_{diff})}{(I_{1o} + I_{2o})\cos(\varphi_{diff})}\Big] \neq 0. \tag{3.11c}$$

The resulting wrapped phase from Equation (2.21) in this case is close to φ_{sum} since φ_c is small for small e_1, but in fact, the wrapped phase is $\varphi_{sum} + \varphi_c$. Additionally, the wrapped phase may have some modulation by I_c where $I_c = 0$, since poor fringe contract occurs where $\cos(\varphi_{diff}) \rightarrow 0$, which will be shown theoretically in the example below in Section 3.3.2.3. This e_1 error will mainly result in some unwrapping errors locally where $\cos(\varphi_{diff}) \rightarrow 0$ and will not greatly affect determining derivatives of $\sigma_1 + \sigma_2$ from the phase maps because for these applications $|\varphi_{sum}| >> \varphi_c$. Despite this error source, the resulting phase maps will generally be a good representation of φ_{sum} for each shearing direction, as shown in the example with small global error in Section 3.3.2.

3.2.3 Combined Experimental Setup

Experimentally, as shown in Figure 3.2, CGS and photoelasticity can be employed simultaneously by sending a plane wave of coherent monochromatic light through the input polarizer, the input $\lambda/4$ plate, and the specimen, after which the light is split by a non-polarizing beamsplitter into two identical wavefronts sent along two separate sets of analyzing optics, one for CGS and the other for photoelasticity. Identical imaging optics and CCD cameras are used to capture the same field of view of the specimen for each technique. Another option for combining these techniques is to replace the non-polarizing beamsplitter with a translating mirror at 45^o to the incoming deformed light after the specimen; to perform photoelasticity, the translating mirror is out of the beam path to allow all of the light to pass through the remaining photoelasticity optics, and to perform CGS, the translating mirror is moved into the beam path to turn the light to pass through the CGS optics. The translating mirror option removes the errors associated with the non-polarizing beamsplitter.

The light is collimated using a spatial filter, consisting of a microscope objective and a pinhole, and a collimating lens placed at one focal length of the collimating lens from the pinhole. The polarizers and $\lambda/4$ plates are mounted in rotation stages with 1^o markings, though the user must align the fast axis fiducial marking on the optic casing with the rotation mount markings by hand. Rotational alignment is achieved by first setting the first polarizer as the standard, and methods for extinguishing the light detected on a CCD are used to set the alignment of the other polarization optics. To obtain each of the six photoelasticity images, the output $\lambda/4$ plate and polarizer must be adjusted manually. In order to induce the $\pi/2$ phase shift for the CGS data, the first Ronchi grating is translated a distance of $p/4$ by 1D piezoelectric positioners, one for each shearing direction. To obtain the two shearing directions for the same load of the specimen, one set of phase-shifted images for one shearing direction is taken, and then the Ronchi gratings are rotated by $\pi/2$ and the imaging optics and filter plane are adjusted to capture the phase-shifted images for the other shearing direction. In the current configuration, the images for both shearing directions and photoelasticity cannot be obtained simultaneously, though this may be achieved with other optical solutions described in Chapter 5.

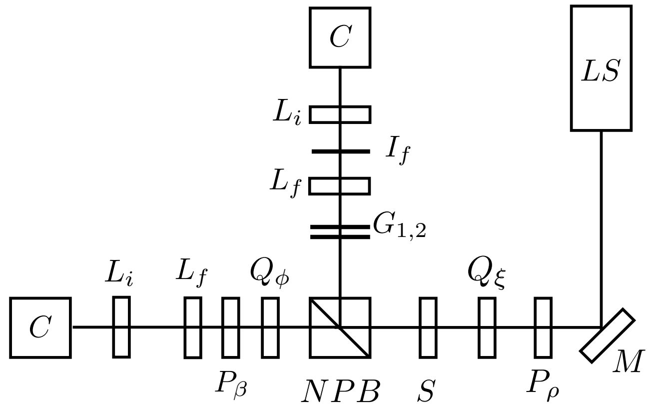

(a)

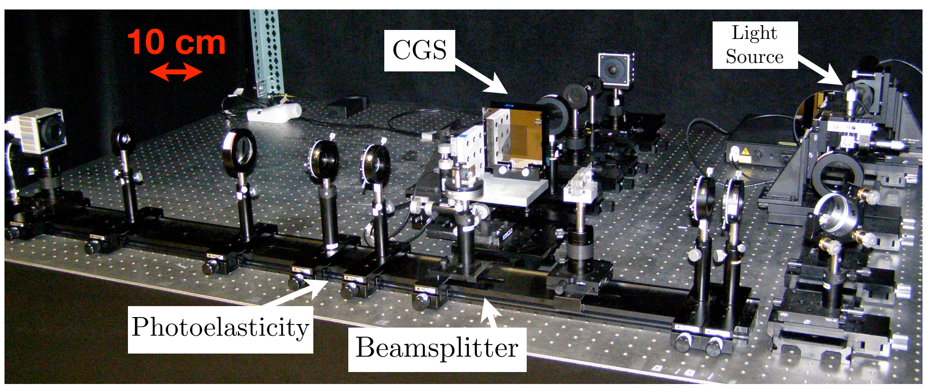

(b)

Figure 3.2: Combined CGS-photoelasticity experimental setup: (a) Schematic of the experimental setup: LS=light source with collimation optics; M=mirror; P=polarizer; Q=$\lambda/4$ plate; S=specimen; NPB=non-polarizing beamsplitter; $G_{1,2}$=gratings 1&2; L_f=filtering lens; I_f=filtering iris diaphragm; L_i=imaging lens; and C=camera; and (b) image of experimental setup from side view of photoelasticity optics

3.2.4 Full-Field Phase Unwrapping and Integration

The data analysis is performed using an analysis program written using MATLAB®. The 2D phase unwrapping method for both photoelastic and CGS data is the PCG algorithm described in Chapter 2. Phase unwrapping of the experimental isoclinic angle requires special care where, prior to unwrapping by the PCG algorithm, the wrapped data is corrected for errors that are due to the non-polarizing beamsplitter and to alignment of the polarization optics as explained in Section 3.2.1. The PCG algorithm may also be applied to numerically integrate the spatial derivatives of $\sigma_1 + \sigma_2$.

3.2.4.1 Phase Unwrapping for the Isoclinic Angle

In the wrapped isoclinic data from Equation (3.3), regions where $\sin(\delta) = 0$ are undefined. These regions may be identified using the isochromatic data. Near $\sin(\delta) = 0$, both the numerator and denominator of the isoclinic arctan() formula in Equation (3.3) are close to zero, but with slightly different small numbers from the nonzero tolerance on $(T_x - T_y)$ and misalignment of the polarization optics. These regions ultimately may appear as false $\pi/2$ discontinuity regions in the wrapped isoclinic angle. Additionally, regions where the numerator and the denominator of the arctan() formula are zero, MATLAB® will return a value of zero for the arctan(), but these points may also require correcting since the isoclinic angle is not necessarily zero at those locations.

With a user-defined threshold value, denoted $thresh$, then the data in zones where $-thresh < \sin(\delta) < thresh$ are identified as likely locations where the data needs correction. The δ used here is the ambiguous wrapped isochromatic phase, described in Section 3.2.1, because this comes from using wrapped α in the formula for wrapped δ in Equation (3.4). The ambiguous wrapped isochromatic phase is a key tool to correcting the wrapped isoclinic angle because the ambiguous wrapped δ should ideally have (i) good phase discontinuities of height 2π that require unwrapping, (ii) continuous phase, or (iii) boundaries of the ambiguous data having opposite sign across the boundaries (where the boundaries of $\sigma_1 - \sigma_2$ and $\sigma_2 - \sigma_1$ regions meet). Phase discontinuities of height 2π and zero-crossings in the wrapped δ correspond to where $\sin(\delta) \approx 0$, so these are precisely where the isoclinic angle data has possible problems. The ambiguity boundaries in the wrapped δ should coincide with the $\pi/2$ phase discontinuities in the wrapped α, which are true wrapped phase discontinuities that must be preserved.

The following are some basic guidelines to correcting the isoclinic angle, but the user must apply judgment, informed by the expected form of the wrapped α and δ, in cases where no single guideline may be applied:

- If the $\pi/2$ phase discontinuity in the wrapped α coincides with an ambiguity boundary in the wrapped δ, then this discontinuity should be preserved and left alone.

- If both the wrapped α and wrapped δ are continuous, and if the wrapped delta is not near where $\sin(\delta) \to 0$, then this data should be left alone.

- If phase discontinuities from both wrapped α and wrapped δ coincide, then the phase discontinuity in α should be interpolated across.

- If a true $\pi/2$ phase discontinuity in the wrapped α *intersects* the location of a wrapped δ discontinuity, great care must be taken when interpolating across the false α discontinuity while preserving the true α discontinuity.

- If a $\sin(\delta) \to 0$ region coincides with a zero-crossing in the wrapped α, then this zero-crossing is likely near where wrapped α is actually close to $\pm\pi/4$. These types of zero-crossings are often where both $\sin(\delta)$ and $\cos(2\alpha)$ are close to zero, leading to a $0/0$ as the argument of the α arctan() formula. The user can insert a phase discontinuity in this region. Another indication for this case is that the ambiguous wrapped δ does not have a phase discontinuity, but a change of direction about $\pm\pi$; this change of direction should be a phase discontinuity that connects to another phase discontinuity in the wrapped δ field.

- Phase discontinuities in α need to either connect or end on a boundary; they should not end in the middle of the field.

Once false phase discontinuities are identified, then these are removed from the wrapped field and replaced with data from 2D linear interpolation across those zones. Then the modified wrapped isoclinic data is unwrapped using the PCG algorithm.

This unwrapped isoclinic angle is used in Equation (3.4) for the unambiguous wrapped isochromatic phase. The wrapped δ calculated from the unwrapped α should not contain phase ambiguities and should only contain continuous phase or phase discontinuities of height 2π; if this is not the case, then the wrapped isoclinic angle was not properly modified and requires correction.

Since the sign of the numerator and of the denominator of the arctan() function in Equation (3.4) are known separately, then the full four quadrants of arctan() phase space may be used, resulting in an isochromatic wrapped phase with range $-\pi \leq \delta < \pi$. Having 2π phase discontinuities instead of π discontinuities reduces the density of discontinuities in the entire field, reducing the computational effort to unwrap the field. For both the isoclinic angle and the CGS phases, unwanted phase information modulates the numerator and denominator, which implies the sign of the numerator and denominator of the arctan() function are not known independently. Thus the arctan() formula produces a phase with a range from $-\pi/2$ to $\pi/2$, giving wrapped phase ranges of $-\pi/4 \leq \alpha < \pi/4$ and $-\pi/2 \leq \varphi_{sum} < \pi/2$.

3.2.4.2 Preconditioned Conjugate Gradient Method for Integration

Letting $s = (\sigma_1 + \sigma_2)$, the solutions to the phase unwrapping for the horizontal and vertical shearing directions result in $\partial s/\partial x$ and $\partial s/\partial y$, which must be integrated to obtain s. This integration problem is a discrete Poisson equation of the form:

$$\begin{aligned}(s_{i+1,j} - 2s_{i,j} + s_{i-1,j}) + (s_{i,j+1} - 2s_{i,j} + s_{i,j-1}) \\ = \left[\left(\frac{\partial s}{\partial x}\right)_{i,j} - \left(\frac{\partial s}{\partial x}\right)_{i-1,j}\right]\Delta x \\ + \left[\left(\frac{\partial s}{\partial y}\right)_{i,j} - \left(\frac{\partial s}{\partial y}\right)_{i,j-1}\right]\Delta y,\end{aligned} \tag{3.12}$$

where Δx and Δy are the specimen distance per pixel. Assuming Neumann boundary conditions, Equation (3.12) may be solved by the same PCG algorithm used for the phase unwrapping with a weight function, $\mathbf{W}$, that is the product of the quality weight functions from the unwrapping in the horizontal and vertical directions.

3.3 In-Plane Tensorial Stress Field Determination: CGS and Photoelasticity

3.3.1 Experimental Verification Test Problem

The experimental verification test specimen is a 12.7 mm $\times$ 12.7 mm square plate with thickness $h = 1.0$ mm and with a 60^o V-notch cut out of the side of the plate, just as it is for the experimental verification Chapter 2, shown in Figure 2.3. The depth of the V-notch, d, is 6.35 mm, and the V-notch opening width, w, is 7.34 mm. The plate is polycarbonate, which is a thermoplastic polymer that is highly photoelastic, with absolute photoelastic constants $A = -2.45 * 10^{-11}$ m^2/N and $B = -9.38*10^{-11}$ m^2/N, and therefore the relative photoelastic constant is $c_o = A - B = 6.93*10^{-11}$ m^2/N (Shimizu et al., 1998). This plastic has a Young's modulus of $E = 2.3$ GPa, Poisson's ratio of $\nu = 0.36$, and refractive index of $n_o = 1.586$. The photoelasticity-related constants used in calculating φ_{sum} and φ_{diff} are therefore $C = 1.51 \times 10^{-10}$ m^2/N and $g = 0.23$. The specimen is from a polycarbonate sheet with residual stress due to forming; for the field of view of the specimen, the through-thickness averaged residual stresses are determined to be $\sigma_{xx}^{resid} \approx 1.9$ MPa, $\sigma_{yy}^{resid} \approx -1.9$ MPa, and $\sigma_{xy}^{resid} \approx -0.1$ MPa. Prior to loading, the specimen is imaged using both photoelasticity and CGS; the full-field residual stresses are determined from these measurements. The data field are fairly uniform for the field of view, so the values stated above are assumed to be uniform for the field of view for the theoretical solution. In this example, the specimen is compressed by 23.4 N along the y axis. The derivation of the stress field based on Williams (1952) presented in Section 2.3 is used as the theoretical stress field solution with the addition of the residual stress. For this particular example, the applied stress σ_{app} is -1.84 MPa, and the fitting parameter C_f is 0.76, as determined by comparing the experimental and theoretical in-plane stress fields.

The monochromatic CCD cameras used in this study are IMPERX model IPX-1M48-L with a 1000 $\times$ 1000 pixel chip. The optical field of view imaged onto the sensor is 4.0 mm $\times$ 4.0 mm, and the image resolution is 4.0 μm. For the CGS setup, the Ronchi grating pitch, p, is 1 mm/40; the grating separation, $\tilde{\Delta}$, is 13.40 mm; the wavelength of light from the linearly polarized HeNe laser is 632.8 nm; and the resulting lateral shearing distance, d_{shear}, is 339 μm. The first polarizer and $\lambda/4$ plate are set to $\rho = \pi/2$ and $\xi = 3\pi/4$.

3.3.2 Phase Analysis and Stress Determination

3.3.2.1 Image Data

The six experimental phase-shifted photoelastic images are shown in Figure 3.3. The origin is located at the notch tip, acting as the reference to colocate the photoelasticity and CGS images. In this experimental setup, due to small wedge angles in the output $\lambda/4$ plate and polarizer, the rotation of these optics to obtain the six photoelastic images results in very small lateral translations of the images relative to the CCD chip, on the order of 10 or fewer pixels. To mitigate errors due to this translation, the notch tip and other spots, such as small dust particles on the surface of the specimen, are used to colocate the six images. This operation slightly reduces the field of view on the order of 3% or less because only pixels that can be colocated are used, but these lost points are only on the edges of the field of view away from the region of interest. The slight rings in the photoelastic images centered around the notch tip are due to interference of reflections from the front and back faces of the specimen and are a by-product of the coherent monochromatic light source necessary for CGS. These weak interference contours are known as Fizeau fringes and scale in frequency by the thickness variation of the specimen (Hecht, 2002). An anti-reflective coating on the specimen can reduce this effect. Prior to phase analysis, these photoelasticity images are lightly filtered using a Wiener filter, which is a 2D adaptive noise-removal filter design to remove additive noise, of window size $[40 \times 40]$ to reduce these rings.

The experimental photoelastic images may be compared to the theoretical images in Figure 3.4, defined by the stress fields from Equation (2.27), using the experimental σ_{app} and the fitting coefficient, C_f, as described above. Generally, these images compare well with the correct shapes, though the theoretical fields appear to be slightly less dense than the experimental images, as evident in the slightly different locations of the dark fringes in I_1 and I_2. These slight differences are due to two factors: (i) the upper compressive platen is designed to tilt as needed to align with the top of the plate by sitting against a spherical ball aligned with the center of vertical loading bar, but large angles of misalignment between the specimen and platen led to slightly nonuniform loading of the specimen along the x axis, and (ii) the fitting coefficient C_f is chosen by minimizing error for all the experimental data, not just the photoelastic data, leading in this case to a smaller C_f than indicated by the photoelastic data alone. Also, the experimental and theoretical I_4 and I_6 do not have quite the same behavior near the notch edges, where the theoretical data seems to have poorer fringe contrast than the experimental data. This difference is likely due to a difference in the experimental and theoretical α, which is based on the assumption of uniform residual stresses. The specimen may have some nonuniform residual stresses near the notch edges where the residual stresses may have been relieved due to the cuts for specimen preparation, leading to a different experimental α near the notch edges. Though with less fringe contrast than in the theoretical I_3 and I_5, the dark fringes emanating from the notch tip for $|\theta| > \pi/2$ in the experimental I_3 and I_5 have the correct shape and location. The theoretical photoelastic images do not exhibit the rings centered around the notch tip that are in the experimental images because the Fizeau fringes are not modeled here, showing that these rings are not due to the photoelastic effect, which motivates the Wiener filtering of the experimental images to reduce the effect of these fringes.

Figures 3.5–3.8 show the experimental and theoretical CGS images for the horizontal and vertical shearing directions for the circularly polarized electric field input configuration. The experimental horizontal shearing data in Figure 3.5 compare well with the theoretical data Figure 3.6 in shape, fringe, density, and the interference beading (breaks in the fringe patterns due to superposition of two interference patterns). The experimental vertical shearing data in Figure 3.7 also compare well with the theoretical images in Figure 3.8, though due to the finite shearing distance, the two lobes are slightly further apart than in the theoretical images. The experimental vertical images have the expected interference beading. For both shearing directions, the $\pi/2$ phase shifts between each successive image matches the expected behavior. The finite shearing distance is visible in the doubling of the V-notch boundary. The theoretical images do not include this, but are purely based on the derivatives of $\sigma_1 + \sigma_2$ with a mask for the V-notch that does not model the doubling of the V-notch. Due to the finite shearing distance, the vertical shearing images in Figure 3.7 cannot capture the lobes on either side of the V-notch boundary prominent in the theoretical data in Figure 3.8.

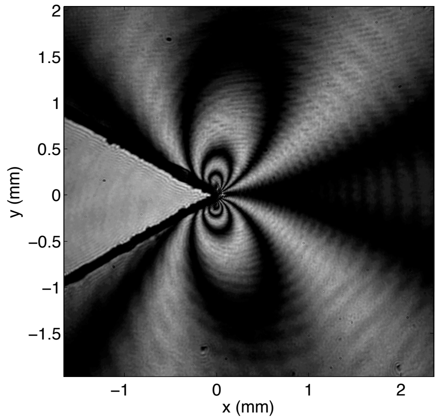

(a) $I_1 = I_o(1 + \cos(\delta))$

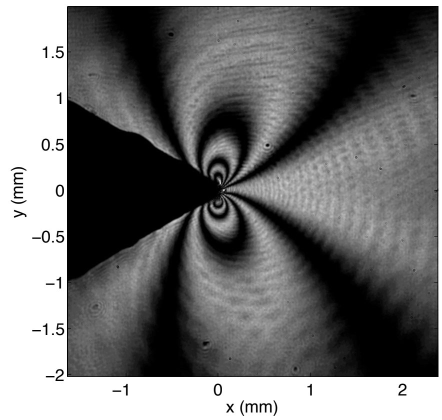

(b) $I_2 = I_o(1 - \cos(\delta))$

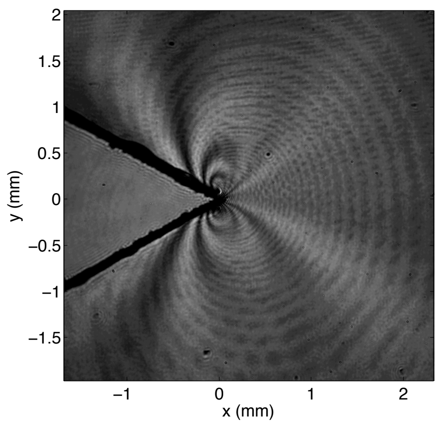

(c) $I_3 = I_o(1 - \sin(\delta)\sin(2\alpha))$

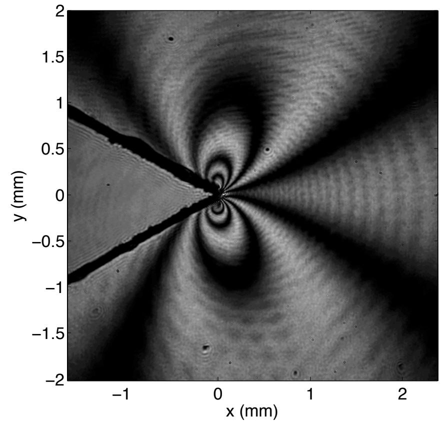

(d) $I_4 = I_o(1 + \sin(\delta)\cos(2\alpha))$

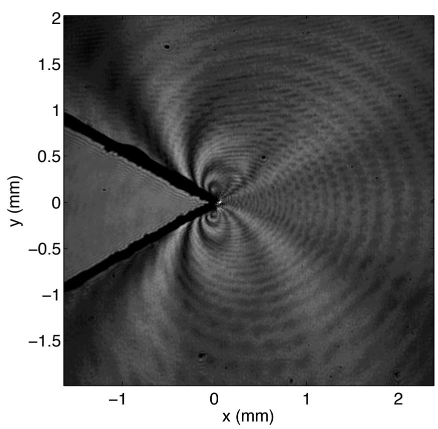

(e) $I_5 = I_o(1 + \sin(\delta)\sin(2\alpha))$

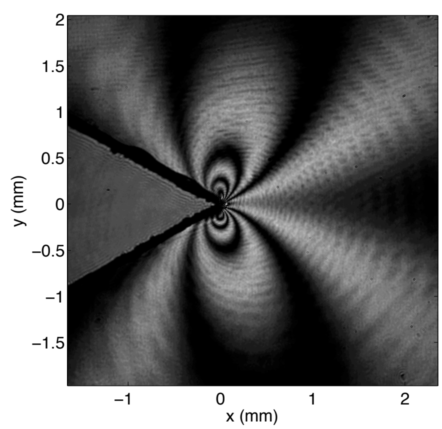

(f) $I_6 = I_o(1 - \sin(\delta)\cos(2\alpha))$

Figure 3.3: Experimental images from six-step phase-shifting photoelasticity for polycarbonate compressed V-notch specimen

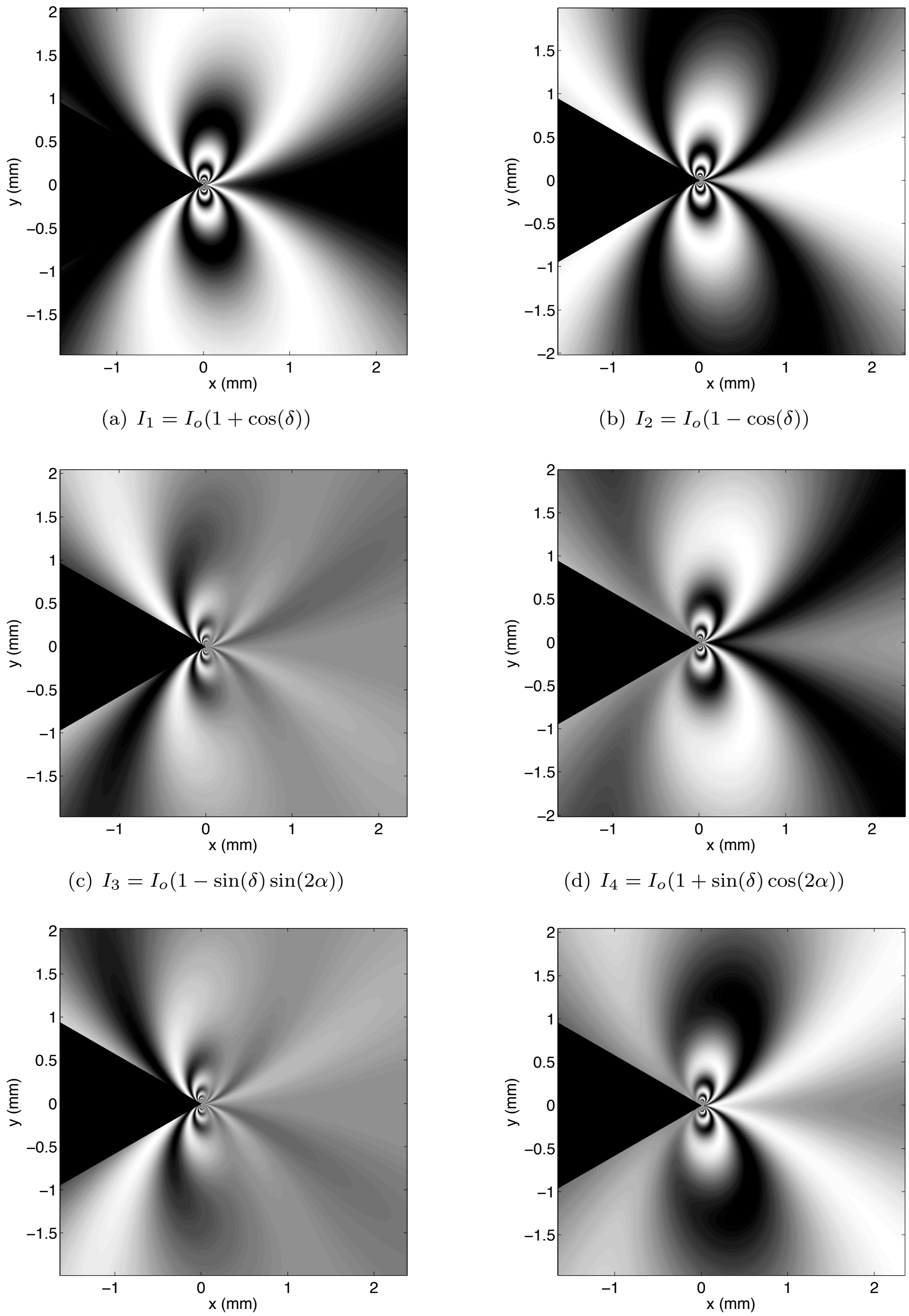

(a) $I_1 = I_o(1 + \cos(\delta))$

(b) $I_2 = I_o(1 - \cos(\delta))$

(c) $I_3 = I_o(1 - \sin(\delta)\sin(2\alpha))$

(d) $I_4 = I_o(1 + \sin(\delta)\cos(2\alpha))$

(e) $I_5 = I_o(1 + \sin(\delta)\sin(2\alpha))$

(f) $I_6 = I_o(1 - \sin(\delta)\cos(2\alpha))$

Figure 3.4: Theoretical images from six-step phase-shifting photoelasticity for polycarbonate compressed V-notch specimen

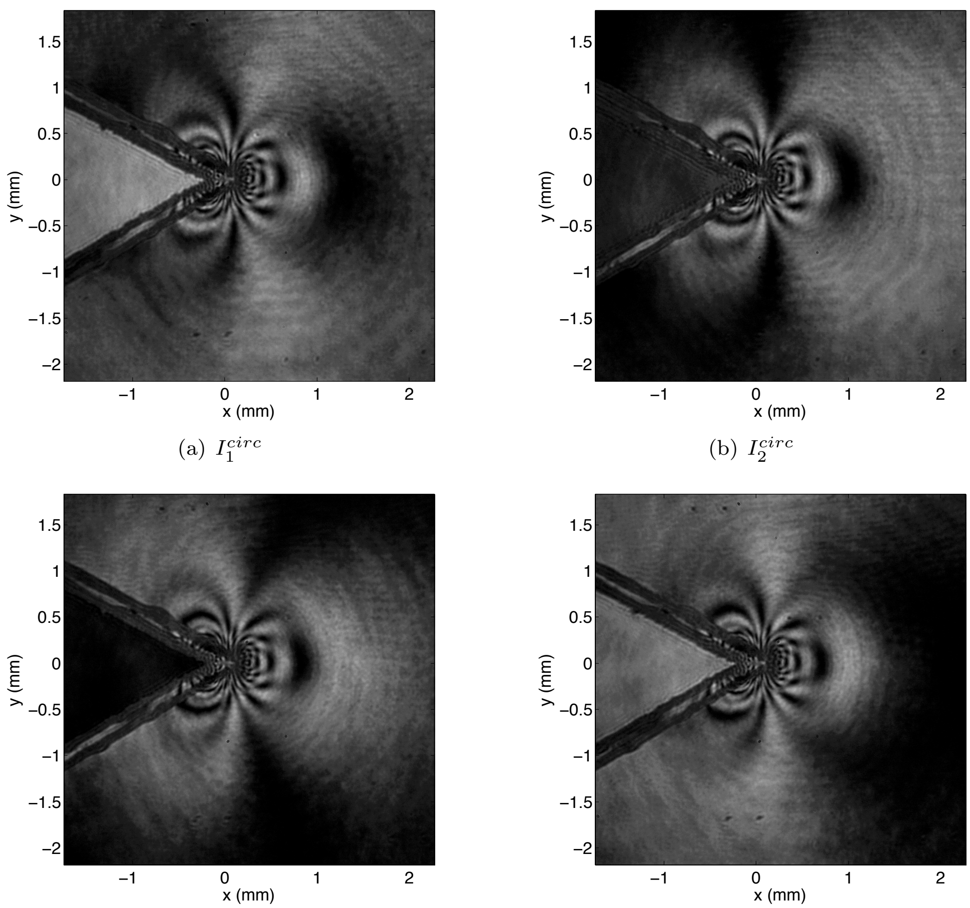

(a) I_1^{circ} (b) I_2^{circ}

(c) I_3^{circ} (d) I_4^{circ}

Figure 3.5: Experimental phase-shifted images from horizontal shearing CGS using the $\lambda/4$ polarization method for compressed polycarbonate V-notch plate

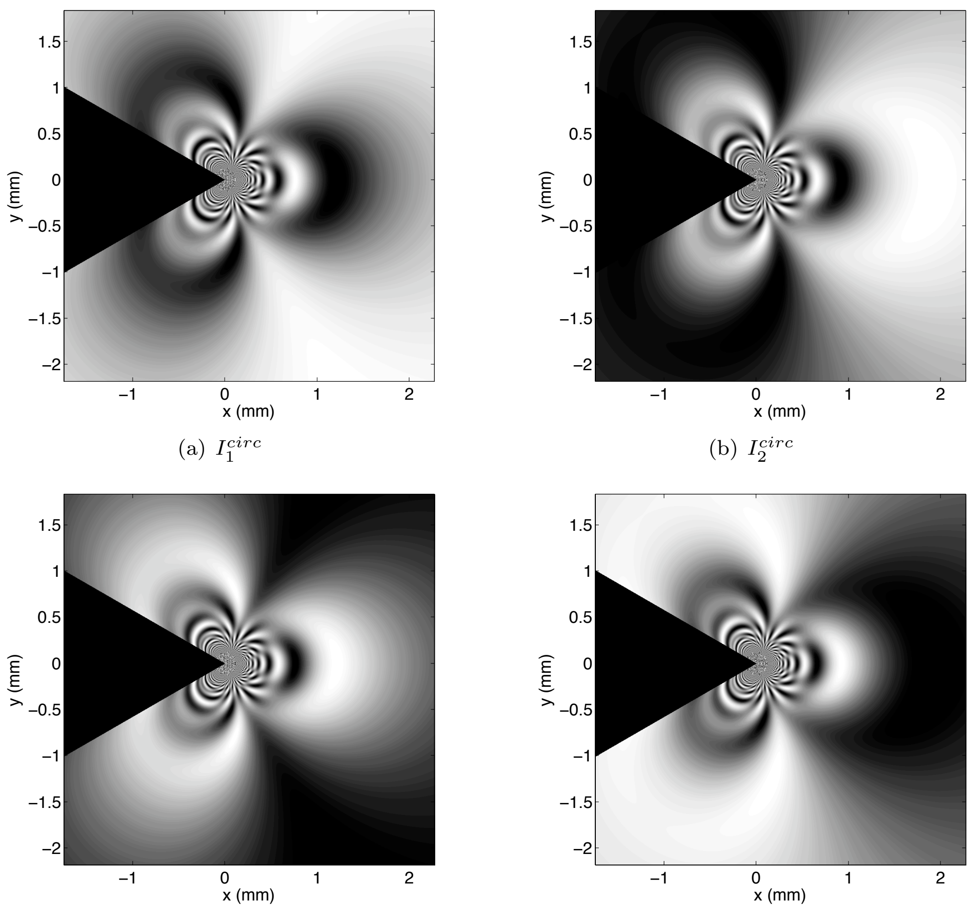

(a) I_1^{circ} (b) I_2^{circ}

(c) I_3^{circ} (d) I_4^{circ}

Figure 3.6: Theoretical phase-shifted images from horizontal shearing CGS using the $\lambda/4$ polarization method for compressed polycarbonate V-notch plate with the notch mask in black

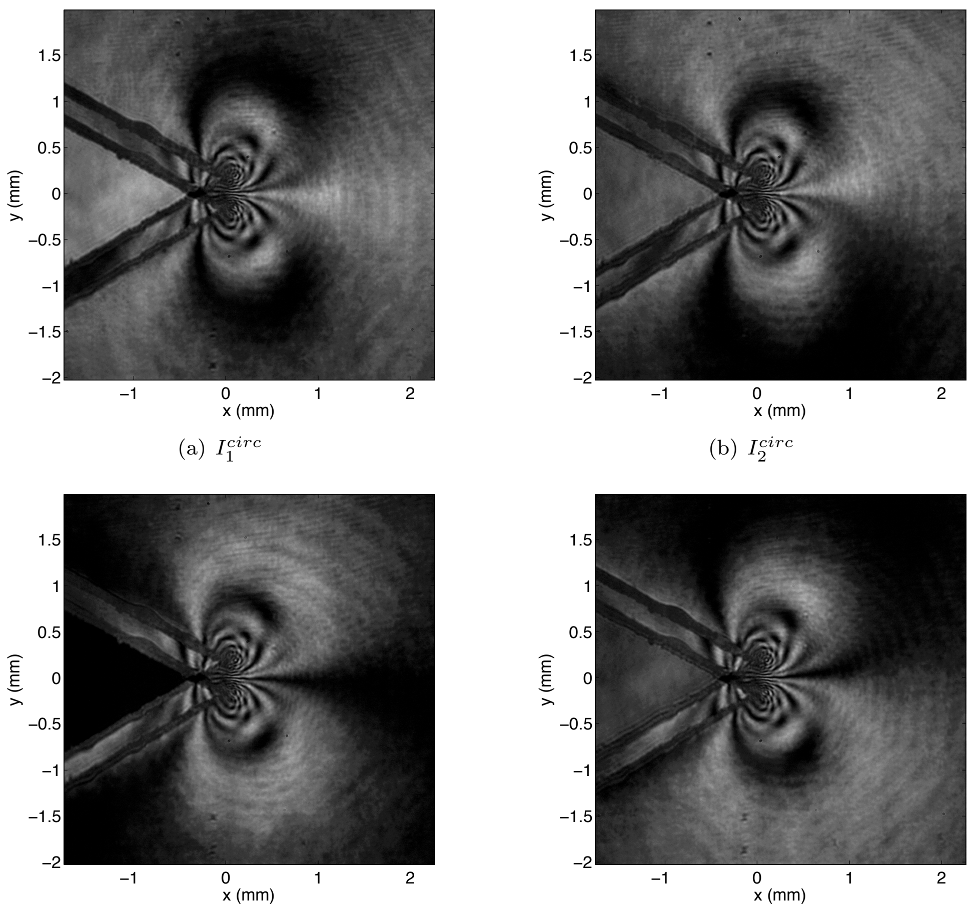

(a) I_1^{circ} (b) I_2^{circ} (c) I_3^{circ} (d) I_4^{circ}

Figure 3.7: Experimental phase-shifted images from vertical shearing CGS using the $\lambda/4$ polarization method for compressed polycarbonate V-notch plate

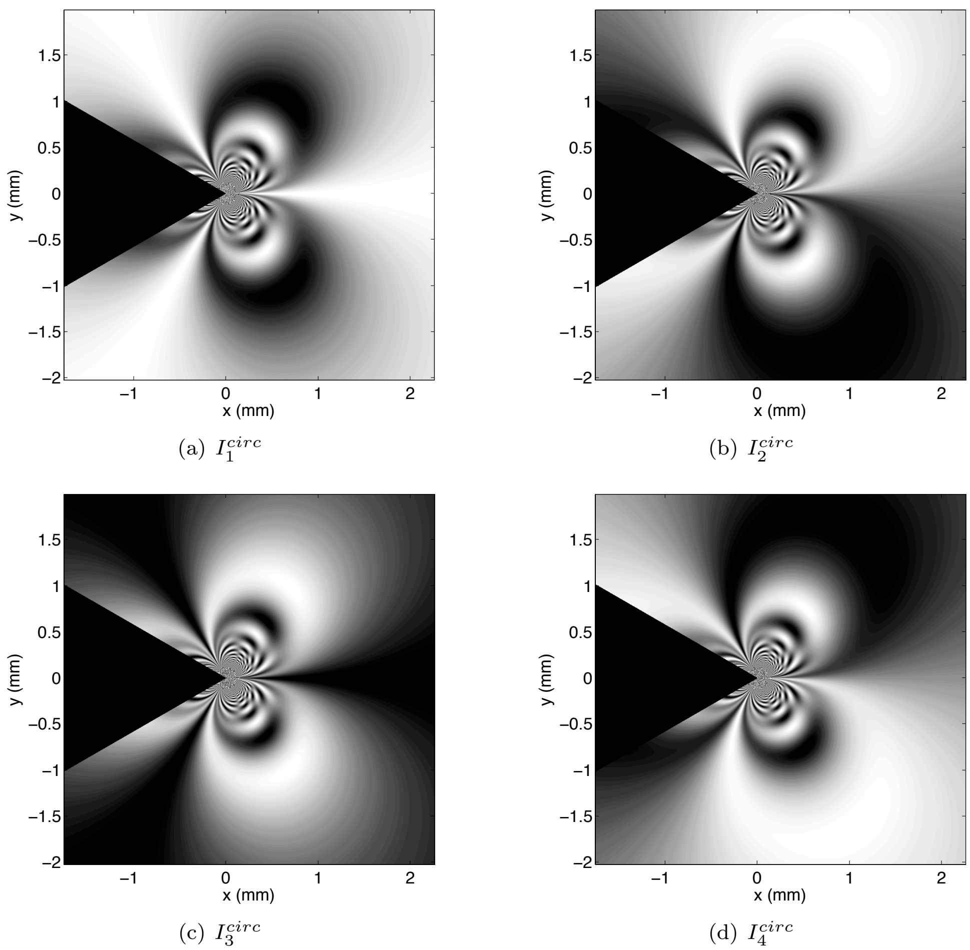

(a) I_1^{circ} (b) I_2^{circ}

(c) I_3^{circ} (d) I_4^{circ}

Figure 3.8: Theoretical phase-shifted images from vertical shearing CGS using the $\lambda/4$ polarization method for compressed polycarbonate V-notch plate with the notch mask in black

3.3.2.2 Photoelasticity Phase Analysis

The V-notch region is masked in all the phase and stress fields to prevent unwrapping errors and to eliminate the region in the field of view with no polycarbonate. The wrapped isoclinic angle calculated using Equation (3.3), as shown in Figure 3.9(a), contains apparent $\pi/2$ phase jumps in regions near $\sin(\delta) = 0$ throughout the field, most likely due to the nonzero tolerance of $(T_x - T_y)$ and $e_1 \neq 0$, but only a very small region on the notch edge near the notch tip actually requires unwrapping. The ambiguous wrapped isochromatic phase based on this wrapped α is shown in Figure 3.9(b), where the ambiguity appears only near the notch tip. This particular wrapped α field does not have the false zero-crossings, but only has false $\pi/2$ discontinuities where the wrapped δ is zero or $\pm\pi$.

Figure 3.9(c) is the theoretical wrapped α that incorporated beamsplitter transmission coefficients $T_x = 0.42$ and $T_x = 0.39$, which are plausible coefficients for the beamsplitter used in this study, based on manufacturer specifications and monitoring the voltage output from a photodiode collecting the transmitted (and reflected) light from the beamsplitter with pure $E_x\hat{\imath}$ or $E_y\hat{\jmath}$ input. The later method is a crude estimate of the transmission and reflectance coefficients. The modulation of the wrapped data near where the theoretical $\sin(\delta) \to 0$ is modest and does not reflect the extent of the false phase discontinuities in the experimental data except near $\theta = 0$. Figure 3.9(d) is the theoretical wrapped α including the error in the first $\lambda/4$ plate of $e_1 = \pi/90$ radians, which is small but possible given the alignment procedure of the polarization optics and the quality of the rotation mounts. This field has much greater modulation near $\sin(\delta) \to 0$, and therefore the misalignment of the first $\lambda/4$ plate is a more prominent source of error except near $\theta = 0$, where the beamsplitter T_x and T_y appear to dominate. Figures 3.9(d) and 3.9(f) are the theoretical wrapped α fields including $e_2 = -\pi/90$ radians with $e_1 = 0$ and $e_1 = \pi/90$ radians, respectively. The field including only e_2 error does not exhibit the false phase discontinuities, while the field with both e_1 and e_2 error has the false phase discontinuities and a slight shift of e_2 radians in the entire field. These theoretical fields demonstrate the types of errors that can occur, as described in Section 3.2.1, and verify that e_1 error has the greatest overall effect on the wrapped isoclinic angle.

The identified false $\pi/2$ discontinuity regions in the experimental data are eliminated and interpolated across as described in Section 3.2.4.1. The corrected wrapped isoclinic angle and the resulting ambiguous wrapped isochromatic phase are shown in Figures 3.10(a) and 3.10(b); though the ambiguous wrapped isochromatic phase does not look much different, the corrections to the wrapped isoclinic angle did smooth the δ data near $\sin(\delta) = 0$. Figures 3.10(c) and 3.10(d) show the theoretical wrapped isoclinic angle and the ambiguous isochromatic phase; the theoretical wrapped α only has phase discontinuities near the notch tip, and the only ambiguities in the wrapped δ field are near the notch tip, similar to the experimental fields. This good qualitative comparison of the experimental and theoretical wrapped data demonstrates that the correction to the wrapped isoclinic angle is acceptable. The main issue with the corrected wrapped isoclinic angle is that the corrected regions still indicate some influence from the δ data, where the wrapped α is not as radially smooth as the theoretical wrapped α. If more data points were removed and interpolated across than the $\sim 27\%$ of the data points (excluding the notch region) already corrected, then the overall nature of the isoclinic angle may have been obscured. The experimental and theoretical unwrapped isoclinic angle fields are shown in Figures 3.10(e) and 3.10(f), with good comparison except where the experimental data appear to have residual errors in the shape of the isochromatic phase that modulate the isoclinic data. For example, the experimental isoclinic angle is not as negative near $\theta = -5\pi/6$, but the regions of negative and positive α in the entire field correspond well. The theoretical isoclinic angle data in Figure 3.10(c) show a slight lobe-like structure, which is present due to the residual stresses. The isoclinic angle would only be a function of θ in a residual stress-free material, demonstrating that the theoretical solution requires inclusion of these residual stresses to compare well with the experimental data.

The experimental unambiguous wrapped isochromatic phase calculated using the unwrapped isoclinic angle, shown in Figure 3.11(a), has distinct 2π discontinuities, allowing for fast unwrapping; the resulting unwrapped isochromatic phase is given in Figure 3.11(c). The theoretical wrapped and unwrapped isochromatic phase in Figures 3.11(b) and 3.11(d) are slightly different than the experimental fields, where the wrapped data have different locations for the 2π phase discontinuities, and the theoretical unwrapped data are smaller near the notch. These differences are expected from the theoretical images, as explained in Section 3.3.2.1. The overall shape of the isochromatic data is correct, with the double lobes slightly bent away from the y axis towards $\theta = 0$, which happens to be due to the residual stress in the material. In a residual stress-free material, the lobes of the isochromatic phase would be symmetric about the y axis.

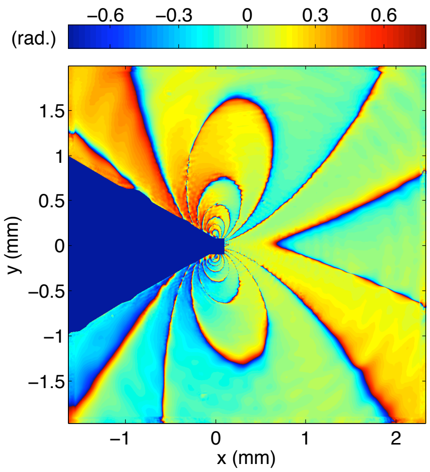

(a) Experimental wrapped α

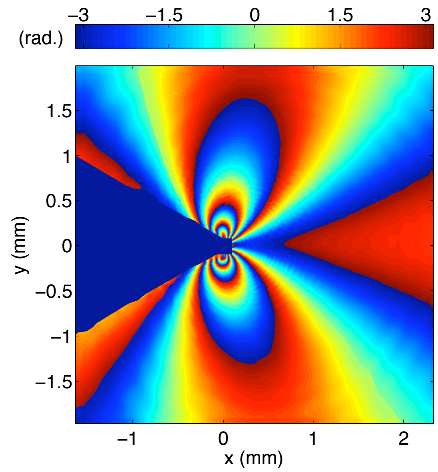

(b) Experimental ambiguous wrapped δ

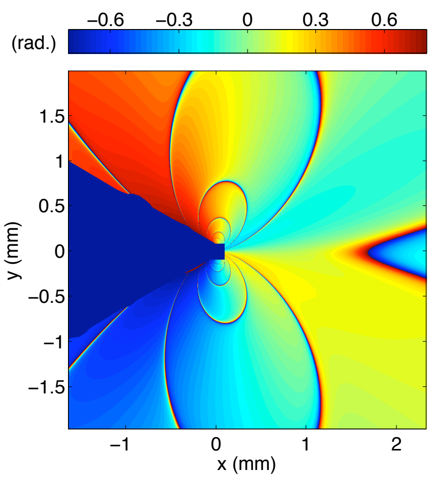

(c) Theoretical wrapped α with $T_x = 0.42$ and $T_y = 0.39$

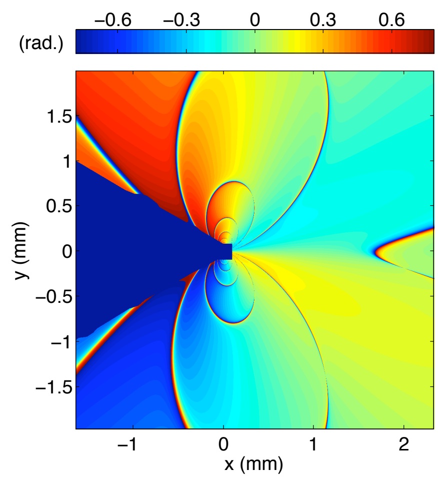

(d) Theoretical wrapped α with $e_1 = \pi/90$

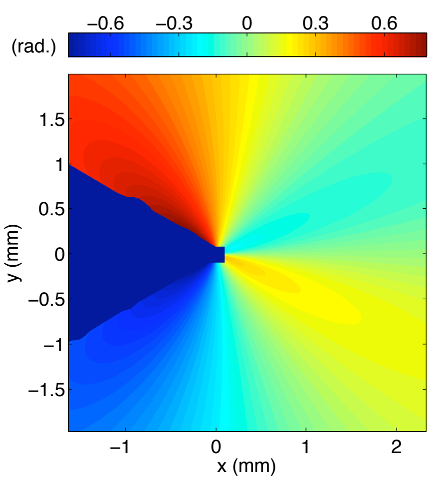

(e) Theoretical wrapped α with $e_2 = -\pi/90$

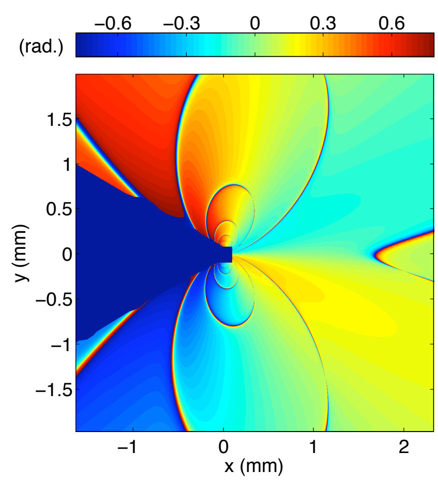

(f) Theoretical wrapped α with $e_1 = \pi/90$ and $e_2 = -\pi/90$

Figure 3.9: Photoelasticity wrapped isoclinic angle with possible error sources modeled for the compressed polycarbonate V-notch specimen with V-notch region masked in blue

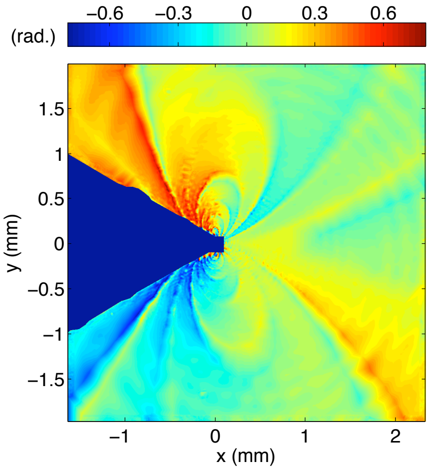

(a) Experimental corrected wrapped α

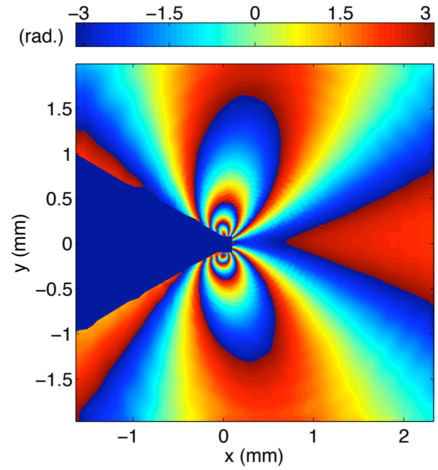

(b) Experimental ambiguous wrapped δ from corrected wrapped α

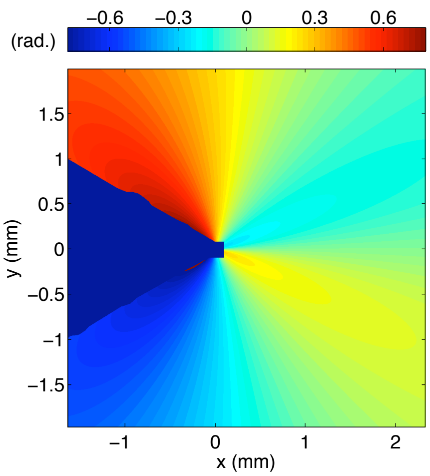

(c) Theoretical wrapped α

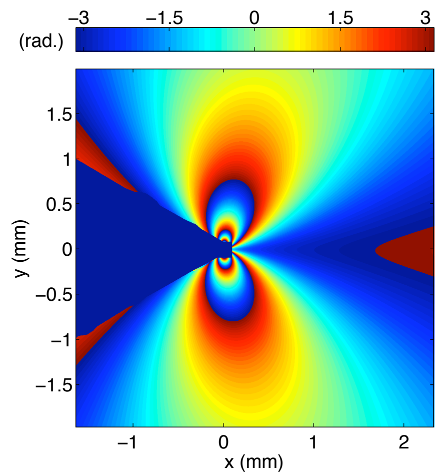

(d) Theoretical ambiguous wrapped δ from uncorrected wrapped α

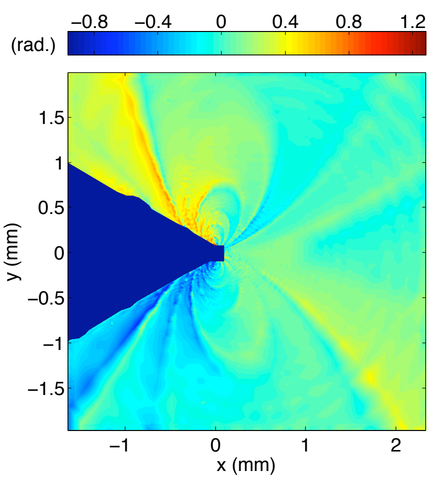

(e) Experimental unwrapped α

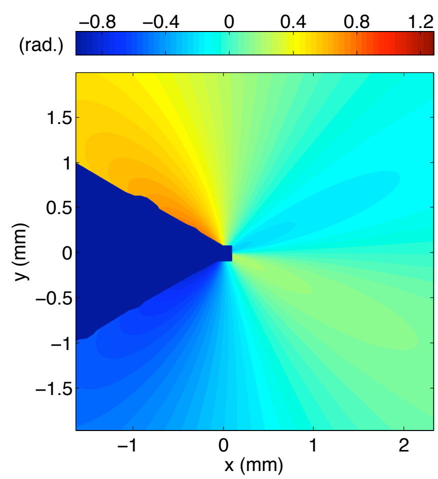

(f) Theoretical unwrapped α

Figure 3.10: Photoelasticity corrected isoclinic angle analysis for the compressed polycarbonate V-notch specimen with V-notch region masked in blue

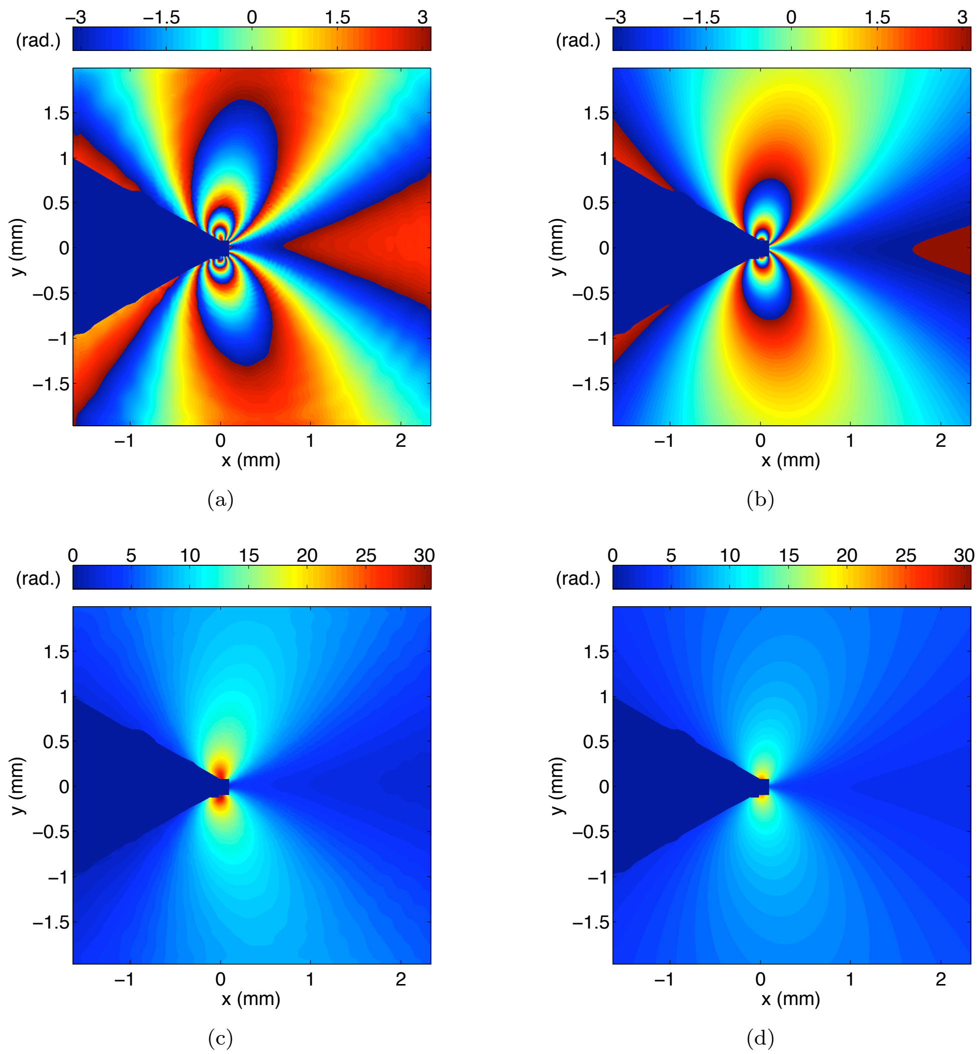

Figure 3.11: Photoelasticity isochromatic phase analysis with V-notch region masked in blue

3.3.2.3 CGS Phase Analysis

Figures 3.12 and 3.13 present the experimental and theoretical wrapped φ_{sum} for the horizontal and vertical shearing directions, respectively. The wrapped CGS phases in Figures 3.12(a) and 3.13(a) have the expected shapes and phase discontinuity density, except where poor fringe contrast in a four-lobed shape in each field disrupts the continuity of the dominant fringes. These four-lobed shapes are where $\cos(\varphi_{diff})$ is near zero in each field. Figures 3.12(c) and 3.13(c) show the theoretical $\cos(\varphi_{diff})$ fields for the horizontal and vertical shearing directions, indicating the four-lobed shapes where $\cos(\varphi_{diff})$ is near zero. These regions in the experimental data are most likely due to the $\lambda/4$ plate error e_1, which would lead to slightly elliptical polarization of the input electric field, as discussed in Section 3.2.2. These four-lobed poor fringe contrast regions are prominent in the wrapped phase quality maps, indicated by values near zero in the four-lobed shapes of $\cos(\varphi_{diff}) = 0$ in Figures 3.12(d) and 3.13(d). Due to these low-quality values in a closed shape, phase information about the monotonically increasing or decreasing phase as $r \to 0$ cannot easily pass accross the low-quality boundary. The resulting unwrapping errors appear as local phase with good quality unwrapped phase inside these four-lobed regions, but that does not have the expected either monotonically increasing or decreasing behavior as $r \to 0$. Theoretical wrapped phases assuming $e_1 = \pi/90$ radians in Figures 3.12(e) and 3.13(e), as with the photoelastic field modeling above, show the poor fringe contrast in the four-lobed shape consistent with $\cos(\varphi_{diff}) \to 0$ and exhibit similar phase modulation near these boundaries as the experimental data. Figures 3.12(f) and 3.13(f) show the theoretical poor wrapped data quality maps in the four-lobed shape for these theoretical wrapped phases including the e_1 error and show the good quality data inside the lobes away from $\cos(\varphi_{diff}) \to 0$ boundaries as in the experimental wrapped data quality maps.

The experimental unwrapped phases in Figures 3.14(a) and 3.14(c) show the types of unwrapping errors discusses above, as compared to the theoretical φ_{sum} fields that do not include e_1 error in Figures 3.14(b) and 3.14(d). The experimental data does not reach the same large phase values near the notch tip because of these unwrapping errors. Despite these local errors, the theoretical and experimental fields compare well in general shape and value away from the notch tip.

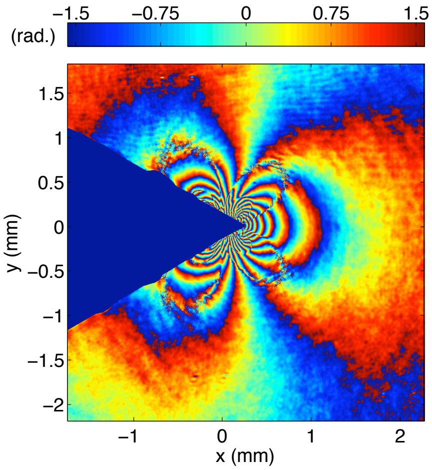

(a) Experimental wrapped φ_{sum}

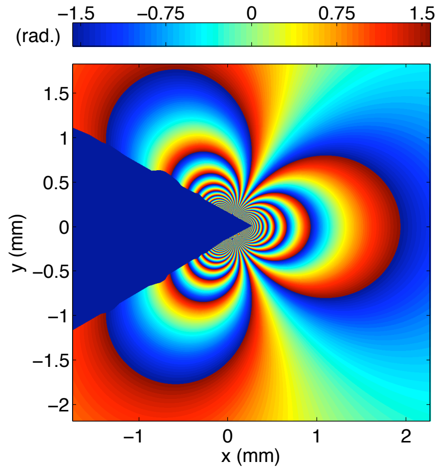

(b) Theoretical wrapped φ_{sum}

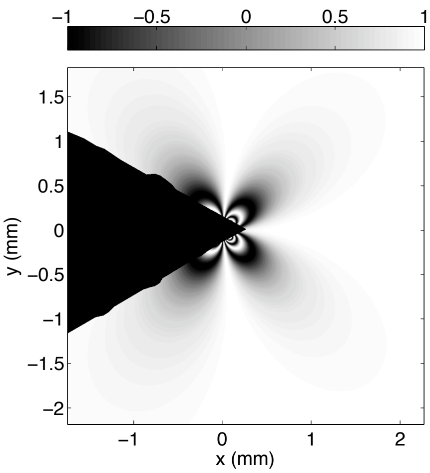

(c) Theoretical $\cos(\varphi_{diff})$

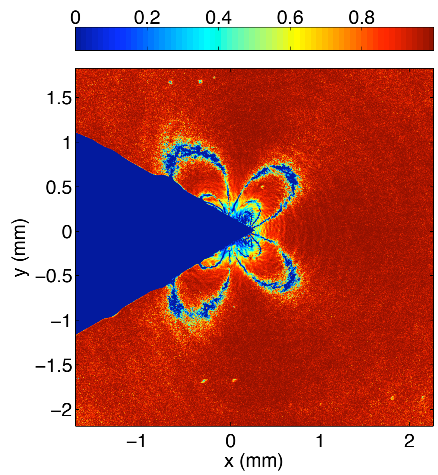

(d) Experimental phase quality map

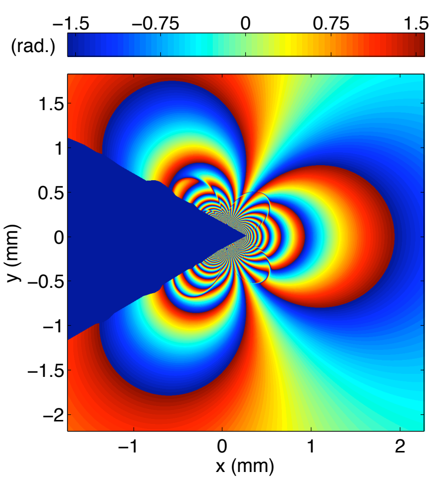

(e) Theoretical wrapped φ_{sum} with $e_1 = \pi/90$ rad.

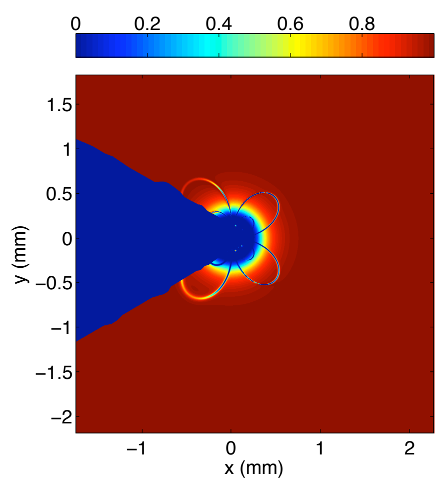

(f) Theoretical phase quality map for field with $e_1 = \pi/90$ rad.

Figure 3.12: CGS wrapped phase analysis for the horizontal shearing direction with V-notch region masked in blue (or black)

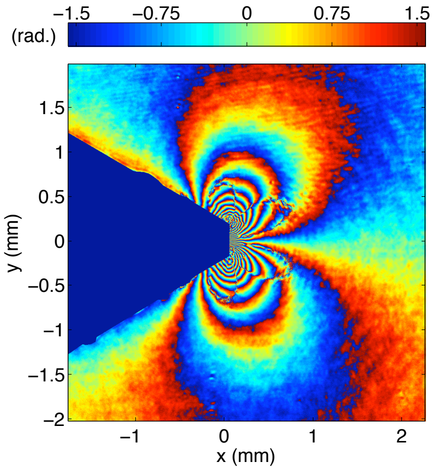

(a) Experimental wrapped φ_{sum}

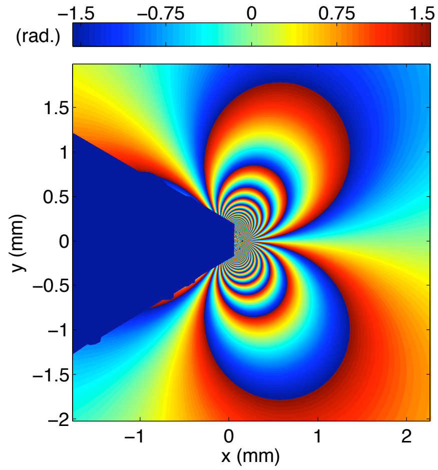

(b) Theoretical wrapped φ_{sum}

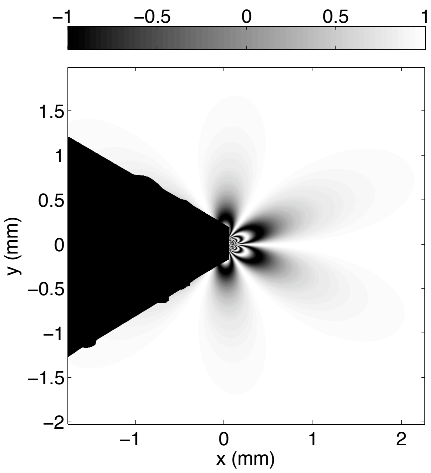

(c) Theoretical $\cos(\varphi_{diff})$

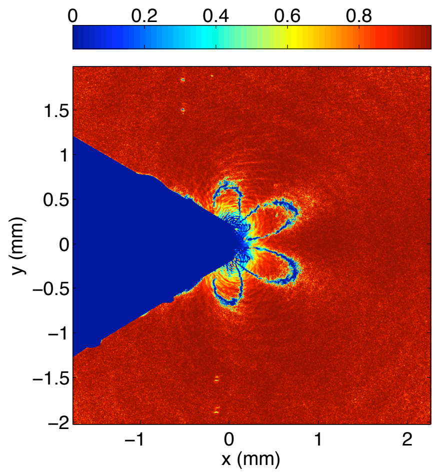

(d) Experimental Phase Quality Map

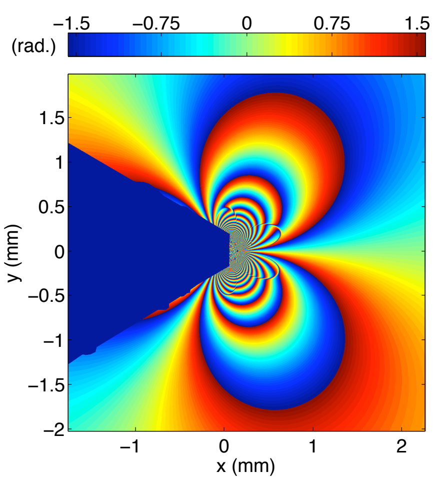

(e) Theoretical wrapped φ_{sum} with $e_1 = \pi/90$ rad.

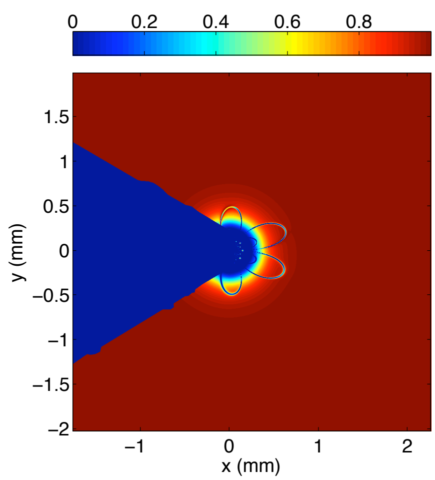

(f) Theoretical phase quality map for field with $e_1 = \pi/90$ rad.

Figure 3.13: CGS wrapped phase analysis for the vertical shearing direction with V-notch region masked in blue (or black)

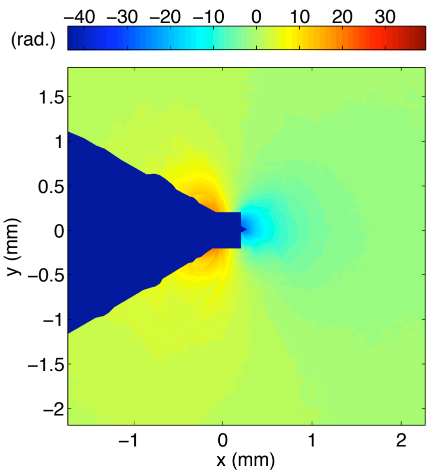

(a) Experimental unwrapped φ_{sum}

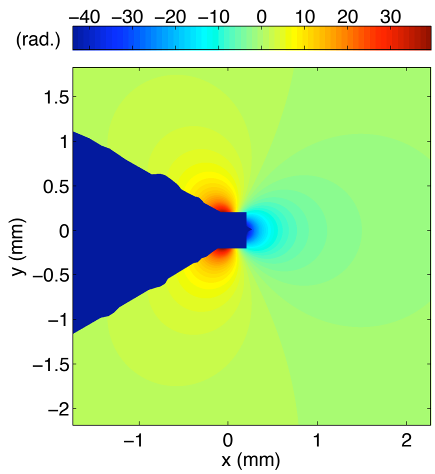

(b) Theoretical unwrapped φ_{sum}

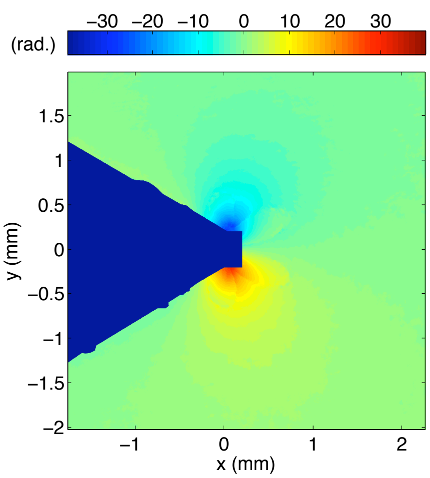

(c) Experimental unwrapped φ_{sum}

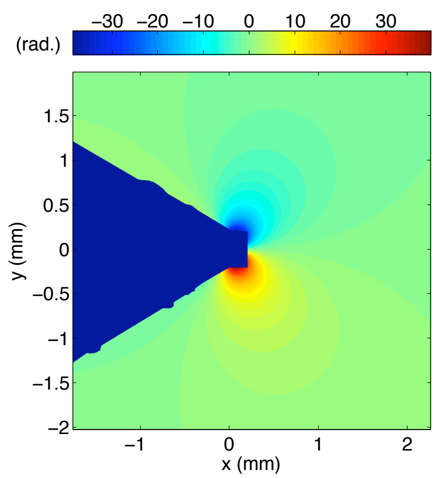

(d) Theoretical unwrapped φ_{sum}

Figure 3.14: CGS wrapped phase analysis for the vertical shearing direction with V-notch region masked in blue (or black)

3.3.2.4 Stress Determination

The isochromatic phase is converted to the $\sigma_1 - \sigma_2$ fields using Equation (3.1). The two CGS phases are converted to stress derivatives using Equation (2.26) and then integrated using the PCG method, producing $\sigma_1 + \sigma_2 + c_i$, where c_i is a constant of integration. This constant may be determined by using one of the traction-free boundary conditions along the notch edge, $\sigma_{\theta\theta} = 0$ or $\sigma_{r\theta} = 0$ for $\theta = \pm 5\pi/6$, where θ denotes the rotational polar coordinate. Utilizing the $\sigma_1 - \sigma_2$, $\sigma_1 + \sigma_2 + c_i$, and α fields, shown in Figures 3.15(a)–3.15(c), the $\sigma_{\theta\theta} = 0$ condition gives a constant of integration calculated by

$$c_i = [(\sigma_1 + \sigma_2 + c_i) - (\sigma_1 - \sigma_2)\cos(2\alpha - 2\theta)]\big|_{\theta = \pm 5\pi/6}. \tag{3.13}$$

With this constant of integration, the $\sigma_1 + \sigma_2$ field is determined, as shown in Figure 3.15(d). The experimental field is asymmetric across the x axis, unlike the theoretical field in Figure 3.15(e), but this is due to an asymmetric x derivative of $\sigma_1 + \sigma_2$, just noticeable along the V-notch boundary in the experimental unwrapped horizontal shearing φ_{sum} in Figure 3.14(a). Otherwise, the stress concentration variation with r appears to generally agree with theory. With full-field $\sigma_1 + \sigma_2$ and $\sigma_1 - \sigma_2$, the principal stresses may be separated, as shown in Figure 3.16. The experimental principal stresses compare well with theory, with the σ_1 field with a single elliptical lobe symmetric about the x axis and the σ_2 field with a kidney bean shape again symmetric about the x axis. The experimental σ_1 is smaller in stress magnitude than the theoretical field, while the experimental σ_2 is larger in stress magnitude than the theoretical field; these differences are likely due to the experimental $\sigma_1 - \sigma_2$ field being slightly larger in stress magnitude than the theoretical data.

The Cartesian stresses, σ_{xx}, σ_{yy}, and σ_{xy}, shown in Figure 3.17, are determined using the separated principal stresses and the isoclinic angle as the angle of rotation for the coordinate transformation. These and the polar stresses may also be written in terms of $\sigma_1 - \sigma_2$, $\sigma_1 + \sigma_2$, α, and θ (for the polar stresses), as shown in Table 3.3 (derivation of these relationships and others concerning stresses may be found in Appendix A); these formulas indicate how the in-plane stresses relate to the fields from the two experimental methods. The experimental σ_{xx} field has the correct single elliptical lobe shape about the x axis as compared to the theoretical σ_{xx}. The kidney bean-shaped contour appears in both the experimental and theoretical σ_{yy}. The interpolated regions in the isoclinic angle visually appear to modulate the experimental σ_{xy} as compared to the theoretical σ_{xy}, but positive stresses for $(-x, +y)$ and $(+x, -y)$ regions and negative stresses for $(+x, +y)$ and $(-x, -y)$ regions are evident. The effect of α on this shear stress field is not surprising since σ_{xy} only depends on the photoelastic data, as seen in the formula in Table 3.3, and thus the error in α is not diffused by $\sigma_1 + \sigma_2$ for this field.

Stress	Relationship to $\sigma_1 - \sigma_2$, $\sigma_1 + \sigma_2$, α, and θ
σ_{xx}	$\frac{1}{2}(\sigma_1 + \sigma_2) + \frac{1}{2}(\sigma_1 - \sigma_2)cos(2\alpha)$
σ_{yy}	$\frac{1}{2}(\sigma_1 + \sigma_2) - \frac{1}{2}(\sigma_1 - \sigma_2)cos(2\alpha)$
σ_{xy}	$\frac{1}{2}(\sigma_1 - \sigma_2)sin(2\alpha)$
σ_{rr}	$\frac{1}{2}(\sigma_1 + \sigma_2) + \frac{1}{2}(\sigma_1 - \sigma_2)cos(2\theta - 2\alpha)$
$\sigma_{\theta\theta}$	$\frac{1}{2}(\sigma_1 + \sigma_2) - \frac{1}{2}(\sigma_1 - \sigma_2)cos(2\theta - 2\alpha)$
$\sigma_{r\theta}$	$-\frac{1}{2}(\sigma_1 - \sigma_2)sin(2\theta - 2\alpha)$

Table 3.3: In-plane stress components and their relationships to $\sigma_1 - \sigma_2$, $\sigma_1 + \sigma_2$, α, and θ

The polar stresses presented in Figure 3.18 are determined by transforming the Cartesian stresses with a rotation matrix with θ as the angle of rotation. Similar to the Cartesian stresses, the experimental polar stresses compare well with theoretical fields, with overall good shape comparison and stress magnitude comparison despite modulation by the errors in the isoclinic angle. The experimental σ_{rr} field is asymmetric about the x axis with larger stress magnitude for positive y values. The experimental $\sigma_{\theta\theta}$ has the wide fan-like structure in front of the notch, though not all of the $\sigma_{\theta\theta}$ data is going to zero along the notch mask boundary, requiring a choice of where to apply the boundary condition for the constant of integration calculation. The portion of the boundary that appears to be furthest in proximity from error sources like interpolated regions in α and far from the $\cos\varphi_{diff} \rightarrow 0$ boundaries is chosen for the constant of integration calculation. The experimental $\sigma_{r\theta}$ is noticeably modulated by the isoclinic angle errors, but the overall asymetric stresses match well with theoretical values, even better than the experimental σ_{xy} compares with theory. Since $\sigma_{r\theta}$ depends on both α and θ in that $\sigma_{r\theta} = \frac{1}{2}(\sigma_1 - \sigma_2)sin(2\theta - 2\alpha)$, the θ contributions appear to diffuse the error associated with α, allowing for better agreement with theory for $\sigma_{r\theta}$ than for σ_{xy}.

In general, the stress fields appear to match well in magnitude for larger r, but the largest difference between the theoretical and experimental stress fields is close to the notch tip. This greater difference near the notch tip is expected because the finite resolution of the experimental techniques and the $1/r^{1-\lambda_o}$ character of the stress fields make the large fringe density near the notch tip more difficult to measure. The slight asymmetry of the stress fields about the x axis, especially along the notch edge, is evidence that the polycarbonate specimen is not perfectly uniformly loaded. Another possible source of error in the data is due to the masking of the notch area, which obscures the exact edge of the notch where the boundary conditions are applied and, hence, where the constant of integration is calculated. The slightly higher stress concentration for $\sigma_1 - \sigma_2$ and slightly lower stress concentration for $\sigma_1 + \sigma_2$ in the experimental data, as compared to the theoretical data, is possibly due to the material constants used to convert the phases to stresses, given in Section 3.3.1. Polymers tend to vary between manufacturers and between different batches of material, leading to variable material properties. Since the material constants used are from published literature, these may not *exactly* correspond to the material properties of the polycarbonate used in this study. The constants in literature are good guidelines and a place to start for converting these phases to stresses. The combination of these constants from literature may lead to an under-determination of the stresses in $\sigma_1 + \sigma_2$, leading to a smaller choice of the fitting coefficient C_f, which is the reason for the theoretical $\sigma_1 - \sigma_2$ appearing too small. In future, to more accurately determine the stresses, these material constants can be measured for the particular batch of polymer used for the specimens.

Given all of these considerations, the data fit remarkably well. One measure of the global error is the root mean square deviation (RMSD) normalized by the range of data, denoted NRMSD. Only data points not masked by notch mask are considered here. Table 3.4 reports the error analysis of several fields. The fields with the lowest NRMSD are the stress derivatives and $\sigma_1 - \sigma_2$, demonstrating the effectiveness of the six-step phase-shifting photoelastic method and small effect of the $T_x \approx T_y$ assumption and the e_1 $\lambda/4$ plate misalignment error. Additionally, since the theoretical stress field fitting factor C_f is calculated by comparison with the all of the experimental fields, the low error for both the stress derivatives and $\sigma_1 - \sigma_2$ fields that come from two separate experimental techniques implies that these two techniques work well together to determine the full-field stress tensor.

The isoclinic angle has a higher NRMSD, though still reasonable at 7.5%, most likely due to the interpolation across the regions near $\sin(\delta) = 0$, since 27% of the data points (excluding the masked notch region) have been removed and interpolated across. Importantly, without this interpolation, the isoclinic angle from this photoelastic data cannot be unwrapped properly with the presence of many false discontinuities due to a nonzero tolerance in $(T_x - T_y)$ and the e_1 $\lambda/4$ plate misalignment error. The interpolation method is a necessary step that makes the isoclinic angle into usable data to combine with the stress fields, making the error introduced by the interpolated regions tolerable. An error source in the stress fields employing the $\sigma_1 + \sigma_2$ field is the constant of integration calculation, which is, first, dependent of the isoclinic angle, and, second, taken not precisely at $\theta = \pm 5\pi/6$. Since the notched area requires a mask to prevent corruption of the data near the edges during phase unwrapping, then $\theta = \pm 5\pi/6$ is obscured. Here, c_i comes from $\theta = -2.54\ rad. = -145^o$. Despite these considerations, the experimental full-field stresses in principal, Cartesian, and polar coordinate systems have acceptable NRMSD error, ranging from 3.3% to 9.7%, demonstrating that the combined CGS-photoelasticity phase-shifting method successfully determines the in-plane tensorial stress for photoelastic materials.

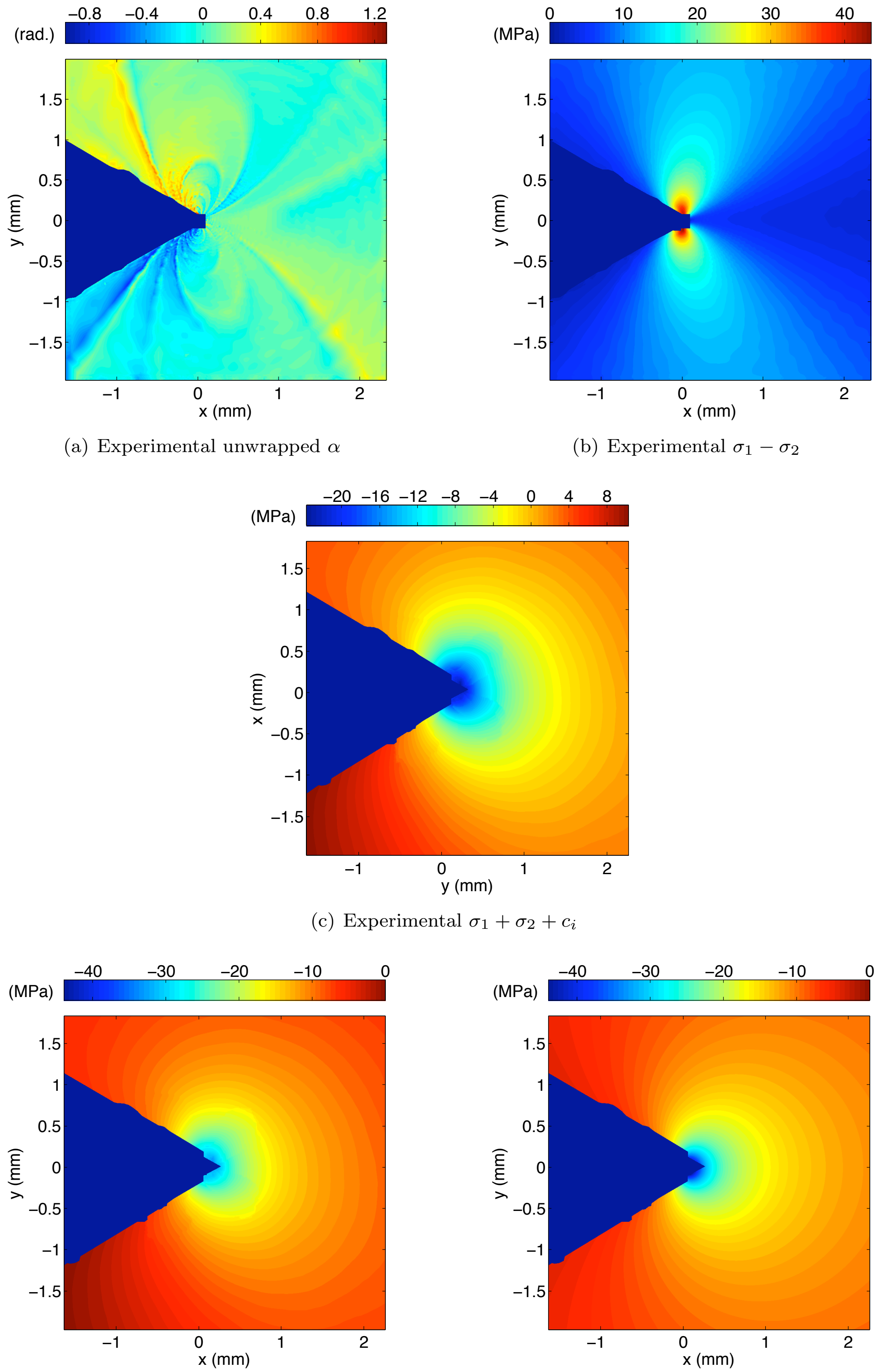

(a) Experimental unwrapped α

(b) Experimental $\sigma_1 - \sigma_2$

(c) Experimental $\sigma_1 + \sigma_2 + c_i$

(d) Experimental $\sigma_1 + \sigma_2$

(e) Theoretical $\sigma_1 + \sigma_2$

Figure 3.15: Combined principal stress fields for the compressed polycarbonate V-notch plate with V-notch masks in blue

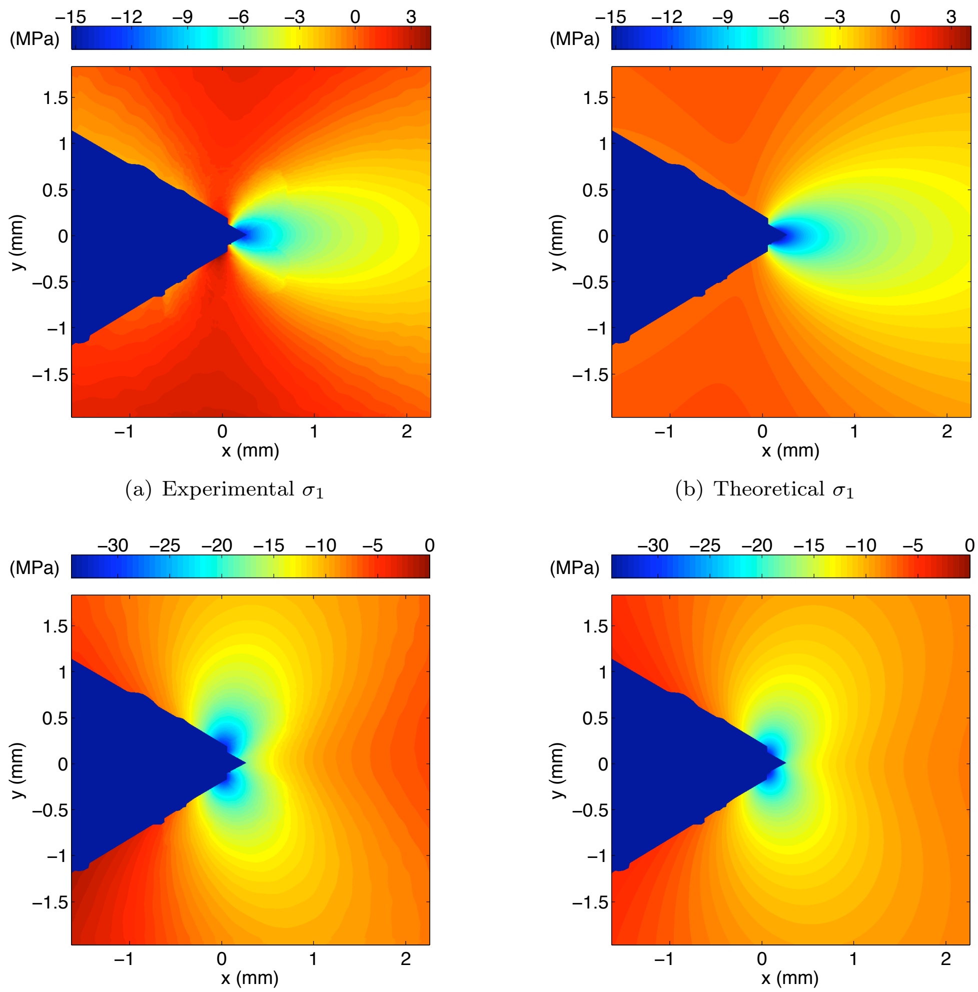

(a) Experimental σ_1

(b) Theoretical σ_1

(c) Experimental σ_2

(d) Theoretical σ_2

Figure 3.16: Experimental and theoretical separated principal stress fields for the compressed polycarbonate V-notch plate with V-notch masks in blue

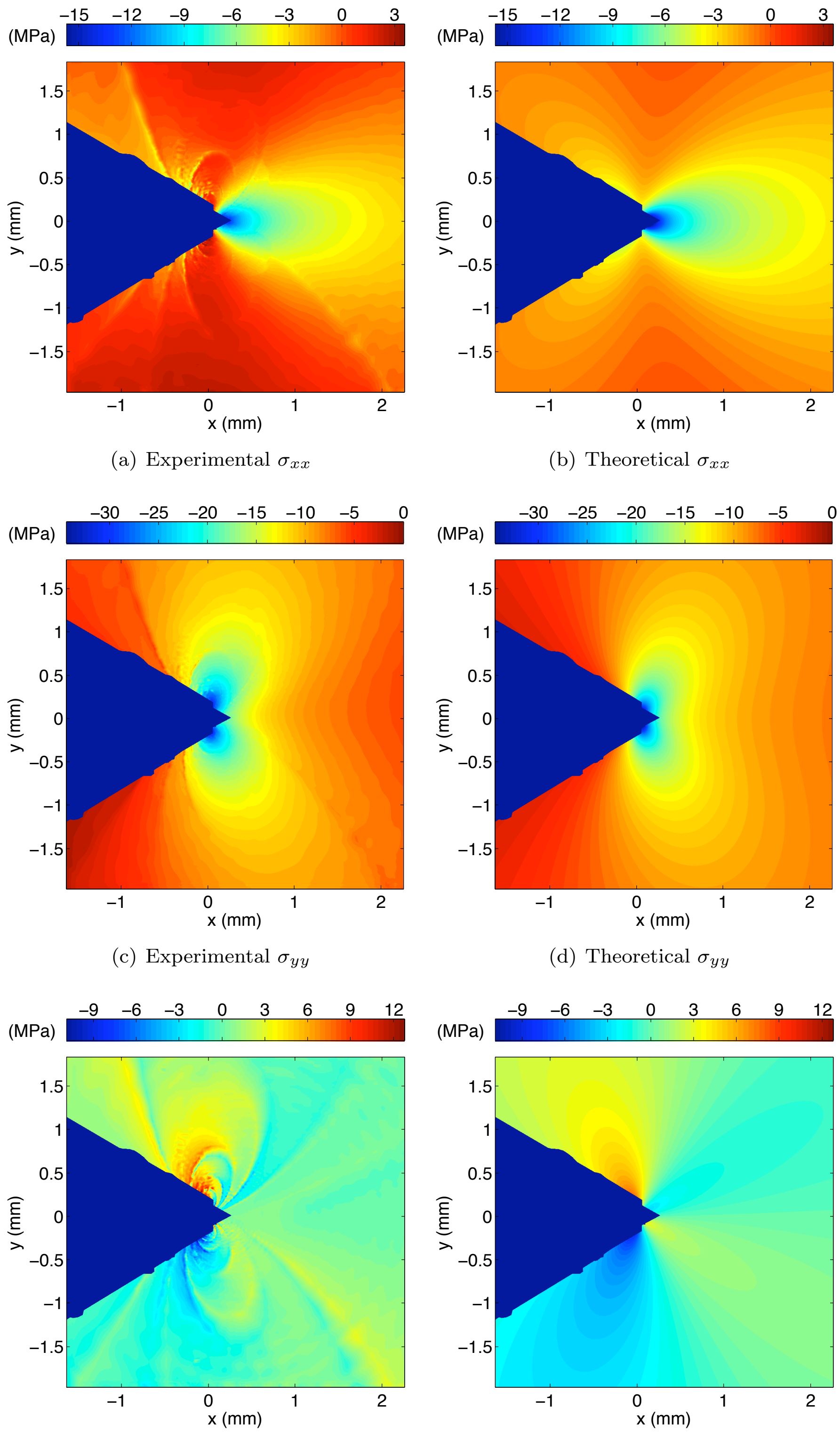

(a) Experimental σ_{xx} (b) Theoretical σ_{xx}

(c) Experimental σ_{yy} (d) Theoretical σ_{yy}

(e) Experimental σ_{xy} (f) Theoretical σ_{xy}

Figure 3.17: Experimental and theoretical Cartesian stress fields for the compressed polycarbonate V-notch plate with V-notch masks in blue

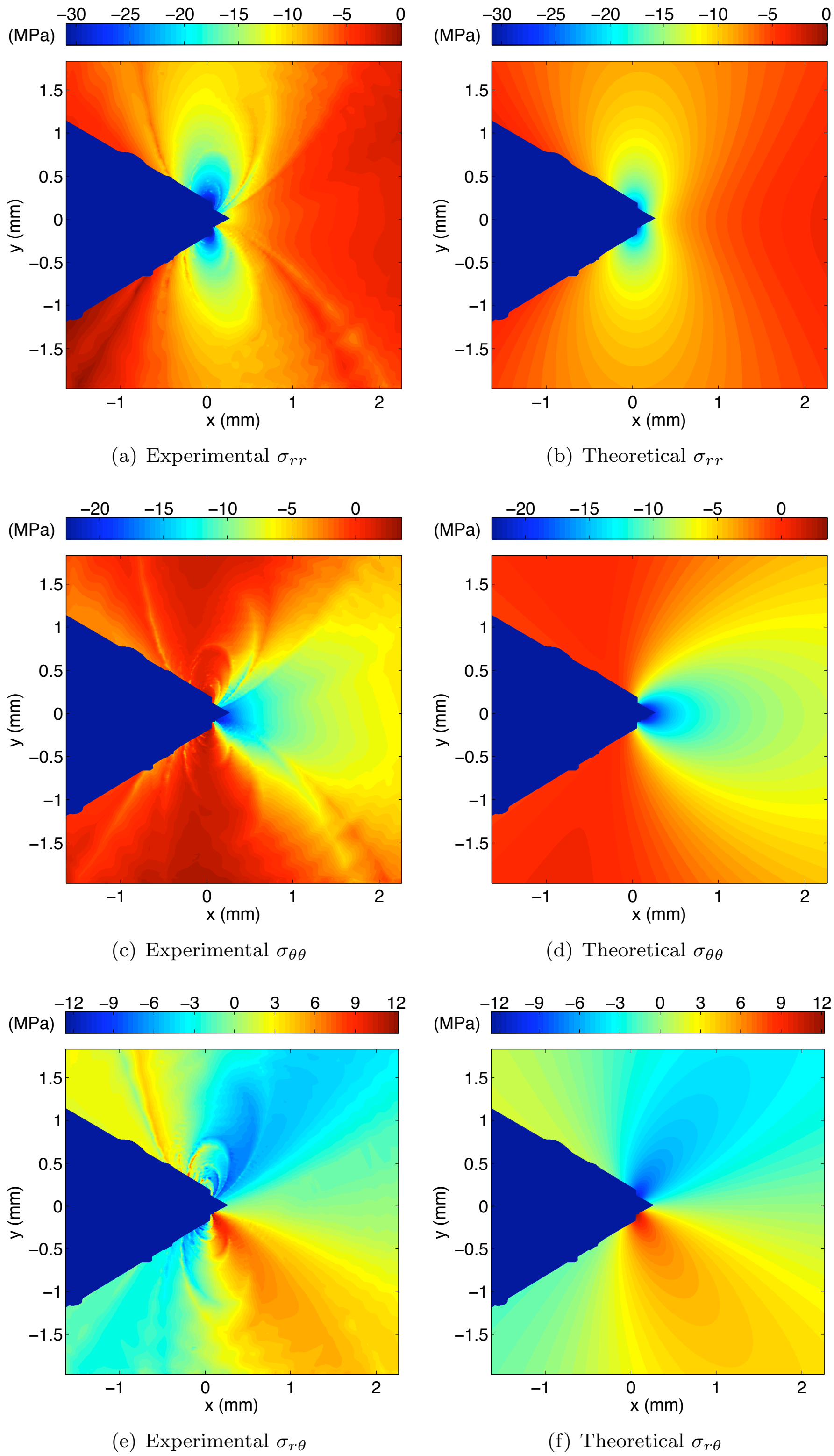

(a) Experimental σ_{rr}

(b) Theoretical σ_{rr}

(c) Experimental $\sigma_{\theta\theta}$

(d) Theoretical $\sigma_{\theta\theta}$

(e) Experimental $\sigma_{r\theta}$

(f) Theoretical $\sigma_{r\theta}$

Figure 3.18: Experimental and theoretical polar stress fields for the compressed polycarbonate V-notch plate with V-notch masks in blue

Quantity	Units	RMSD (in Units)	Data Range (in Units)	NRMSD (No Units)
α	rad.	0.17	2.25	0.075
$\partial(\sigma_1+\sigma_2)/\partial x$	MPa/mm	1.55	94.2	0.016
$\partial(\sigma_1+\sigma_2)/\partial y$	MPa/mm	1.31	110.0	0.012
$\sigma_1+\sigma_2$	MPa	1.52	33.7	0.045
$\sigma_1-\sigma_2$	MPa	1.62	42.1	0.038
σ_1	MPa	1.28	17.3	0.074
σ_2	MPa	0.99	30.1	0.033
σ_{xx}	MPa	1.62	16.9	0.097
σ_{yy}	MPa	1.17	29.8	0.039
σ_{xy}	MPa	1.95	23.7	0.040
σ_{rr}	MPa	1.14	13.4	0.085
$\sigma_{\theta\theta}$	MPa	1.41	34.6	0.041
$\sigma_{r\theta}$	MPa	1.26	23.1	0.055

Table 3.4: Error analysis for various experimental fields for the compressed polycarbonate V-notch plate

3.4 Conclusions

The combined phase-shifting photoelasticity and CGS method presented in this study demonstrates the full-field determination of the in-plane tensorial stress for photoelastic materials. A six-step phase-shifting photoelasticity method gives $\sigma_1 - \sigma_2$ and the isoclinic angle, which requires some careful consideration in regions where $\sin(\delta) \to 0$ to minimize errors in phase unwrapping. Transmission CGS for a photoelastic material requires a four-step phase-shifting method in conjunction with polarization optics prior to the specimen to extract the desired phases related to x and y derivatives of $\sigma_1 + \sigma_2$. A weighted PCG algorithm is used for both phase unwrapping and integration of the $\sigma_1 + \sigma_2$ derivatives. The $\sigma_1 + \sigma_2$ field is determined by using a boundary condition to determine the constant of integration. The principal stresses are then separable from the $\sigma_1 + \sigma_2$ and $\sigma_1 - \sigma_2$ fields. The Cartesian and polar coordinate stress fields are also determined by simple coordinate transformations using the isoclinic angle and the polar coordinate. The entire method is demonstrated for a compressed polycarbonate plate with a side V-notch.

Possible error sources in the experimental method are identified as the transmission and reflectance coefficients of the non-polarizing beamsplitter and rotational misalignment of the polarization optics. Theoretical data including these possible errors demonstrate the extent of their effect on the data and identify the dominant error source in the experimental data as the misalignment of the first $\lambda/4$ plate. Mitigation techniques, such as correction of the modulated wrapped isoclinic angle and implementation of the PCG algorithm, a data quality-driven unwrapping algorithm, help to minimize propagation of error through the data. Despite these errors, the experimental stresses compare well with the theoretical stresses for the polycarbonate example. Establishing the use of this hybrid experimental technique in a compressed plate with a V-notch is the foundation for its application to determine the in-plane tensorial stress around a loaded crack in a photoelastic material.

Chapter 4

Stress Analysis for Fracture

4.1 Introduction

This chapter describes the application of the hybrid phase-shifting full-field experimental CGS-photoelasticity method to fracture studies in a photoelastic material. Section 4.2 presents the theoretical 2D asymptotic crack solution, which is the basis for determining the stress intensity factors for the experimental stress fields, and four cases of stress determination around Mode I–dominant cracks in Homalite-100. Section 4.3 provides some discussion on the use of this experimental method for fracture studies based on the variety of cases presented in this chapter.

4.2 Stresses Around Cracks in Homalite-100

4.2.1 2D Asymptotic Crack Solution (Mode I and Mode II)

Assuming that the loaded crack has both symmetric and antisymmetric stress components and that the stresses are characterized by singular terms with constant stress intensity factors K_I and K_{II}, the stress field is the sum of the Mode I and Mode II stress field components as follows (Anderson, 2005):

$$\sigma_{xx} = \frac{K_I}{\sqrt{2\pi r}} \cos\left(\frac{\theta}{2}\right)\left[1 - \sin\left(\frac{\theta}{2}\right)\sin\left(\frac{3\theta}{2}\right)\right] - \frac{K_{II}}{\sqrt{2\pi r}} \sin\left(\frac{\theta}{2}\right)\left[2 + \cos\left(\frac{\theta}{2}\right)\cos\left(\frac{3\theta}{2}\right)\right] \tag{4.1a}$$

$$\sigma_{yy} = \frac{K_I}{\sqrt{2\pi r}} \cos\left(\frac{\theta}{2}\right)\left[1 + \sin\left(\frac{\theta}{2}\right)\sin\left(\frac{3\theta}{2}\right)\right] + \frac{K_{II}}{\sqrt{2\pi r}} \sin\left(\frac{\theta}{2}\right)\cos\left(\frac{\theta}{2}\right)\cos\left(\frac{3\theta}{2}\right) \tag{4.1b}$$

$$\sigma_{xy} = \frac{K_I}{\sqrt{2\pi r}} \sin\left(\frac{\theta}{2}\right) \cos\left(\frac{\theta}{2}\right) \cos\left(\frac{3\theta}{2}\right) + \frac{K_{II}}{\sqrt{2\pi r}} \cos\left(\frac{\theta}{2}\right) \left[1 - \sin\left(\frac{\theta}{2}\right) \sin\left(\frac{3\theta}{2}\right)\right]. \tag{4.1c}$$

4.2.2 Calculation of K_I and K_{II} for Mixed-Mode Fracture

The mixed-mode stress intensity factors K_I and K_{II} may be determined from the interference patterns of both photoelasticity and CGS, assuming the field of view contains K-dominant points, i.e., points where the stresses may be characterized by Equation (4.1). From inspiration from Smith and Smith (1972), Sanford and Dally (1979), and Smith and Olaosebikan (1984), who used photoelastic interference patterns, and from Mason et al. (1992), who used CGS interference patterns, an iterative nonlinear least-squares approach using many points from both photoelastic and CGS phase data has been developed for calculating K_I and K_{II} for the mixed-mode fracture presented in this chapter.

Since the hybrid method presented in this thesis utilizes two interference techniques, the method for calculating K_I and K_{II} naturally includes data from both techniques. The method starts with relationships between the interference phases from both techniques and the variables K_I, K_{II}, r and θ. Using Equations (3.1) and (4.1), the photoelastic isochromatic phase for mixed-mode K-dominant fracture is

$$\delta(r,\theta) = \left(\frac{2\pi c_o h}{\lambda}\right) \frac{1}{\sqrt{2\pi r}} \sqrt{[K_I \sin(\theta) + 2K_{II}\cos(\theta)]^2 + [K_{II}\sin(\theta)]^2}, \tag{4.2}$$

and using Equations (2.18a) and (4.1), the CGS phases related to the x and y derivatives of the sum of principal stresses for mixed-mode K-dominant fracture, $\varphi_{sum}^{\partial x}$ and $\varphi_{sum}^{\partial y}$, respectively, are

$$\varphi_{sum}^{\partial x}(r,\theta) = \left(\frac{2\pi\tilde{\Delta}Ch}{p}\right) \frac{1}{\sqrt{2\pi r^3}} \left[- K_I \cos\left(\frac{3\theta}{2}\right) + K_{II} \sin\left(\frac{3\theta}{2}\right)\right] \tag{4.3a}$$

$$\varphi_{sum}^{\partial y}(r,\theta) = \left(\frac{2\pi\tilde{\Delta}Ch}{p}\right) \frac{1}{\sqrt{2\pi r^3}} \left[- K_I \sin\left(\frac{3\theta}{2}\right) - K_{II} \cos\left(\frac{3\theta}{2}\right)\right]. \tag{4.3b}$$

The errors at any point i for the three phases are dimensionless so that the errors from different types data are comparable and, therefore, may be used in the same nonlinear least-squares algorithm; the errors are defined as the difference between the experimental phases and their theoretical values, normalized by the range of experimental data of the M points used in the algorithm for that phase, similar to the NRMSD error measure described in Chapters 2 and 3:

$$\epsilon_i^{\delta} = \frac{\left[\delta(r_i,\theta_i) - \left(\frac{2\pi c_o h}{\lambda}\right)\frac{1}{\sqrt{2\pi r_i}}\sqrt{[K_I\sin(\theta_i) + 2K_{II}\cos(\theta_i)]^2 + [K_{II}\sin(\theta_i)]^2}\right]}{(\max[\delta] - \min[\delta])} \tag{4.4a}$$

$$\epsilon_i^{\partial x} = \frac{\left[\varphi_{sum}^{\partial x}(r_i,\theta_i) - \left(\frac{2\pi\tilde{\Delta}Ch}{p}\right)\frac{1}{\sqrt{2\pi r_i^3}}\left[-K_I\cos\left(\frac{3\theta_i}{2}\right) + K_{II}\sin\left(\frac{3\theta_i}{2}\right)\right]\right]}{(\max[\varphi_{sum}^{\partial x}] - \min[\varphi_{sum}^{\partial x}])} \tag{4.4b}$$

$$\epsilon_i^{\partial y} = \frac{\left[\varphi_{sum}^{\partial y}(r_i,\theta_i) - \left(\frac{2\pi\tilde{\Delta}Ch}{p}\right)\frac{1}{\sqrt{2\pi r_i^3}}\left[-K_I\sin\left(\frac{3\theta_i}{2}\right) - K_{II}\cos\left(\frac{3\theta_i}{2}\right)\right]\right]}{(\max[\varphi_{sum}^{\partial y}] - \min[\varphi_{sum}^{\partial y}])}. \tag{4.4c}$$

The normalization is done by the range of the experimental data instead of the theoretical data in order to avoid dividing the differences between the experimental and theoretical phases by zero.

Since the experimental phases used in the error calculations come from an unwrapping process that incorporates a data-quality weight function given by Equation (2.28), the errors ϵ_i^{δ}, $\epsilon_i^{\partial x}$, and $\epsilon_i^{\partial y}$ are multiplied by the appropriate weight functions calculated for the PCG unwrapping algorithm for every point i, such that the higher quality data points receive more weight in the least-squares minimization algorithm. The weight functions for the isochromatic phase and the CGS phases related to the x and y derivatives of $\sigma_1 + \sigma_2$ are denoted W_i^{δ}, $W_i^{\partial x}$, and $W_i^{\partial y}$, respectively.

The iterative nonlinear least-squares algorithm minimizes the function $f(K_I, K_{II})$, which is a vector function incorporating these error definitions and appropriate weight functions described above, by iteratively choosing K_I and K_{II} values using the trust-region-reflective algorithm based on the interior-reflective Newton method, which is a standard nonlinear least-squares algorithm; this algorithm has been implemented in MATLAB®. The function $f(K_I, K_{II})$ and the minimization of the squared L_2 norm is as follows, for M points of δ, N points of $\varphi_{sum}^{\partial x}$, and P points of $\varphi_{sum}^{\partial y}$:

$$\boldsymbol{f}(K_I, K_{II}) = \left[\tfrac{1}{\sqrt{2}}W_1^{\delta}\epsilon_1^{\delta}, \ldots, \tfrac{1}{\sqrt{2}}W_M^{\delta}\epsilon_M^{\delta},\ \tfrac{1}{2}W_1^{\partial x}\epsilon_1^{\partial x}, \ldots, \tfrac{1}{2}W_N^{\partial x}\epsilon_N^{\partial x},\ \tfrac{1}{2}W_1^{\partial y}\epsilon_1^{\partial y}, \ldots, \tfrac{1}{2}W_P^{\partial y}\epsilon_P^{\partial y}\right]^T \tag{4.5}$$

$$\begin{aligned}\min_{K_I,K_{II}} \left\|\boldsymbol{f}(K_I,K_{II})\right\|_2^2 &= \min_{K_I,K_{II}} (f_1^2+f_2^2+\cdots+f_{M+N+P}^2)\\ &= \min_{K_I,K_{II}} \Big(\frac{1}{2}\sum_{i=1}^{M}(W_i^{\delta}\epsilon_i^{\delta})^2+\frac{1}{4}\sum_{j=1}^{N}(W_j^{\partial x}\epsilon_j^{\partial x})^2+\frac{1}{4}\sum_{k=1}^{P}(W_k^{\partial y}\epsilon_k^{\partial y})^2\Big).\end{aligned} \tag{4.6}$$

The constant coefficients in front of the elements of the vector function $\boldsymbol{f}$ in Equation (4.5) and the constants in front of the summation symbols of Equation (4.6) are present to equally weight the contributions of the two experimental techniques to the minimization algorithm since photoelasticity gives only one stress-related phase and CGS gives two, i.e., the photoelasticity data set receives twice the weight in the minimization algorithm as each of the CGS data sets.

Another consideration in the determination of K_I and K_{II} is the assumption of plane stress in these specimens; the mixed-mode fracture stress fields in Equation (4.1) are only valid for plane stress K-dominant regions. The stresses determined by transmission interference techniques are inherently through-thichness averages of the stresses, so if the specimen is under plane stress, then the measured stresses are constant through the theickness. Since the field of view is small in cases presented here, a notable portion of the field of view of the interference patterns are subject to 3D (triaxial) stress effects around the crack tip, meaning the stresses measured in this region vary through the thickness and are not purely plane stress. According to Rosakis et al. (1990) and Krishnaswamy et al. (1991), who studied 3D effects in elastodynamic crack problems, the extent of the 3D zone has a radius around 0.4–0.5h. Using this as a general guideline for excluding points in the field of view that may be subject to 3D effects, all of the points inside a circle of radius 0.5h centered around the crack tip are excluded from the points used in calculating K_I and K_{II}. Additionally, all points that have been excluded by a user-defined mask in the unwrapping algorithm are also excluded from consideration. In the spirit of having full-field phase maps, all the points not excluded for the three phases in the field of view are used in the nonlinear least-squares minimization algorithm to determine K_I and K_{II}.

4.2.3 Wedge Opening Experiments: Mode I–Dominant Cracks

The experimental loading configuration is a symmetric wedge with an angle $2\chi = \pi/9$ symmetrically opening a straight notch of length a_1 that is at the tip of a V-shaped notch and that has a sharp crack of length a_2 emanating from the straight notch tip, as shown in Figure 4.1(a). The sharp crack is formed from two steps. First, a straight razor blade is pressed into the tip of the straight notch, initiating two sharp, short, crack-like defects, one on each face of the specimen moving partly through the thickness. Second, the loading condition for the experiments is used to gently and slowly open the notch to fill in the crack through-thickness from these two defects as shown in Figure 4.1(b); the crack generally propagates and then arrests a few millimeters from the straight notch tip. Fast loading of this notch leads to sudden and complete fracture of the specimen, so modest displacement rates of the wedge around 50 μm/s produces cracks that do not propagate the length of the specimen. The specimen is then unloaded before the experimental loads to adjust the specimen height such that the crack tip is in the field of view of the optical setup. This precracking method is useful for brittle photoelastic materials, but may be less successful in ductile photoelastic materials because the defects made by the razor blade do not coalesce when wedged open in ductile materials.

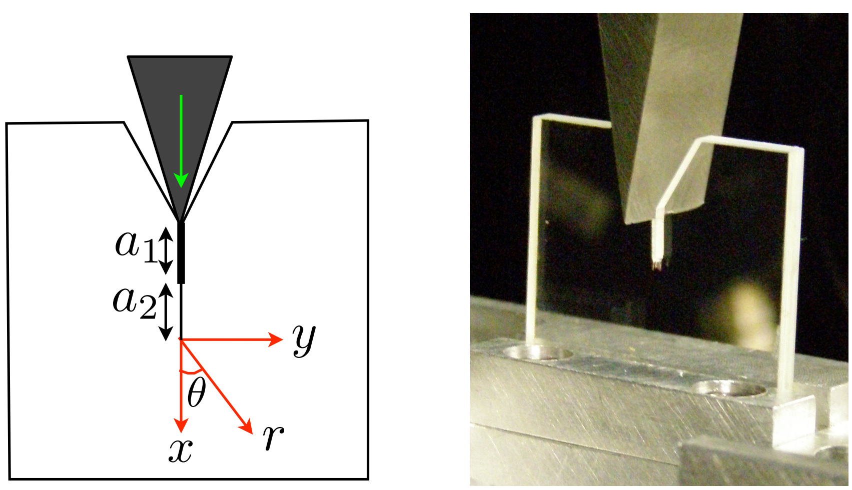

(a) Schematic

(b) Pre-cracking Setup

Figure 4.1: Experimental loading configuration for wedge opening

During experimental loading, the wedge can be slightly misaligned with the x axis, and therefore the downward motion of the wedge can impart a slight Mode II load to the crack, evident in slight asymmetry in the stress fields. Another possibility for a Mode II contribution to the stress field is the symmetric Mode I loading of a crack with a slight angle β_c to the x axis (Anderson, 2005). With these experiments, the theoretical model is a straight crack along the x axis with superposed dominant Mode I and slight Mode II loadings. The level of mode-mixity is characterized by the stress intensity factor ratio $\mu_{SIF} = K_{II}/K_I$. In these experiments, the translating mirror setup is used instead of the non-polarizing beamsplitter to remove possible errors due to the transmission and reflectance coefficients of the beamsplitter. Use of a beamsplitter with well-matched coefficients should not change the applicability of this experimental method to fracture studies.

4.2.4 Crack with $K_I = 0.514$ MPa$\sqrt{\text{m}}$ and $K_{II} = 4.4$ kPa$\sqrt{\text{m}}$

In specimen called HomC1, the material is Homalite-100, with thickness of $h = 2.19$ mm, outer dimensions 25.48 mm $\times$ 25.48 mm, V-notch depth of 6.25 mm, straight notch length of $a_1 = 4.01$ mm and crack length of $a_2 = 4.05$ mm. The material properties of Homalite-100 are Young's modulus $E = 4.55$ GPa, refractive index $n_o = 1.561$, Poisson's ratio $\nu = 0.31$, photoelastic constants $A = -9.058 * 10^{-11}$ m^2/N, $B = -1.143 * 10^{-10}$ m^2/N, $C = -1.41 * 10^{-10}$ m^2/N, and $g = -0.0844$ (RaviChandar, 1982; Kobayashi, 1993). The optical field of view imaged onto the sensor is 4.60 mm $\times$ 4.60 mm, and the image resolution is 4.6 μm. For this CGS setup, the Ronchi grating pitch is $p = 1$ mm/40; the grating separation is $\tilde{\Delta}$ =8 .87 mm; the wavelength of light from the linearly polarized HeNe laser is $\lambda = 632.8$ nm; and the resulting lateral shearing distance is $d_{shear} = 225$ μm. Figure 4.2.4 shows the specimen before loading with the experimental field of view indicated on the specimen. The measured stresses in this small field of view indicate local through-thickness average stress information around the crack tip.

K_I and K_{II} values of 0.514 MPa$\sqrt{\text{m}}$ and 4.4 kPa$\sqrt{\text{m}}$ are determined for this load case from by using the least-squares algorithm described in Section 4.2.2. This specimen HomC1 has the highest K_I of all the loadings of similar configurations. The K_{II} component is small with a stress

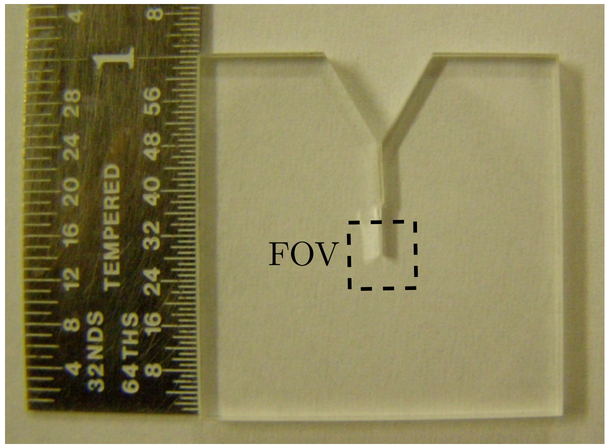

Figure 4.2: Specimen HomC1 before loading with field of view (FOV) indicated

intensity factor ratio $\mu_{SIF} = 0.0085$, so the dominant features of the stress field are Mode I, which is symmetric about the x axis.

The static initiation fracture toughness K_{Ic} values for Homalite-100 vary in literature and can vary for the same set of experiments. Bradley and Kobayashi (1971) reported fracture toughness values ranging from 0.593 MPa$\sqrt{\text{m}}$ to 0.690 MPa$\sqrt{\text{m}}$ with an average of 0.636 MPa$\sqrt{\text{m}}$. Irwin et al. (1979) and Dally (1979) state that Bradley and Kobayashi (1971) overestimates the initiation fracture toughness and report a value of only 0.445 MPa$\sqrt{\text{m}}$. The calculated K_I value for this load is around the reported fracture toughness values; since the next load increment during this experiment caused crack propagation, the measured K_I value seems reasonable to be close to reported fracture toughness values.

The experimental data is compared to theoretical data from the average K_I and K_{II} values. The main differences arise from errors in the isoclinic angle, which is highly dependent on the alignment of the polarization optics, as explained in Chapter 3, and due to the breakdown in the derivative approximation of the CGS data near the crack tip where the fringe density is high.

Given the experimental configuration, the optical coordinate system is the $\pi/2$ rotation of the conventional crack-plane coordinate system. Due to possible confusion, in this chapter, the x and y axes refer to the crack-plane coordinate systems, the variables defined in the optical coordinate system in previous chapters retain their original meaning in reference to the optical coordinate system (such as $E_x\hat{\imath}$ is the optical-x component of the electric field, and vertical shearing CGS is shearing in the optical-y axis), and any other possible confusion is clearly denoted as either relative to the optical or specimen coordinate systems.

4.2.4.1 Experimental and Theoretical Phase-Shifted Interference Images

Figures 4.3 and 4.4 show the experimental and theoretical six phase-shifted photoelasticity images for specimen HomC1. The features of the experimental images match remarkably well with the the theoretical images, taking into account for the slightly Gaussian behavior of the background intensity field I_o in the experimental images as opposed to the uniform theoretical I_o. The experimental images also appear to have similar high-frequency, low-amplitude undulation on top of the underlying photoelastic fringes as was present in the polycarbonate data in Figure 3.3 in Chapter 3. These undulations are Fizeau fringes. This noise source is minimized using a Wiener filter with window size of $[25 \times 25]$ pixels before processing the data. As expected, the high stresses at the crack tip result in caustic shadows in the experimental images; these caustic shadows are not modeled in the theoretical fields. The caustic shadows are present in all of the experimental images for both experimental techniques in the data presented in this chapter because the imaging method used in the experiment is unable to capture the divergent light rays at the crack tip for these cases.

Figures 4.5–4.10 are the experimental and theoretical image sets of four phase-shifted images for vertical shear CGS for the pure $E_x\hat{\imath}$ input, pure $E_y\hat{\jmath}$ input, and circularly polarized electric field input from the $\lambda/4$ polarization method. Since Homalite-100 has a modest value for g of -0.0844, which dictates the relative strength of secondary CGS phase φ_{diff} related to $\sigma_1 - \sigma_2$, then φ_{sum} phase dominates the images for each of the different electric field inputs. The difference between the images from the various polarization states of the input electric field are rather subtle. The images from the circularly polarized field (Figures 4.9 and 4.10) have the dominant circular features of φ_{sum} with some slight modulation of the intensity near the crack tip where $\cos(\varphi_{diff})$ is close to zero. (Figure 4.22(f) shows that the $\cos(\varphi_{diff})$ field is fairly uniform and close to a value of 1 except near the crack). Both the experimental and theoretical images from pure $E_x\hat{\imath}$ input (Figures 4.5

and 4.6) are elongated along the vertical optical direction, while the images from the pure $E_y\hat{\imath}$ input (Figures 4.7 and 4.8) are elongated along the horizontal optical direction, as compared to the images from the circularly polarized input case in Figures 4.9 and 4.10). Overall, the experimental images tend to be stretched along the shearing direction as compared to the theoretical images because the experimental phases, which approximately relate to the derivatives of stress, cannot capture the large changes in the derivatives of stress near the crack tip with a finite shearing distance $d_{shear} = 225\ \mu$m that is 5% of the field of view. Despite this finite shearing distance, the experimental and theoretical images compare well in fringe density, shape, and contrast.

Figures 4.11–4.16 are the experimental and theoretical image sets of four phase-shifted images for horizontal shear CGS for the pure $E_x\hat{\imath}$ input, pure $E_y\hat{\jmath}$ input, and circularly polarized electric field input from the $\lambda/4$ polarization method. As with the vertical shear, the experimental images compare well with the theoretical images, with slight differences near the crack tip due to the finite shearing distance issue described above. The circularly polarized light result in the expected circular lobes to the side of the crack in Figures 4.15 and 4.16, while the pure $E_x\hat{\imath}$ and $E_y\hat{\jmath}$ inputs result in slightly elongated fringes along the vertical and horizontal optical directions, respectively. The finite shearing distance is visible in the horizontal shear; the crack appears to be doubled in the experimental images. Data points between the crack are not reliable because these arise from interference of light on opposite sides of the crack, and therefore this data is masked in the analysis.

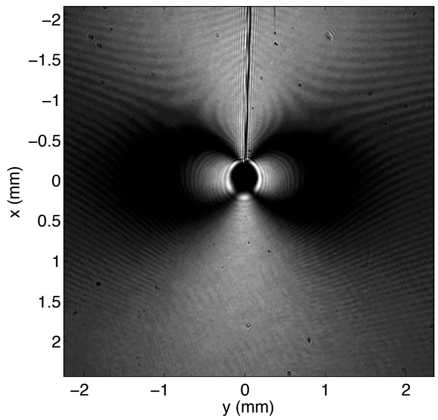

(a) $I_1 = I_o(1 + \cos(\delta))$

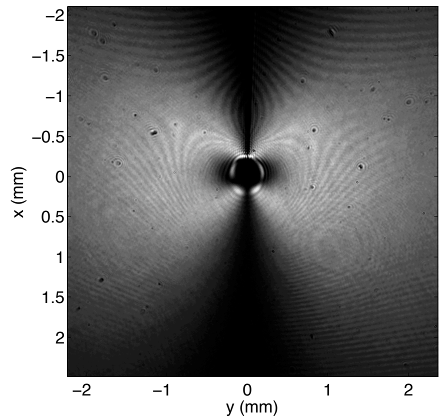

(b) $I_2 = I_o(1 - \cos(\delta))$

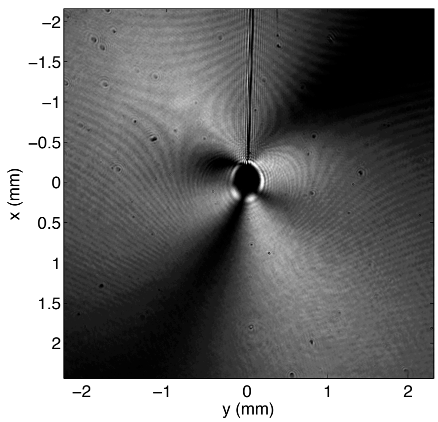

(c) $I_3 = I_o(1 - \sin(\delta)\sin(2\alpha))$

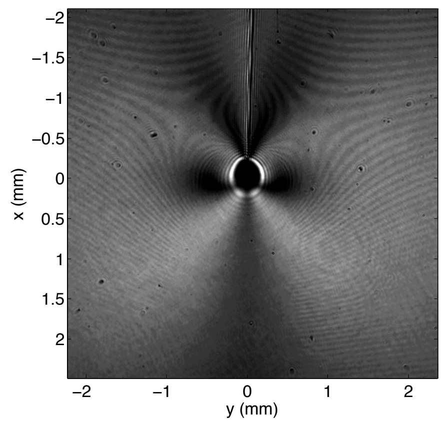

(d) $I_4 = I_o(1 + \sin(\delta)\cos(2\alpha))$

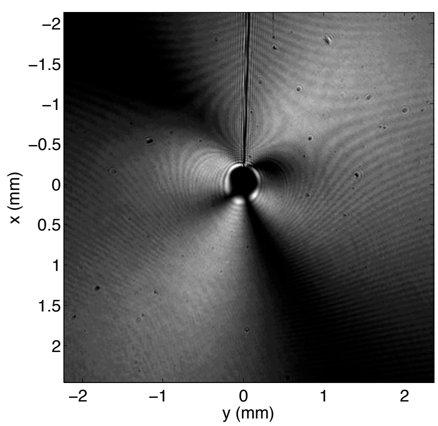

(e) $I_5 = I_o(1 + \sin(\delta)\sin(2\alpha))$

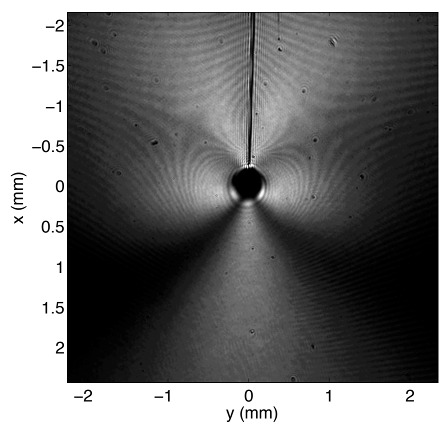

(f) $I_6 = I_o(1 - \sin(\delta)\cos(2\alpha))$

Figure 4.3: Experimental mages from six-step phase-shifting photoelasticity for specimen HomC1 for $K_I = 0.514$ MPa$\sqrt{\text{m}}$ and $K_{II} = 4.4$ kPa$\sqrt{\text{m}}$: Caustic shadows obscure the data at the crack tip due to the stress concentration, and the weak high density fringes overlaying the photoelastic fringes are due to the interference of the reflections from the front and back faces of the specimen.

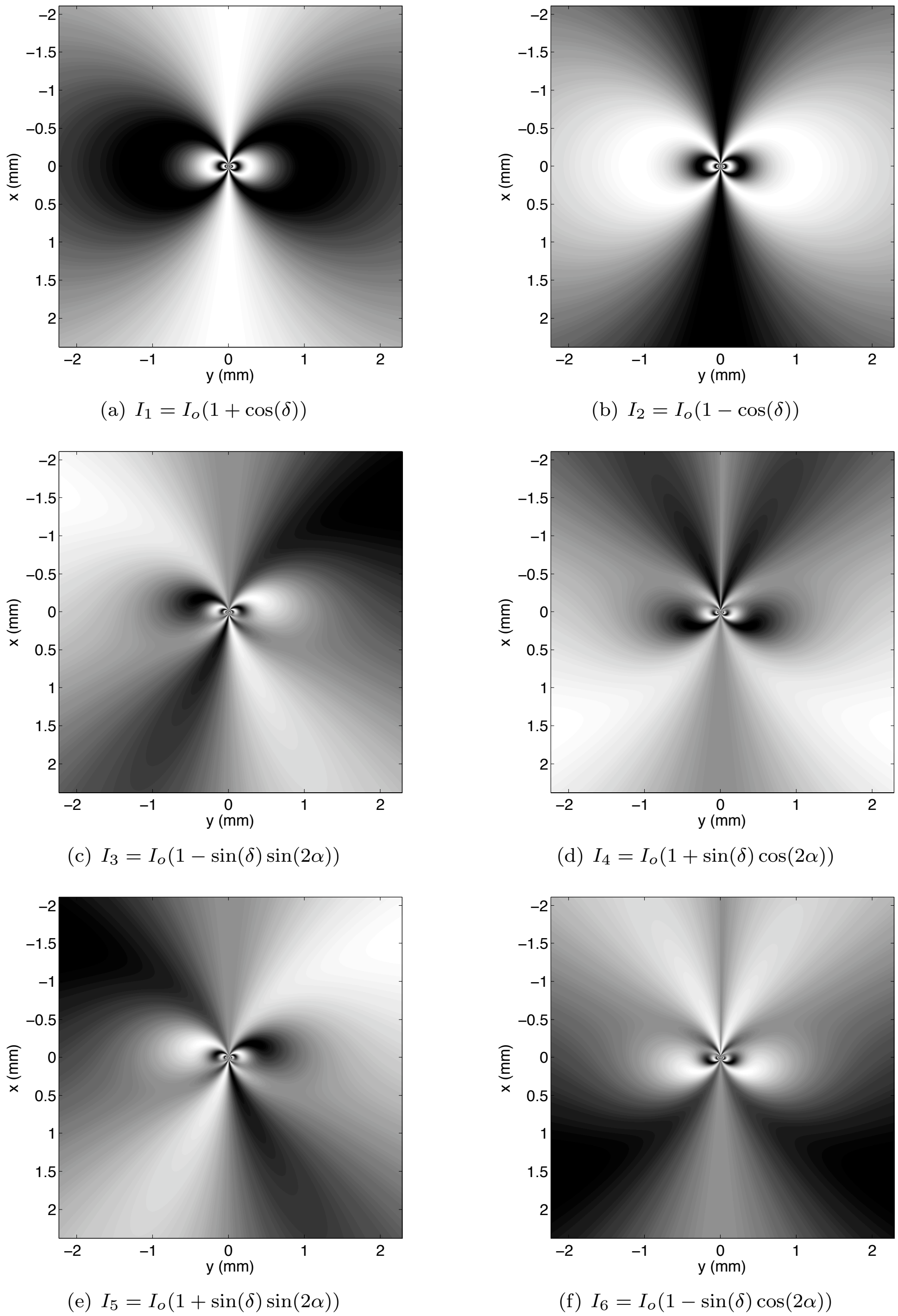

(a) $I_1 = I_o(1 + \cos(\delta))$

(b) $I_2 = I_o(1 - \cos(\delta))$

(c) $I_3 = I_o(1 - \sin(\delta)\sin(2\alpha))$

(d) $I_4 = I_o(1 + \sin(\delta)\cos(2\alpha))$

(e) $I_5 = I_o(1 + \sin(\delta)\sin(2\alpha))$

(f) $I_6 = I_o(1 - \sin(\delta)\cos(2\alpha))$

Figure 4.4: Theoretical mages from six-step phase-shifting photoelasticity for specimen HomC1 with $K_I = 0.514$ MPa$\sqrt{\text{m}}$ and $K_{II} = 4.4$ kPa$\sqrt{\text{m}}$, where I_o is uniform over the field of view, unlike the experimental images, where the intensity is Gaussian in nature

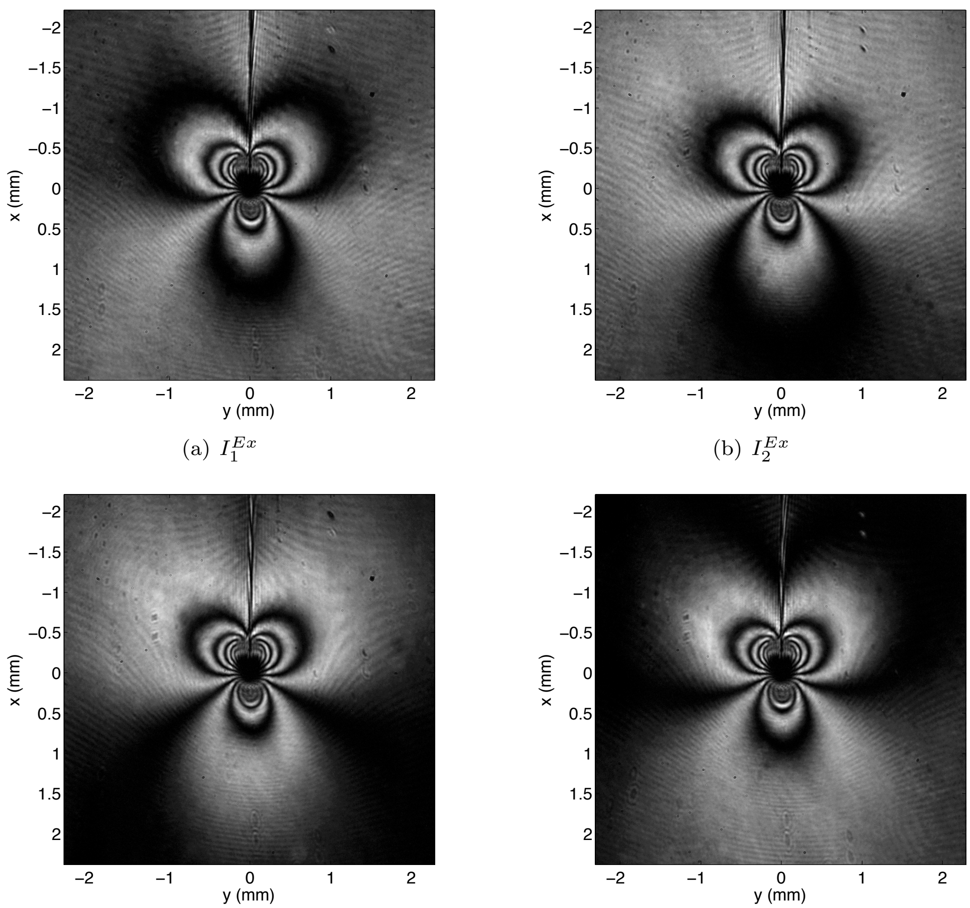

(a) I_1^{Ex} (b) I_2^{Ex} (c) I_3^{Ex} (d) I_4^{Ex}

Figure 4.5: Experimental phase-shifted images from vertical shearing CGS using pure $E_x\hat{\imath}$ input for specimen HomC1 for $K_I = 0.514$ MPa$\sqrt{\mathrm{m}}$ and $K_{II} = 4.4$ kPa$\sqrt{\mathrm{m}}$

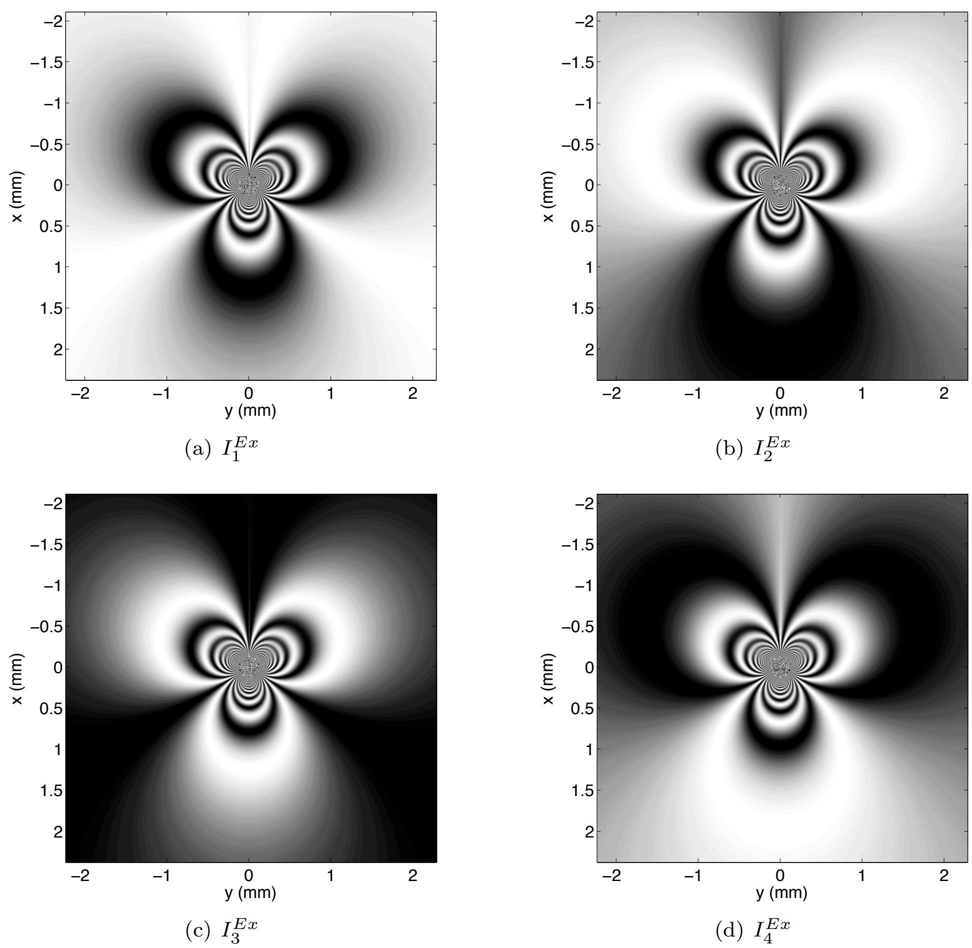

(a) I_1^{Ex} (b) I_2^{Ex}

(c) I_3^{Ex} (d) I_4^{Ex}

Figure 4.6: Theoretical phase-shifted images from vertical shearing CGS using pure $E_x\hat{\imath}$ input for specimen HomC1 for $K_I = 0.514$ MPa$\sqrt{\mathrm{m}}$ and $K_{II} = 4.4$ kPa$\sqrt{\mathrm{m}}$

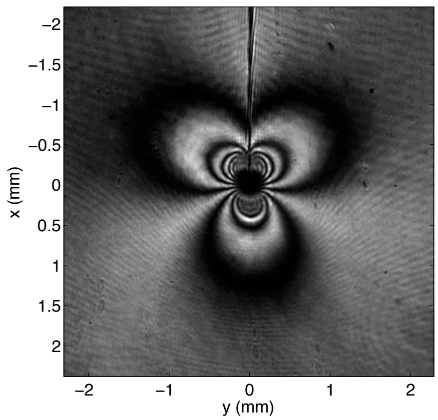

(a) I_1^{Ey}

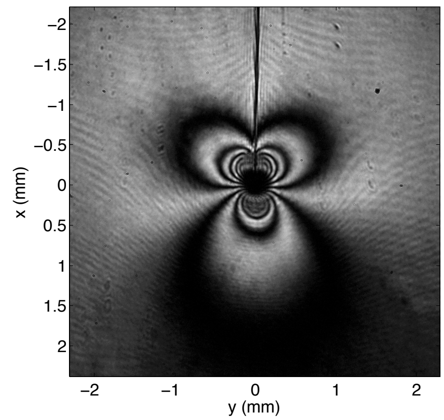

(b) I_2^{Ey}

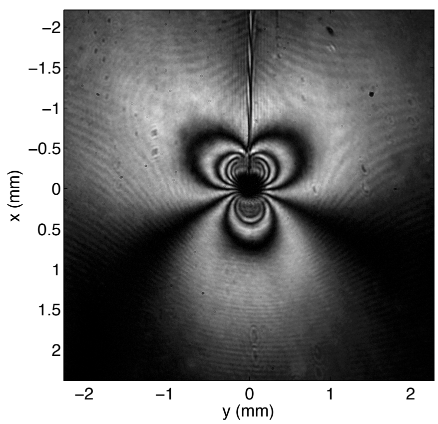

(c) I_3^{Ey}

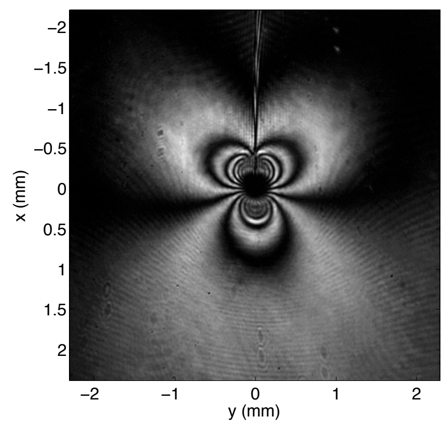

(d) I_4^{Ey}

Figure 4.7: Experimental phase-shifted images from vertical shearing CGS using pure $E_y\hat{\jmath}$ input for specimen HomC1 for $K_I = 0.514$ MPa$\sqrt{\mathrm{m}}$ and $K_{II} = 4.4$ kPa$\sqrt{\mathrm{m}}$

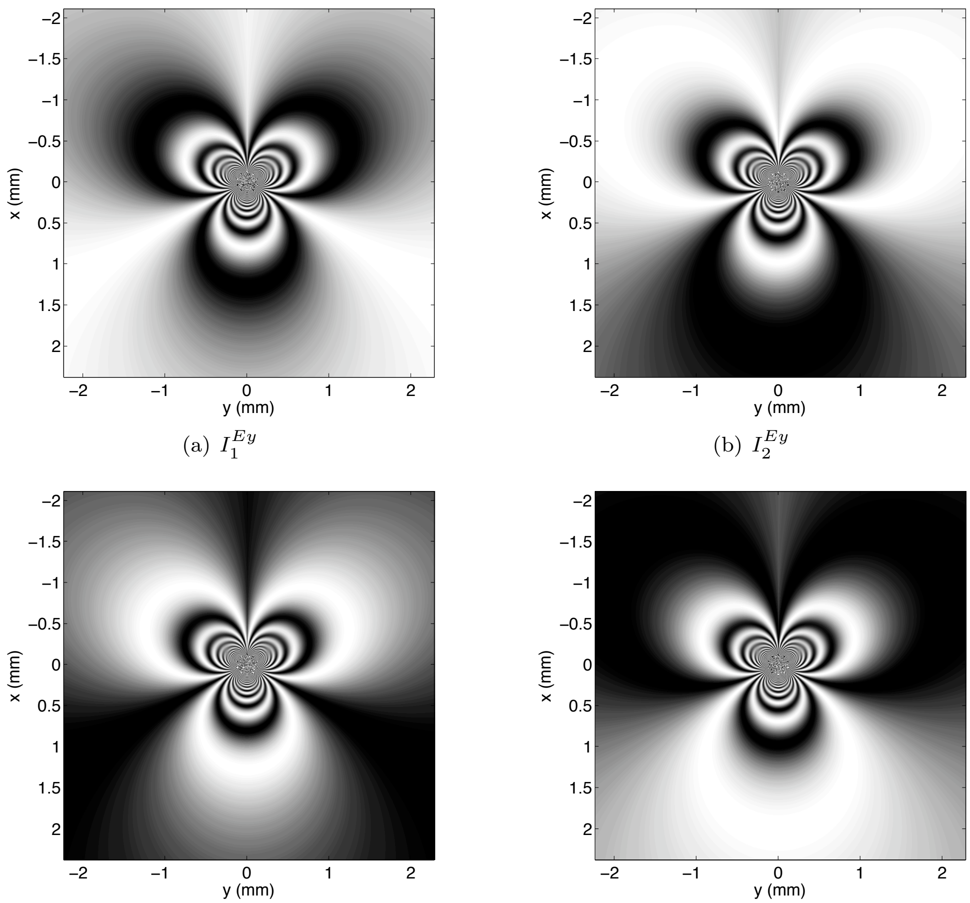

(a) I_1^{Ey} (b) I_2^{Ey} (c) I_3^{Ey} (d) I_4^{Ey}

Figure 4.8: Theoretical phase-shifted images from vertical shearing CGS using pure $E_y\hat{\jmath}$ input for specimen HomC1 for $K_I = 0.514$ MPa$\sqrt{\mathrm{m}}$ and $K_{II} = 4.4$ kPa$\sqrt{\mathrm{m}}$

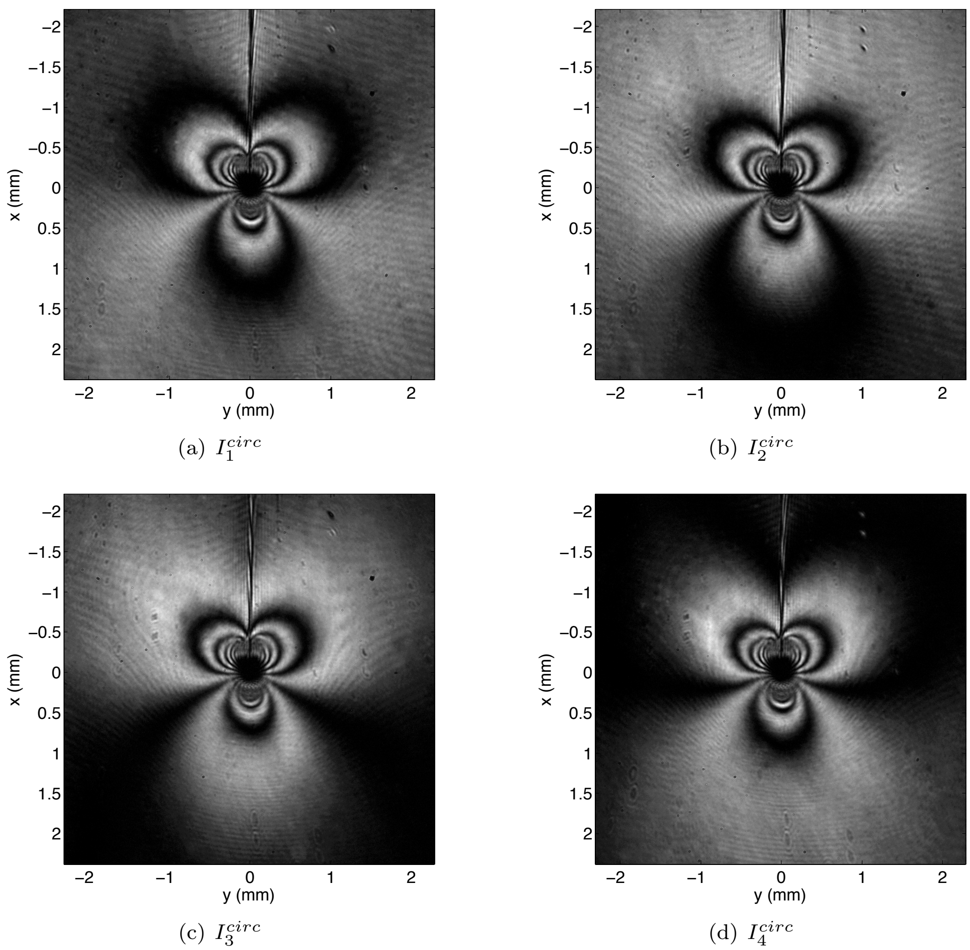

(a) I_1^{circc} (b) I_2^{circ} (c) I_3^{circ} (d) I_4^{circ}

Figure 4.9: Experimental phase-shifted images from vertical shearing CGS using the $\lambda/4$ polarization method for specimen HomC1 for $K_I = 0.514$ MPa$\sqrt{\text{m}}$ and $K_{II} = 4.4$ kPa$\sqrt{\text{m}}$

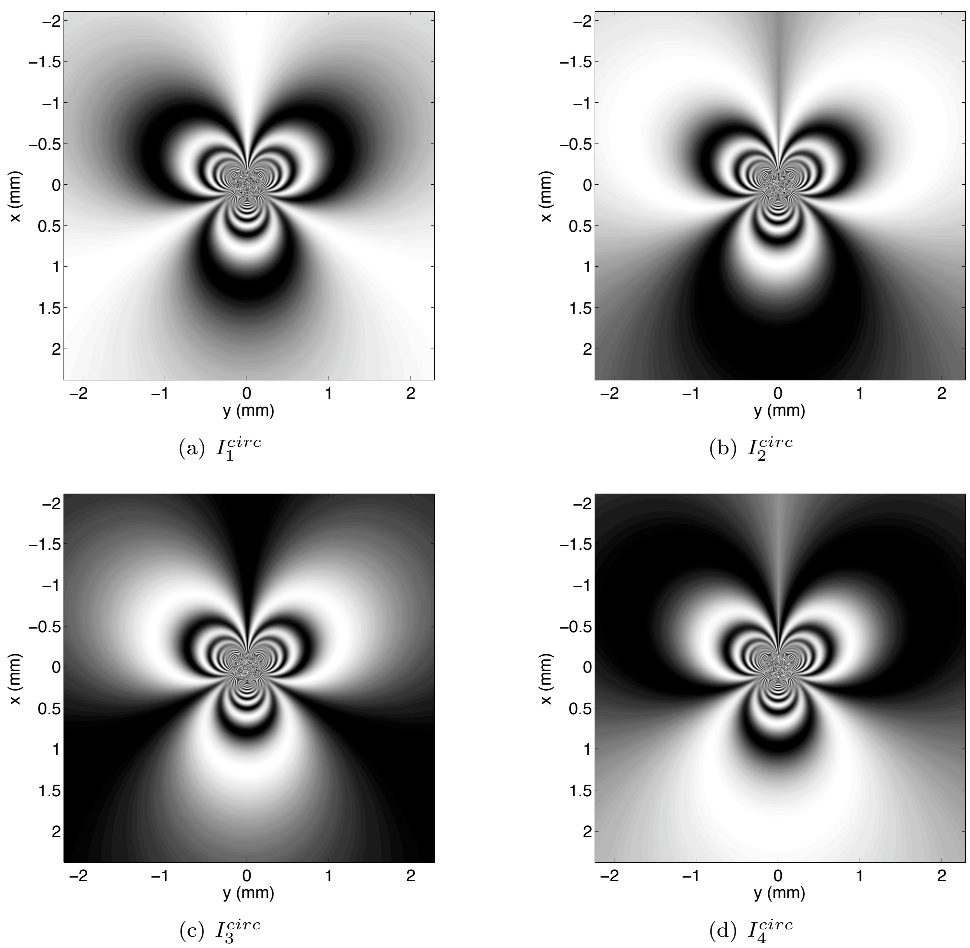

(a) I_1^{circ}

(b) I_2^{circ}

(c) I_3^{circ}

(d) I_4^{circ}

Figure 4.10: Theoretical phase-shifted images from vertical shearing CGS using the $\lambda/4$ polarization method for specimen HomC1 for $K_I = 0.514$ MPa$\sqrt{\mathrm{m}}$ and $K_{II} = 4.4$ kPa$\sqrt{\mathrm{m}}$

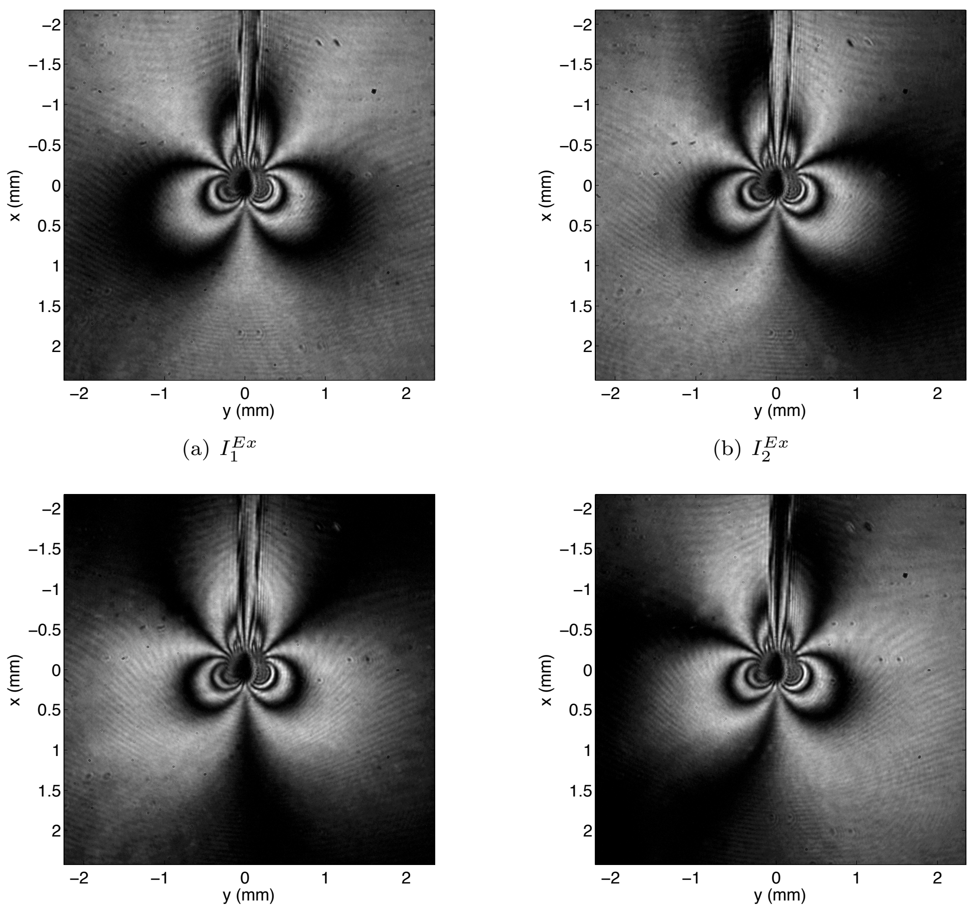

(a) I_1^{Ex} (b) I_2^{Ex} (c) I_3^{Ex} (d) I_4^{Ex}

Figure 4.11: Experimental phase-shifted images from horizontal shearing CGS using pure $E_x\hat{\imath}$ input for specimen HomC1 for $K_I = 0.514$ MPa$\sqrt{\text{m}}$ and $K_{II} = 4.4$ kPa$\sqrt{\text{m}}$

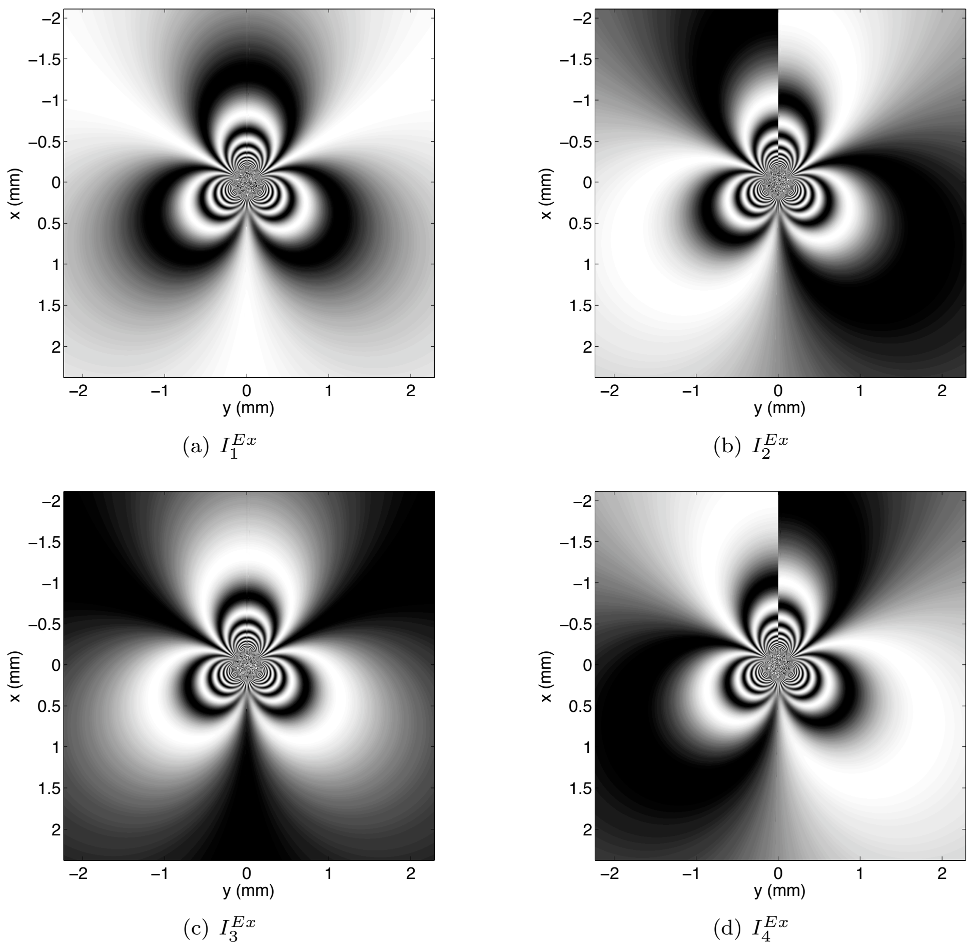

(a) I_1^{Ex} (b) I_2^{Ex}

(c) I_3^{Ex} (d) I_4^{Ex}

Figure 4.12: Theoretical phase-shifted images from horizontal shearing CGS using pure $E_x\hat{\imath}$ input for specimen HomC1 for $K_I = 0.514$ MPa$\sqrt{\text{m}}$ and $K_{II} = 4.4$ kPa$\sqrt{\text{m}}$

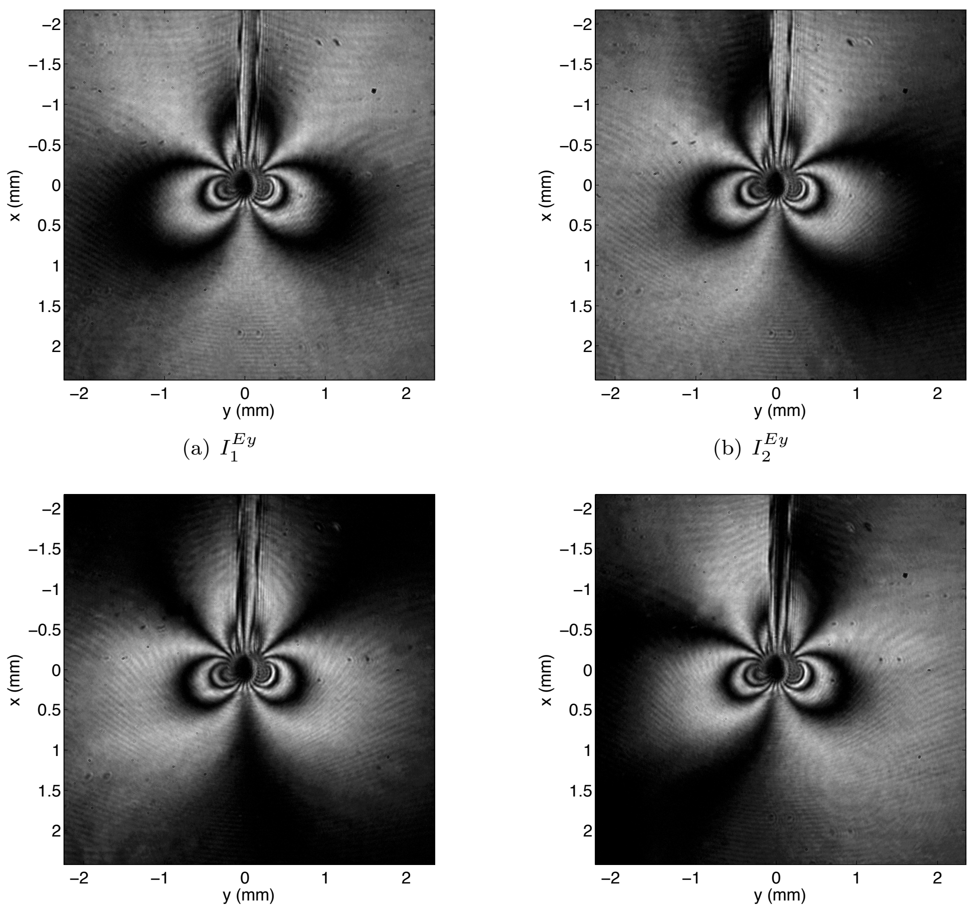

(a) I_1^{Ey}

(b) I_2^{Ey}

(c) I_3^{Ey}

(d) I_4^{Ey}

Figure 4.13: Experimental phase-shifted images from horizontal shearing CGS using pure $E_y \hat{\jmath}$ input for specimen HomC1 for $K_I = 0.514$ MPa$\sqrt{\text{m}}$ and $K_{II} = 4.4$ kPa$\sqrt{\text{m}}$

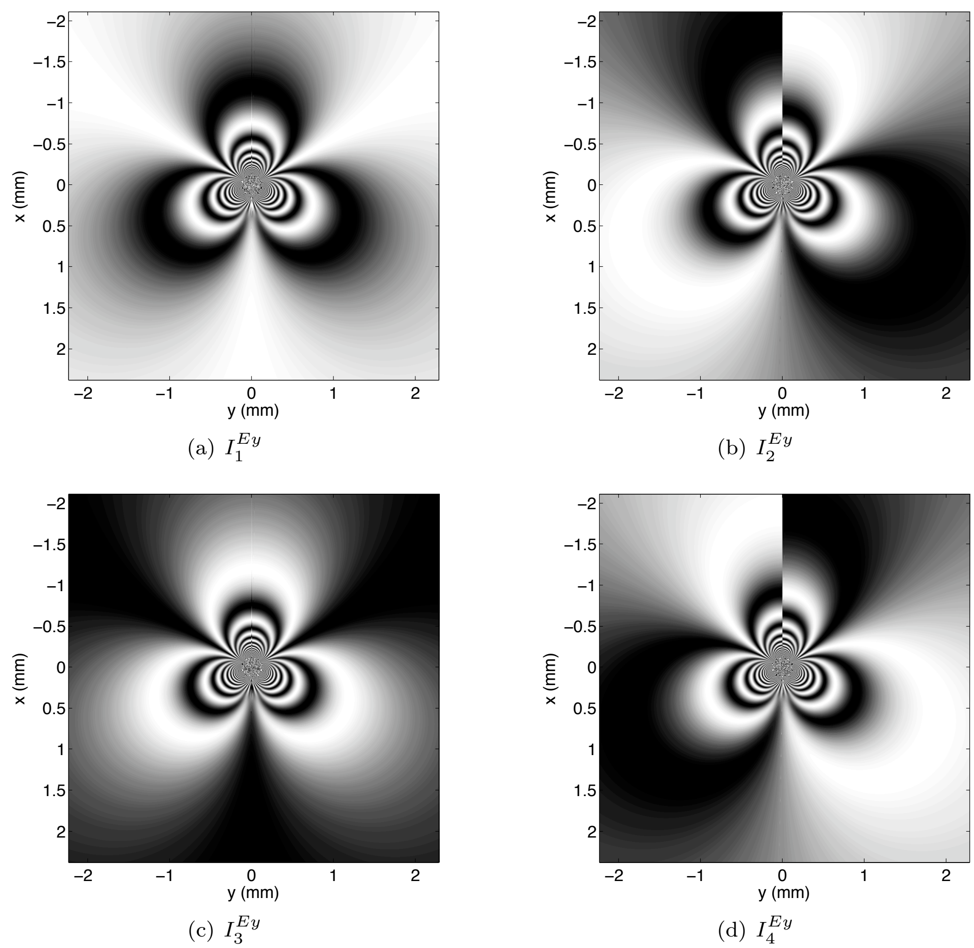

Figure 4.14: Theoretical phase-shifted images from horizontal shearing CGS using pure $E_y\hat{\jmath}$ input for specimen HomC1 for $K_I = 0.514$ MPa$\sqrt{\text{m}}$ and $K_{II} = 4.4$ kPa$\sqrt{\text{m}}$

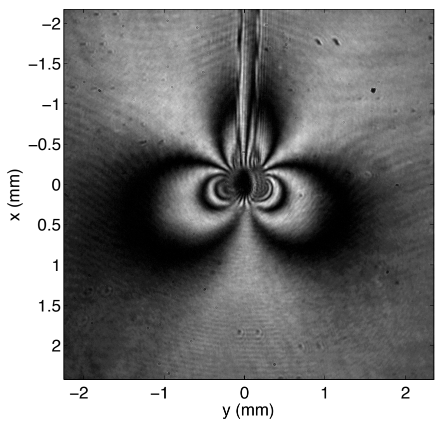

(a) I_1^{circ}

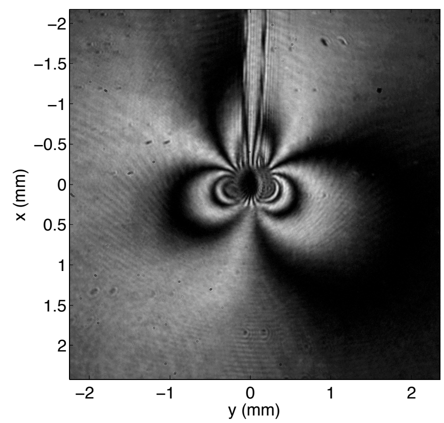

(b) I_2^{circ}

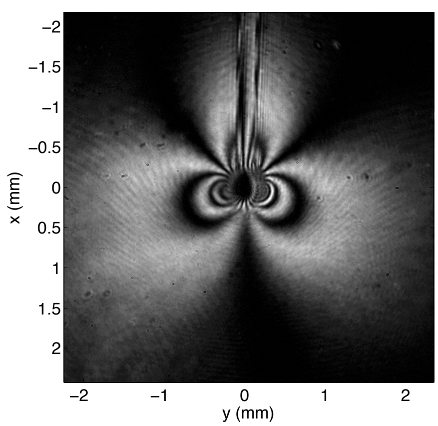

(c) I_3^{circ}

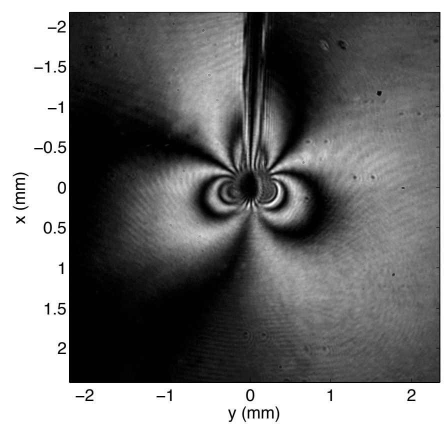

(d) I_4^{circ}

Figure 4.15: Experimental phase-shifted images from horizontal shearing CGS using the $\lambda/4$ polarization method for specimen HomC1 for $K_I = 0.514$ MPa$\sqrt{\text{m}}$ and $K_{II} = 4.4$ kPa$\sqrt{\text{m}}$

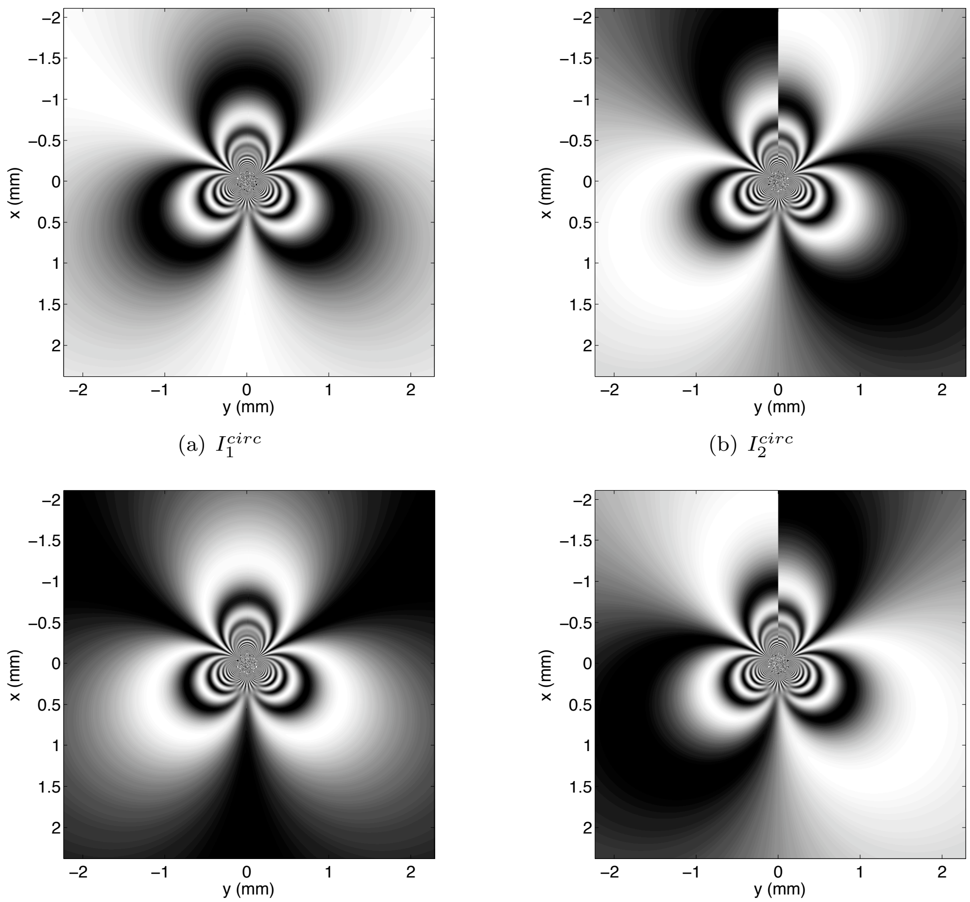

(a) I_1^{circ} (b) I_2^{circ} (c) I_3^{circ} (d) I_4^{circ}

Figure 4.16: Theoretical phase-shifted images from horizontal shearing CGS using the $\lambda/4$ polarization method for specimen HomC1 for $K_I = 0.514$ MPa$\sqrt{\text{m}}$ and $K_{II} = 4.4$ kPa$\sqrt{\text{m}}$

4.2.4.2 Photoelastic Data Analysis

Figures 4.17 and 4.18 present the isoclinic angle analysis from photoelastic images I_3 through I_6. As described in Chapter 3, the rotational alignment of the polarization optics relative to the first polarizer has a prominent effect on the wrapped isoclinic angle data. Figures 4.17(a)–4.17(b) show how the isoclinic angle measurement is sensitive to errors in the polarization alignment, particularly to the misalignment of the first $\lambda/4$ plate, resulting in false discontinuities and regions that incorrectly sweep through zero. These features, which are near regions where $\sin(\delta) = 0$, are not apparent in the theoretical wrapped isoclinic angle from well-aligned optics in Figure 4.17(d). The theoretical field in Figure 4.17(b) incorporates a small misalignment in the first $\lambda/4$ plate of $\pi/180$ from the ideal position of $\xi = \pi/4$, resulting in similar error features as the experimental field in Figure 4.17(a).

The false discontinuities and regions that incorrectly sweep through zero are corrected manually, as outlined in Section 3.2.4.1, focusing on regions near $\sin(\delta) = 0$ and the viewing the ambiguous wrapped isochromatic phase generated from the wrapped isoclinic angle, given in Figure 4.17(e). Regions in wrapped δ that correspond to phase ambiguities, obvious in the theoretical ambiguous wrapped δ along lines near $\theta = \pm 2\pi/3$ in Figure 4.17(f), should correspond to real $\pi/2$ discontinuities in the wrapped α that will require unwrapping later, like those near $\theta = \pm 2\pi/3$ in Figure 4.17(d). False $\pi/2$ discontinuities in α lie where the ambiguous wrapped δ has good modulation, often near $\sin(\delta) = 0$, such as near the lower parts of the lobes around $x = 0.25$ mm in Figure 4.17(e); these false α discontinuities are interpolated across to remove the discontinuities. Regions in the wrapped α where the angle sweeps through zero but corresponds to ambiguous wrapped δ or near broken 2π δ discontinuities, such as on the upper parts of the lobes around $x = -0.5$ mm in Figure 4.17(e), require careful consideration; a $\pi/2$ discontinuity is added to these regions, and the surrounding data is smoothed appropriately.

All of these manual changes of the wrapped isoclinic angle are guided by some basic *a priori* knowledge of the general trend of α, keeping in mind that α does not often have large gradients, though the 2D asymptotic crack problem is unusual with a large gradient across the crack plane. The crack problem is ideally radially symmetric, so the phase discontinuities should be radial in nature.

The corrected wrapped α in Figure 4.17(c) is close to this expectation, with slightly more variance from radial symmetry near the interpolated regions near the crack tip. The corrected wrapped α in Figure 4.17(c) unwraps well, as shown in comparing the experimental and theoretical values in Figures 4.18(a)–4.18(b) with the largest errors near regions where $\sin(\delta) = 0$. The experimental α does not capture the large jump near $\theta = 0$, but moves continuously through that region, evident in the line plot of the theoretical and experimental wrapped and unwrapped α at $x = 1.10$ mm in Figure 4.18(c). Since $\sin(\delta)$ is close to zero in this region, the $\lambda/4$ plate error causes false discontinuities emanating from the crack tip radially, as shown in Figures 4.17(a) and 4.17(b). This affected region obscures the large jump in α near $\theta = 0$. From the guidelines stated above for correcting the wrapped α, the discontinuities near $\theta = 0$ appear, upon first consideration, to be real discontinuities with their radial behavior and their correspondence to ambiguous wrapped δ. The only indication that these might be false discontinuities is that these are near regions with $\sin(\delta) = 0$. Corrections to such discontinuities to mimic the theoretical wrapped data would be difficult without knowing the *exact* behavior of α, which is not possible without knowing K_I and K_{II} that are calculated after the phase analysis is complete. Fortunately, the false discontinuities in this case lead to unwrapped α that loosely approximates the theoretical α in these Mode I–dominant fracture cases, evident in Figure 4.18(c), such that the subsequent isochromatic data appears to be reasonable, as discussed below; thus, these particular false discontinuities are not modified.

Figure 4.19 shows the experimental and theoretical wrapped and unwrapped isochromatic phase with excellent agreement globally. Both experimental and theoretical fields are slightly rotated in the $-\theta$ direction due to the slight Mode II component, have similar lobe shapes, and have similar locations for the 2π phase discontinuities in the wrapped phase. Due to the slight error in the isoclinic angle near $\theta = 0$, the experimental field does not reach to the low values close to zero as the theoretical field does in this region, but the general trend of smaller phase values does hold.

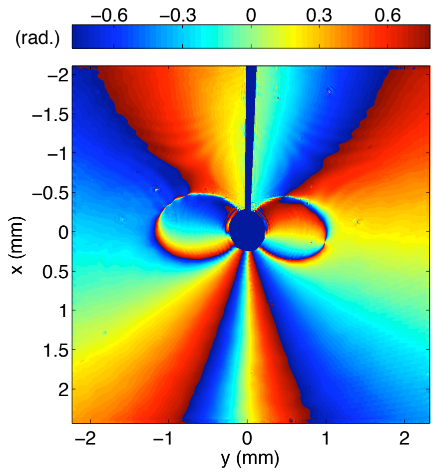

(a) Experimental wrapped α

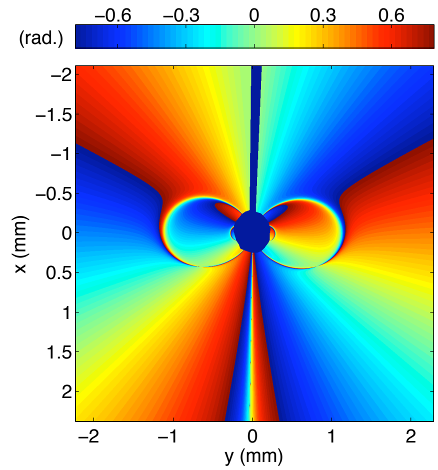

(b) Theoretical wrapped α from $e_{1}=\frac{\pi}{180}$

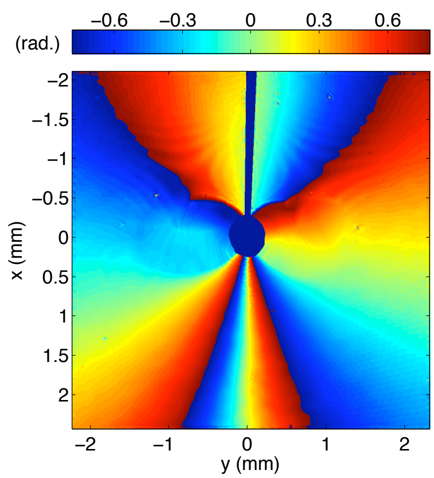

(c) Corrected experimental wrapped α

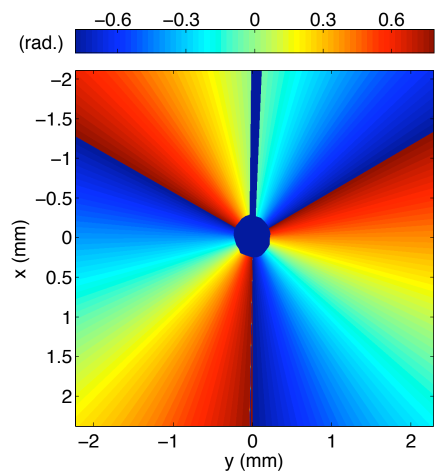

(d) Theoretical wrapped α

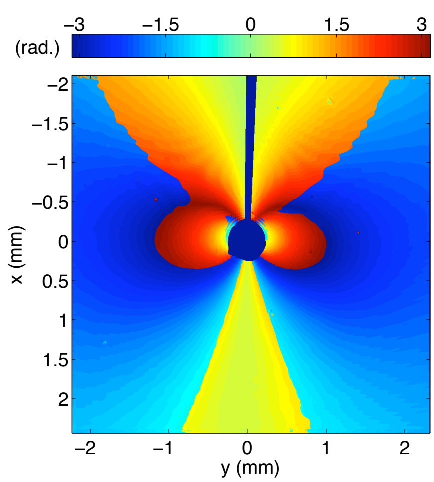

(e) Experimental ambiguous wrapped δ from uncorrected wrapped α

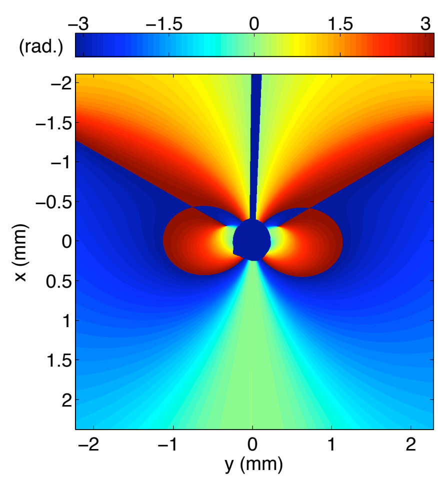

(f) Theoretical ambiguous wrapped δ from ideal wrapped α

Figure 4.17: Experimental and theoretical data for the isoclinic angle for specimen HomC1 for $K_I = 0.514$ MPa$\sqrt{\text{m}}$ and $K_{II} = 4.4$ kPa$\sqrt{\text{m}}$ with crack region masked in blue

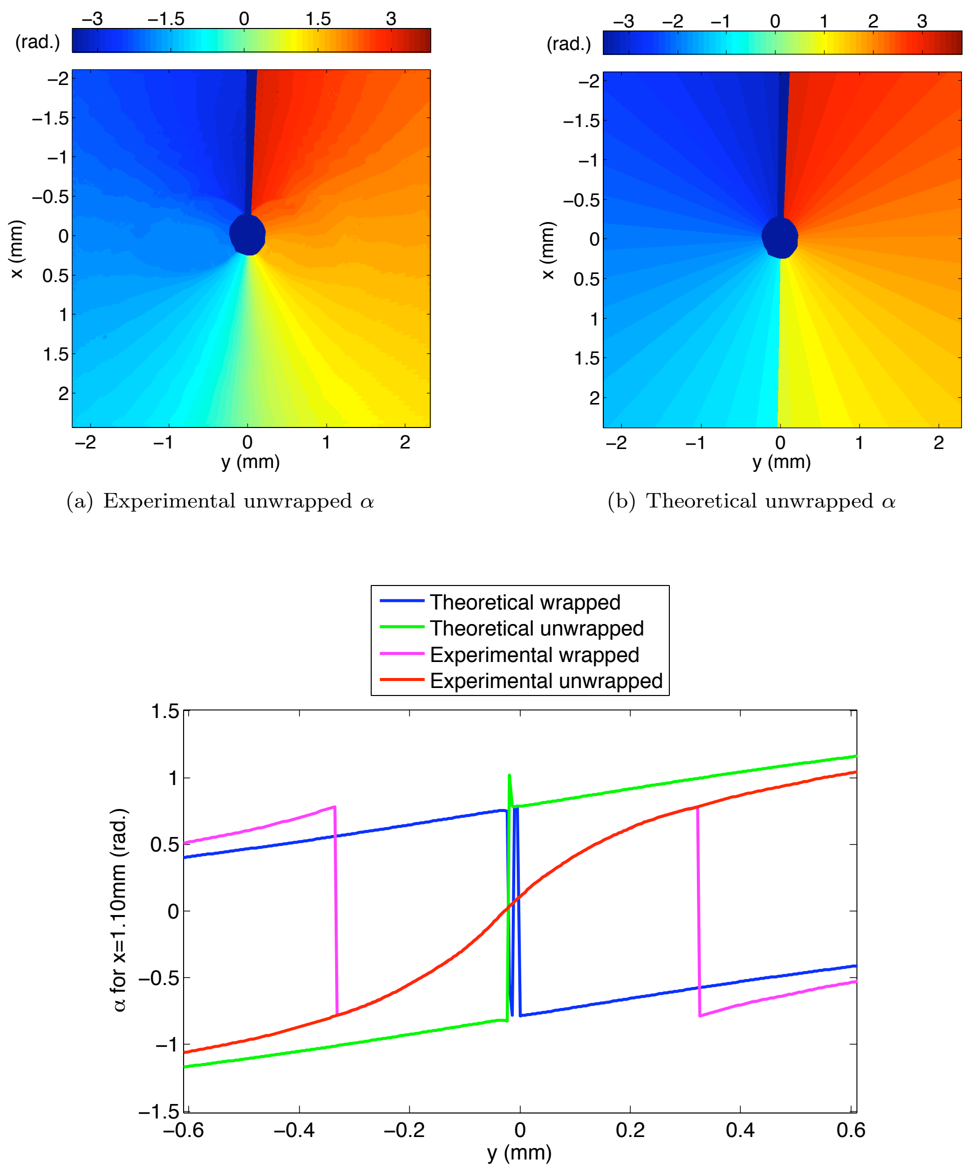

(a) Experimental unwrapped α

(b) Theoretical unwrapped α

(c) Experimental and theoretical wrapped and unwrapped α

Figure 4.18: Experimental and theoretical unwrapped isoclinic angle with crack region masked in blue and comparison of experimental and theoretical wrapped and unwrapped α for $x = 1.10$ mm

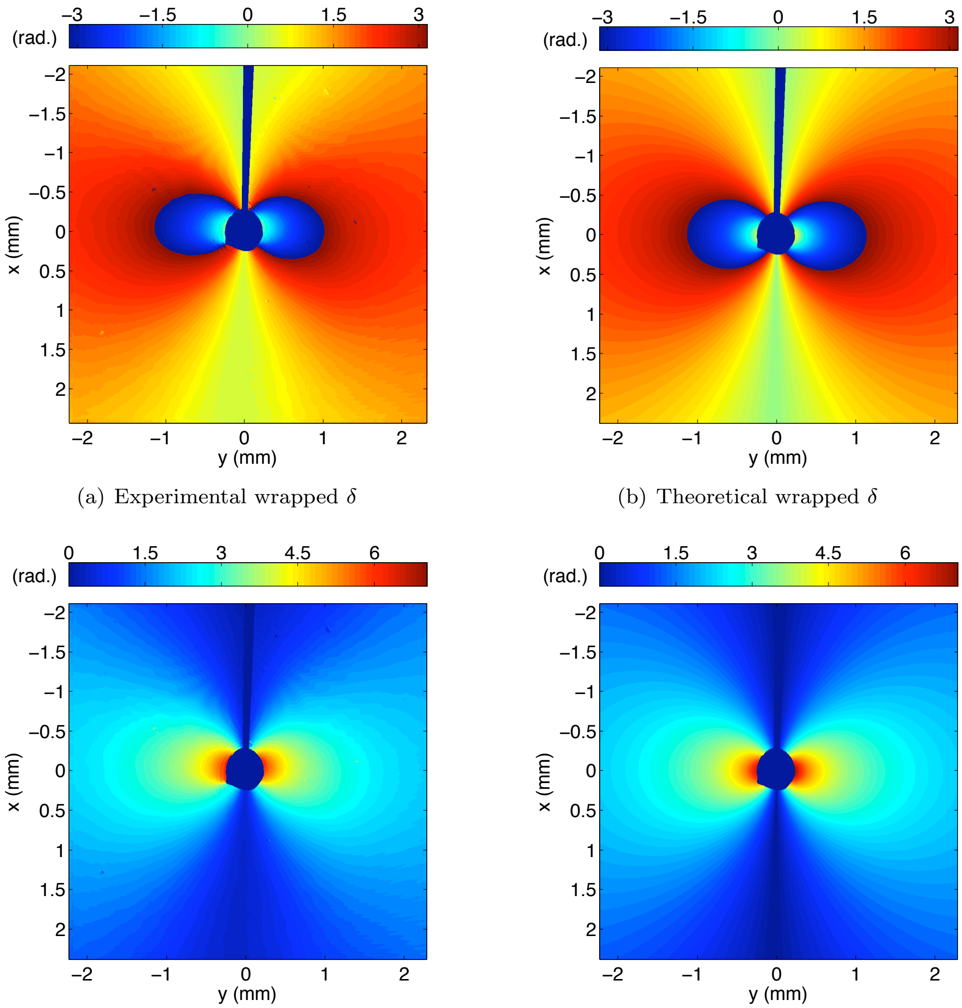

(a) Experimental wrapped δ

(b) Theoretical wrapped δ

(c) Experimental unwrapped δ

(d) Theoretical unwrapped δ

Figure 4.19: Experimental and theoretical data for the isochromatic phase for specimen HomC1 for $K_I = 0.514$ MPa$\sqrt{\text{m}}$ and $K_{II} = 4.4$ kPa$\sqrt{\text{m}}$ with crack region masked in blue

4.2.4.3 CGS Data Analysis

Figures 4.20 and 4.21 present the experimental and theoretical wrapped and unwrapped vertical shearing CGS data from the pure $E_x\hat{\imath}$ and pure $E_y\hat{\jmath}$ inputs, respectively. The experimental and theoretical wrapped data show similar lobe structures and fringe density, though the experimental data seems to be slightly elongated behind the crack along the vertical shearing direction as explained in Section 4.2.4.1 about the finite shearing distance. Figure 4.20(e) shows a map of the theoretical amplitude $I_c^{Ex} = I_c^{Ey}$, which modulates the $\cos(\varphi_{sum} \pm \varphi_{\alpha d})$ interference term of the intensity expressions in Equations (2.22) and (2.23); the arctan() formula in Equation (2.21) does not hold for $I_c^{Ex} = I_c^{Ey} = 0$, so those points are likely places for poor fringe quality. In this case, only small regions near the crack tip have $I_c^{Ex} = I_c^{Ey}$ values close to zero; since these points are collected together and do not form a boundary of low-quality data points across which the unwrapping program cannot pass information, the unwrapping algorithm can confine any error to those points.

Figure 4.22 shows the experimental and theoretical wrapped and unwrapped vertical shearing CGS data from the circularly polarized electric field input from the $\lambda/4$ polarization method, the φ_{sum} phase determined from $(\varphi^{Ex} + \varphi^{Ey})/2$, and the $\cos(\varphi_{diff})$ field that modulates the phase from the $\lambda/4$ polarization method, as explained in Section 2.2.3.2. The experimental and theoretical wrapped φ_{sum} from the circularly polarized electric field input data in Figures 4.22(a) and 4.22(b) have similar fringe density and shape, though the lobes behind the crack tip of the experimental data are slightly larger than the theoretical. The experimental fringes have slight errors in a four-leaf clover pattern around the crack tip near where $\cos(\varphi_{diff})$ is close to zero. As expected, data near $\cos(\varphi_{diff}) = 0$ is prone to higher error since the arctan() function for φ_{sum} in Equation (2.25) is indeterminate at $\cos(\varphi_{diff}) = 0$ and since these locations are where the misalignment of the first $\lambda/4$ plate can affect the CGS data, as discussed in Section 3.2.2. Since Homalite-100 has a small value for the photoelasticity-related constant $g = -0.0844$, which is related to the magnitude of φ_{diff} as defined in Section 2.2.2.2, the effect of the φ_{diff} phase is generally confined to very close to the crack tip even for this case with significant K_I loading; many of these errors are masked by the user-defined crack tip mask, and therefore do not have large influence on the data. The unwrapped phase in

Figure 4.22(c) and the φ_{sum} phase determined from $(\varphi^{Ex}+\varphi^{Ey})/2$ in Figure 4.22(e) are comparable; the experimental fields are able to capture the theoretical change in phase globally except that the negative phase lobes are slightly further back from the crack tip than in the theoretical fields. Since the $\cos(\varphi_{diff})$ field is fairly uniform, the φ_{sum} from the circularly polarized electric field input has few unwrapping errors and is thus a good measure for the derivative of stress, implying that the only the single set of four phase-shifted images are required for Homalite-100 in this configuration.

In Figures 4.23 and 4.24, the experimental and theoretical wrapped and unwrapped horizontal shearing CGS data from the pure $E_x\hat{\imath}$ and pure $E_y\hat{\jmath}$ inputs have similar fringe density and shape, though in the experimental data the lobes ahead of the crack appear larger, and the lobes along the crack appear smaller than in the theoretical data. The theoretical amplitude $I_c^{Ex} = I_c^{Ey}$ in Figure 4.25(f) is uniform over the field of view except just in front of the crack, which goes to zero; this small area is masked to prevent unwrapping problems due to the poor fringe quality where the arctan() formula for φ^{Ex} and φ^{Ey} is indeterminate. The experimental and theoretical wrapped and unwrapped φ_{sum} data from the circularly polarized electric field input shown in Figure 4.25 again compare well but with smaller lobes along the crack in the experimental data. The φ_{sum} fields from the circularly polarized electric field input and from $(\varphi^{Ex} + \varphi^{Ey})/2$ in Figures 4.25(c) and 4.25(e), respectively, are nearly identical and nearly match the theoretical phase in Figure 4.25(d), except on either side of the crack where the phase is rather large theoretically. Since $\cos(\varphi_{diff})$ for the horizontal shearing direction is only close to zero just in front of the crack, and the wrapped phase is easily masked there to reduce unwrapping errors, the φ_{sum} data from the circularly polarized electric field input gives as good comparison to the theoretical phase as the φ_{sum} data from $(\varphi^{Ex}+\varphi^{Ey})/2$. Like the vertical shearing, the horizontal shearing CGS for Homalie-100 in this configuration only requires one set of phase-shifted images to determine φ_{sum}.

From the phase data from the pure $E_x\hat{\imath}$ and pure $E_y\hat{\jmath}$ inputs, Figure 4.26 shows the secondary phases $\varphi_{\alpha d}$ from Equations (2.22) and (2.23) for the vertical and horizontal shearing directions. The experimental $\varphi_{\alpha d}$ for the horizontal direction compares extremely well with the theoretical phase, while the experimental $\varphi_{\alpha d}$ for the vertical direction does not compare as well. The rear lobes of the vertical $\varphi_{\alpha d}$ are larger and further from the crack in the experimental data than in the theoretical data; the distance that the rear lobes are behind the predicted location is about half of the shearing distance $d_{shear} = 225$ μm. A larger shearing distance increases the fringe density of the images, which improves the measurement for lower-stress regions, but also weakens the approximation of the phase relating to a derivative of stress. Therefore, a careful balance of large enough fringe density with a small enough shearing distance must be struck for quality data. In this case, the errors are localized to the crack tip region of approximately $r < d_{shear}$, most of which is lost due to caustic shadows anyway. This CGS data shows that this method can well approximate the expected phase to within a small distance from the crack tip.

Figure 4.27 shows the x and y derivatives of $\sigma_1 + \sigma_2$ maps and the integrated $\sigma_1 + \sigma_2 + c_i$ map, where c_i is the constant of integration that is determined by a traction-free boundary condition along the crack. Calculated from Equation (2.26), the x and y derivatives of $\sigma_1 + \sigma_2$ come from the vertical and horizontal shearing directions, respectively, for this specimen coordinate system. The integrated $\sigma_1 + \sigma_2 + c_i$ has good symmetry across the crack, though the frontal lobe is slightly skewed to the $-\theta$ direction due to the Mode II loading component.

The initial assumption for using CGS to determine derivatives of the principal stress sum is that the shearing distance is small enough to approximate a finite difference as a first derivative. Bruck and Rosakis (1992, 1993) considered the accuracy of this assumption for CGS in fracture mechanics applications. They calculated the error of this assumption for a K_I-dominant field for both shearing directions around a loaded crack, using the following expression for the x direction (with an equivalent expression for the y direction shear):

$$\epsilon = 1 - \frac{\dfrac{\partial(\sigma_1(x,y) + \sigma_2(x,y))}{\partial x}}{\left[\dfrac{(\sigma_1(x + \frac{d_{shear}}{2}, y) + \sigma_2(x + \frac{d_{shear}}{2}, y) - \sigma_1(x - \frac{d_{shear}}{2}, y) - \sigma_2(x - \frac{d_{shear}}{2}, y)}{d_{shear}}\right]}. \tag{4.7}$$

If the loading condition only has a K_I component, as was the only case considered by Bruck and Rosakis (1992, 1993), then the error field plots for the vertical and horizontal shearing directions for the 4.6 mm $\times$ 4.6 mm field of view and lateral shearing distance of $d_{shear} = 225$ μm are given in Figure 4.28. These plots indicate regions with error less than 1%, 1%–5%, and greater than 5%, showing symmetry across the crack plane. The regions with greater than 5% error are concentrated around the crack. Since these plots only include a K_I component, then the value of K_I does not affect the error calculation in Equation (4.7) for a given d_{shear}; therefore, these plots hold for any K_I-dominant field with pure K_I loading.

Given mixed-mode loading conditions, the actual values of K_I and K_{II} play a role in the error calculated with Equation (4.7). For this case where $K_I = 0.514$ MPa$\sqrt{\text{m}}$ and $K_{II} = 4.4$ kPa$\sqrt{\text{m}}$, the error plots for both shearing directions in Figure 4.29 show different behavior than for the K_I-only error plots, where the symmetry across the crack plane is lost, the error in the horizontal shearing direction is very similar to the K_I-only case, and the error in the vertical shearing direction is larger behind the crack with more area with greater than 1% error. These plots indicate why the experimental vertical shearing data appears to be different than the theoretical data behind the crack in Figure 4.22. This error analysis shows the potential regions of higher error in the $\sigma_1 + \sigma_2$, such as behind the crack and close to the crack tip, which may give rise to higher error in the separated stresses in those regions. Fortunately, Figure 4.29 indicates that the majority of the field should have less than 5% error (indicated by the yellow and green regions), so the CGS data may confidently be used to determine the derivative of stress in a global sense.

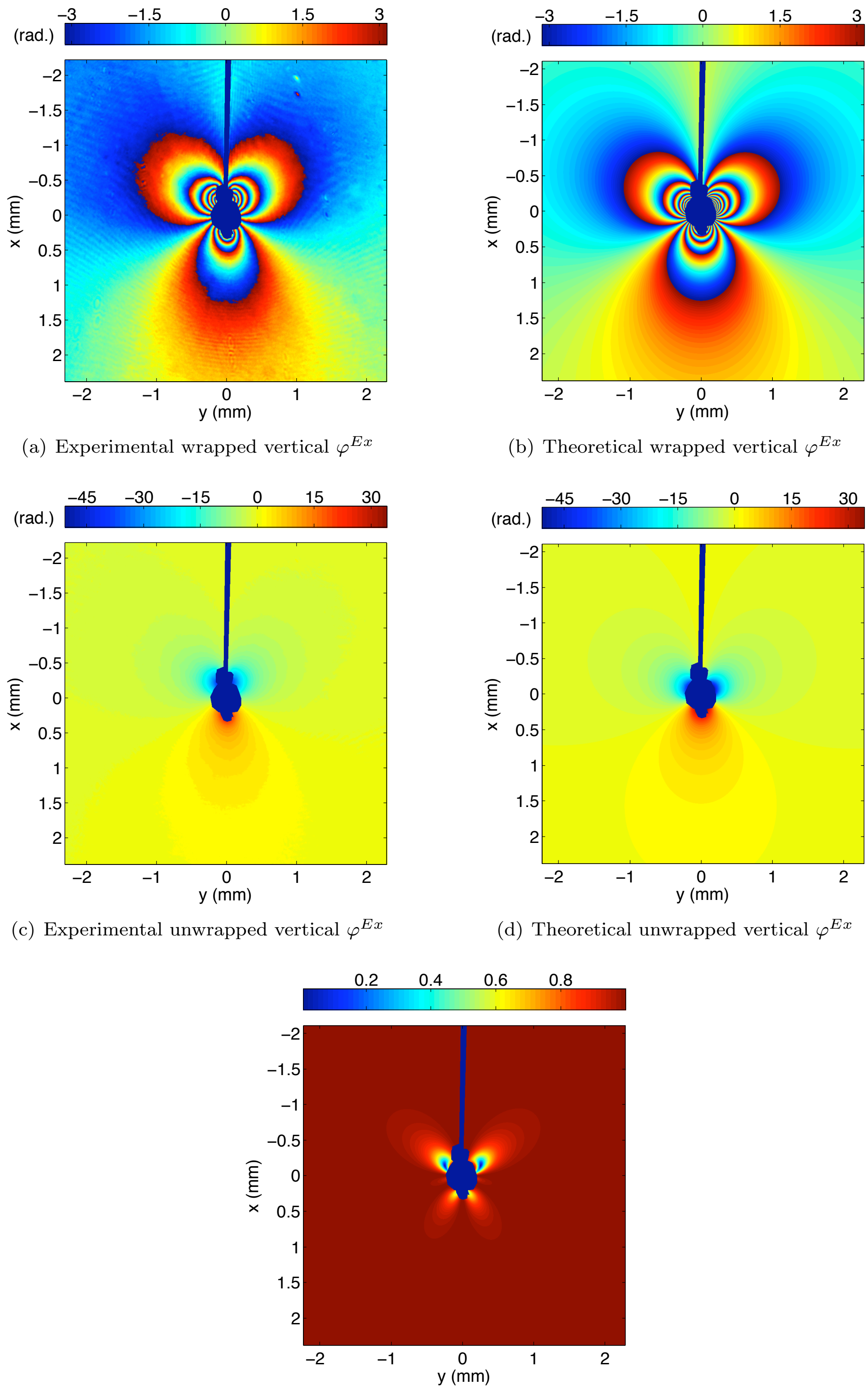

(a) Experimental wrapped vertical φ^{Ex}

(b) Theoretical wrapped vertical φ^{Ex}

(c) Experimental unwrapped vertical φ^{Ex}

(d) Theoretical unwrapped vertical φ^{Ex}

(e) Theoretical vertical $I_o^{Ex} = I_o^{Ey}$

Figure 4.20: Experimental and theoretical φ^{Ex} data for vertical CGS for specimen HomC1 for $K_I = 0.514$ MPa$\sqrt{\text{m}}$ and $K_{II} = 4.4$ kPa$\sqrt{\text{m}}$ with crack region masked in blue

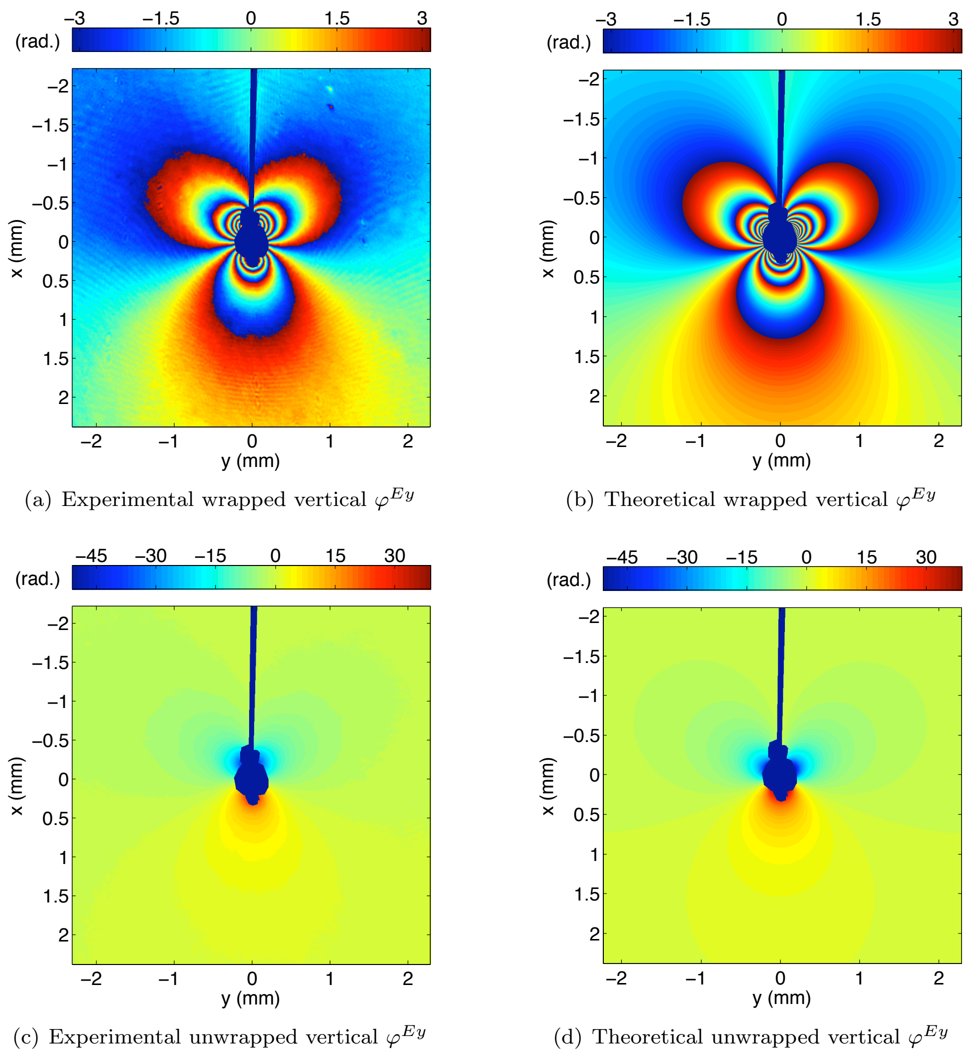

Figure 4.21: Experimental and theoretical φ^{Ey} data for vertical CGS for specimen HomC1 for $K_I = 0.514$ MPa$\sqrt{\text{m}}$ and $K_{II} = 4.4$ kPa$\sqrt{\text{m}}$ with crack region masked in blue

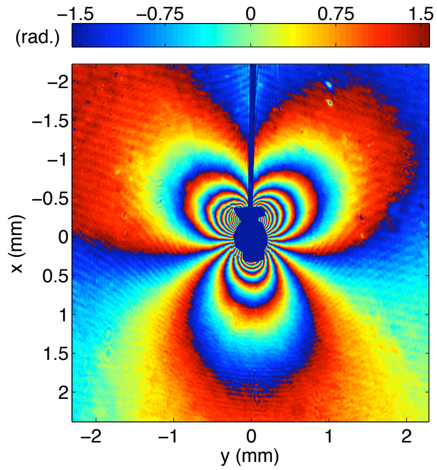

(a) Experimental wrapped vertical φ_{sum}

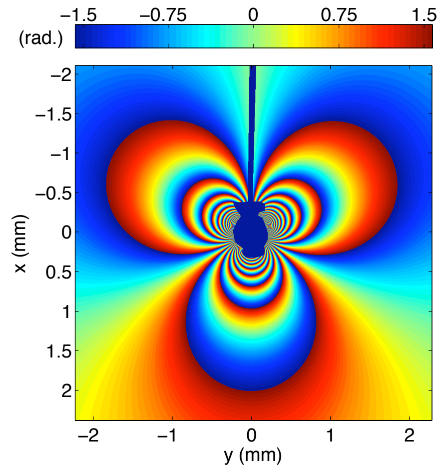

(b) Theoretical wrapped vertical φ_{sum}

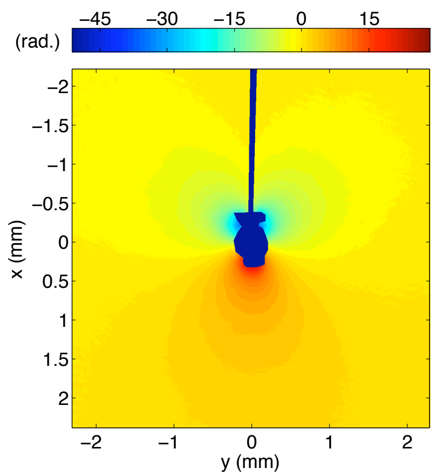

(c) Experimental unwrapped vertical φ_{sum}

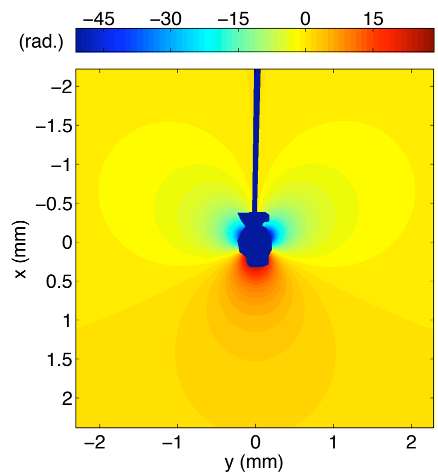

(d) Theoretical unwrapped vertical φ_{sum}

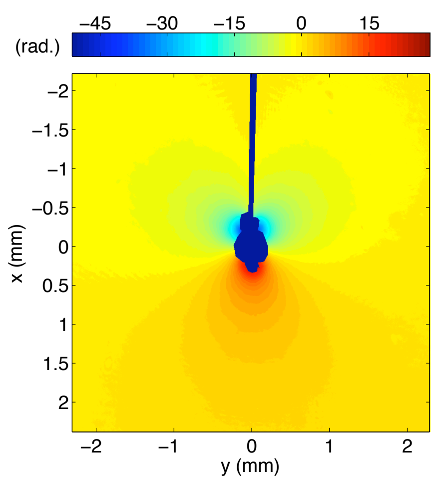

(e) Experimental vertical φ_{sum} from $\varphi^{Ex} + \varphi^{Ey}/2$

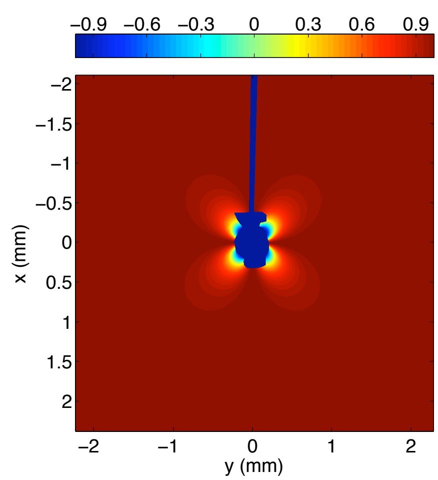

(f) Theoretical vertical $\cos(\varphi_{diff})$

Figure 4.22: Experimental and theoretical φ_{sum} data for vertical CGS from the circularly polarized electric field input data and from the combined pure $E_x\hat{\imath}$ and $E_y\hat{\jmath}$ data for specimen HomC1 for $K_I = 0.514$ MPa$\sqrt{\text{m}}$ and $K_{II} = 4.4$ kPa$\sqrt{\text{m}}$ with crack region masked in blue

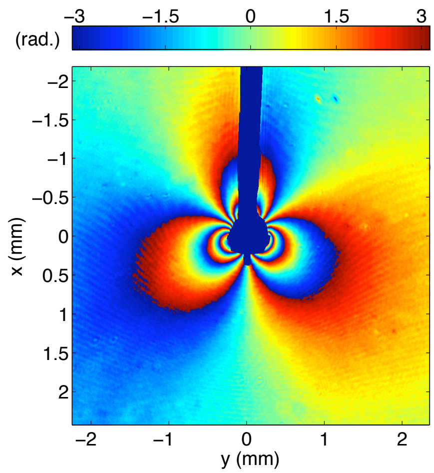

(a) Experimental wrapped horizontal φ^{Ex}

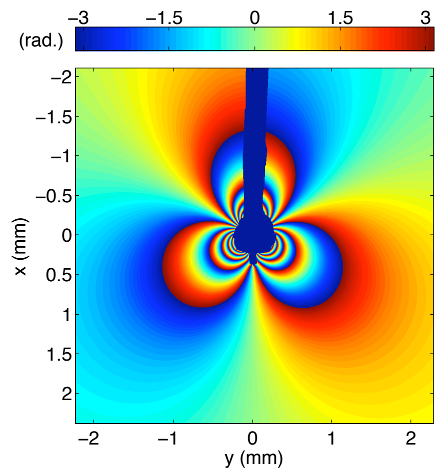

(b) Theoretical wrapped horizontal φ^{Ex}

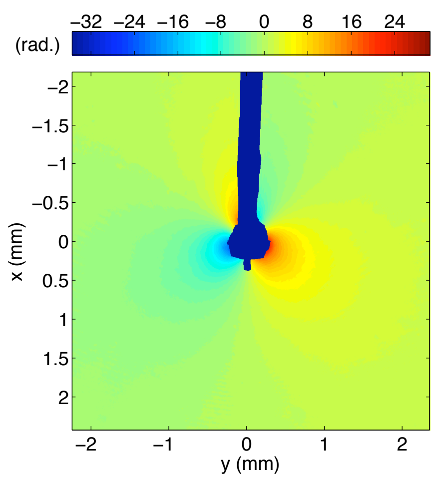

(c) Experimental unwrapped horizontal φ^{Ex}

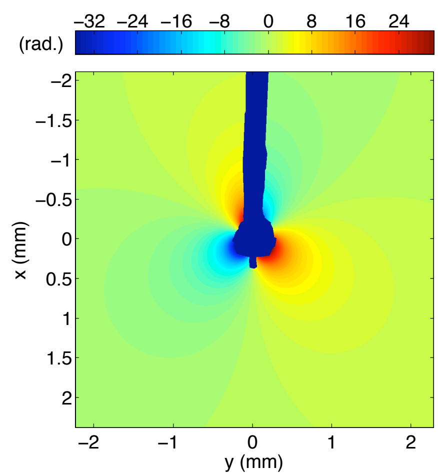

(d) Theoretical unwrapped horizontal φ^{Ex}

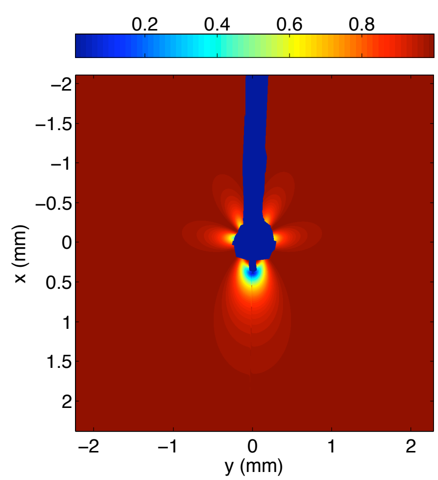

(e) Theoretical horizontal $I_o^{Ex} = I_o^{Ey}$

Figure 4.23: Experimental and theoretical φ^{Ex} data for horizontal CGS for specimen HomC1 for $K_I = 0.514$ MPa$\sqrt{\text{m}}$ and $K_{II} = 4.4$ kPa$\sqrt{\text{m}}$ with crack region masked in blue

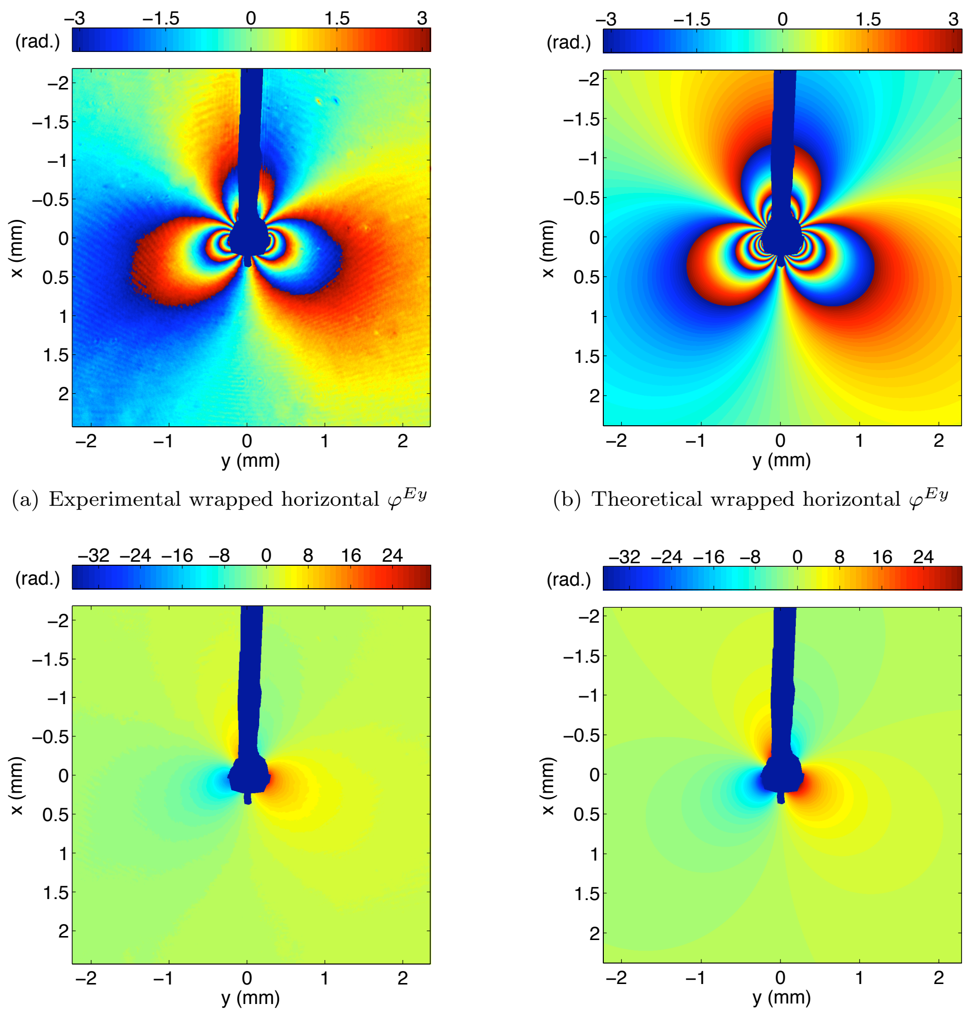

(a) Experimental wrapped horizontal φ^{Ey}

(b) Theoretical wrapped horizontal φ^{Ey}

(c) Experimental unwrapped horizontal φ^{Ey}

(d) Theoretical unwrapped horizontal φ^{Ey}

Figure 4.24: Experimental and theoretical φ^{Ey} data for horizontal CGS for specimen HomC1 for $K_I = 0.514$ MPa$\sqrt{\text{m}}$ and $K_{II} = 4.4$ kPa$\sqrt{\text{m}}$ with crack region masked in blue

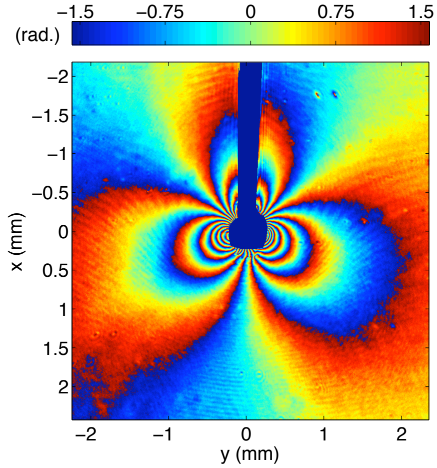

(a) Experimental wrapped horizontal φ_{sum}

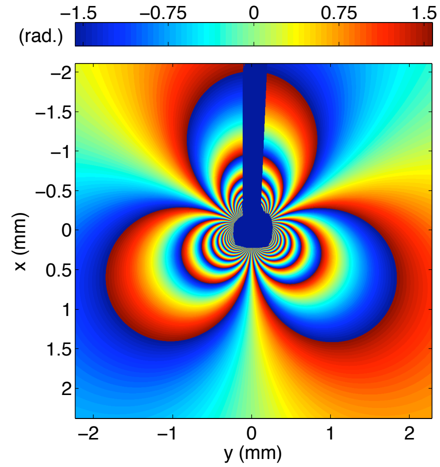

(b) Theoretical wrapped horizontal φ_{sum}

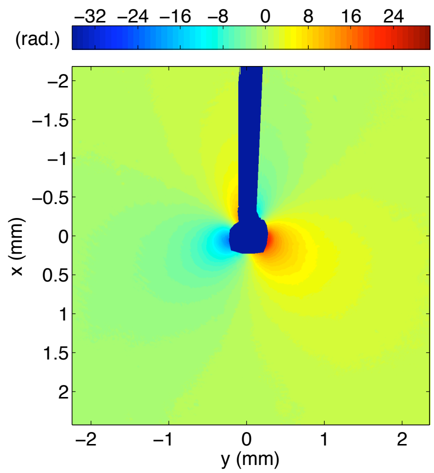

(c) Experimental unwrapped horizontal φ_{sum}

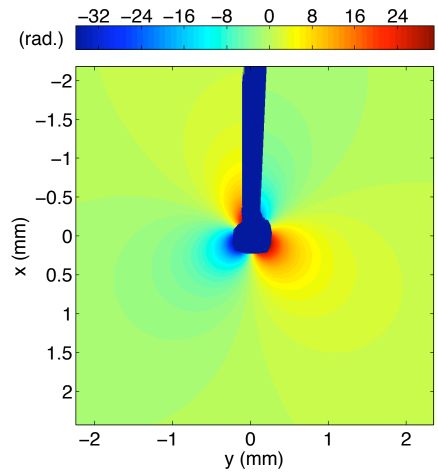

(d) Theoretical unwrapped horizontal φ_{sum}

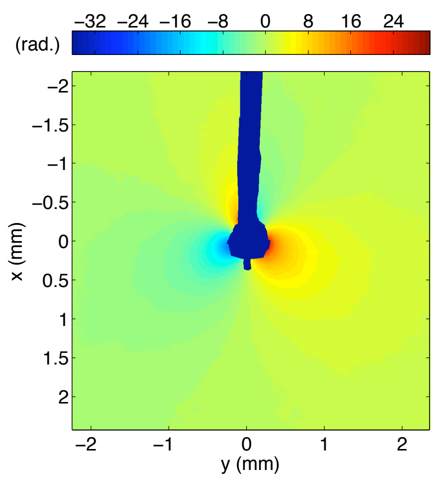

(e) Experimental horizontal φ_{sum} from $\varphi^{Ex} + \varphi^{Ey}/2$

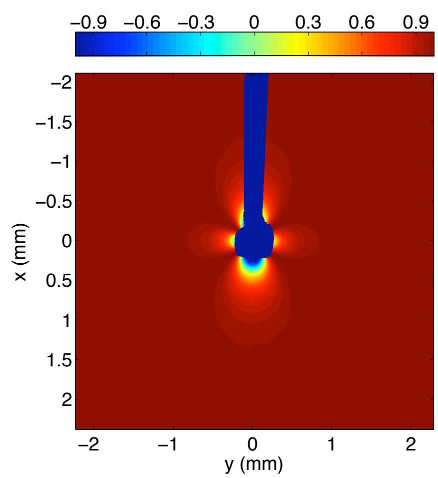

(f) Theoretical horizontal $\cos(\varphi_{diff})$

Figure 4.25: Experimental and theoretical data for horizontal CGS for specimen HomC1 for $K_I = 0.514$ MPa$\sqrt{\text{m}}$ and $K_{II} = 4.4$ kPa$\sqrt{\text{m}}$ with crack region masked in blue

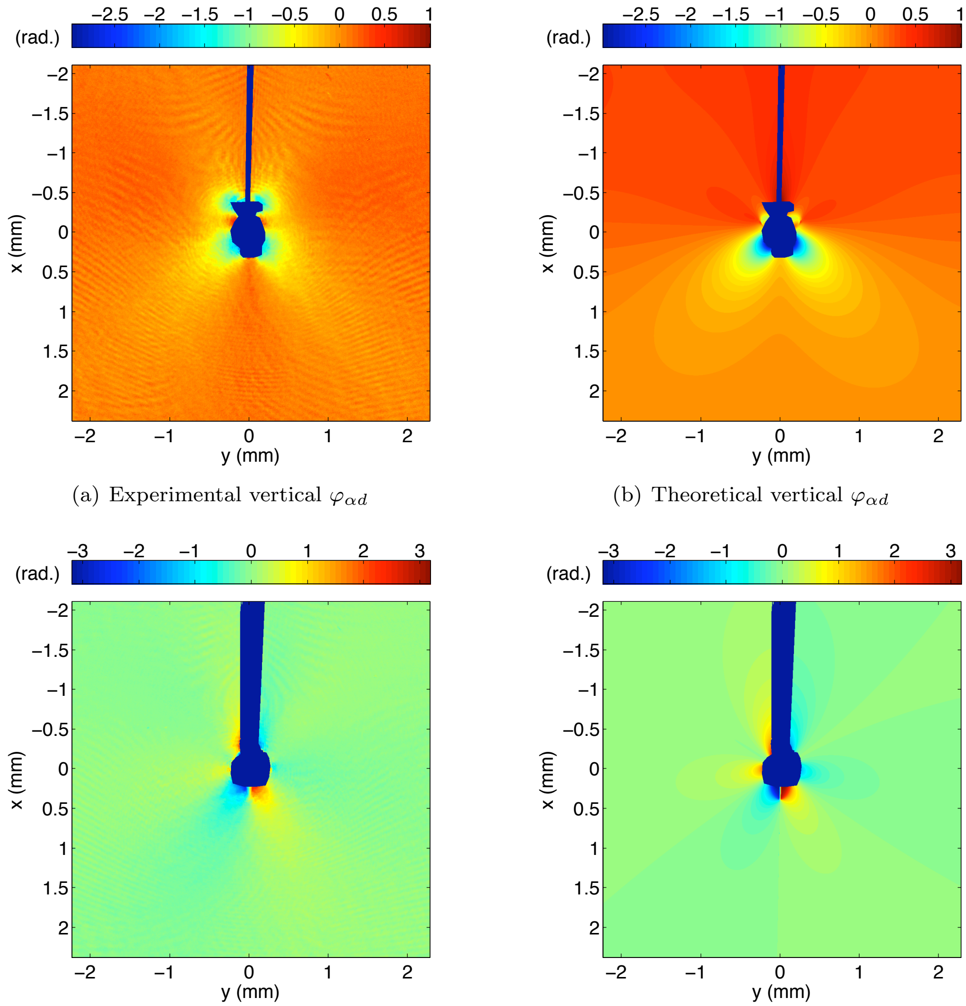

(a) Experimental vertical $\varphi_{\alpha d}$

(b) Theoretical vertical $\varphi_{\alpha d}$

(c) Experimental horizontal $\varphi_{\alpha d}$

(d) Theoretica horizontal $\varphi_{\alpha d}$

Figure 4.26: Experimental and theoretical data from vertical and horizontal CGS for the extra phase term $\varphi_{\alpha d}$ for specimen HomC1 for $K_I = 0.514$ MPa$\sqrt{\text{m}}$ and $K_{II} = 4.4$ kPa$\sqrt{\text{m}}$ with crack region masked in blue

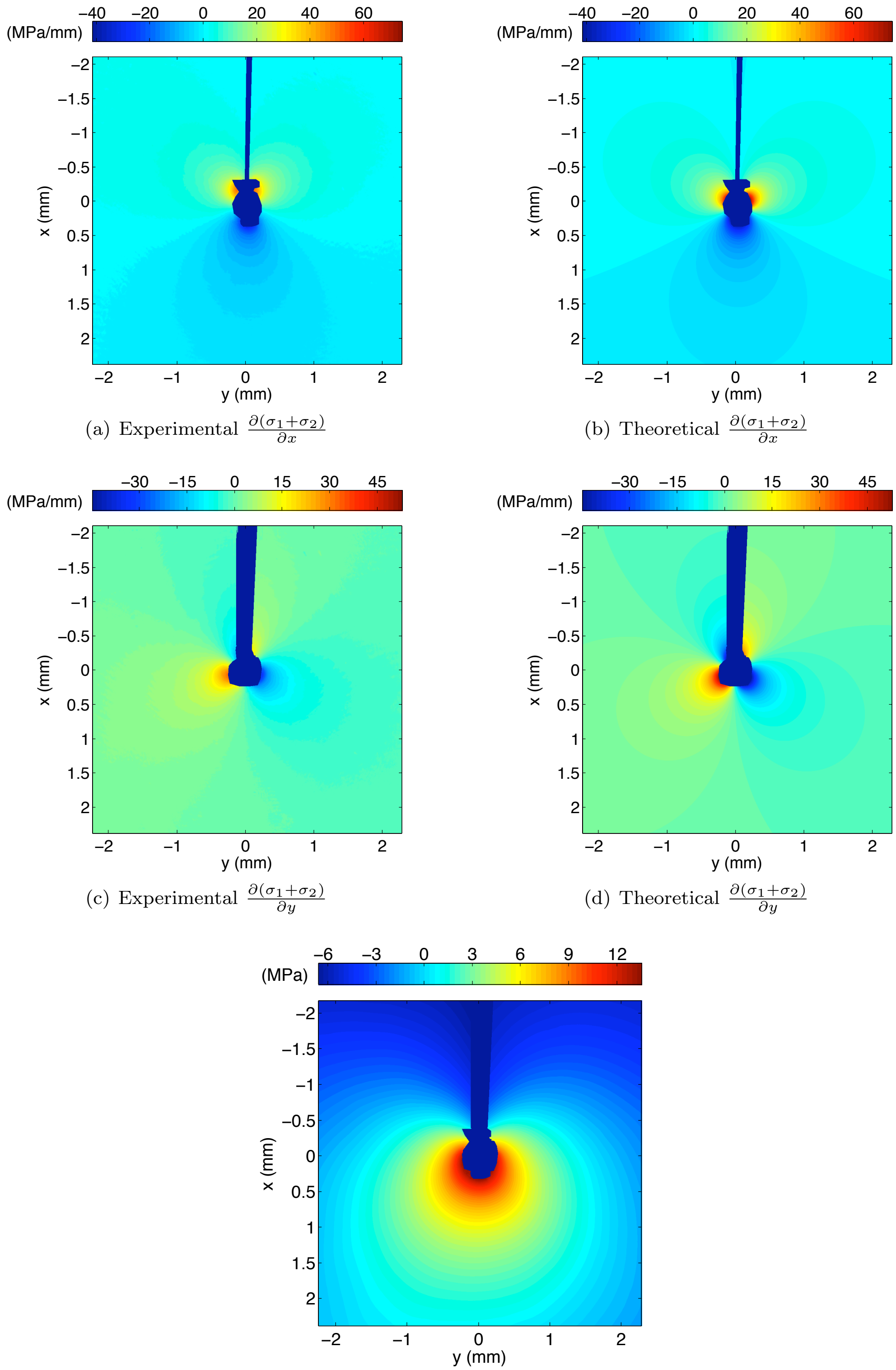

(a) Experimental $\frac{\partial(\sigma_1+\sigma_2)}{\partial x}$

(b) Theoretical $\frac{\partial(\sigma_1+\sigma_2)}{\partial x}$

(c) Experimental $\frac{\partial(\sigma_1+\sigma_2)}{\partial y}$

(d) Theoretical $\frac{\partial(\sigma_1+\sigma_2)}{\partial y}$

(e) Experimental $\sigma_1 + \sigma_2 + c_i$

Figure 4.27: Experimental and theoretical data for the derivatives of $\sigma_1 + \sigma_2$ and the experimental integrated $\sigma_1 + \sigma_2 + c_i$ for specimen HomC1 for $K_I = 0.514$ MPa$\sqrt{\text{m}}$ and $K_{II} = 4.4$ kPa$\sqrt{\text{m}}$ with crack region masked in blue

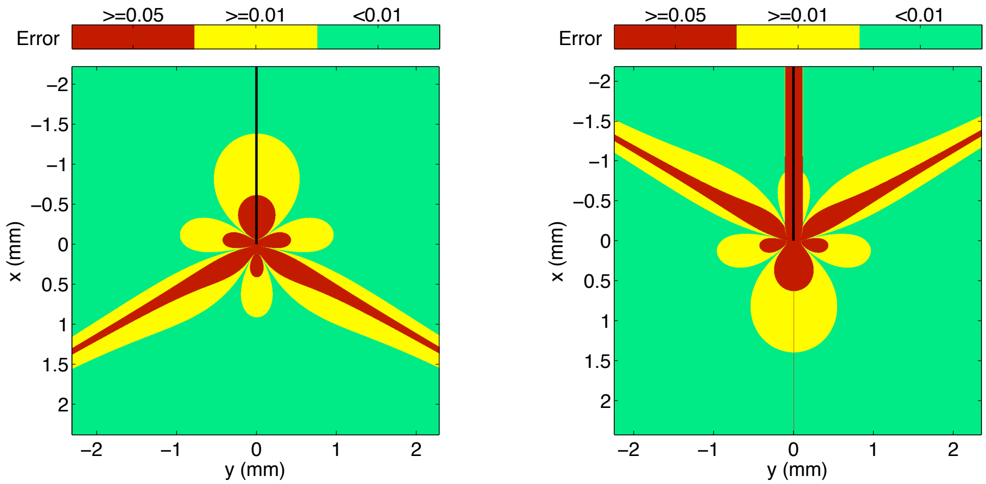

(a) Error for vertical shearing direction

(b) Error for horizontal shearing direction

Figure 4.28: Theoretical error for CGS approximating the derivatives of $\sigma_1+\sigma_2$, assuming K_I loading only for the 4.6 mm $\times$ 4.6 mm field of view and lateral shearing distance of $d_{shear} = 225$ μm [crack indicated in black]

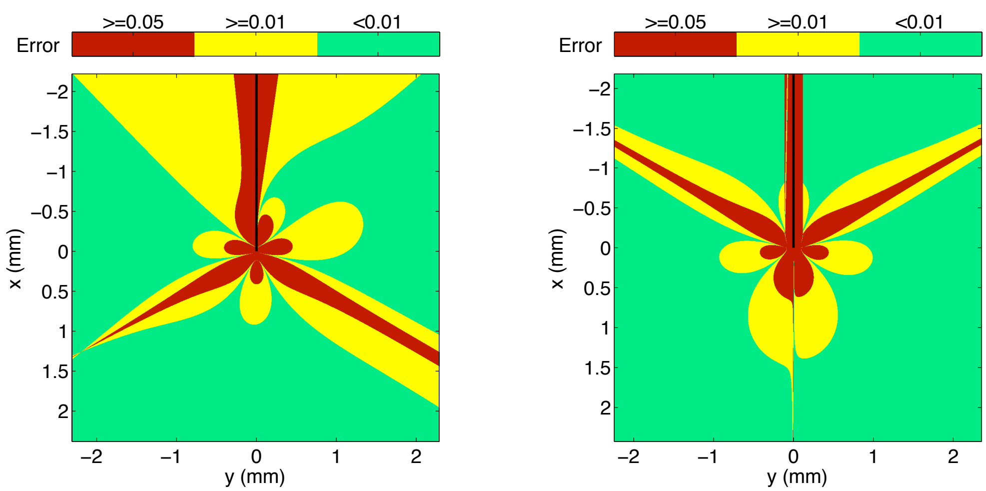

(a) Error for vertical shearing direction

(b) Error for horizontal shearing direction

Figure 4.29: Theoretical error for CGS approximating the derivatives of $\sigma_1+\sigma_2$, assuming $K_I = 0.514$ MPa$\sqrt{\text{m}}$ and $K_{II} = 4.4$ kPa$\sqrt{\text{m}}$ for the 4.6 mm $\times$ 4.6 mm field of view and lateral shearing distance of $d_{shear} = 225$ μm [crack indicated in black]

4.2.4.4 Stress Field Determination

With the photoelasticity and CGS analysis complete, the in-plane stress tensor may be determined. Figure 4.30 shows the experimental and theoretical sum and difference of principal stress fields. The $\sigma_1 - \sigma_2$ field is calculated from δ using the Stress-Optic Law in Equation (3.1); the experimental $\sigma_1 - \sigma_2$ compares to the theoretical field just as the δ field compared. The constant of integration c_i is determined from the boundary condition of $\sigma_{\theta\theta} = 0$ along $\theta = \pm\pi$, which requires α, $\sigma_1 - \sigma_2$, and $\sigma_1 + \sigma_2 + c_i$ to calculate. In this case, the crack front has been masked to prevent unwrapping errors across the crack plane; since the horizontal shearing direction data appears to spread the crack region, the actual location of the crack front is under the mask. Therefore a pixel very close to the crack, but a long distance from the crack tip away from error sources, just to the side of the masked region, is chosen as the the location to apply the boundary condition. Here $\sigma_{\theta\theta}$ is taken to be zero at $(r, \theta) = (2.06 \text{ mm}, -3.08 \text{ rad.})$. The resulting experimental $\sigma_1 + \sigma_2$ in Figure 4.30(c) matches the shape of the theoretical field, but does not quite reach as low in value along the crack or as high in front of the crack tip. These errors are most likely due to the smaller experimental x and y derivatives of $\sigma_1 + \sigma_2$ near the crack tip as compared to the theoretical derivatives and due to the slightly smaller x derivative and larger y derivative along the crack.

In Figure 4.31, the experimental and theoretical separated principal stresses are comparable with the same double lobe feature in σ_1 that indents towards the crack tip near $\theta = 0$ and similar flame-like structure emanating for the crack tip in σ_2. The experimental σ_1 does not indent quite as much as the theoretical case, the experimental σ_2 is not quite as sharp along near $\theta = 0$, and both experimental fields have slightly different behavior approaching the crack behind the tip, but the general structures are similar. These slight differences are due to the errors in those regions from the isoclinic angle, the isochromatic phase, and the CGS phase data as discussed previously. From the isoclinic angle and the principal stresses, the Cartesian stresses in Figure 4.32 are determined. Though the experimental Cartesian stresses have some slight differences from the theoretical fields near the crack tip, due to the error from interpolated points in the isoclinic angle, the experimental fields have similar shape and values as the theoretical. The polar stresses in Figure 4.33 have the same error locations as the Cartesian stresses due to the isoclinic angle errors, but the experimental polar fields again compare well with the theoretical fields a short distance from the crack tip. The errors ahead and to the side of the crack tip in σ_{rr} and $\sigma_{\theta\theta}$ are along the line of the wrapped isoclinic angle in Figure 4.17(a) corresponding to the false discontinuities that are removed by interpolation. The errors just behind the crack tip in $\sigma_{r\theta}$ are from the isoclinic angle regions that falsely swept through zero in Figure 4.17(a).

These errors propagated from the isoclinic angle demonstrate that the manual corrections to the wrapped field are not perfect, but the generally good comparison of the stress fields demonstrates that these manual corrections are close. New algorithms for correcting for errors in the isoclinic angle data require development; currently, these and other related issues with the isoclinic angle are the last hurdle in phase-shifting photoelasticity (Ramesh, 2009). Each individual user of phase-shifting photoelasticity must determine methods to correct for isoclinic angle errors based on the error sources of their system.

Despite the errors discussed above, the global agreement of the experimental and theoretical fields is excellent, as seen in Table 4.1, which reports the root mean squared deviation (RMS) and the normalized RMS. The low NRMSD values range from 0.012 to 0.051. The lower errors are generally for the fields directly related to the experimental phases such as the derivatives of $\sigma_1 + \sigma_2$, α, and $\sigma_1 - \sigma_2$, with the higher errors in stress fields from combining different fields, like the Cartesian and polar stresses. These higher errors are due to accumulation of errors locally around the crack tip and along the x axis.

A measure of the comparison of the experimental data with the theoretical fracture model is to consider σ_{yy} behavior versus r along the crack plane, since $\sigma_{yy} = K_I/(2\pi r)$ for $\theta = 0$. Figure 4.34 shows the experimental and theoretical σ_{yy} versus r plot and the $\log(\sigma_{yy})$ versus $\log(r)$ plot for $\theta = 0$. The experimental σ_{yy} is slightly smaller than the theoretical, implying a smaller K_I value of 0.442 $\text{MPa}\sqrt{\text{m}}$ on average, but this is most likely due to the errors in the isoclinic angle near $\theta = 0$. The theoretical values fall around the upper error bar, which is $\sigma_{yy} + \text{RMSD}_{\sigma yy}$, showing that this difference along $\theta = 0$ is around the global difference. Despite the smaller absolute values, the experimental σ_{yy} has the correct $r^{-1/2}$ behavior, evident in the nearly uniform $-1/2$ slope of the experimental $\log(\sigma_{yy})$ versus $\log(r)$ plot in Figure 4.34(b). This $-1/2$ slope also implies that most of the field of view, excluding the masked regions, is in a K_I-dominant region (Anderson, 2005).

Given the K_I dominance for this field of view for this load condition, the error analysis in Section 4.2.4.3 is applicable to the CGS data. Figure 4.35 shows line plots of the experimental $\partial(\sigma_1+\sigma_2)/\partial x_i$ with $\pm$RMSD lines and the theoretical $\partial(\sigma_1+\sigma_2)/\partial x_i$ along the y axis. These plots also indicate the theoretical error ϵ regions given by Equation (4.7) for the CGS approximation of the derivatives of the principal stress sum. For the x derivative from the vertical shearing direction in Figure 4.35(a), the experimental and the theoretical values agree well for $y > \pm 1$ mm, with the theoretical values within the $\pm$RMSD bounds. The differences between the experimental and theoretical x derivative grow as $|y| \rightarrow 0$, as expected from the $\epsilon > 1\%$ and $\epsilon > 5\%$ error regions. For the y derivative from the horizontal shearing direction in Figure 4.35(b), the experimental and theoretical values compare well for almost all of y, except in the $\epsilon > 5\%$ region for $-y$, with the theoretical values within the RMSD bounds. In comparing the two shearing directions, the vertical shearing data has more error than the horizontal shearing data, indicated by more of y being in the $\epsilon > 1\%$ and $\epsilon > 5\%$ regions, the RMSD being larger, and a larger difference from the theoretical near the crack tip. The general trend of higher error in the vertical shearing data as compared to the horizontal shearing data is true here for this line data and globally as described in Section 4.2.4.3. Error along the crack plane from the vertical shearing direction may explain the slightly higher error in the stress fields directly behind the crack. Despite these errors near the crack, the behavior a short distance from the crack are reasonable, and lead to good global comparison of experimental and theoretical stresses.

Another measure of the comparison of the experimental and theoretical data is the calculated average values for K_I and K_{II}. Theoretical data based on poor K_I and K_{II} values would not compare well globally with experimental data, especially data from two separate experimental methods. The excellent comparison of all the experimental data, spanning two experimental methods, and the theoretical data from the calculated K_I and K_{II} values validates the use of these hybrid experimental methods to investigate stresses near cracks in photoelastic materials.

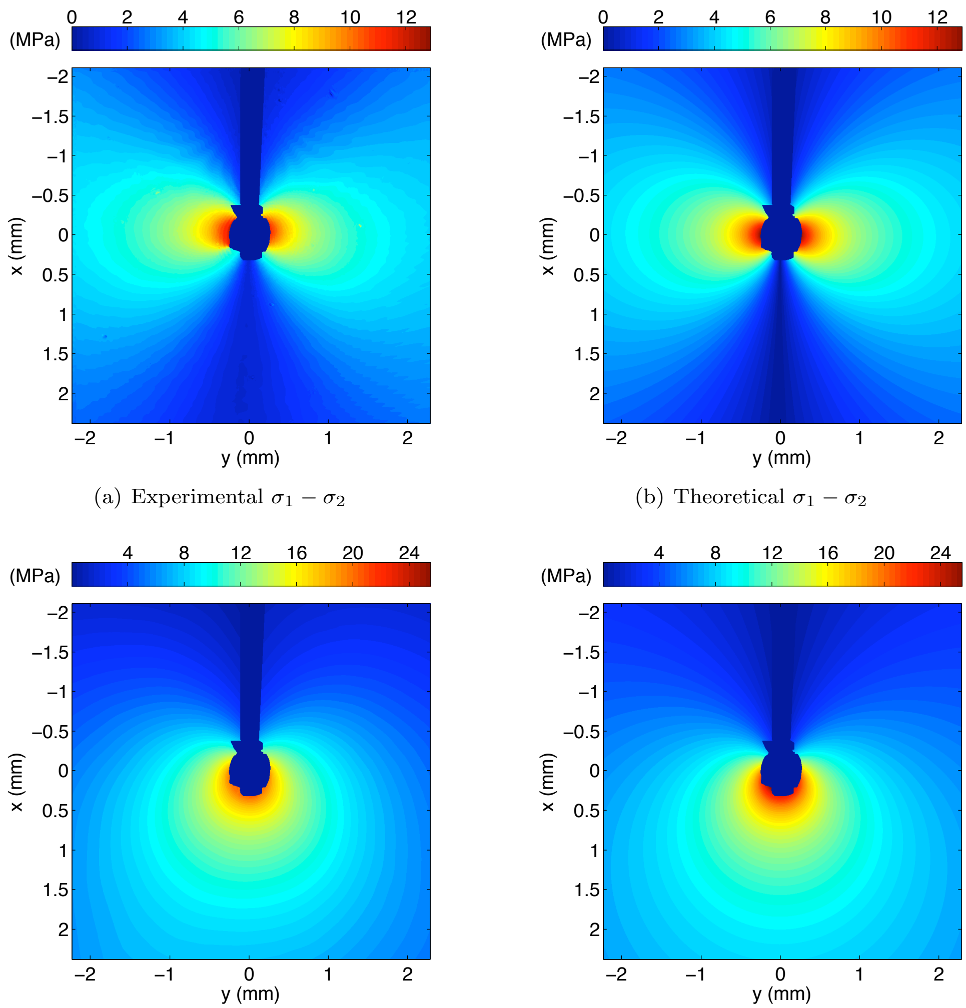

(a) Experimental $\sigma_1 - \sigma_2$

(b) Theoretical $\sigma_1 - \sigma_2$

(c) Experimental $\sigma_1 + \sigma_2$

(d) Theoretical $\sigma_1 + \sigma_2$

Figure 4.30: Experimental and theoretical data for $\sigma_1 - \sigma_2$ and $\sigma_1 + \sigma_2$ for specimen HomC1 for $K_I = 0.514$ MPa$\sqrt{\text{m}}$ and $K_{II} = 4.4$ kPa$\sqrt{\text{m}}$ with crack region masked in blue

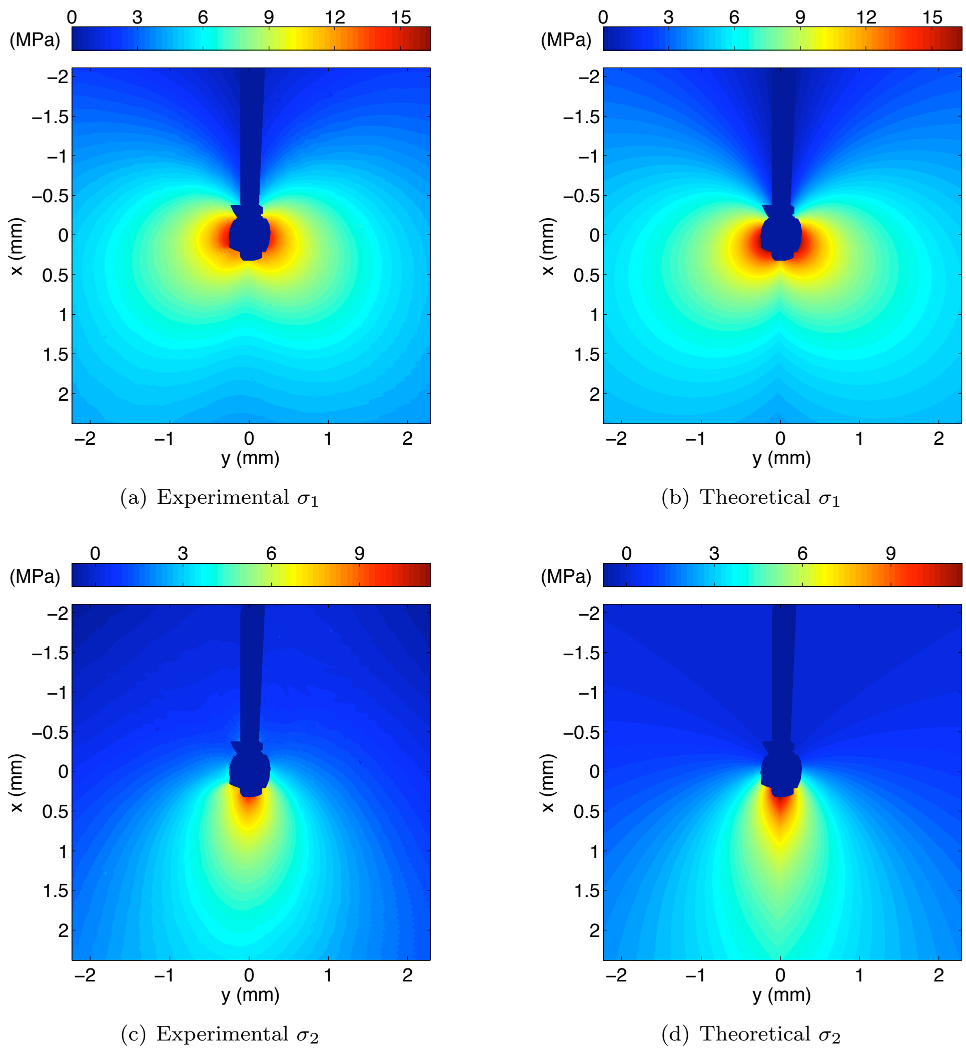

Figure 4.31: Experimental and theoretical data for the principal stresses for specimen HomC1 for $K_I = 0.514$ MPa$\sqrt{\text{m}}$ and $K_{II} = 4.4$ kPa$\sqrt{\text{m}}$ with crack region masked in blue

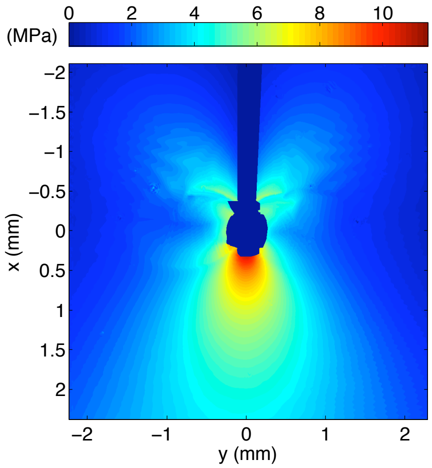

(a) Experimental σ_{xx}

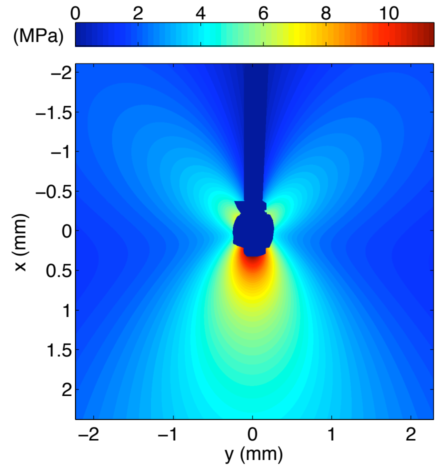

(b) Theoretical σ_{xx}

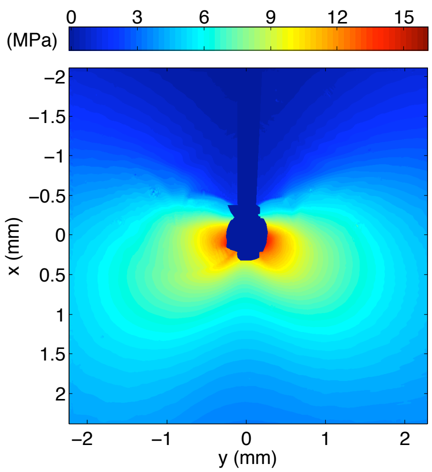

(c) Experimental σ_{yy}

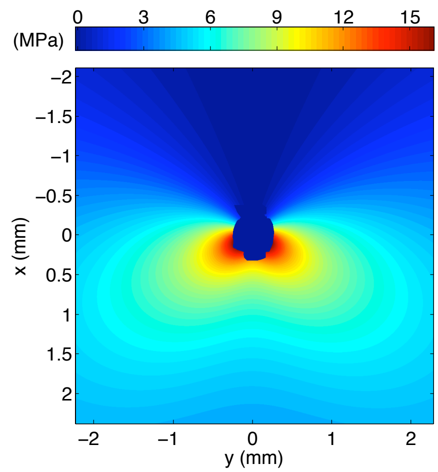

(d) Theoretical σ_{yy}

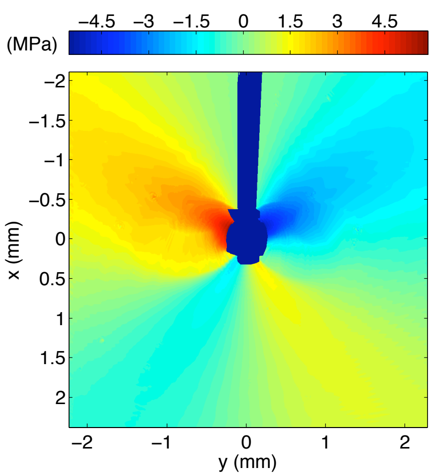

(e) Experimental σ_{xy}

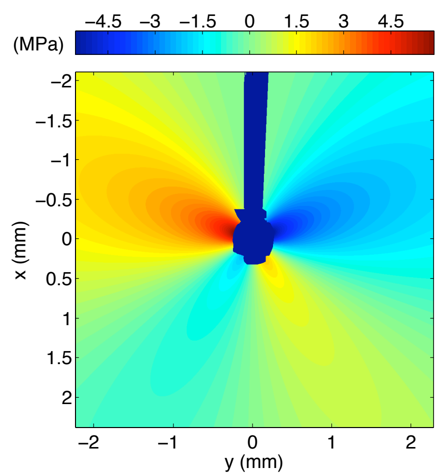

(f) Theoretical σ_{xy}

Figure 4.32: Experimental and theoretical data for the Cartesian stresses for specimen HomC1 for $K_I = 0.514$ MPa$\sqrt{\text{m}}$ and $K_{II} = 4.4$ kPa$\sqrt{\text{m}}$ with crack region masked in blue

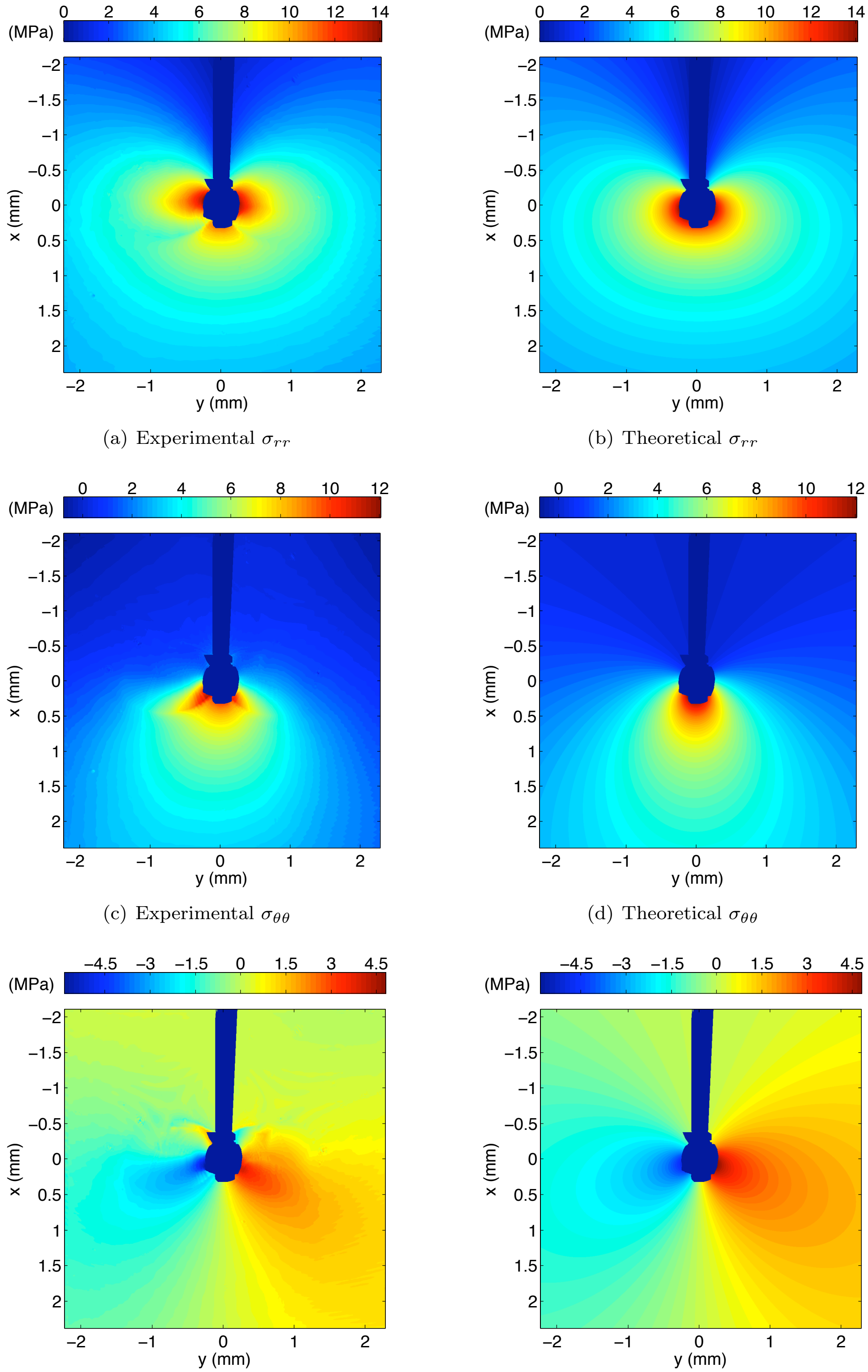

(a) Experimental σ_{rr}

(b) Theoretical σ_{rr}

(c) Experimental $\sigma_{\theta\theta}$

(d) Theoretical $\sigma_{\theta\theta}$

(e) Experimental $\sigma_{r\theta}$

(f) Theoretical $\sigma_{r\theta}$

Figure 4.33: Experimental and theoretical data for the polar stresses for specimen HomC1 for $K_I = 0.514$ MPa$\sqrt{\text{m}}$ and $K_{II} = 4.4$ kPa$\sqrt{\text{m}}$ with crack region masked in blue

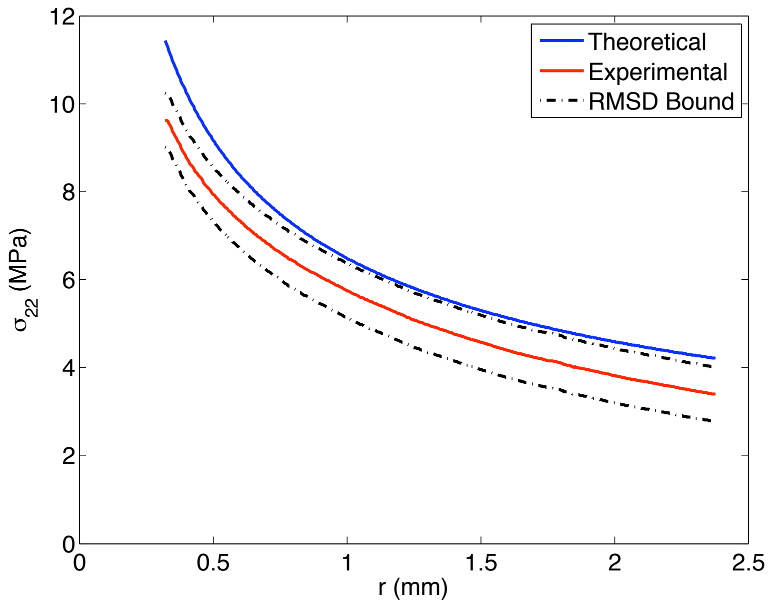

(a) σ_{yy} vs. r for $\theta = 0$

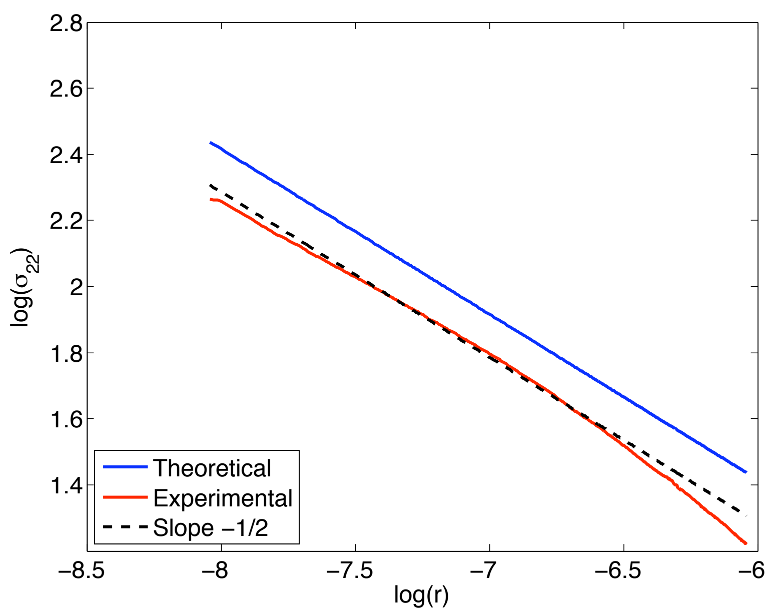

(b) $\log(\sigma_{yy})$ vs. $\log(r)$ for $\theta = 0$

Figure 4.34: Experimental and theoretical data for σ_{yy} along $\theta = 0$ for specimen HomC1 for $K_I = 0.514$ MPa$\sqrt{\text{m}}$ and $K_{II} = 4.4$ kPa$\sqrt{\text{m}}$: The experimental data is slightly lower than the theoretical data, but with similar $r^{-1/2}$ dependence seen by the near $-1/2$ slope on the log-log plot of σ_{yy} versus r.

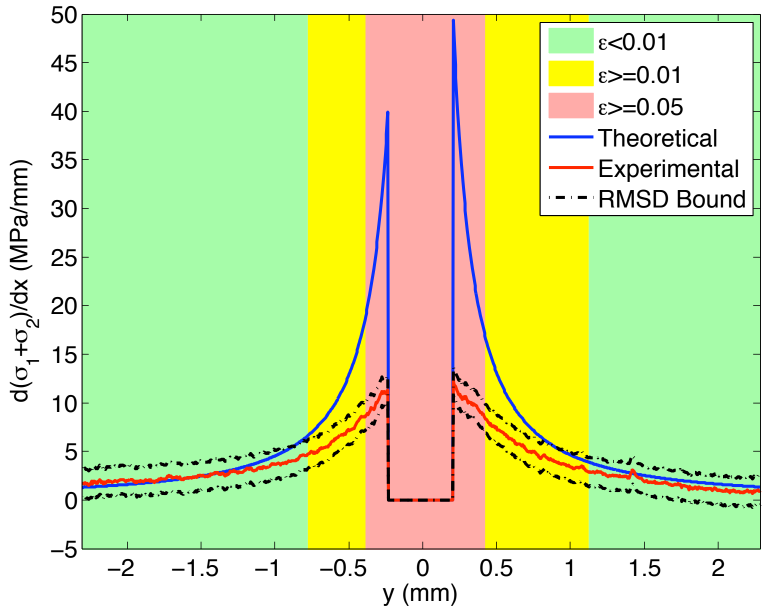

(a) $\frac{\partial(\sigma_1+\sigma_2)}{\partial x}$ vs. y for $\theta = \pm\pi$

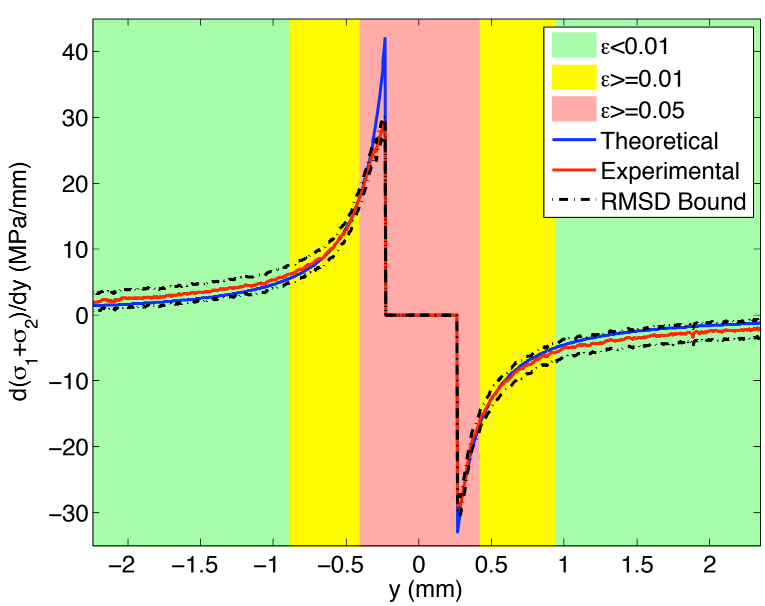

(b) $\frac{\partial(\sigma_1+\sigma_2)}{\partial y}$ vs. y for $\theta = \pm\pi$

Figure 4.35: Experimental and theoretical data for $\partial(\sigma_1 + \sigma_2)/\partial x_i$ vs. y for $\theta = \pm\theta$ for specimen HomC1 for $K_I = 0.514$ MPa$\sqrt{\text{m}}$ and $K_{II} = 4.4$ kPa$\sqrt{\text{m}}$: The $\pm$RMSD error lines and the CGS derivative-approximation error ϵ regions are indicated; the region near the crack tip is masked to zero.

Quantity	Units	RMSD (in Units)	Data Range (in Units)	NRMSD (No Units)
α	rad.	0.17	7.33	0.023
$\varphi_{\alpha d}^{vertical}$	rad.	0.21	4.10	0.051
$\varphi_{\alpha d}^{horizontal}$	rad.	0.06	5.11	0.012
$\partial(\sigma_1 + \sigma_2)/\partial x$ from pure E_x and E_y	MPa/mm	1.53	87.8	0.017
$\partial(\sigma_1 + \sigma_2)/\partial y$ from pure E_x and E_y	MPa/mm	1.30	63.3	0.021
$\partial(\sigma_1 + \sigma_2)/\partial x$ from $\lambda/4$ plate method	MPa/mm	1.47	80.8	0.019
$\partial(\sigma_1 + \sigma_2)/\partial y$ from $\lambda/4$ plate method	MPa/mm	1.33	64.2	0.021
$\sigma_1 + \sigma_2$	MPa	0.60	20.1	0.030
$\sigma_1 - \sigma_2$	MPa	0.25	12.3	0.020
σ_1	MPa	0.36	15.4	0.023
σ_2	MPa	0.29	10.4	0.028
σ_{xx}	MPa	0.48	10.5	0.046
σ_{yy}	MPa	0.62	14.4	0.043
σ_{xy}	MPa	0.30	10.7	0.028
σ_{rr}	MPa	0.42	14.1	0.030
$\sigma_{\theta\theta}$	MPa	0.44	11.8	0.037
$\sigma_{r\theta}$	MPa	0.44	9.0	0.049

Table 4.1: Error analysis for various experimental fields for specimen HomC1 for $K_I = 0.514$ MPa$\sqrt{\text{m}}$ and $K_{II} = 4.4$ kPa$\sqrt{\text{m}}$

4.2.5 Crack with $K_I = 0.259$ MPa$\sqrt{\text{m}}$ and $K_{II} = 5.0$ kPa$\sqrt{\text{m}}$

At a smaller displacement of the wedge that opens the crack in specimen HomC1, the load on the crack causes a stress field with stress intensity factors of $K_I = 0.259$ MPa$\sqrt{\text{m}}$ and $K_{II} = 5.0$ kPa$\sqrt{\text{m}}$. This load is smaller in magnitude than the case presented above, but has a larger mode-mixity with stress intensity factor ratio $\mu_{SIF} = K_{II}/K_I = 0.020$ than the previous case with $\mu_{SIF} = 0.0085$, leading to more asymmetry about the crack plane in the higher mode-mixity case. The experimental parameters are the same for this load case as in the case presented above.

As discussed in the previous case in Section 4.2.4.3, the circularly polarized electric field input for CGS is sufficient for determining the derivatives of $\sigma_1 + \sigma_2$, with similar NRMSD errors presented in Table 4.1 as the pure $E_x\hat{\imath}$ and $E_y\hat{\jmath}$ method for determining φ_{sum}. The data presented here and for subsequent cases only includes this circularly polarized electric field input case for CGS.

Figures 4.36–4.38 present the photoelasticity and the vertical and horizontal shear CGS images. As expected, the fringe densities are smaller as compared to the larger $K_I = 0.514$ MPa$\sqrt{\text{m}}$ load case for photoelastic I_1 and I_2 in Figures 4.36(a) and 4.36(a) and for the CGS images in Figures 4.37 and 4.38. To reduce the noise source of the weak Fizeau fringes from the interference of the reflected light from the surfaces of the specimen, a Wiener filter with window size of $[25 \times 25]$ pixels is used on the photoelastic images before processing the data.

Before the presentation and discussion of the full-field data, Table 4.2 includes the RMSD values, experimental data ranges, and NRMSD values for the data for this load case. Overall, the global error (i.e., NRMSD) is low, ranging from 0.017 to 0.078, but higher for certain fields like $\sigma_1 + \sigma_2$, σ_{xx} and $\sigma_{\theta\theta}$ than for the larger $K_I = 0.514$ MPa$\sqrt{\text{m}}$ load case shown in Table 4.1. The higher NRMSD values are due to a smaller range of data; the RMSD values are comparable or even smaller for this smaller $K_I = 0.259$ MPa$\sqrt{\text{m}}$ load case. Unfortunately, for this case, $\sigma_{\theta\theta}$ has one of the highest errors, which diminishes confidence in the calculation of the constant of integration that uses $\sigma_{\theta\theta}$ along the crack, which may lead to some nominal propagated error in fields that utilize the $\sigma_1 + \sigma_2$ field. Here, σ_{xx} has the highest NRMSD value at 0.078, which is still overall remarkably low for data stemming from a hybrid experimental technique; most of the NRMSd values are under 0.05, which is quite low.

The photoelastic images are processed in the same manner as previously described with the correction of the wrapped isoclinic angle, the unwrapping of the isoclinic angle, the determination of the unambiguous wrapped isochromatic phase, the unwrapping of the isochromatic phase, and finally the determination of $\sigma_1 - \sigma_2$ field. The resulting photoelastic data, the isoclinic angle and the $\sigma_1 - \sigma_2$ fields shown in Figure 4.39, have similar features to the higher load case, where α has a radial symmetry and $\sigma_1 - \sigma_2$ is double lobed on either side of the crack tip. This lower load case has more apparent asymmetry about the crack plane due to the higher mode-mixity, seen in the larger rotation of the double lobes about the crack tip in the $-\theta$ direction. The experimental α again does not have the large change in value near $\theta = 0$ as found in the theoretical α, but exhibits

Quantity	Units	RMSD (in Units)	Data Range (in Units)	NRMSD (No Units)
α	rad.	0.17	7.10	0.025
$\partial(\sigma_1 + \sigma_2)/\partial x$ from $\lambda/4$ plate method	MPa/mm	1.28	49.8	0.026
$\partial(\sigma_1 + \sigma_2)/\partial y$ from $\lambda/4$ plate method	MPa/mm	1.81	52.3	0.035
$\sigma_1 + \sigma_2$	MPa	0.70	12.2	0.058
$\sigma_1 - \sigma_2$	MPa	0.15	8.83	0.017
σ_1	MPa	0.36	7.97	0.045
σ_2	MPa	0.34	6.28	0.055
σ_{xx}	MPa	0.47	6.05	0.078
σ_{yy}	MPa	0.39	8.16	0.036
σ_{xy}	MPa	0.17	6.41	0.026
σ_{rr}	MPa	0.30	8.69	0.034
$\sigma_{\theta\theta}$	MPa	0.44	5.68	0.077
$\sigma_{r\theta}$	MPa	0.24	5.43	0.044

Table 4.2: Error analysis for various experimental fields for specimen HomC1 for $K_I = 0.259$ MPa$\sqrt{\text{m}}$ and $K_{II} = 5.0$ kPa$\sqrt{\text{m}}$

a smoothing effect through this region that approximates the large change, evident in the line plot of the wrapped and unwrapped α for the experimental and theoretical data in Figure 4.39(c). This approximation is due to modulation of the wrapped α by the polarization optic misalignment error discussed in detail in Sections 3.2.1 and 4.2.4.2. The experimental $\sigma_1 - \sigma_2$ matches the theoretical data well evident by the small RMSD of only 0.15 MPa, which is mainly due to the larger load concentration near the crack tip in the theoretical field.

The experimental CGS data produce x and y derivatives of $\sigma_1 + \sigma_2$ that compare well with the theoretical derivatives, shown in Figure 4.40, except very close to the crack tip, which has higher stresses than the CGS method is likely to be able to detect with the shearing distance of 225 μm used for this case. The theoretical range of data for the x derivative is more than twice of the range captured by the experimental data, and the theoretical range for the y derivative is more than four times the experimental range. Though these observations are stark, they are misleading about the CGS data quality. Given a slightly larger mask around the crack tip with an added area of an annulus of radius ~ 200 μm, the data ranges would agree well. Visually, the x derivative has the correct shape, and its values are mostly 25 MPa/mm or less as is the case for the theoretical data except very close to the tip. The theoretical y derivative data is mostly between -20 MPa/mm and 20 MPa/mm, which is true for the experimental data as well.

The asymmetry of the experimental $\sigma_1+\sigma_2$ compares well with that of the theoretical $\sigma_1+\sigma_2$ for $+x$ values, but the experimental field has a different asymmetry for $-x$ values, where the $(-x,+y)$ data points have a different curvature to the stress contour. This difference is most likely due to limitation of the CGS phases to represent derivatives of stress. Figure 4.41 reports the ϵ error maps due to the CGS assumption that the finite difference of $\sigma_1+\sigma_2$ between two points divided by the distance between those points can represent the derivative of $\sigma_1+\sigma_2$, as described above in Section 4.2.4.3. The error maps for pure Mode I loading, given in Figure 4.28, do not change for the same field of view and shearing distance, but the the addition of Mode II loading requires the calculation of these error maps for each individual case. Comparing the CGS error maps for the two load cases with $\mu_{SIF}=0.0085$ and $\mu_{SIF}=0.020$ in Figures 4.29 and 4.41, respectively, shows that the area with $\epsilon>5\%$ is larger in the case with larger mode-mixity behind the crack in the vertical shearing direction, but the error maps for the horizontal shearing direction are similar for the two cases. These ϵ error maps do not show the actual error in the data, but show the regions where the data is more likely to be suspect. For example, the higher ϵ error behind the crack in the vertical shearing data corresponds to the greater difference between the experimental and theoretical $\sigma_1+\sigma_2$. Despite these error predictions, the CGS data and related fields have reasonable NRMSD values.

The experimental and theoretical in-plane tensorial stresses have good agreement in form and stress concentration for most of the field. In Figure 4.42, the asymmetries due to the Mode II loading component are apparent in front of the crack in σ_1 and σ_2, the latter of which exhibits the sharp flame-like shape canted at an angle from $\theta=0$ just as in the theoretical field. Due to errors from $\sigma_1+\sigma_2$ behind the crack, σ_2 behind the crack does not agree as well with theory, especially for $(-x,+y)$ locations. In Figure 4.43, the experimental Cartesian stresses exhibit the expected form where σ_{xx} has a fish shape, σ_{yy} has a small kidney-bean shape, and σ_{xy} has a butterfly shape. The theoretical σ_{xx} has less asymmetry across the x axis just behind the crack than the experimental

σ_{xx} and a larger stress concentration, leading to the highest NRMSD error of 0.078 even though the RMSD is only 0.47 MPa. The theoretical σ_{yy} has a slightly higher stress concentration on the sides of the crack tip than the experimental field, and the experimental σ_{yy} for $(-x, +y)$ is different than predicted; yet, these differences only results in an NRMSD error of 0.036. The theoretical and experimental σ_{xy} compare extremely well with one of the lowest RMSD at 0.17 MPa and NRMSD at 0.026. The experimental polar stresses in Figure 4.44 have the correct form, but with local errors. The experimental σ_{rr} field more asymmetric behind the crack tip, but has low RMSD and NRMSD values. The experimental $\sigma_{\theta\theta}$ agrees well with theory in front of the crack, but not well behind the crack, leading to a a larger NRMSD at 0.077. The experimental $\sigma_{r\theta}$ does not compare well near the crack tip, most likely due to errors propagated from the isoclinic angle, but otherwise has good comparison with theory with average RMSD and NRMSD.

Line plots of the σ_{yy} stress along the crack plane, shown in Figure 4.45, are used to verify that the stress fields measured for this case are K-dominant stress fields that obey the 2D asymptotic crack solution. The experimental σ_{yy} in Figure 4.45(a) again is slightly lower than the theoretical, but the theoretical σ_{yy} is close to the RMSD bounds. The log-log plot of σ_{yy} versus r for $\theta = 0$ establishes the r dependence of the field, i.e., the experimental data fits the $-1/2$ slope, indicating that the data has the correct $1/\sqrt{r}$ behavior of a K-dominant stress field. The K dominance of the experimental stress allows for confident comparison of the experimental data with the the 2D asymptotic crack solution using the experimentally determined K_I and K_{II} values.

This lower load case for specimen HomC1 demonstrates that the hybrid CGS-photoelasticity method successfully determines the in-plane tensorial stress for a moderate load with K_I about half of the fracture toughness of Homalite-100. Stress determination at loading conditions significantly lower than the load condition required for crack propagation is necessary in fracture studies for monitoring of stress development, establishing the type of loading asymmetries and possible crack propagation directions in anisotropic materials. This lower load case, along with the higher load case, establishes that this experimental method is sensitive enough for determination of small Mode II contributions in Mode I–dominant stress fields, useful in future anisotropic material fracture studies.

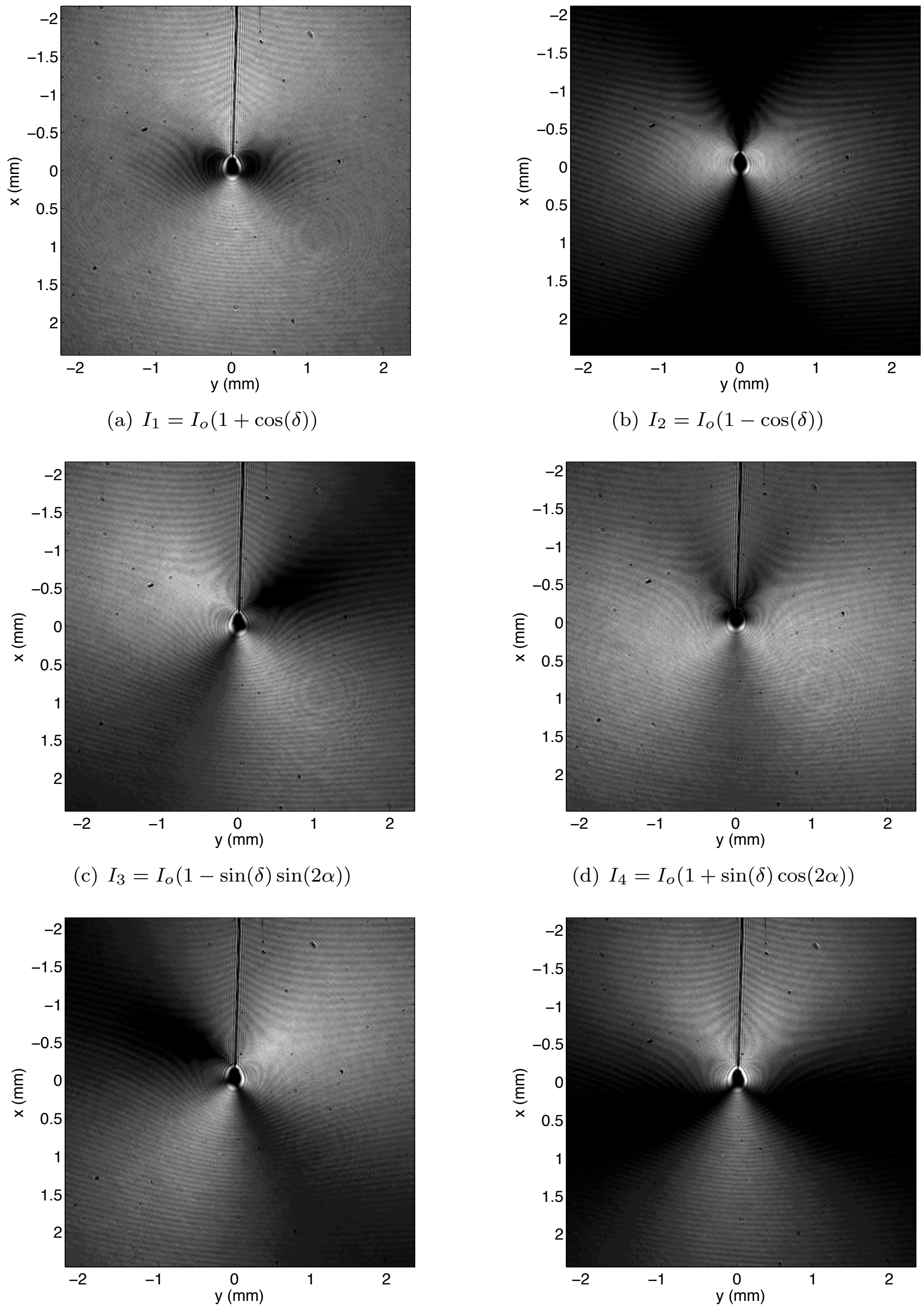

(a) $I_1 = I_o(1 + \cos(\delta))$

(b) $I_2 = I_o(1 - \cos(\delta))$

(c) $I_3 = I_o(1 - \sin(\delta)\sin(2\alpha))$

(d) $I_4 = I_o(1 + \sin(\delta)\cos(2\alpha))$

(e) $I_5 = I_o(1 + \sin(\delta)\sin(2\alpha))$

(f) $I_6 = I_o(1 - \sin(\delta)\cos(2\alpha))$

Figure 4.36: Experimental mages from six-step phase-shifting photoelasticity for specimen HomC1 for $K_I = 0.259$ MPa$\sqrt{\text{m}}$ and $K_{II} = 5.0$ kPa$\sqrt{\text{m}}$. Caustic shadows obscure the data at the crack tip due to the stress concentration, and the weak high density fringes overlaying the photoelastic fringes are due to the interference of the reflections from the front and back faces of the specimen.

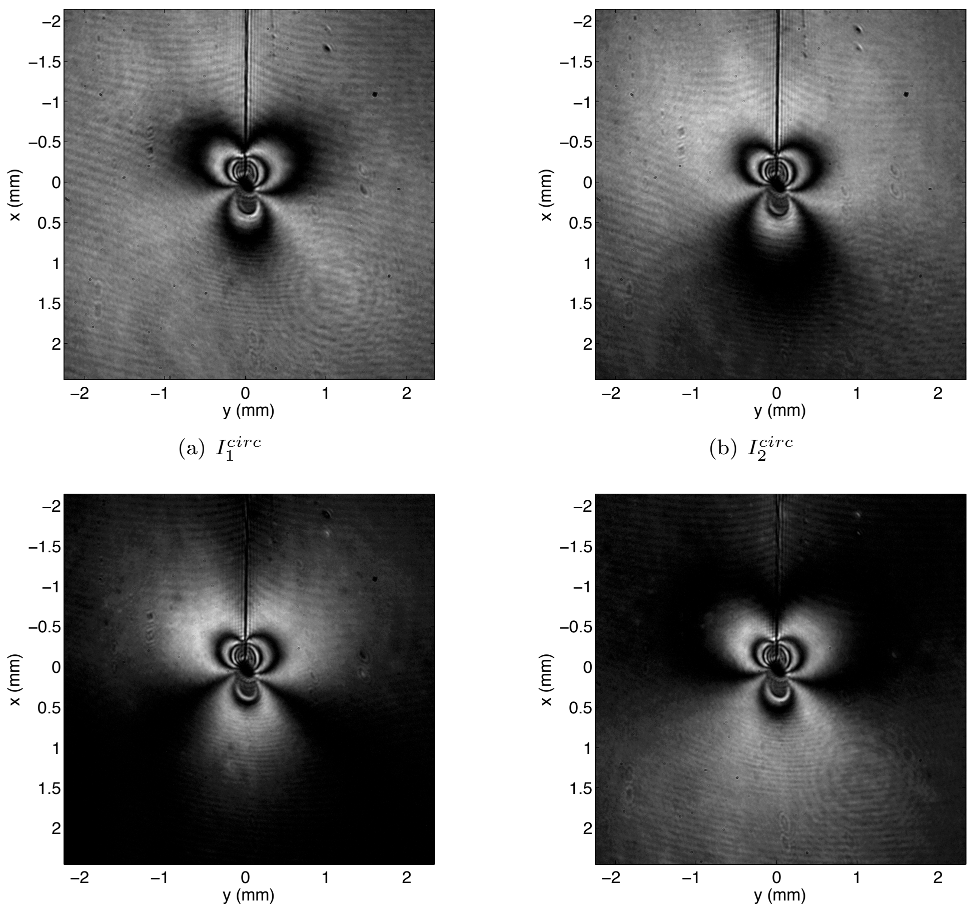

(a) I_1^{circ}

(b) I_2^{circ}

(c) I_3^{circ}

(d) I_4^{circ}

Figure 4.37: Experimental phase-shifted images from vertical shearing CGS using the $\lambda/4$ polarization method for specimen HomC1 for $K_I = 0.259$ MPa$\sqrt{\text{m}}$ and $K_{II} = 5.0$ kPa$\sqrt{\text{m}}$

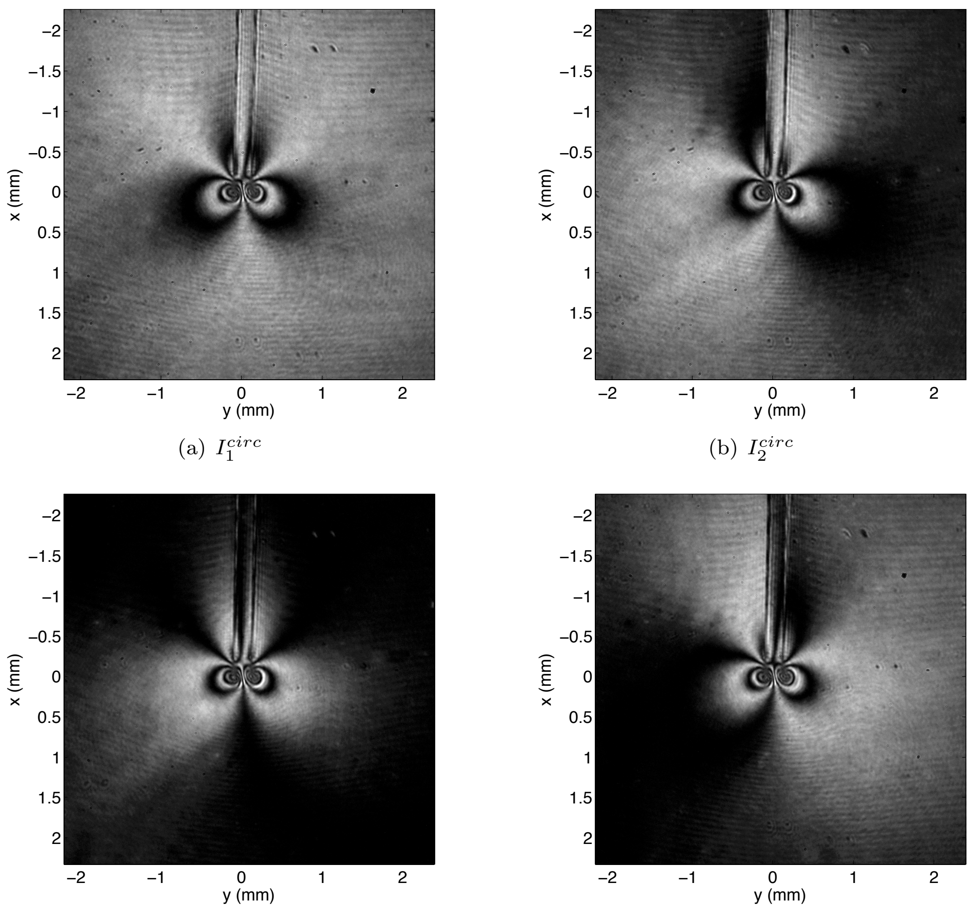

(a) I_1^{circ} (b) I_2^{circ}

(c) I_3^{circ} (d) I_4^{circ}

Figure 4.38: Experimental phase-shifted images from horizontal shearing CGS using the $\lambda/4$ polarization method for specimen HomC1 for $K_I = 0.259$ MPa$\sqrt{\mathrm{m}}$ and $K_{II} = 5.0$ kPa$\sqrt{\mathrm{m}}$

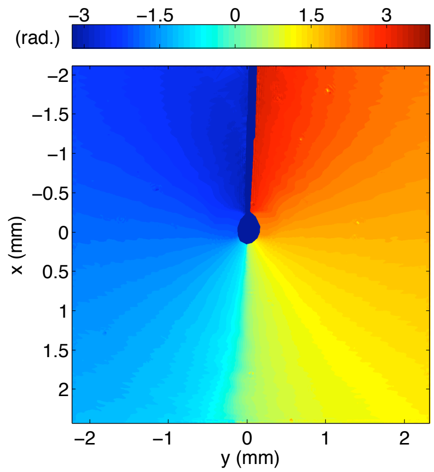

(a) Experimental unwrapped α

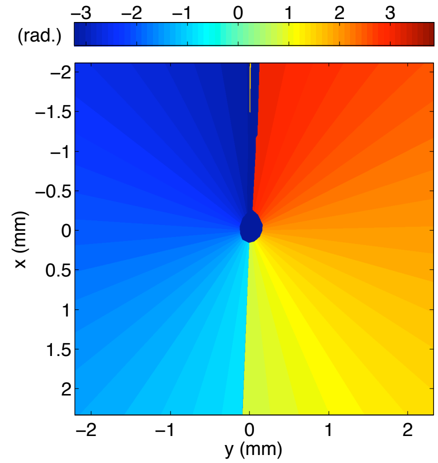

(b) Theoretical unwrapped α

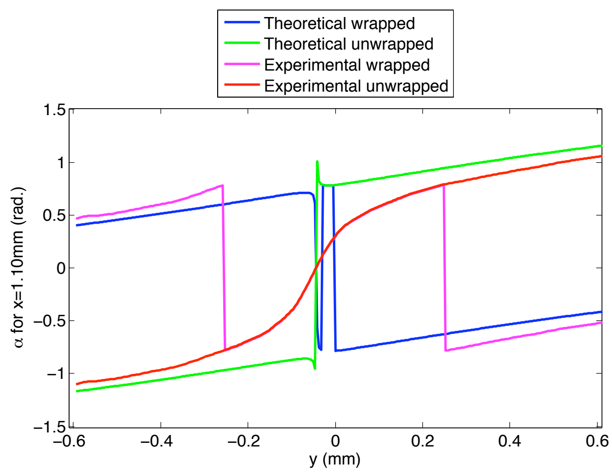

(c) Experimental and theoretical wrapped and unwrapped α

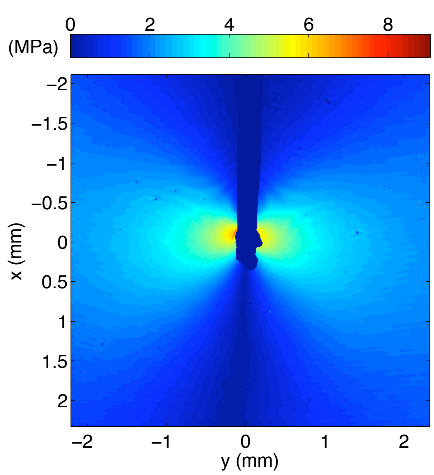

(d) Experimental $\sigma_1 - \sigma_2$

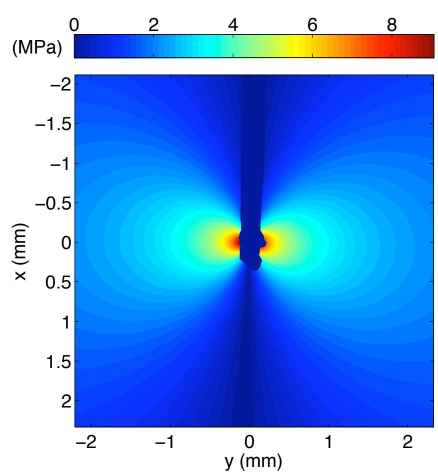

(e) Theoretical $\sigma_1 - \sigma_2$

Figure 4.39: Experimental and theoretical unwrapped α and $\sigma_1 - \sigma_2$ with crack region masked in blue and comparison of experimental and theoretical α for $x = 1.10$ mm

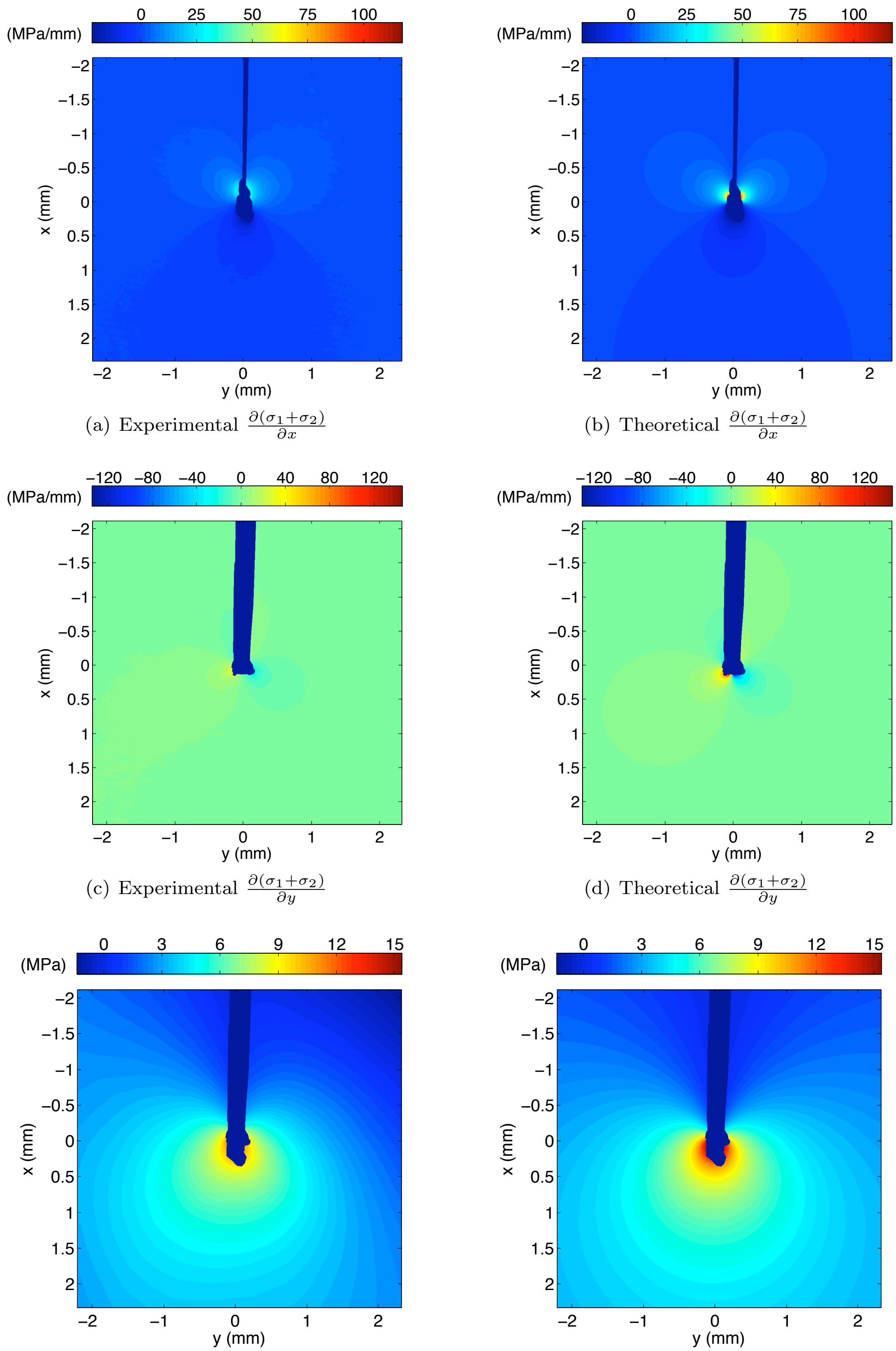

(a) Experimental $\frac{\partial(\sigma_1+\sigma_2)}{\partial x}$

(b) Theoretical $\frac{\partial(\sigma_1+\sigma_2)}{\partial x}$

(c) Experimental $\frac{\partial(\sigma_1+\sigma_2)}{\partial y}$

(d) Theoretical $\frac{\partial(\sigma_1+\sigma_2)}{\partial y}$

(e) Experimental $\sigma_1 + \sigma_2$

(f) Theoretical $\sigma_1 + \sigma_2$

Figure 4.40: Experimental and theoretical data for the derivatives of $\sigma_1 + \sigma_2$ and the experimental integrated $\sigma_1 + \sigma_2$ for specimen HomC1 for $K_I = 0.259$ MPa$\sqrt{\text{m}}$ and $K_{II} = 5.0$ kPa$\sqrt{\text{m}}$ with crack region masked in blue

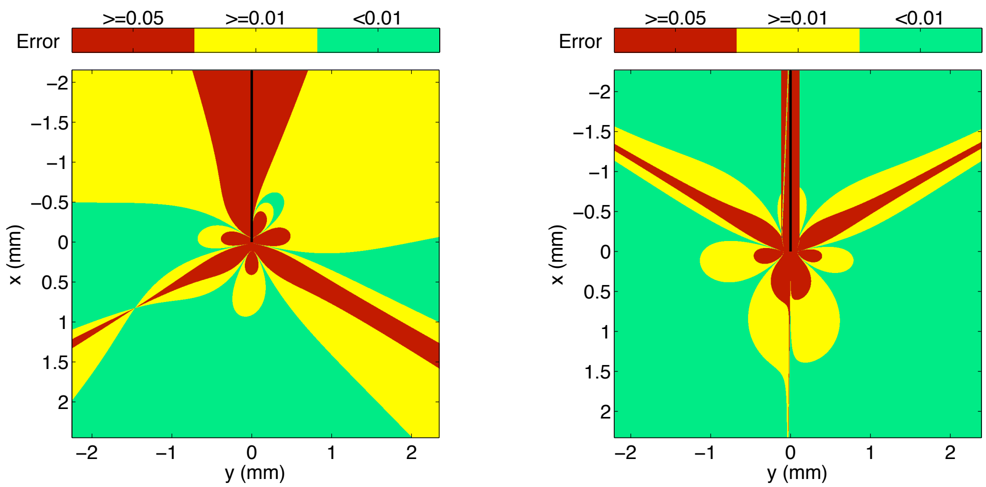

(a) Error for vertical shearing direction

(b) Error for horizontal shearing direction

Figure 4.41: Theoretical error for CGS approximating the derivatives of $\sigma_1+\sigma_2$, assuming $K_I = 0.259$ MPa$\sqrt{\text{m}}$ and $K_{II} = 5.0$ kPa$\sqrt{\text{m}}$ for the 4.6 mm $\times$ 4.6 mm field of view and lateral shearing distance of $d_{shear} = 225$ μm [Crack indicated in black]

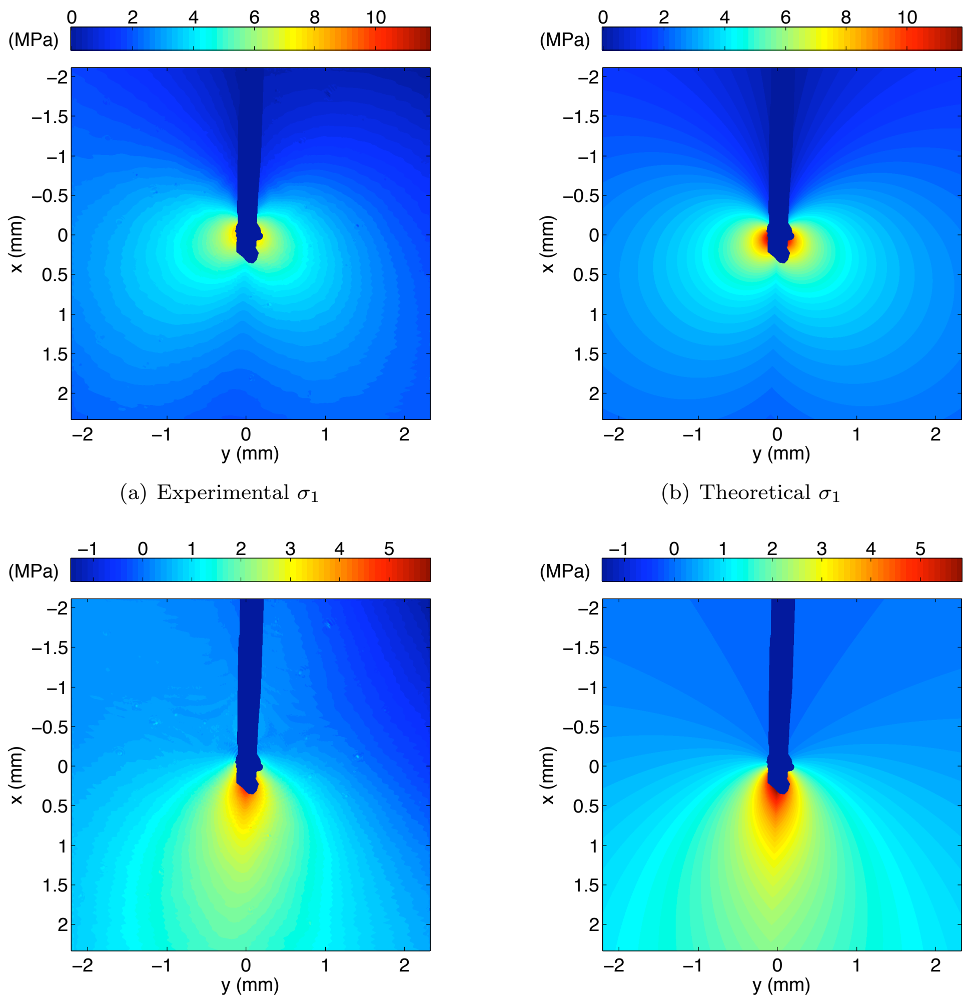

(a) Experimental σ_1

(b) Theoretical σ_1

(c) Experimental σ_2

(d) Theoretical σ_2

Figure 4.42: Experimental and theoretical data for the principal stresses for specimen HomC1 for $K_I = 0.259$ MPa$\sqrt{\text{m}}$ and $K_{II} = 5.0$ kPa$\sqrt{\text{m}}$ with crack region masked in blue

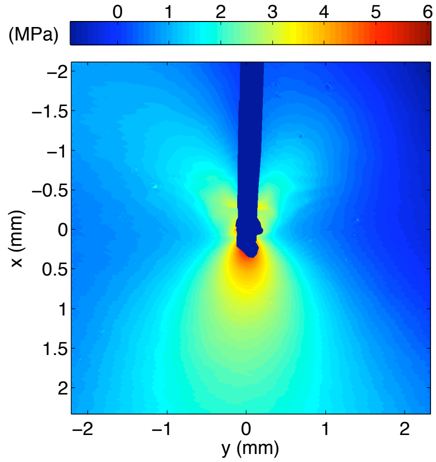

(a) Experimental σ_{xx}

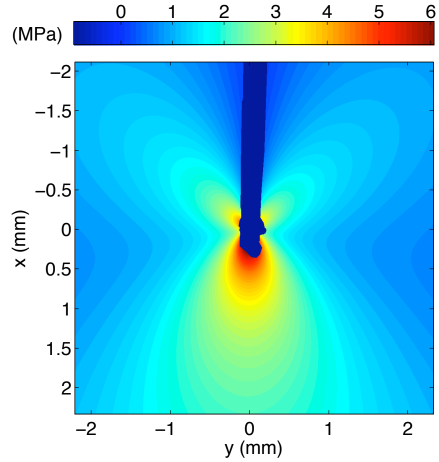

(b) Theoretical σ_{xx}

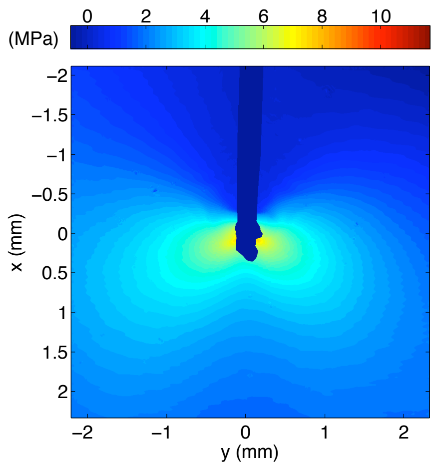

(c) Experimental σ_{yy}

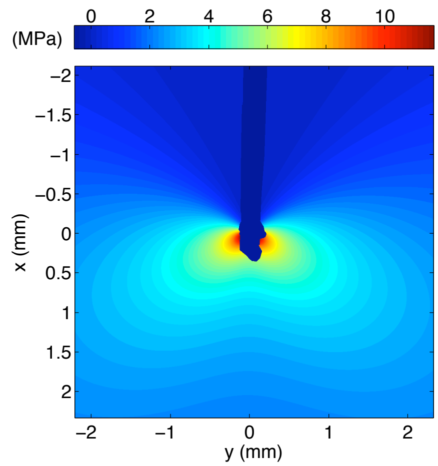

(d) Theoretical σ_{yy}

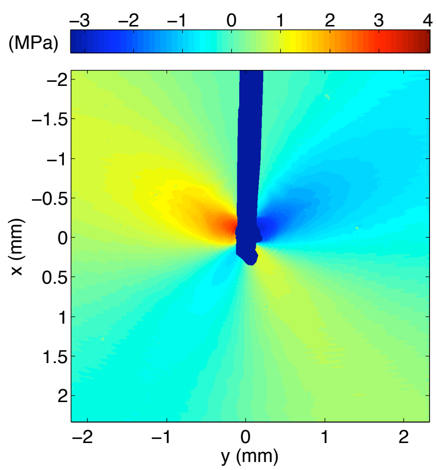

(e) Experimental σ_{xy}

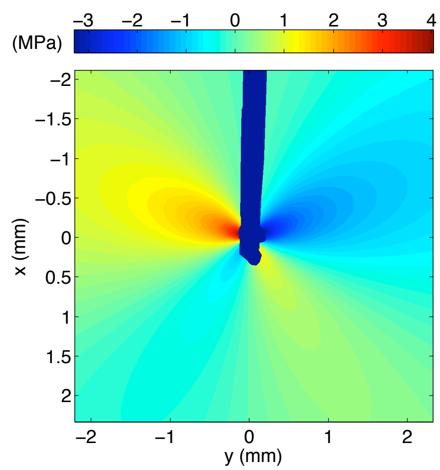

(f) Theoretical σ_{xy}

Figure 4.43: Experimental and theoretical data for the Cartesian stresses for specimen HomC1 for $K_I = 0.259$ MPa$\sqrt{\text{m}}$ and $K_{II} = 5.0$ kPa$\sqrt{\text{m}}$ with crack region masked in blue

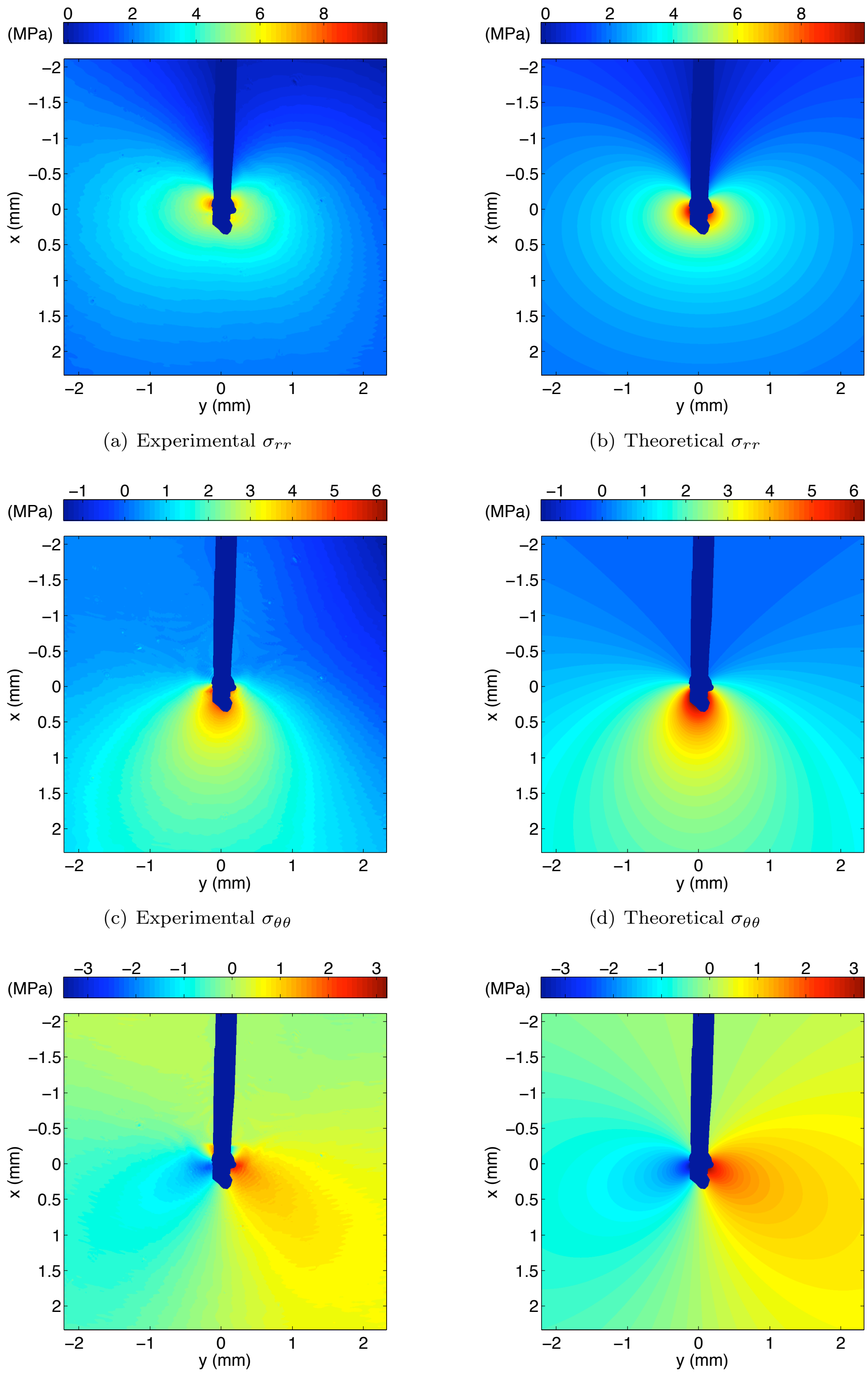

(a) Experimental σ_{rr}

(b) Theoretical σ_{rr}

(c) Experimental $\sigma_{\theta\theta}$

(d) Theoretical $\sigma_{\theta\theta}$

(e) Experimental $\sigma_{r\theta}$

(f) Theoretical $\sigma_{r\theta}$

Figure 4.44: Experimental and theoretical data for the polar stresses for specimen HomC1 for $K_I = 0.259$ MPa$\sqrt{\text{m}}$ and $K_{II} = 5.0$ kPa$\sqrt{\text{m}}$ with crack region masked in blue

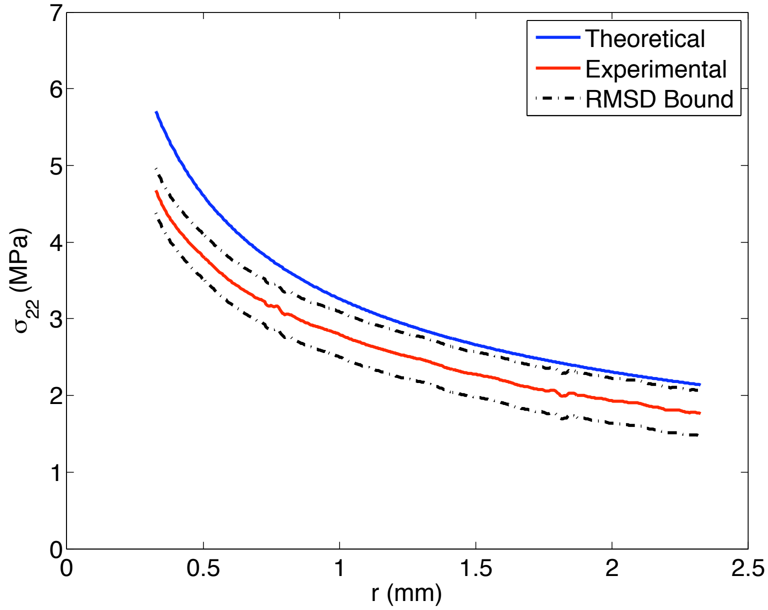

(a) σ_{yy} vs. r for $\theta = 0$

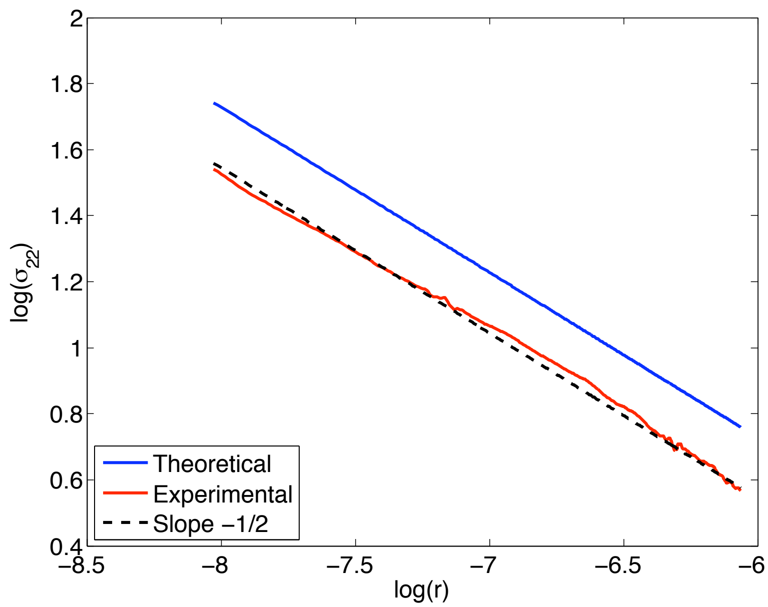

(b) $\log(\sigma_{yy})$ vs. $\log(r)$ for $\theta = 0$

Figure 4.45: Experimental and theoretical data for σ_{yy} along $\theta = 0$ for specimen HomC1 for $K_I = 0.259$ MPa$\sqrt{\text{m}}$ and $K_{II} = 5.0$ kPa$\sqrt{\text{m}}$: The experimental data is slightly lower than the theoretical data, but with similar $r^{-1/2}$ dependence seen by the near $-1/2$ slope on the log-log plot of σ_{yy} versus r.

4.2.6 Crack with $K_I = 0.145$ MPa$\sqrt{\text{m}}$ and $K_{II} = 0.63$ kPa$\sqrt{\text{m}}$

This specimen, called HomC2, is made of Homalite-100, but this specimen has thickness of $h = 3.43$ mm, outer dimensions 25.46 mm $\times$ 25.46 mm, V-notch depth of 6.25 mm, straight notch length of $a_1 = 3.53$ mm and crack length of $s_2 = 8.67$ mm. The optical field of view imaged onto the sensor is 4.57 mm $\times$ 4.57 mm, and the image resolution is 4.57 μm. For this CGS setup, the Ronchi grating pitch, p, is 1 mm/40; the grating separation, $\tilde{\Delta}$, is 8.84 mm; the wavelength of light from the linearly polarized HeNe laser is 632.8 nm; and the resulting lateral shearing distance, d_{shear}, is 224 μm. Figure 4.46(a) shows the specimen before loading with the experimental field of view indicated on the specimen. Figure 4.46(a) shows the specimen in the load apparatus prior to loading; the angled view of the specimen shows a very slight curvature to the crack tip through the thickness. The image is from taken looking towards the light source. The measured stress intensity values are $K_I = 0.145$ MPa$\sqrt{\text{m}}$ and $K_{II} = 0.63$ kPa$\sqrt{\text{m}}$, which give a mode-mixity ratio of $\mu_{SIF} = 0.0043$. This load case has the lowest recorded K_I for cracks in Homalite-100 during this study.

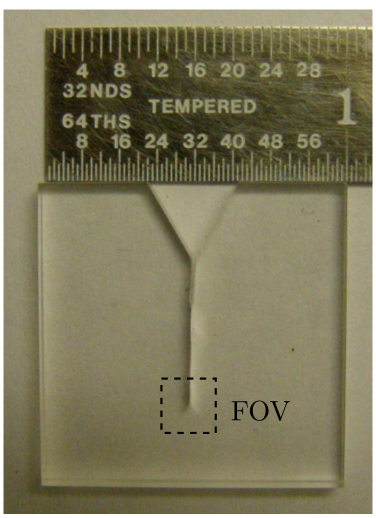

(a) Specimen with marked FOV

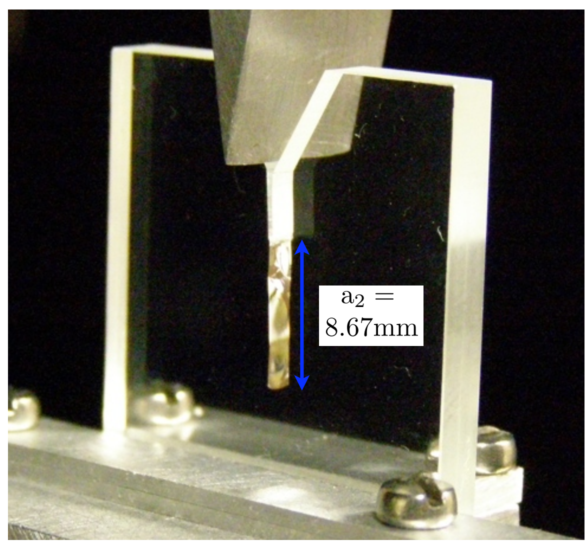

(b) Specimen with marked a_2

Figure 4.46: Specimen HomC2 before loading: (a) the small FOV is indicated; (b) the specimen is in the loading apparatus with the crack length a_2 indicated

Figures 4.47–4.49 present the photoelasticity and the vertical and horizontal shear CGS images. The fringe densities in these images are small due to the small K_I and K_{II}. These images have similar fringe density as the $K_I = 0.259$ MPa$\sqrt{\text{m}}$ case in specimen HomC1 even with a smaller K_I because specimen HomC2 is 56% thicker than specimen HomC1, meaning the two interferometric methods that scale by the specimen thickness can report similar fringe density for different loads. To reduce the noise source of the weak Fizeau fringes from the interference of the reflected light from the surfaces of the specimen, a Wiener filter with window size of $[25 \times 25]$ pixels is used on the photoelastic images before processing the data. In the images, a small dark ring is apparent on the crack plane about 250 μm behind the crack tip; this ring is a second crack tip at one of the surfaces of the specimen. As noted in Figure 4.46(b), the crack tip is not perfectly straight through the thickness. The curvature does not appear to affect the shape of the interference patterns except for blurring the data in the immediate vicinity of this back surface crack tip. Close observation of the crack tip shape in Figure 4.46(b) shows that the tip is mostly straight, but curves up on one surface, so the dominant stress concentration is at the crack tip identified by the origin. These blurred data points are masked to prevent error propagation.

Table 4.3 presents the RMSD values, experimental data ranges, and NRMSD values for the experimental fields of interest for this small load case. As expected for this case, the data ranges are small. The RMSD values are also small for all of the fields, resulting in reasonably low NRMSD values from 0.023 to 0.069. Good comparison for this case indicates that the experimental method is sensitive enough to consider smaller stress fields that may be useful for high-cycle fatigue testing in materials similar to Homalite-100 or to consider fracture in materials with smaller photoelastic constants than Homalite-100.

As with the analysis previously presented, the photoelastic images are processed first by determination of the isoclinic angle, which requires some manual correction for error due to misalignment of the polarization optics, and then the determination of the isochromatic phase, which is converted to $\sigma_1 - \sigma_2$. Figure 4.50 presents the experimental and theoretical unwrapped isoclinic angle and $\sigma_1 - \sigma_2$ fields, showing good qualitative agreement. The isoclinic angle has the errors common to other isoclinic angle fields previously presented, such as the smoothing of the angle through the region near $\theta = 0$, as shown in Figure 4.50(c). With this small mode-mixity, the isoclinic angle is

Quantity	Units	RMSD (in Units)	Data Range (in Units)	NRMSD (No Units)
α	rad.	0.21	6.69	0.031
$\partial(\sigma_1+\sigma_2)/\partial x$ from $\lambda/4$ plate method	MPa/mm	0.95	31.1	0.030
$\partial(\sigma_1+\sigma_2)/\partial y$ from $\lambda/4$ plate method	MPa/mm	0.78	34.5	0.023
$\sigma_1+\sigma_2$	MPa	0.26	7.18	0.036
$\sigma_1-\sigma_2$	MPa	0.14	3.89	0.035
σ_1	MPa	0.13	5.14	0.026
σ_2	MPa	0.15	3.74	0.040
σ_{xx}	MPa	0.21	3.91	0.054
σ_{yy}	MPa	0.16	5.26	0.031
σ_{xy}	MPa	0.16	3.73	0.044
σ_{rr}	MPa	0.14	5.39	0.026
$\sigma_{\theta\theta}$	MPa	0.24	3.48	0.069
$\sigma_{r\theta}$	MPa	0.14	3.68	0.038

Table 4.3: Error analysis for various experimental fields for specimen HOMC2 for $K_I = 0.145$ MPa$\sqrt{\text{m}}$ and $K_{II} = 0.63$ kPa$\sqrt{\text{m}}$

behaving very close to that of a pure Mode I case, which would have a $\pi/2$ discontinuity at $\theta = 0$ due to the definition of the principal stresses; the larger principal stress changes between the eigenvalues that correspond to the principal stresses when going from $+y$ to $-y$, resulting in a $\pi/2$ change in the angle corresponding to the larger principal stress. This α field has similar RMSD and NRMSD as other presented experimental α fields, indicating consistency of the the error correction methods, regardless of load level. The $\sigma_1 - \sigma_2$ field exhibits the correct shape and almost reaches the same level of stress concentration near the crack tip as the theoretical field, with reasonable NRMSD at 0.035. The higher deviation regions for $\sigma_1 - \sigma_2$ are in front of the crack tip and behind the crack, where the experimental values do not go as low as predicted due to the errors in α in those regions. The wavy nature to the contours is the modulation by the weak interference of the reflected light from the surfaces of the specimen. Since these Fizeau fringes scale up in frequency with increasing thickness (Hecht, 2002), the thicker specimen would experience greater frequency of these weak fringes than the thin specimen for a comparable load. If a heavier Wiener filter (larger window size) had been used on this data, the real photoelastic data may have been obscured. The waviness to the contours further is one reason for the larger difference between the experimental and theoretical photoelasticity-related fields.

The x and y derivatives of $\sigma_1 + \sigma_2$ and the integrated $\sigma_1 + \sigma_2$ fields from the CGS data are presented in Figure 4.51. The derivatives of $\sigma_1 + \sigma_2$ have some of the lowest NRMSD values, which corroborates the excellent qualitative comparison of the experimental and theoretical fields with the correct shapes and values for most of the field. The region with most difference is at the usual location near the crack tip, where the experimental stress concentration is not high enough. Also, the x derivative field from the vertical shearing phase appears to be elongated in the $-x$ direction behind the crack. The resulting experimental $\sigma_1 + \sigma_2$ in Figure 4.51(f), which no longer includes the constant of integration, has a similar shape to the theoretical field, but the stress concentration is smaller at the crack tip, and the stresses for $-x$ do not curve enough towards the crack tip. These differences are directly due to the previously noted differences in the derivative fields. Even with these errors, the experimental $\sigma_1 + \sigma_2$ has similar NRMSD as the $\sigma_1 - \sigma_2$ field.

The ϵ error related to the derivative assumption for CGS is lower for this case with modest mode-mixity of $\mu_{SIF} = 0.0043$, as indicated in the ϵ error maps in Figure 4.52. Similar to the $K_I = 0.514$ MPa$\sqrt{\text{m}}$ case for HomC1, the largest error is located behind the crack in the vertical shearing direction and around the crack tip for both directions, which is consistent with the noted differences in the derivative fields. Interestingly, even though the CGS interference patterns for this case are closer in density to that of the $K_I = 0.259$ MPa$\sqrt{\text{m}}$ case for HomC1 with its higher mode-mixity of $\mu_{SIF} = 0.058$, the ability of the CGS phases in this case to represent a derivatives of $\sigma_1 + \sigma_2$ is closer to that of the high $K_I = 0.514$ MPa$\sqrt{\text{m}}$ case for HomC1 with its higher $\mu_{SIF} = 0.0085$, demonstrating that the level of mode-mixity has a significant effect on the CGS data. Further quantitative investigation is required to characterize the error involved with using CGS in mixed-mode loading configurations.

The experimental in-plane tensorial stresses all exhibit the same types of good agreement, with a few local problem areas, as the previously discussed cases for HomC1, except the asymmetry in the experimental fields in front of the crack is not as great as in the theoretical fields. In Figure 4.53, the principal stresses have the correct shapes, but they do not appear to shift toward $-\theta$ as much as the theoretical field. The σ_1 and σ_2 fields have good NRMSD values at 0.026 and 0.40, respectively. In Figure 4.54, the experimental Cartesian stresses presented compare well with theory, except σ_{xx} is more negative for $(-x, +y)$ points and more asymmetric about the x axis than the theoretical case. The experimental polar stresses in Figure 4.55 have the correct shape, but $\sigma_{\theta\theta}$ does not reach the same stress concentration as theory, resulting in a higher NRMSD value of 0.069. Since the experimental $\sigma_{\theta\theta}$ is fairly uniform along the crack and appears to agree well with theory there, the higher error does not appear to have affected the constant of integration calculation, leading to the low error for $\sigma_1 + \sigma_2$.

Figure 4.56 shows two line plots for σ_{yy} along $\theta = 0$. The first shows σ_{yy} versus r, where the theoretical data is within the RMSD bound of the experimental data for $r > 1$ mm, but increases faster than the experimental data near the crack tip. The second figure of the log-log plot of σ_{yy} versus r shows the $-1/2$ slope of the experimental data for larger r, but the slope decreases for smaller r, indicating either a loss of K dominance or large experimental error in this region of σ_{yy}. K dominance near the crack tip is usually lost due to plasticity or 3D stress effects near the crack tip, but plasticity is not likely for this small K_I. The 3D stress effects, which is the breakdown of the basic assumption of plane stress (Rosakis et al., 1990; Krishnaswamy et al., 1991), are the likely culprit for larger error in this field, and the other stress fields, near the crack tip. Since $\sigma_{yy} = \frac{1}{2}(\sigma_1 + \sigma_2) - \frac{1}{2}(\sigma_1 - \sigma_2)cos(2\alpha)$, all of the errors in $\sigma_1 + \sigma_2$, $\sigma_1 - \sigma_2$, and α conspire near the crack tip to reduce σ_{yy} here. First, the value of $\sigma_1 + \sigma_2$ in front of crack is smaller; second, α is closer to zero than in theory, leading to a larger value of $\cos(2\alpha)$ than in theory; third, $\sigma_1 - \sigma_2$ is slightly larger than theory; and fourth, the combination of a smaller $\sigma_1 + \sigma_2$ with a larger negative $-\frac{1}{2}(\sigma_1 - \sigma_2)cos(2\alpha)$ results in an under-determination of σ_{yy} as compared to the theoretical plane stress value. This type of error in this line plot prompts checking the $1/\sqrt{r}$ behavior along other values of θ. Unfortunately, this is not a simple matter in the current implementation of the analysis program in MATLAB®, since the stress fields are represented by a matrix, requiring interpolation of the stress along a line for a given θ. Since the 3D stress effects are confined to near the crack tip, K dominance can be determined away from the crack tip, as shown in the $1/\sqrt{r}$ behavior for larger r in the σ_{yy} plot. The thicker specimen appears to have greater variation in r behavior along the $\theta = 0$ plane than in the thinner specimen, which is expected given that the 3D effects scale with the thickness of the specimen. The overall smaller σ_{yy} values in the experimental data along the $\theta = 0$ plane in the K-dominant regions in both HomC1 and HomC2 must be due to fields with radial natures on $\theta = 0$, which point to the errors in the isoclinic angle and in $\sigma_1 - \sigma_2$ due to the polarization optic misalignment.

With the overall good comparison of the experimental data with the theoretical data and a few identified errors, this $K_I = 0.145$ MPa$\sqrt{\text{m}}$ load case demonstrates the capability of this experimental method to monitor small K_I cases and also highlights some of improvements that can be made. This K_I is on the order of $K_{Ic}/4$, which is a useful load level for high cycle fatigue testing. The modulation due to the Fizeau interference patterns on top of the photoelastic data needs further mitigation beyond the Wiener filter, such as an anti-reflective coating on the specimen surfaces. Also, the errors due to the rotational misalignment that lead to the local α errors on the crack plane appear to affect the reported behavior of the stresses markedly in this low K_I case, spurring better alignment methods and wrapped α error correction methodologies for Mode I–dominant crack applications.

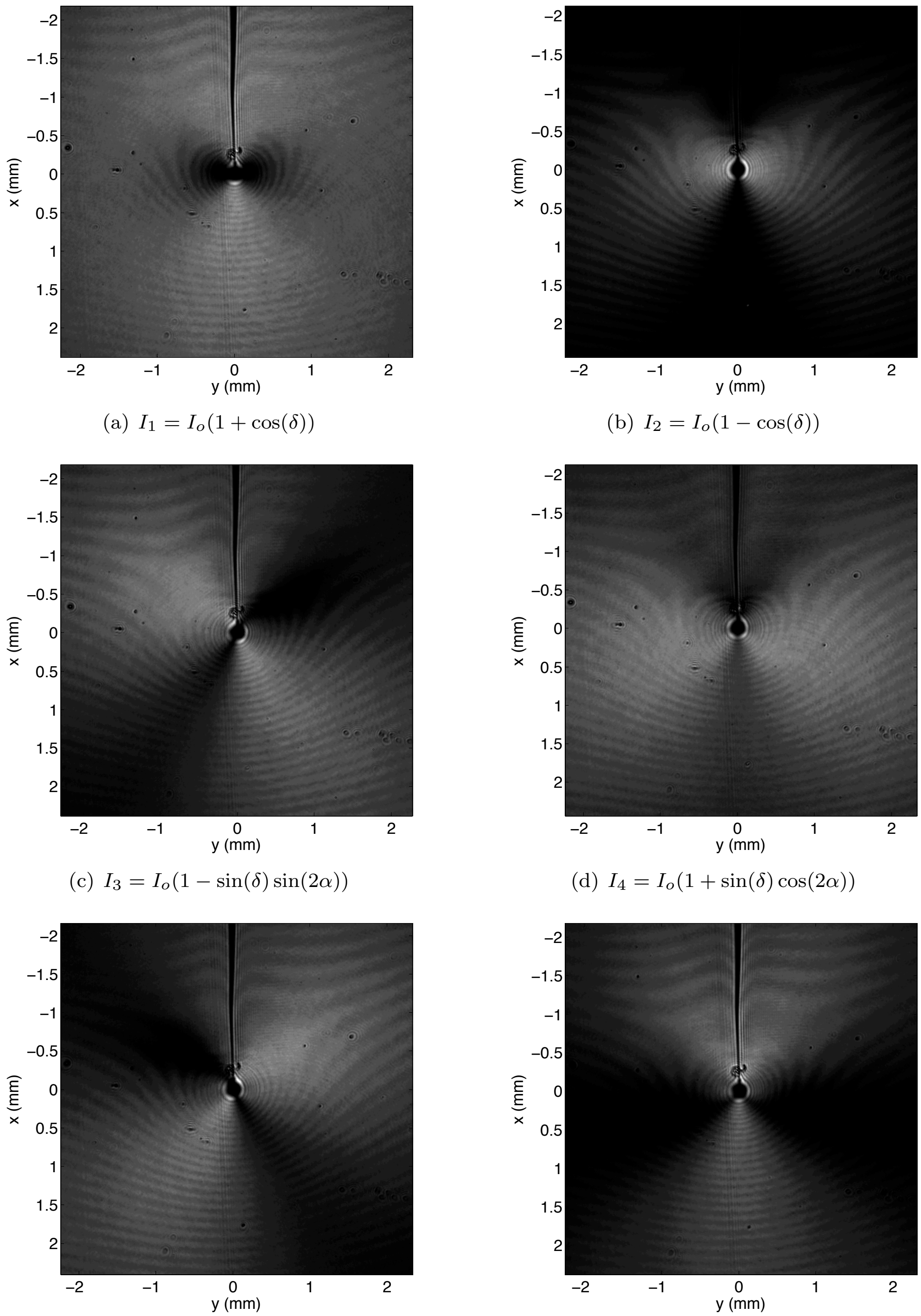

(a) $I_1 = I_o(1 + \cos(\delta))$

(b) $I_2 = I_o(1 - \cos(\delta))$

(c) $I_3 = I_o(1 - \sin(\delta)\sin(2\alpha))$

(d) $I_4 = I_o(1 + \sin(\delta)\cos(2\alpha))$

(e) $I_5 = I_o(1 + \sin(\delta)\sin(2\alpha))$

(f) $I_6 = I_o(1 - \sin(\delta)\cos(2\alpha))$

Figure 4.47: Experimental mages from six-step phase-shifting photoelasticity for specimen HomC2 for $K_I = 0.145$ MPa$\sqrt{\mathrm{m}}$ and $K_{II} = 0.63$ kPa$\sqrt{\mathrm{m}}$: Caustic shadows obscure the data at the crack tip due to the stress concentration, and the weak high density fringes overlaying the photoelastic fringes are due to the interference of the reflections from the front and back faces of the specimen.

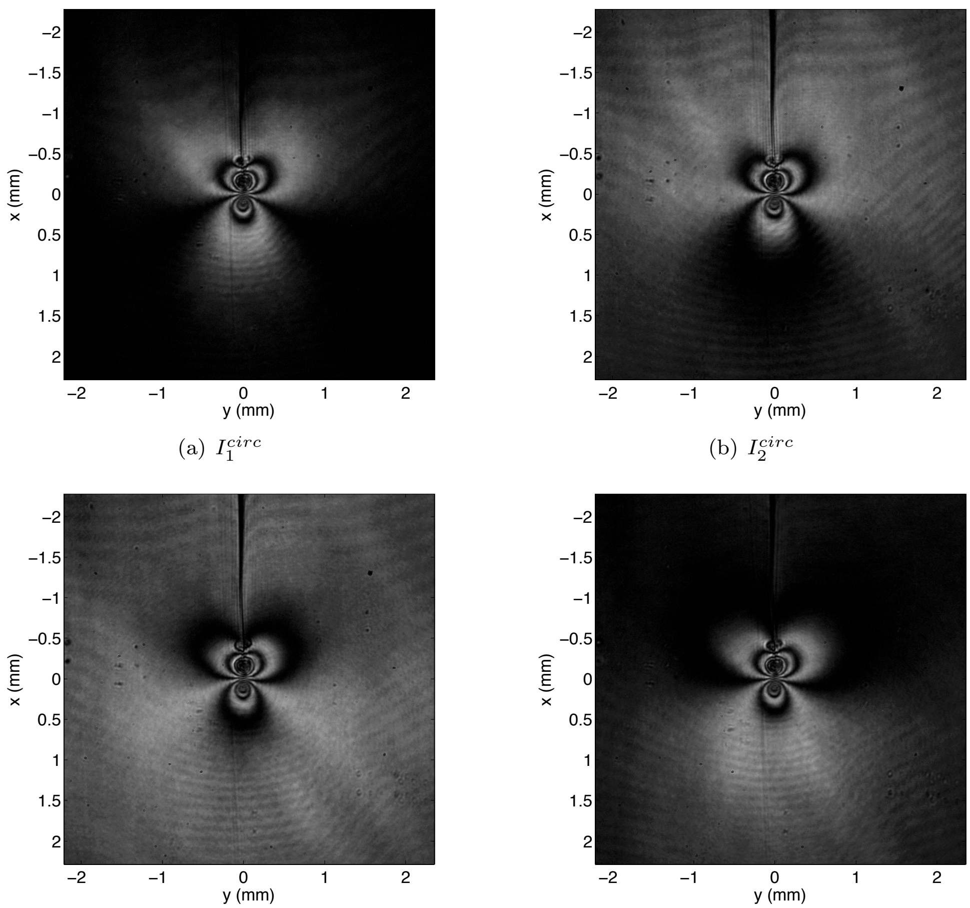

(a) I_1^{circ} (b) I_2^{circ}

(c) I_3^{circ} (d) I_4^{circ}

Figure 4.48: Experimental phase-shifted images from vertical shearing CGS using the $\lambda/4$ polarization method for specimen HomC2 for $K_I = 0.145$ MPa$\sqrt{\mathrm{m}}$ and $K_{II} = 0.63$ kPa$\sqrt{\mathrm{m}}$

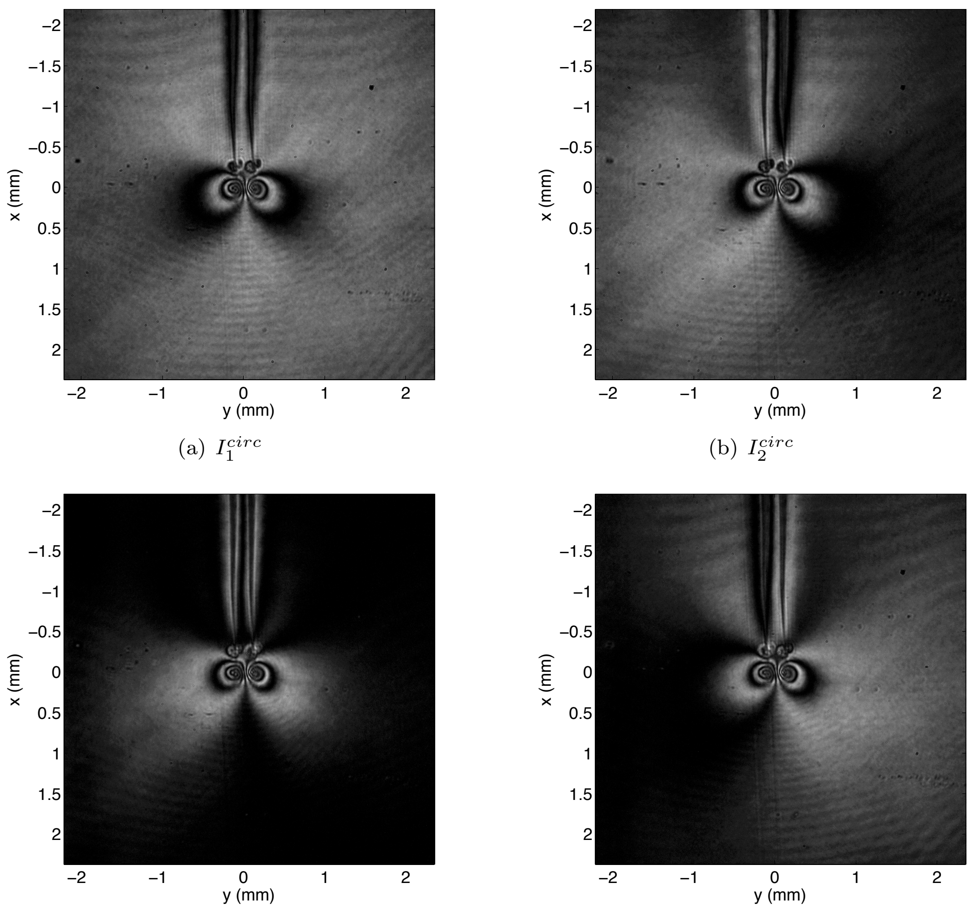

(a) I_1^{circ}

(b) I_2^{circ}

(c) I_3^{circ}

(d) I_4^{circ}

Figure 4.49: Experimental phase-shifted images from horizontal shearing CGS using the $\lambda/4$ polarization method for specimen HomC2 for $K_I = 0.145$ MPa$\sqrt{\text{m}}$ and $K_{II} = 0.63$ kPa$\sqrt{\text{m}}$

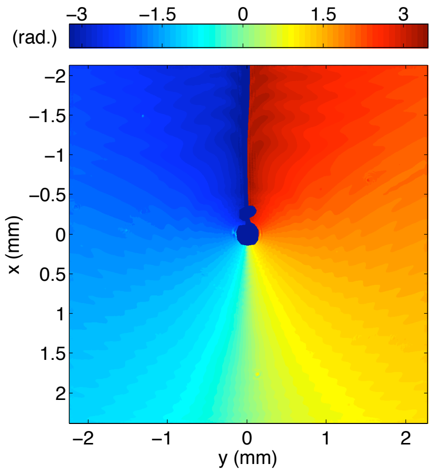

(a) Experimental unwrapped α

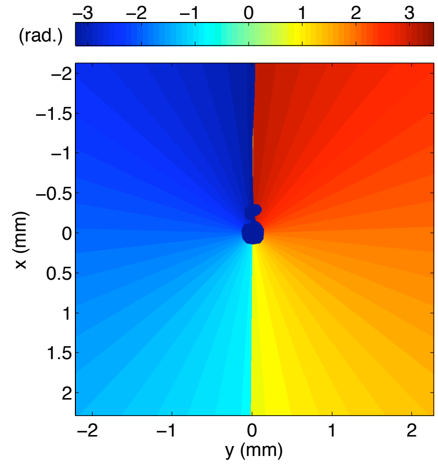

(b) Theoretical unwrapped α

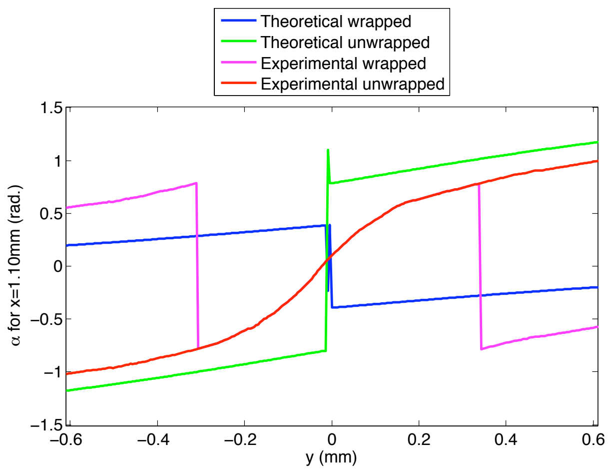

(c) Experimental and theoretical wrapped and unwrapped α

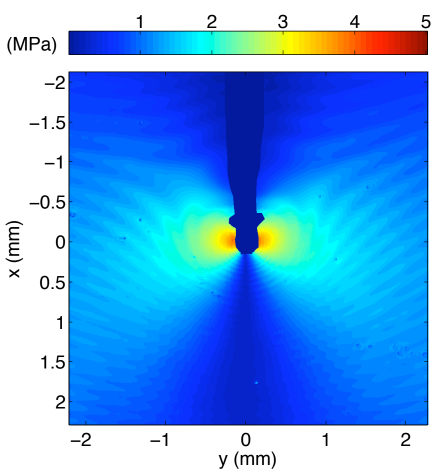

(d) Experimental $\sigma_1 - \sigma_2$

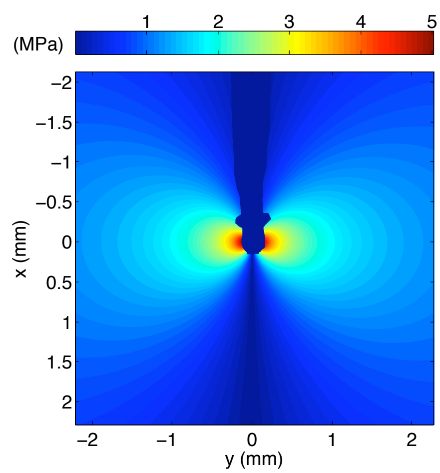

(e) Theoretical $\sigma_1 - \sigma_2$

Figure 4.50: Experimental and theoretical unwrapped isoclinic angle with crack region masked in blue and comparison of experimental and theoretical wrapped and unwrapped α for $x = 1.10$

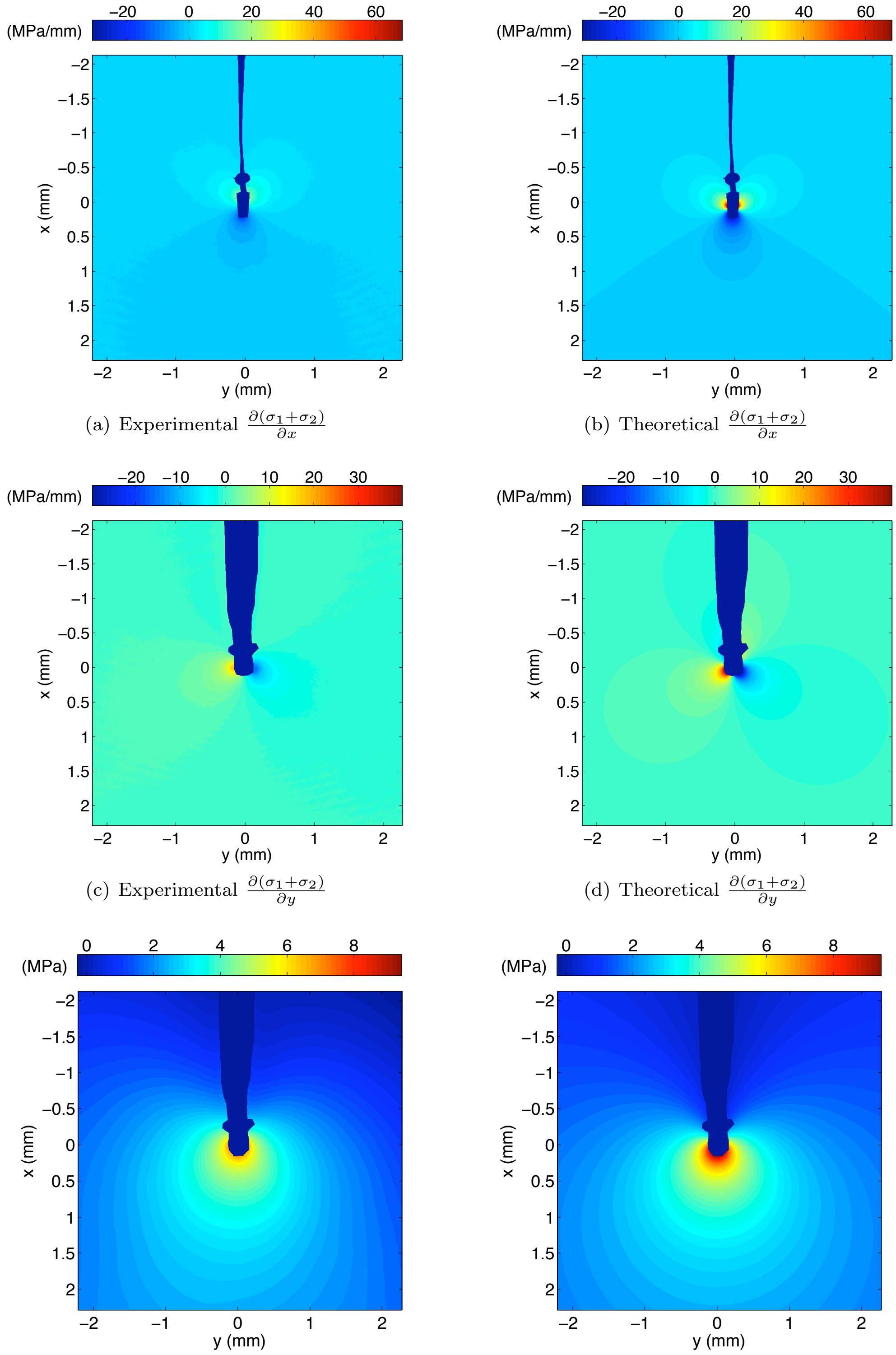

(a) Experimental $\frac{\partial(\sigma_1+\sigma_2)}{\partial x}$

(b) Theoretical $\frac{\partial(\sigma_1+\sigma_2)}{\partial x}$

(c) Experimental $\frac{\partial(\sigma_1+\sigma_2)}{\partial y}$

(d) Theoretical $\frac{\partial(\sigma_1+\sigma_2)}{\partial y}$

(e) Experimental $\sigma_1 + \sigma_2$

(f) Theoretical $\sigma_1 + \sigma_2$

Figure 4.51: Experimental and theoretical data for the derivatives of $\sigma_1 + \sigma_2$ and the experimental integrated $\sigma_1 + \sigma_2$ for specimen HomC2 for $K_I = 0.145$ MPa$\sqrt{\text{m}}$ and $K_{II} = 0.63$ kPa$\sqrt{\text{m}}$ with crack region masked in blue

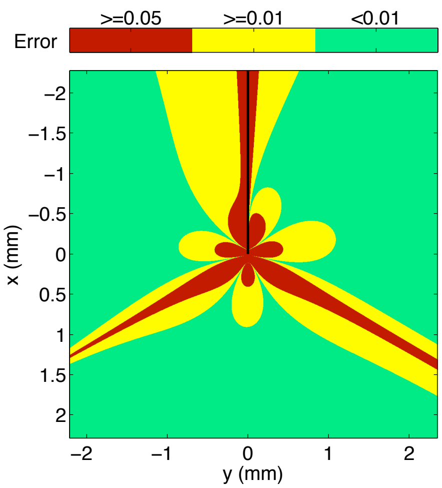

(a) Error for vertical shearing direction

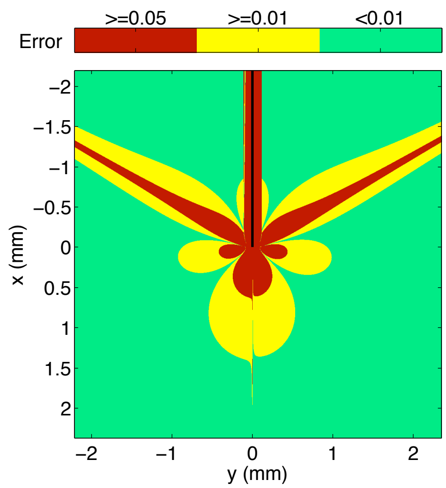

(b) Error for horizontal shearing direction

Figure 4.52: Theoretical error for CGS approximating the derivatives of $K_I = 0.145$ MPa$\sqrt{\text{m}}$ and $K_{II} = 0.63$ kPa$\sqrt{\text{m}}$ for the 4.6 mm $\times$ 4.6 mm field of view and lateral shearing distance of $d_{shear} = 225\ \mu$m [Crack indicated in black]

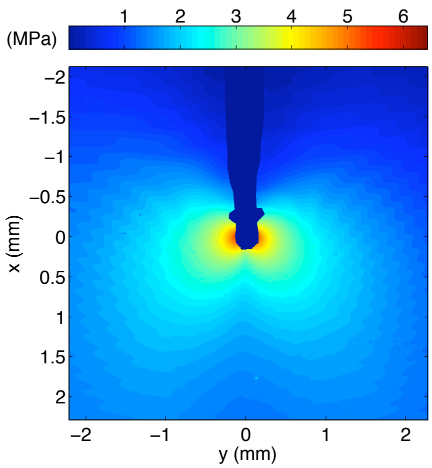

(a) Experimental σ_1

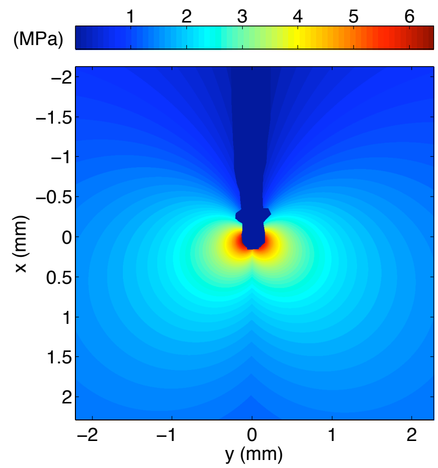

(b) Theoretical σ_1

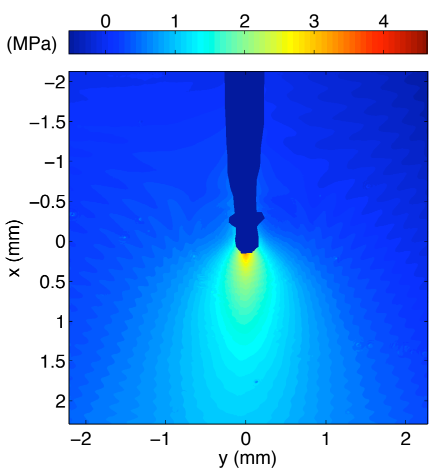

(c) Experimental σ_2

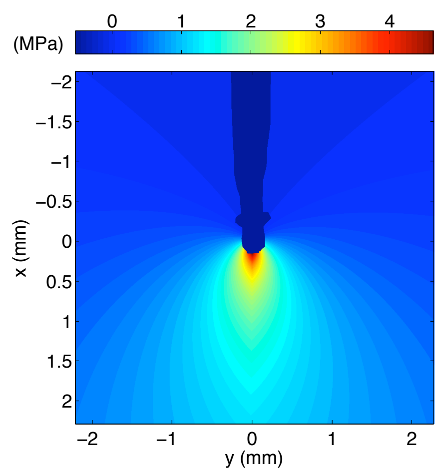

(d) Theoretical σ_2

Figure 4.53: Experimental and theoretical data for the principal stresses for specimen HomC2 for $K_I = 0.145$ MPa$\sqrt{\text{m}}$ and $K_{II} = 0.63$ kPa$\sqrt{\text{m}}$ with crack region masked in blue

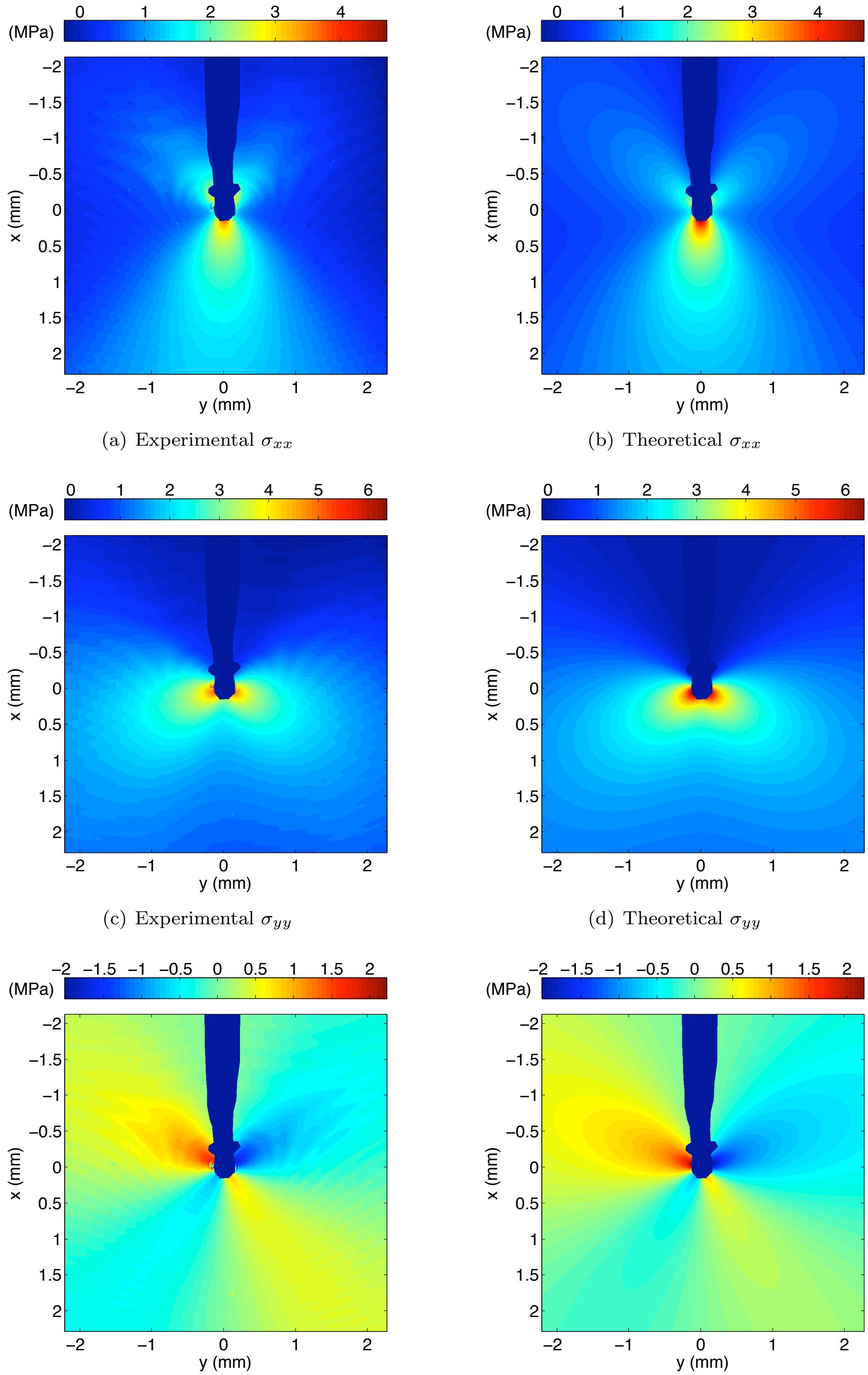

(a) Experimental σ_{xx} (b) Theoretical σ_{xx}

(c) Experimental σ_{yy} (d) Theoretical σ_{yy}

(e) Experimental σ_{xy} (f) Theoretical σ_{xy}

Figure 4.54: Experimental and theoretical data for the Cartesian stresses for specimen HomC2 for $K_I = 0.145$ MPa$\sqrt{\text{m}}$ and $K_{II} = 0.63$ kPa$\sqrt{\text{m}}$ with crack region masked in blue

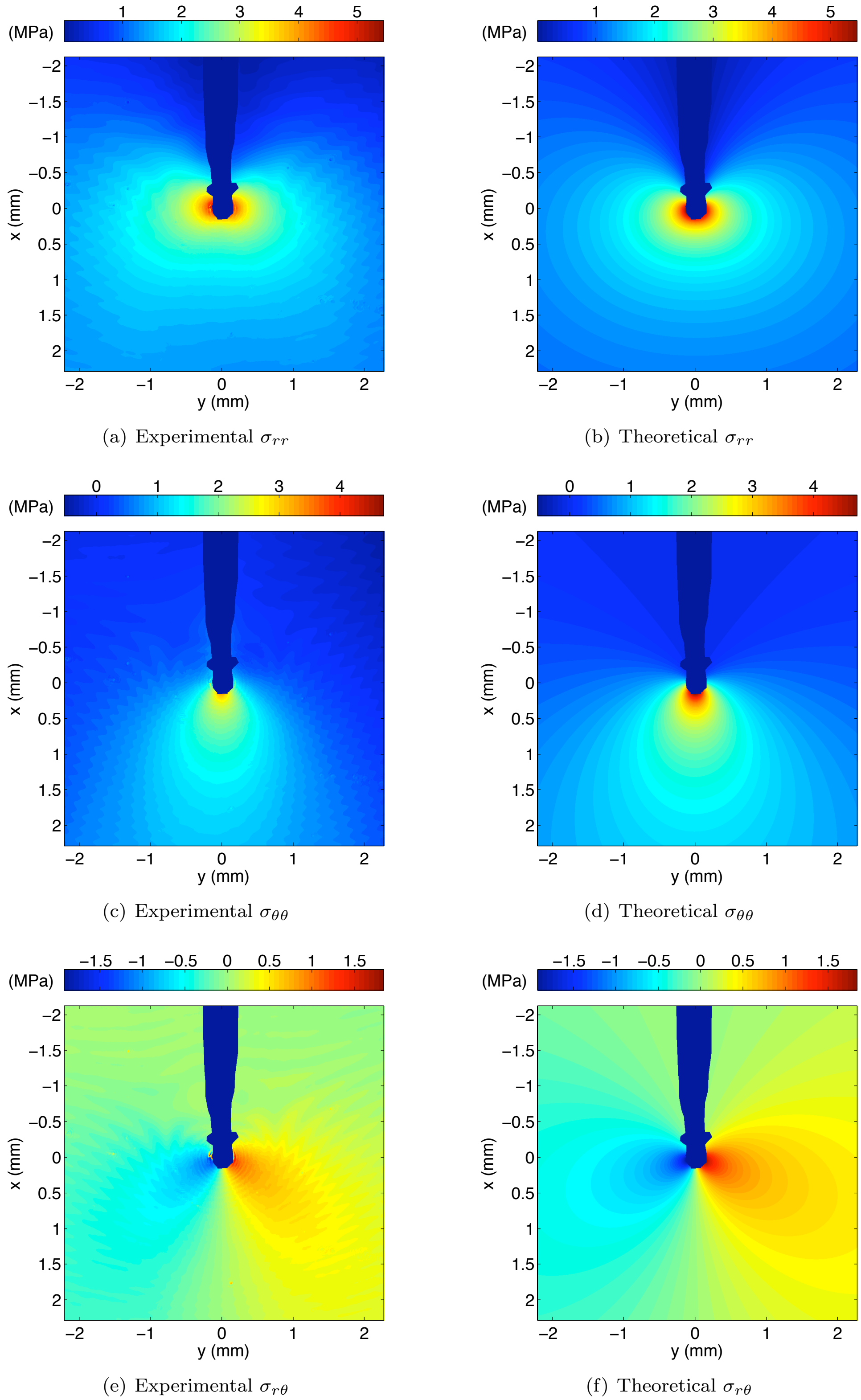

Figure 4.55: Experimental and theoretical data for the polar stresses for specimen HomC2 for $K_I = 0.145$ MPa$\sqrt{\text{m}}$ and $K_{II} = 0.63$ kPa$\sqrt{\text{m}}$ with crack region masked in blue

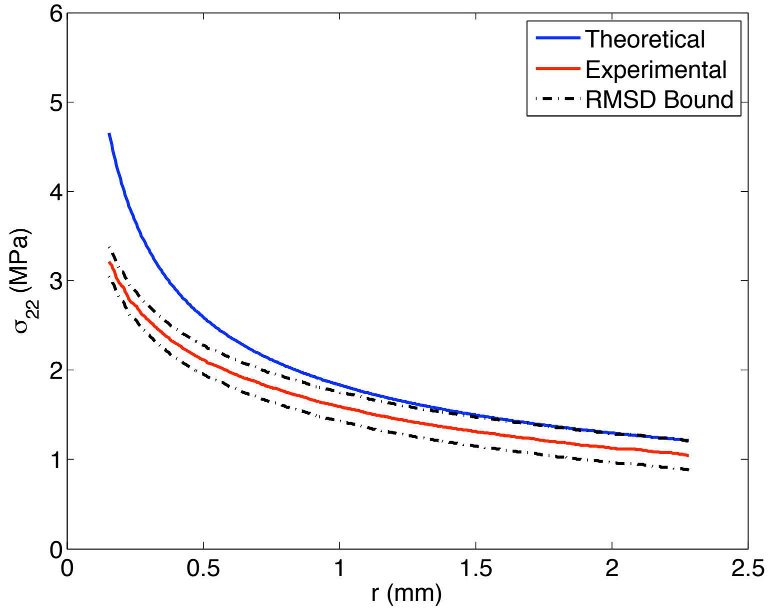

(a) σ_{yy} vs. r for $\theta = 0$

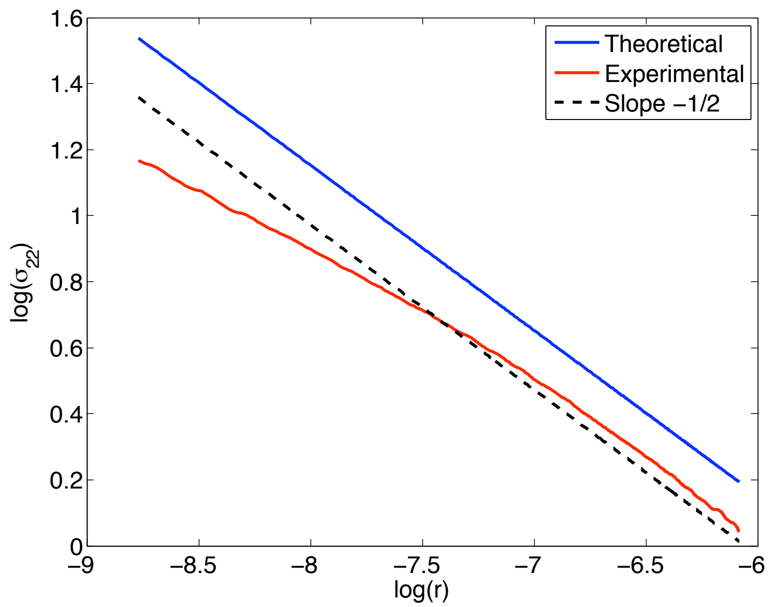

(b) $\log(\sigma_{yy})$ vs. $\log(r)$ for $\theta = 0$

Figure 4.56: Experimental and theoretical data for σ_{yy} along $\theta = 0$ for specimen HomC2 for $K_I = 0.145$ MPa$\sqrt{\text{m}}$ and $K_{II} = 0.63$ kPa$\sqrt{\text{m}}$: The experimental data is slightly lower than the theoretical data, but with similar $r^{-1/2}$ dependence seen by the near $-1/2$ slope on the log-log plot of σ_{yy} versus r.

4.2.7 Crack with $K_I = 0.289$ MPa$\sqrt{\text{m}}$ and $K_{II} = -2.9$ kPa$\sqrt{\text{m}}$

For this larger wedge displacement case in specimen HomC2, the experimental stress intensity factors are $K_I = 0.289$ MPa$\sqrt{\text{m}}$ and $K_{II} = -2.9$ kPa$\sqrt{\text{m}}$ with a mode-mixity ratio $\mu_{SIF} = -0.010$; thus this example has a similar moderate-level K_I as the $K_I = 0.259$ MPa$\sqrt{\text{m}}$ case for specimen HomC1, but with smaller magnitude, negative mode-mixity. The experimental parameters are the same for this load case as in the previous case.

Figures 4.57–4.59 present the photoelasticity and the vertical and horizontal shear CGS images. Since this specimen is thicker than HomC1, the fringes are closer in density to the $K_I = 0.514$ MPa$\sqrt{\text{m}}$ case than the $K_I = 0.259$ MPa$\sqrt{\text{m}}$ case. The small blur due to notch tip on the surface is still present in the images, but again do not appear to distort the field, and therefore a mask is sufficient to remove its influence. The weak Fizeau interference patterns in the photoelastic images are minimized used the Wiener filter with window size of $[25 \times 25]$ pixels before processing the data. Table 4.4 reports the RMSD values, data ranges, and NRMSD values for this $K_I = 0.289$ MPa$\sqrt{\text{m}}$ case. The NRMSD values are good for all of the fields ranging from 0.0019 to 0.063, with the highest value for σ_{xx}, which is still quite acceptable.

The isoclinic angle in Figure 4.60(a) for the $K_I = 0.289$ MPa$\sqrt{\text{m}}$ has the same form as the other cases, with (i) the radial symmetry about the crack tip, (ii) the NRMSD of 0.033, (iii) higher local errors where the wrapped α was manually corrected near the crack tip, (iv) the error of smoothing the data through 0 around $\theta = 0$, and (v) otherwise generally good comparison with theory. The theoretical isoclinic angle in this case slightly differs from those of the other cases near $\theta = 0$ due to the negative mode-mixity, as seen in Figure 4.60(c). The experimental and theoretical $\sigma_1 - \sigma_2$ fields in Figures 4.60(d) and 4.60(e) have generally good agreement with NRMSD of 0.048, except the stress concentrations at the crack tip are not as large in the experimental field, and the experimental stresses do not go towards zero near $\theta = 0$ as in the theoretical field.

The experimental and theoretical derivatives of $\sigma_1 + \sigma_2$ in Figure 4.61 compare very well globally. The experimental x derivative of $\sigma_1 + \sigma_2$ has the correct shape and stress concentration for the range of -20 MPa/mm to 20 MPa/mm, leading to an NRMSD of only 0.021, but does not quite obtain

Quantity	Units	RMSD (in Units)	Data Range (in Units)	NRMSD (No Units)
α	rad.	0.22	6.71	0.033
$\partial(\sigma_1 + \sigma_2)/\partial x$ from $\lambda/4$ plate method	MPa/mm	1.04	48.6	0.021
$\partial(\sigma_1 + \sigma_2)/\partial y$ from $\lambda/4$ plate method	MPa/mm	0.89	47.5	0.019
$\sigma_1 + \sigma_2$	MPa	0.71	12.5	0.056
$\sigma_1 - \sigma_2$	MPa	0.32	6.67	0.048
σ_1	MPa	0.41	9.05	0.046
σ_2	MPa	0.33	5.86	0.055
σ_{xx}	MPa	0.41	6.49	0.063
σ_{yy}	MPa	0.40	9.27	0.043
σ_{xy}	MPa	0.25	6.14	0.040
σ_{rr}	MPa	0.46	7.74	0.059
$\sigma_{\theta\theta}$	MPa	0.40	7.70	0.052
$\sigma_{r\theta}$	MPa	0.17	6.25	0.026

Table 4.4: Error analysis for various experimental fields for specimen HomC2 for $K_I = 0.289$ MPa$\sqrt{\text{m}}$ and $K_{II} = -2.9$ kPa$\sqrt{\text{m}}$

the localized higher stress concentration just behind the crack tip. The experimental y derivative of $\sigma_1 + \sigma_2$ does a good job of reaching close to the stress concentration at the sides of the crack tip, allowing for a good NRMSD of 0.019, though the derivative is a little small behind the crack tip. These smaller experimental derivatives behind the crack tip lead to an experimental $\sigma_1 + \sigma_2$ in Figure 4.61(e) that does not decrease enough towards zero along the crack as compared to the theoretical field in Figure 4.61(f). Elsewhere in the field, $\sigma_1 + \sigma_2$ matches theory well with a good stress concentration level at the crack tip. These experimental derivative fields appear to compare well because the CGS phase inherently better approximates the theoretical derivatives due to the smaller mode-mixity $\mu_{SIF} = -0.010$, evident in the lower ϵ error globally for the CGS fields in Figure 4.62. The errors in both shearing directions, but particularly in the vertical shearing direction, are markedly lower than for the highest mode-mixity case $\mu_{SIF} = 0.020$ that has a similar $K_I = 0.259$ MPa$\sqrt{\text{m}}$, implying that for modest mode-mixity cases employing CGS, the shearing direction related to the y derivative will most likely better represent a derivative than the other shearing direction. This observation is restricted to these low mode-mixity cases because this may not be true for larger mode-mixity, as seen in a mixed-mode fracture study by Mason et al. (1992) that demonstrated reasonable K_{II}/K_I calculation agreement with theory and finite elements.

The experimental and theoretical principal stresses in Figure 4.63 compare well in front of and close to the crack, but the experimental σ_2 is too large for $(-x, -y)$ data points due to the errors in $\sigma_1 + \sigma_2$ in that region, leading to the largest NRMSD for this case at 0.056. The Cartesian stresses in Figure 4.64 all exhibit the correct behavior and stress levels globally. The higher stress levels in the fish-shaped σ_{xx} extends further from the crack than predicted. The manually corrected regions near the crack tip in α appear to spread the side lobes located along the y axis in σ_{xy}, and the stresses seem higher in magnitude in the $+x$ region. The σ_{yy} field agrees well visually except for $(-x, -y)$ data points along the crack. The polar stresses in Figure 4.65 have similar NRMSD values as the Cartesian stresses, but appear to have more local errors. These visual differences are due to the manually corrected regions in α that slightly distort the radial symmetry of the theoretical α. Regardless of local errors, the experimental and theoretical polar stresses match well globally.

The σ_{yy} versus r line plots for $\theta = 0$ in Figure 4.66 indicate reasonable agreement in behavior with theory for $r < 1.5$ mm. The $1/\sqrt{r}$ behavior is excellent for $r < 1.5$ mm, but the slope of $\log \sigma_{yy}$ versus $\log r$ slightly increases for $r > 1.5$ mm. This is most likely due to experimental error since this is the opposite behavior from the smaller load case for the same specimen, but may be due to the finite size of the specimen; far from the crack, the stress field is not K-dominant due to boundary effects of a finite size specimen. The loss of K dominance far from the crack is usually indicated by a decrease (in magnitude) in the slope of the $\log \sigma_{yy}$ versus $\log r$ plot for $\theta = 0$, which is not the case here; thus, the errors in $\sigma_1 - \sigma_2$ and α are the likely error sources for σ_{yy}, since $\sigma_1 - \sigma_2$ is larger than predicted here. Given the reasonable agreement with $1/\sqrt{r}$ behavior of this case, the stress fields are likely in a K-dominant region of the crack. This case demonstrates the experimental method to determine full-field stresses for a moderate K_I with low mode-mixity. The same error sources appear in this case as with others, but these are well-characterized and possibly can be minimized with some improvements. This case does not appear to show any new errors, but does add to the range of capability of this experimental method.

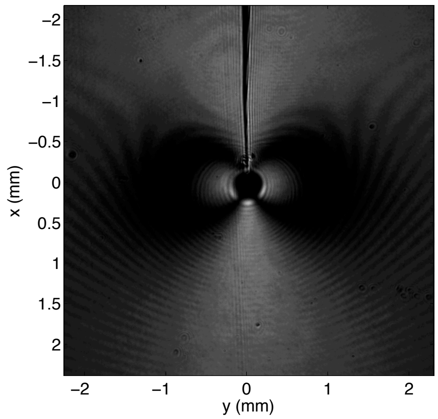

(a) $I_1 = I_o(1 + \cos(\delta))$

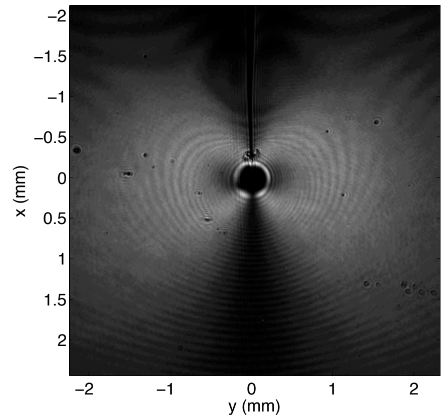

(b) $I_2 = I_o(1 - \cos(\delta))$

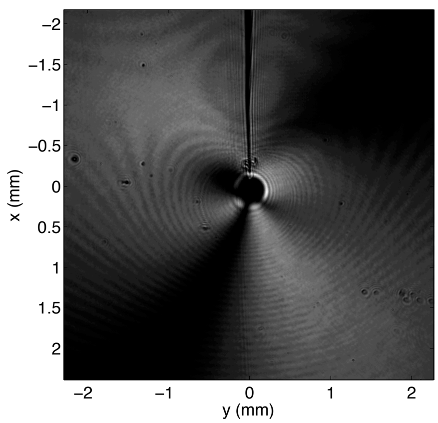

(c) $I_3 = I_o(1 - \sin(\delta)\sin(2\alpha))$

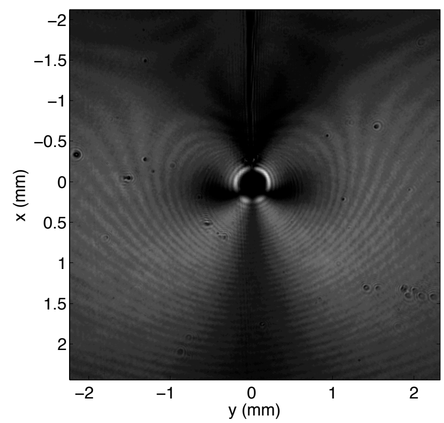

(d) $I_4 = I_o(1 + \sin(\delta)\cos(2\alpha))$

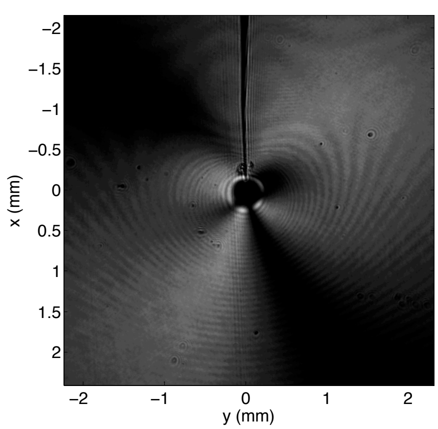

(e) $I_5 = I_o(1 + \sin(\delta)\sin(2\alpha))$

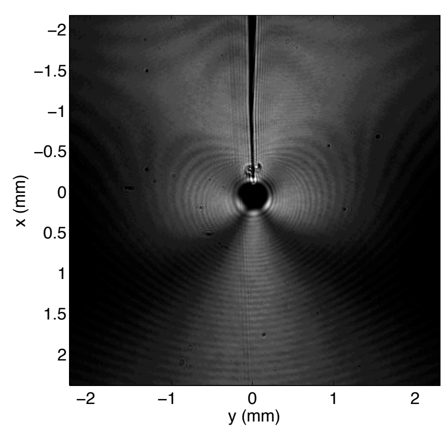

(f) $I_6 = I_o(1 - \sin(\delta)\cos(2\alpha))$

Figure 4.57: Experimental mages from six-step phase-shifting photoelasticity for specimen HomC2 for $K_I = 0.289$ MPa$\sqrt{\text{m}}$ and $K_{II} = -2.9$ kPa$\sqrt{\text{m}}$. Caustic shadows obscure the data at the crack tip due to the stress concentration, and the weak high density fringes overlaying the photoelastic fringes are due to the interference of the reflections from the front and back faces of the specimen

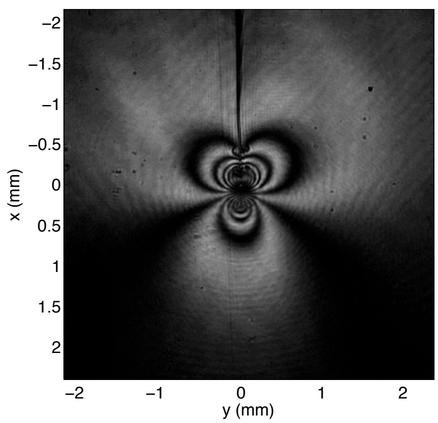

(a) I_1^{circ}

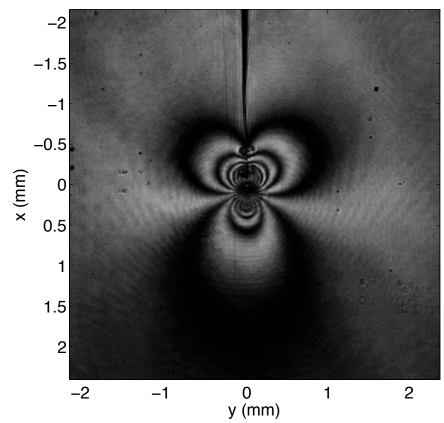

(b) I_2^{circ}

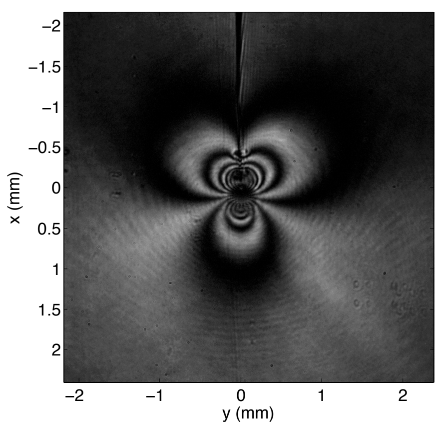

(c) I_3^{circ}

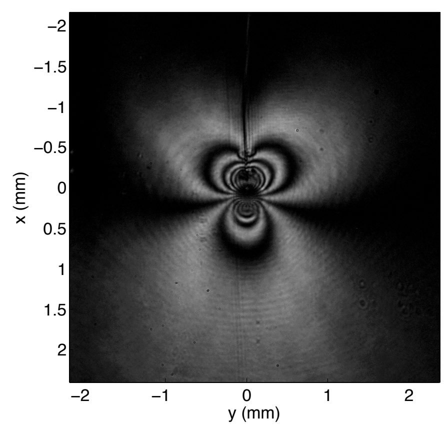

(d) I_4^{circ}

Figure 4.58: Experimental phase-shifted images from vertical shearing CGS using the $\lambda/4$ polarization method for specimen HomC2 for $K_I = 0.289$ MPa$\sqrt{\text{m}}$ and $K_{II} = -2.9$ kPa$\sqrt{\text{m}}$

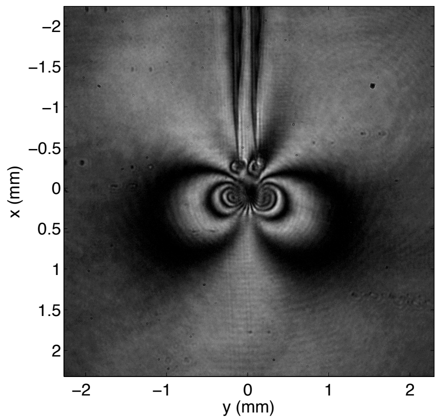

(a) I_1^{circ}

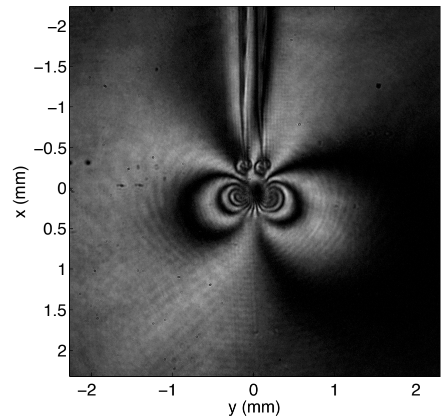

(b) I_2^{circ}

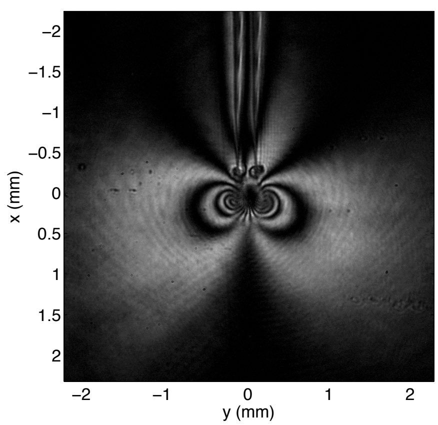

(c) I_3^{circ}

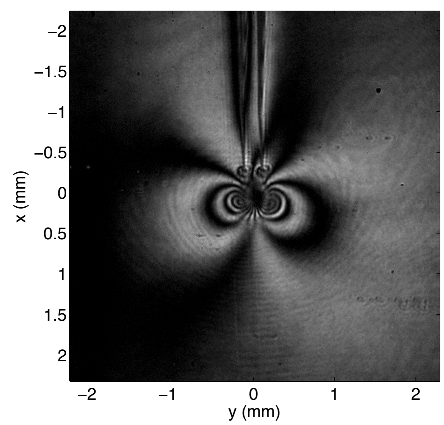

(d) I_4^{circ}

Figure 4.59: Experimental phase-shifted images from horizontal shearing CGS using the $\lambda/4$ polarization method for specimen HomC2 for $K_I = 0.289$ MPa$\sqrt{\text{m}}$ and $K_{II} = -2.9$ kPa$\sqrt{\text{m}}$

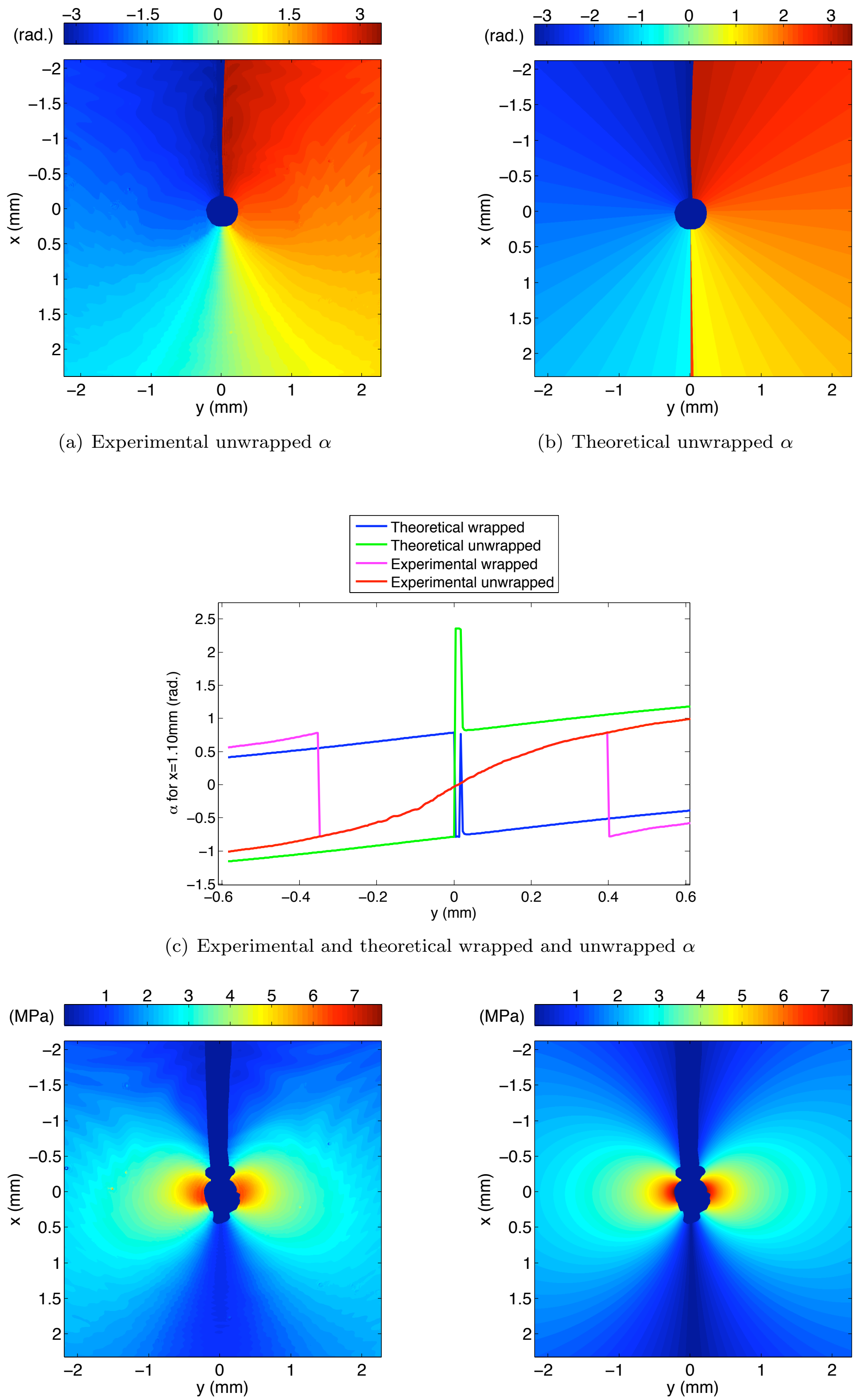

(a) Experimental unwrapped α

(b) Theoretical unwrapped α

(c) Experimental and theoretical wrapped and unwrapped α

(d) Experimental $\sigma_1 - \sigma_2$

(e) Theoretical $\sigma_1 - \sigma_2$

Figure 4.60: Experimental and theoretical unwrapped isoclinic angle with crack region masked in blue and comparison of experimental and theoretical wrapped and unwrapped α for $x = 1.10$

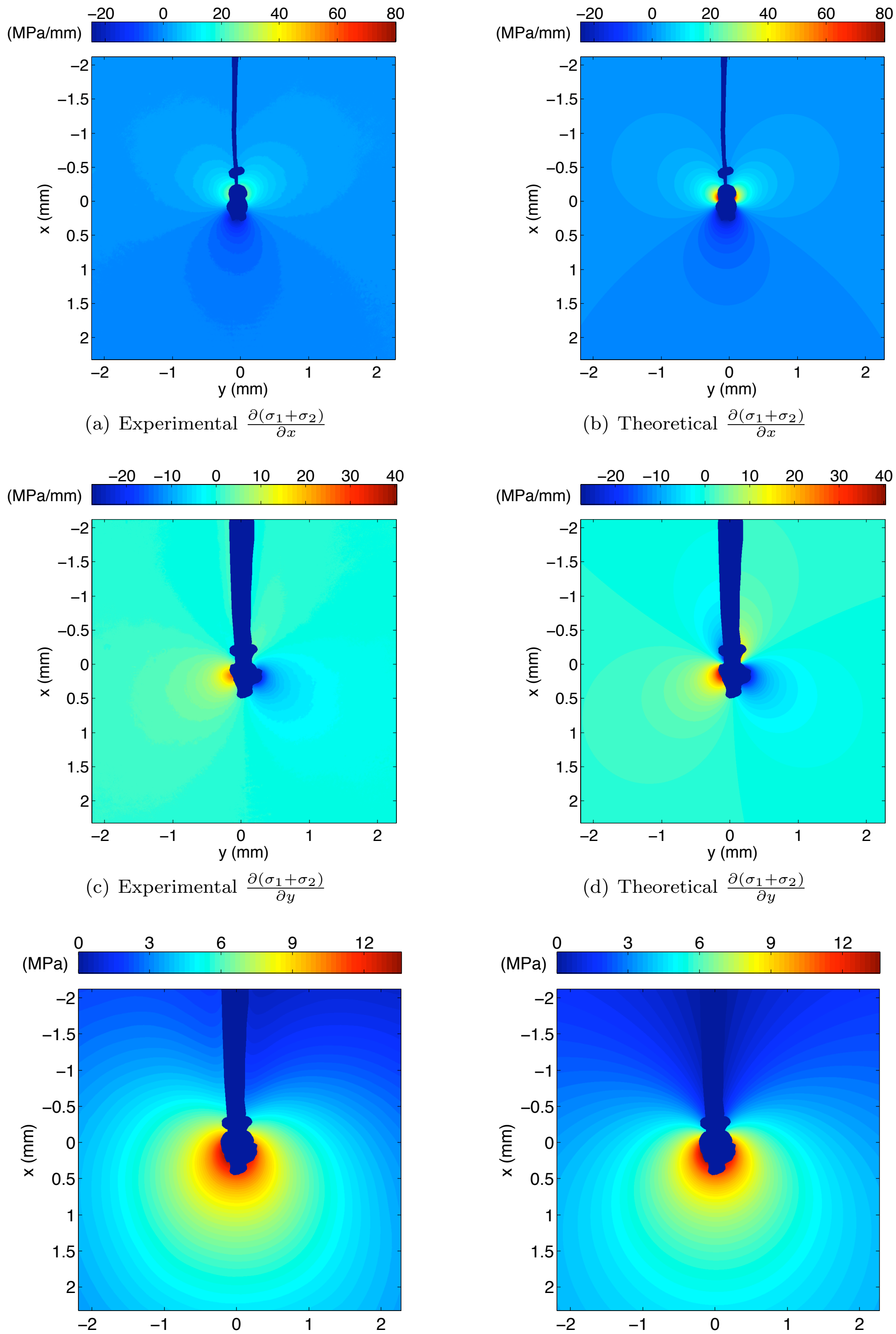

(a) Experimental $\frac{\partial(\sigma_1+\sigma_2)}{\partial x}$

(b) Theoretical $\frac{\partial(\sigma_1+\sigma_2)}{\partial x}$

(c) Experimental $\frac{\partial(\sigma_1+\sigma_2)}{\partial y}$

(d) Theoretical $\frac{\partial(\sigma_1+\sigma_2)}{\partial y}$

(e) Experimental $\sigma_1 + \sigma_2$

(f) Theoretical $\sigma_1 + \sigma_2$

Figure 4.61: Experimental and theoretical data for the derivatives of $\sigma_1 + \sigma_2$ and the experimental integrated $\sigma_1 + \sigma_2$ for specimen HomC2 for $K_I = 0.289$ MPa$\sqrt{\text{m}}$ and $K_{II} = -2.9$ kPa$\sqrt{\text{m}}$ with crack region masked in blue

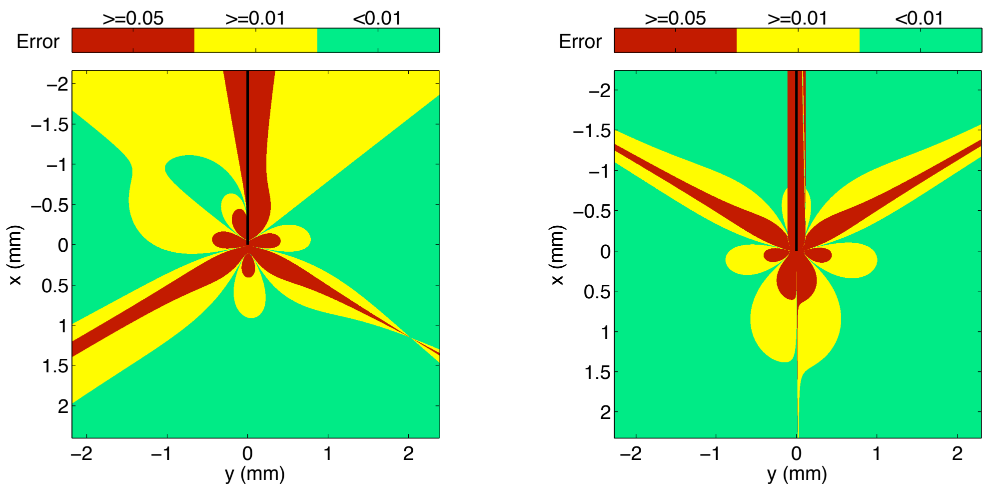

(a) Error for vertical shearing direction

(b) Error for horizontal shearing direction

Figure 4.62: Theoretical error for CGS approximating the derivatives of $K_I = 0.289$ MPa$\sqrt{\text{m}}$ and $K_{II} = -2.9$ kPa$\sqrt{\text{m}}$ for the 4.6 mm $\times$ 4.6 mm field of view and lateral shearing distance of $d_{shear} = 225$ μm [Crack indicated in black]

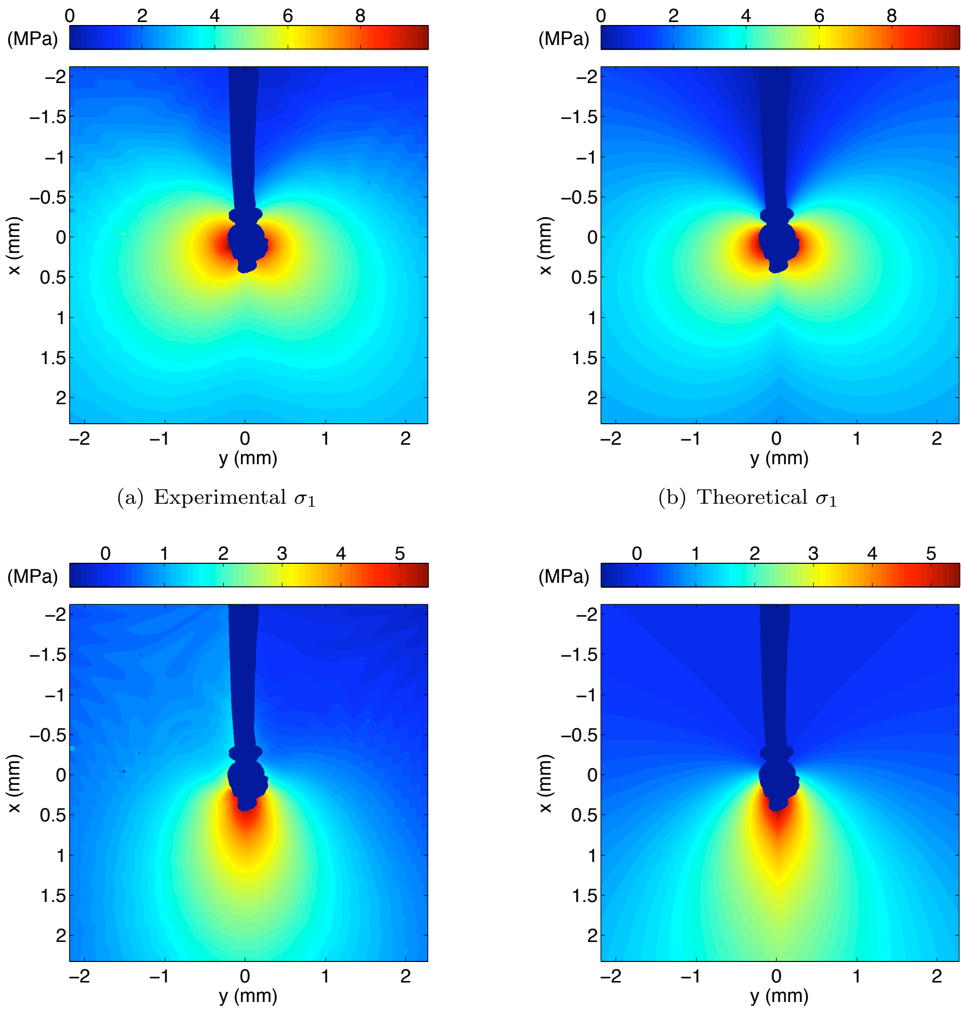

(a) Experimental σ_1 (b) Theoretical σ_1

(c) Experimental σ_2 (d) Theoretical σ_2

Figure 4.63: Experimental and theoretical data for the principal stresses for specimen HomC2 for $K_I = 0.289$ MPa$\sqrt{\text{m}}$ and $K_{II} = -2.9$ kPa$\sqrt{\text{m}}$ with crack region masked in blue

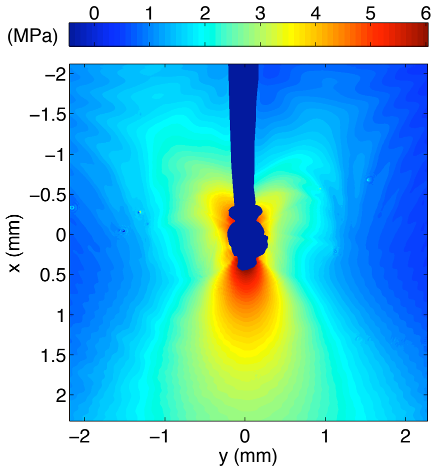

(a) Experimental σ_{xx}

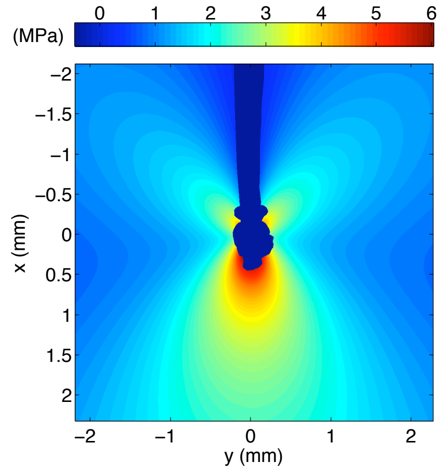

(b) Theoretical σ_{xx}

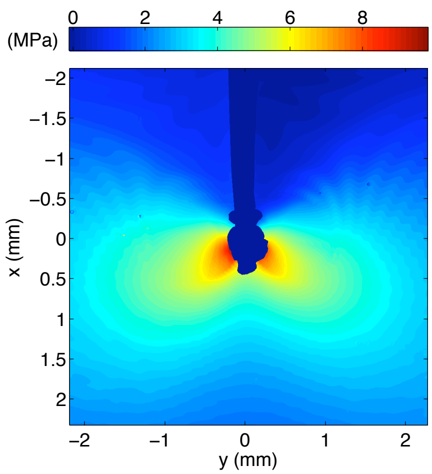

(c) Experimental σ_{yy}

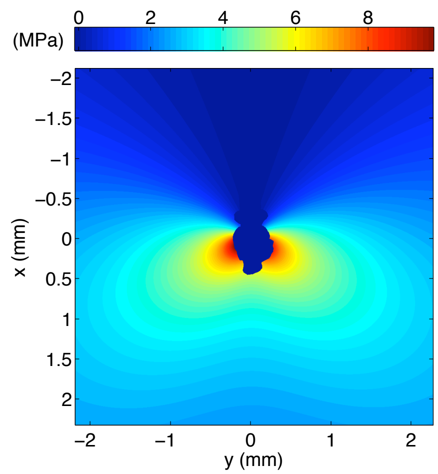

(d) Theoretical σ_{yy}

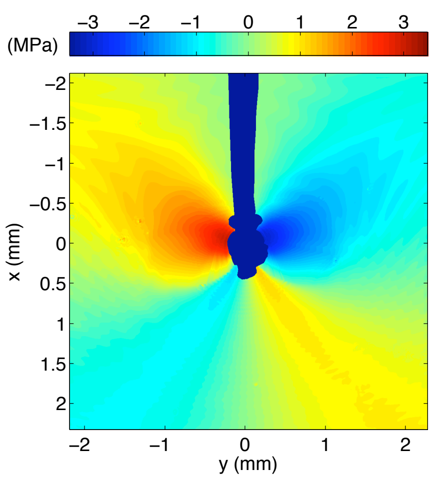

(e) Experimental σ_{xy}

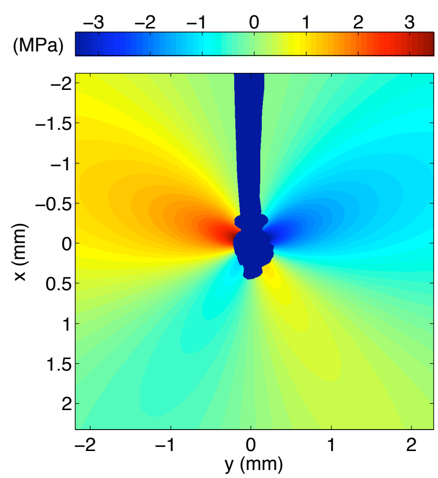

(f) Theoretical σ_{xy}

Figure 4.64: Experimental and theoretical data for the Cartesian stresses for specimen HomC2 for $K_I = 0.289$ MPa$\sqrt{\text{m}}$ and $K_{II} = -2.9$ kPa$\sqrt{\text{m}}$ with crack region masked in blue

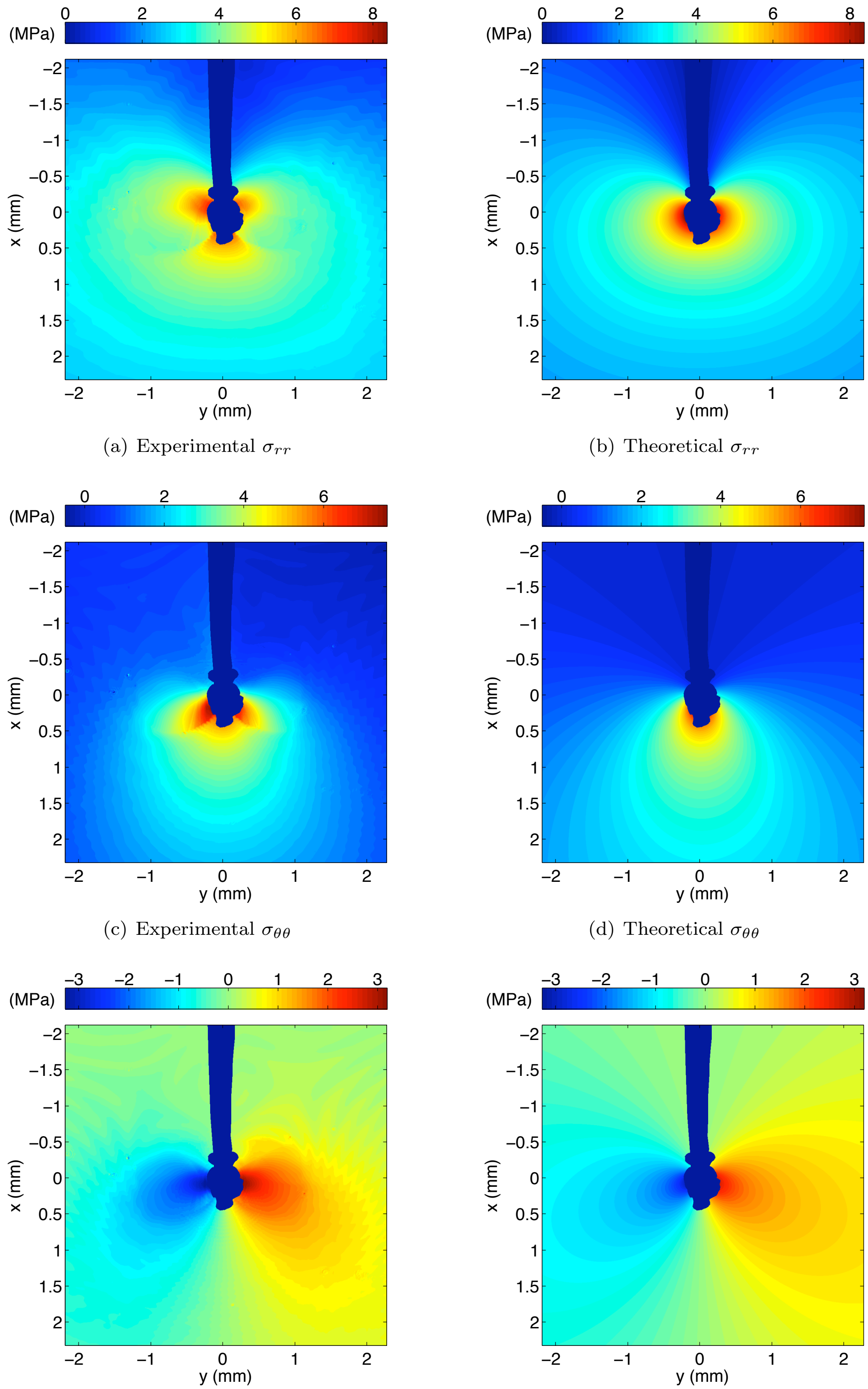

(a) Experimental σ_{rr} (b) Theoretical σ_{rr}

(c) Experimental $\sigma_{\theta\theta}$ (d) Theoretical $\sigma_{\theta\theta}$

(e) Experimental $\sigma_{r\theta}$ (f) Theoretical $\sigma_{r\theta}$

Figure 4.65: Experimental and theoretical data for the polar stresses for specimen HomC2 for $K_I = 0.289$ MPa$\sqrt{\text{m}}$ and $K_{II} = -2.9$ kPa$\sqrt{\text{m}}$ with crack region masked in blue

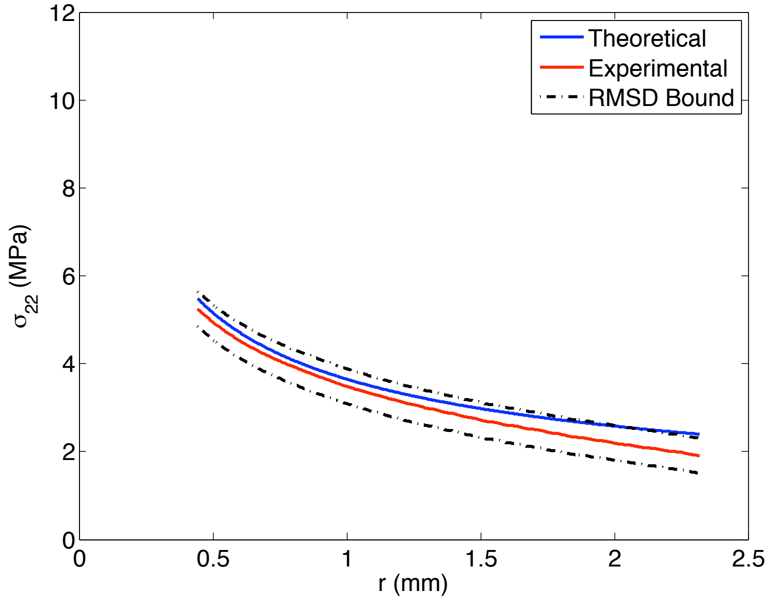

(a) σ_{yy} vs. r for $\theta = 0$

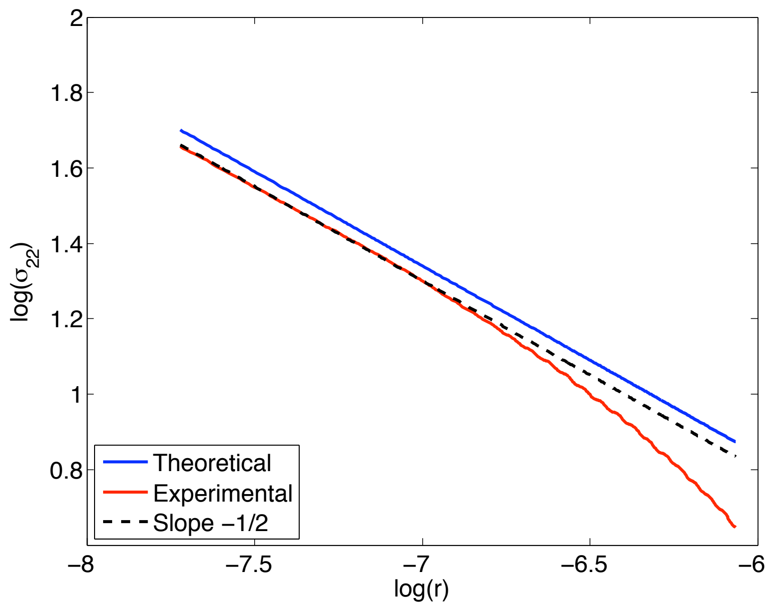

(b) $\log(\sigma_{yy})$ vs. $\log(r)$ for $\theta = 0$

Figure 4.66: Experimental and theoretical data for σ_{yy} along $\theta = 0$ for specimen HomC2 for $K_I = 0.289\ \mathrm{MPa}\sqrt{\mathrm{m}}$ and $K_{II} = -2.9\ \mathrm{kPa}\sqrt{\mathrm{m}}$: The experimental data is slightly lower than the theoretical data, but with similar $r^{-1/2}$ dependence seen by the near $-1/2$ slope on the log-log plot of σ_{yy} versus r.

4.3 Discussion of Experimental Method for Fracture Studies

The four Mode I–dominant, mixed-mode crack cases presented above demonstrate the ability of the hybrid experimental method to determine the in-plane tensorial stress around a crack in a photoelastic material. The full analysis of the highest K_I case establishes the validity of the experimental method to determine stress near a crack close to initial crack propagation, with the others demonstrating good quality data in a variety of cases. The different cases represent a significant range of K_I values for Homalite-100, whose fracture toughness is around 0.445 MPa$\sqrt{\mathrm{m}}$ to 0.636 MPa$\sqrt{\mathrm{m}}$ (Bradley and Kobayashi, 1971; Irwin et al., 1979; Dally, 1979): $K_I = 0.145$ MPa$\sqrt{\mathrm{m}}$, $K_I = 0.259$ MPa$\sqrt{\mathrm{m}}$, $K_I = 0.289$ MPa$\sqrt{\mathrm{m}}$, and $K_I = 0.514$ MPa$\sqrt{\mathrm{m}}$, which are from about $0.25K_{Ic}$ to $\sim K_{Ic}$. Each of these cases demonstrate K-dominant stress behavior, allowing for excellent comparison to the 2D asymptotic crack solution for a mixed-mode crack. This K dominance allows for calculation of the Mode I and Mode II stress intensity factors from a nonlinear least-squares fitting algorithm, excluding data points in the masked regions along the crack and a circle of radius $0.5h$ around the crack tip to remove points that may have 3D stress effects. Even though the K_I and K_{II} values come from full-field data from two different experimental techniques, these values lead to theoretical data that compare well with all of the experimental data, implying that CGS and photoelasticity are compatible for use in this hybrid method. If the K_I and K_{II} values only allowed for good agreement in a few fields, then the experimental method would be suspect. Across all of these cases, the NRMSD ranges from 0.012 to 0.078 with most of the fields below 0.05, indicating excellent global error for all of these cases. This experimental method also allows for determination of not only K_I values, but small K_{II} values as well, and therefore is able to detect small mode-mixity μ_{SIF} from -0.010 to 0.020. These small mode-mixities have a noticeable affect on the stress fields, giving rise to asymmetries in the stress fields that are apparent in the experimental data. Exclusion of K_{II} would lead to larger errors in the data by a few percent.

The four cases illuminate consistent error sources in the data. The rotational misalignment of the polarization optics, particularly the first $\lambda/4$ plate, lead to false discontinuities and zero-crossings that require manual correction. These corrections generally work, allowing for the determination of the isoclinic angle without detrimental and completely incorrect unwrapping. The isoclinic angle is a key component to the experimental method, so the manual corrections to the wrapped α field enable the method to work even with some localized errors in the subsequent stress fields. Obviously, a robust algorithm for correcting these errors due to polarization optic misalignment would improve confidence in the method, especially for fracture studies where the theoretical stress field solution is not known. In the cases presented in this chapter, the experimental isoclinic angle has error along the crack plane because the polarization optic misalignment leads to discontinuities near $\theta = 0$ that appear to be real discontinuities. Corrections here would not be simple and would require a variety of experiences with this method; hence, leaving the discontinuities as they are leads to α fields with known error sources, but with acceptable error levels. One way to reduce this need for corrections in the first place is to introduce strict polarization optic alignment techniques. Another error source in the data is the Fizeau fringes, but these are easily removed with anti-reflective coatings on the specimen.

The CGS assumption that the phase is related to a stress derivative is pushed to its limit due to three factors in this study: the small field of view, the finite shearing distance, and small mode-mixity. The first two factors work together to push the limit of the derivative assumption in that having a small field of view and requiring a reasonable phase sensitivity over a wide range of K_I cases requires a shearing distance that is a significant size relative to the field of view like the 5% of the side of the field of view in the cases presented above. Evident in the ϵ error analysis in Section 4.2.4.3, larger shearing distance produces more error in the derivative assumption over more area of the field of view. Also, the addition of a small K_{II} component appears to increase the ϵ error, particularly behind the crack for the shearing direction related to the x derivative, as the mode-mixity increases for the range of mode-mixity in this study. The effect of this on the stress fields is higher error behind the crack, seen with increasing severity with increasing mode-mixity. A full error analysis of the effect of mode-mixity on CGS derivative measurements is required if this method is applied to mixed-mode fracture cases. Characterization of these error sources explains the differences between experiment and theory in the cases presented here, but should not detract from the overall ability of this experimental method to determine full-field stresses around cracks in a photoelastic material. The experimental data have remarkable agreement with theory and allow for calculation of a range of stress intensity factors for Mode I–dominant cracks.

4.4 Conclusions

The hybrid CGS-photoelasticity experimental method is demonstrated for in-plane tensorial stress determination around Mode I–dominant cracks in Homalite-100 for a range of stress intensity factors for small fields of view, the first experimental study for full-field tensorial stress determination around cracks in photoelastic materials. Four cases across a range of $K_I = 0.145$ MPa$\sqrt{\text{m}}$ to $K_I = 0.514$ MPa$\sqrt{\text{m}}$, which is near the fracture toughness of Homalite-100, show K-dominant behavior, allowing for excellent comparison of the experimental stress fields with the 2D asymptotic crack solution for mixed-mode loading; the global error is less than 5% for most fields and no greater than 7.8%. The experimental method allows for calculation of K_I and small K_{II} values based on experimental data derived from both CGS and photoelasticity, showing that the two techniques work well together for stress determination. Common error sources over all four cases are characterized and can be mitigated with careful experimentation and with improved analysis algorithms. Overall, this experimental method successfully demonstrates the goal of stress determination near cracks in optically anisotropic, but otherwise isotropic materials, which lays the foundation for extending this method to studying stresses around cracks in anisotropic materials like crystals.

Chapter 5

Future Research

5.1 Introduction

This chapter describes future research that can improve the current hybrid method and extend it to fracture studies in anisotropic crystals. Section 5.2 details improvements to the current method that can reduce the error sources from the optics, from the analysis method, and from some basic CGS assumptions. Section 5.3 describes the practical requirements for extending this method to anisotropic crystals and demonstrates the need for further analysis by a preliminary investigation of using the current hybrid method for stresses in a ferroelectric crystal, barium titanate.

5.2 Improvements to Experimental Method

5.2.1 Optics

The rotational misalignments of the polarization optics have a significant impact on both the CGS and photoelasticity data, as described in Chapter 3. Simple alignment methods can be implemented to reduce the errors, where the user does not rely on an axis labeled on each individual optic as the reference, but relies on one optic as the reference optic to base all of the alignment. The objective is to set the axes of these optics such that transmitted light is extinguished when the optics are properly aligned. Either a CCD or a photodiode may be used to monitor the transmitted light. Firstly, the first polarizer alignment must be fixed as the reference axis for the other optics. Ideally, this first polarizer is also aligned with the coordinates of the specimen, which may be achieved by assuring that light is extinguished for a polarized crystal at the specimen plane with the first polarizer at $\pi/2$ radians from the polarization of the crystal. Secondly, the second polarizer alignment is set to $\pi/2$ radians from the first polarizer to extinguish transmitted light. Thirdly, the $\lambda/4$ plates, when between the two crossed polarizers, should have light extinction when aligned with either of the two polarization optics. Fourthly, a loaded test specimen should be used to test the alignment for both photoelasticity and CGS by checking for the phase modulation errors in the wrapped φ_{sum} for CGS and in the wrapped α for photoelasticity. Small alignment adjustments can be made before a full experiment is conducted, which can especially reduce the errors in the isoclinic angle. In the proof of concept studies for the polycarbonate and Homalite-100 specimens presented in this thesis, the first three steps were taken for alignment, but not the fourth step, which can correct for the last degree or two of misalignment. A small $\pi/90$ radians misalignment in just the first $\lambda/4$ plate, such as those modeled in Sections 3.3.2.2, 3.3.2.3, and 4.2.4.2, can lead to significant errors (if not corrected). This systematic alignment should minimize phase modulation in both techniques.

If a non-polarizing beamsplitter is used for this experimental method, purchasing one with $T_x = T_y$ and $R_x = R_y$ coefficients eliminates the errors for the data. If this is not possible or prohibitively expensive, obtaining these coefficients from the manufacturer will help to at least quantify the error. These coefficients may easily be incorporated into the phase-shifting solution as detailed in Section 3.2.1, but incorporation of these coefficients into CGS requires rederiving the equations of intensity from Chapter 2. Another option is to perform CGS on the beam after the beamsplitter that has transmission/reflectance coefficients that are better matched and perform photoelasticity with the other beam since the transmission/reflectance coefficients can be incorporated for photoelasticity.

5.2.2 Isoclinic Angle Determination

If rotational alignment of the polarization optics is not precise, then the analysis program should be able to correct the errors in the wrapped isoclinic angle. The current manual methodology is sufficient for these photoelastic cases since the form of α is expected to be slowly varying for most of the field, except in cases like that near the crack plane in Mode I–dominant fracture. Before extending this method to materials where the isoclinic angle may be more complicated or even have a new relationship to stresses due to the generalization of photoelasticity to anisotropic crystals, a robust algorithm should be developed for correcting for errors in the wrapped α. Some helpful features of this algorithm would be (i) removal of the errors even in the presence of other experimental errors, in the spirit of the quality-guided PCG unwrapping algorithm, (ii) user's ability to define masks to prevent removal of physical boundaries, and (iii) user's ability to define regions of high and low confidence based on metrics detailed in Section 3.2.4.1.

5.2.3 CGS Phase Relationship with Stress

The error associated with assuming the CGS phases are related to the first derivatives of $\sigma_1 + \sigma_2$, first characterized by Bruck and Rosakis (1992, 1993) for Mode I fracture and here in Chapter 4, requires revisiting to provide a full picture for applications of mixed-mode fracture. As indicated in the present study, small mode-mixity μ_{SIF} from -0.010 to 0.020 demonstrated increased error over the field of view as mode-mixity increased, particularly for the shearing direction related to the x derivative of $\sigma_1 + \sigma_2$. Since Mason et al. (1992) established that CGS can be applied to dynamic mixed-mode applications using the x derivative with good K_{II}/K_I measurement agreement with theory and finite elements, then possibly CGS studies with higher mode-mixity have acceptable error. Determining if these conjectures are true requires careful theoretical and experimental study with a wide range mode-mixity.

Beyond dealing with the error of the derivative assumption, another possible route to extracting $\sigma_1 + \sigma_2$ from CGS data is to treat the CGS phase precisely as a finite difference, where

$$\varphi_{sum} = \frac{2\pi Ch}{\lambda}[s(x + d_{shear}/2, y) - s(x - d_{shear}/2, y)] \tag{5.1}$$

where $s = (\sigma_1 + \sigma_2)$. Written in terms of pixel location, for $L = d_{shear}/[2 * \text{pixel resolution}]$, the

CGS phase for the i-shearing direction is

$$[\varphi^i_{sum}]_{i,j} = \frac{2\pi Ch}{\lambda}[s_{i+L,j} - s_{i-L,j}]. \tag{5.2}$$

This type of finite difference problem is a well defined concept in numerical methods called staggered grids. Taking the data from both shearing directions allows for an inverse determination of $\sigma_1 + \sigma_2$, still assuming that the "integration" of the finite difference data is a discrete Poisson equation. This change only requires a modification to the current Poisson equation in Equation (3.12) by changing the assumed resolution of the "derivative" from one pixel to the actual finite difference spacing of $2L$, such that

$$\begin{aligned}(s_{i+2L,j} - 2s_{i,j} + s_{i-2L,j}) &+ (s_{i,j+2L} - 2s_{i,j} + s_{i,j-2L}) \\ &= \left[\left(\frac{\varphi^i_{sum}\lambda}{2\pi Ch}\right)_{i+L,j} - \left(\frac{\varphi^i_{sum}\lambda}{2\pi Ch}\right)_{i-L,j}\right](2L) \\ &\quad + \left[\left(\frac{\varphi^j_{sum}\lambda}{2\pi Ch}\right)_{i,j+L} - \left(\frac{\varphi^j_{sum}\lambda}{2\pi Ch}\right)_{i,j-L}\right](2L),\end{aligned} \tag{5.3}$$

where φ^i_{sum} is the CGS phase in the i-shearing direction and φ^j_{sum} is the CGS phase in the j-shearing direction. Solving this Poisson equation would require a new algorithm because the PCG algorithm used in the current method is based on pixel distance as the finite difference spacing. This method is a more direct way of determining $\sigma_1 + \sigma_2$ without requiring the derivative assumption, which introduces the ϵ error discussed before. Previous fracture studies using CGS did not attempt to integrate the data to determine $\sigma_1 + \sigma_2$ as in this study, but instead use the CGS phases directly to make physical observations. The key to their studies is making the derivative assumption, giving the interference phase physical meaning as opposed to a finite difference that is difficult to physically interpret. The use of CGS to extract $\sigma_1 + \sigma_2$ lifts this need for a physical interpretation of the finite difference and in turn can eliminate the error associated with the derivative assumption.

5.3 Extensions of Method to Crystalline Materials

5.3.1 Development of Anisotropic Fracture Criteria

The phase-shifting CGS-photoelasticity experimental method has been demonstrated in stress-induced birefringent materials that are otherwise isotropic, but the method cannot in general be used for other types of materials in its current form. In order to extend the experimental method, the following requirements for both the materials of interest and the method must be met:

1. The crystalline materials must be transparent and have a detectable photoelastic (stress-optic) effect.

2. The appropriate photoelasticity governing equations are determined using the generalized theory for photoelasticity in crystals (Narasimhamurty, 1981). The basics of this theory are derived in Appendix C.

3. The governing equations for CGS in crystalline materials must be developed, utilizing the generalized theory for photoelasticity and elasticity in crystals.

With these requirements met, appropriate modifications to the optical setup and analysis may be developed to accommodate the new theory, if necessary. A full study of optically active ferroelectric crystals may be started once this method is extended to general crystals. These ferroelectrics have an additional challenge of spontaneous birefringence, discussed below.

Given the development of this hybrid method for transparent crystals with a detectable stress-optic effect, evalutation of full-field stresses around a crack may allow for development of general anisotropic fracture criteria. Experiments using crystals with different symmetries acting as model anisotropic materials may quanitify how anisotropic fracture depends on crystal symmetry in addition to local stresses and energy-related values ($\sigma_{\theta\theta}$, K_I, K_{II}, and G). For example, a crystal with cubic symmetry may require different fracture criteria than a crystal with monoclinic symmetry. Full-field stress determinination allows for calculation of the local crack tip stresses and energy-related values so that different fracture criteria depending on θ (max-K_I, $K_{II} = 0$, max-$\sigma_{\theta\theta}$, and max-G) may be evaluated for each crystal symmetry. Determining fracture criteria for crystals that are not active materials can serve as a good foundation for studying active materials that bring an added level of complexity beyond crystal anisotropy.

5.3.2 Preliminary Investigation for Application to Ferroelectrics

Before investing in a full study of ferroelectric materials using this CGS-photoelasticity experimental method, a logical first step is to blindly attempt to image a loaded single-crystal ferroelectric using the current experimental method. The ferroelectric crystal used for this preliminary investigation is barium titanate ($BaTiO_3$), which is a tetragonal crystal at room temperature, meaning the crystal structure is a square base with side length a and perpendicular rectangular sides with long side length c (Jona and Shirane, 1993). $BaTiO_3$ has a large c/a ratio of 1.06, which leads to 6% actuation strain when electromechanically loaded. $BaTiO_3$ is of particular interest for photonic microdevices due to its high electro-optic nonlinearity. The spontaneous birefringence without stress is $\Delta n = -0.072$ with $n_o = 2.432$ (Yariv and Yeh, 2007), which implies in a stressed $BaTiO_3$ crystal, the birefringence viewed by an optical method is due to both the spontaneous birefringence and the stress-induced birefringence. The basis of the use of photoelasticity to study ferroelectric materials is if the crystal has a large enough stress-induced birefringence that can be detected, especially when coupled with a spontaneous birefringence.

The crystal used here is a single crystal with <001> orientation, meaning the long axis is aligned with thickness of the crystal and with the optical axis of the light source (z axis). The crystal then has two possible polarization states, along the $+z$ or $-z$ axis; a region with the same polarization state is called a domain. The specimen is 5 mm × 5 mm and 1.01 mm thick. The loading configuration is a distributed load by a wedge on the side of the crystal, which is clamped on the opposite side by a specimen holder. The image field of view is 4.52 mm × 4.52 mm with 4.5 μm resolution. The light source is a He-Ne laser with $\lambda = 632.8$ nm. The CGS parameters are the following: $p = 1$ mm/40, $\tilde{\Delta}$ =8 .87 mm, and $d_{shear} = 226$ μm. The phase-shifting methods in terms of the procedure of changing the optics are the same as for the photoelastic materials, introduced in Chapters 2 and 3, but the physical interpretations of the interference patterns are not necessarily applicable to ferroelectrics. All three possible polarization configurations for CGS are employed.

Figure 5.1 shows the six photoelasticity images from the six combinations of polarization optic angles in Table 3.1. The images that pertain only to the isochromatic phase in photoelastic materials, I_1 and I_2, appear more complicated than usual, with breaks in continuity of the fringes along vertical lines. These vertical lines are likely 180^o domain walls, which are the boundaries between domains with polarization state that are 180^o different. Since the stresses in the crystal should be continuous across these domain walls, the breaks in the interference fringes at these domain walls likely implies that two adjacent domains affect the Δn differently, modulating the stress-related Δn term. The other four images that usually pertain to both the isochromatic phase and the isoclinic angle do appear different from each other and from I_1 and I_2. I_4 and I_6 are similar to I_1 and I_2 in structure, but I_3 and I_5 only exhibit faint weak fringes and a crack in the crystal emanating from the load application point. The presence of the crack appears to further complicate the interference patterns.

The next step in the experimental method is to try to determine the isoclinic angle and the isochromatic phase using Equations 3.3 and 3.4. Using the $BaTiO_3$ experimental images I_1 through I_6 as if they originated from an ordinary photoelastic material yields the "wrapped isoclinic angle" in Figure 5.2(a), which is then used without unwrapping to give an "ambiguous wrapped isochromatic phase" in Figure 5.2(b). These wrapped phases do exhibit behavior consistent with the isoclinic angle and isochromatic phase. Figure 5.2(a) has many phase discontinuities reminiscent of the false phase discontinuities in α for the photoelastic materials that appear to correspond to the sine of the phase in Figure 5.2(b) going to zero. Otherwise, this α-like phase does not have phase discontinuities except near the crack. Ignoring the modulation by the δ-like phase, the α-like phase has mostly values close to zero, implying that the principal axes of the crystal are aligned with the Cartesian axes. Since this is a crystal, the principal axes will align with the crystal structure, so an α-like quantity in a tetragonal crystal is likely to be close to zero or $\pi/2$. The wrapped δ-like phase in Figure 5.2(b) has breaks in the phase discontinuities at the domain walls, illustrating the effect of the spontaneous birefringence of different domains on the Δn. The wrapped δ-like phase also has what appears to be ambiguous data near the crack, possibly due to the regions in the α-like phase that require unwrapping. These conjectures require further investigation to determine the physical meaning behind these phases and to determine if these are even the appropriate quantities to consider. The interference patterns from the photoelasticity setup, though without quantified relationships to stresses, do exhibit some change in refractive index related to stresses that is large enough to detect using polarization optics. These images give hope to the idea that photoelasticity can be used to investigate stresses in ferroelectric crystals.

The images from the phase-shifting vertical and horizontal shearing CGS for all three polarization configurations introduced in Chapter 2 are presented in Figure 5.3. These images are complicated for two main reasons: (i) the polarization of different domains lead to discontinuous Δn, which then produce discontinuous CGS phases, and (ii) the finite shearing distance leads to interference of ΔS (optical path difference) from parts of the crystal that may have different domains, which can also lead to discontinuous CGS phases. In this case, the least complicated images come from the pure $E_y\hat{\jmath}$ input, which may have some polarization significance. Having acquired four phase-shifted images for each case in Figure 5.3, the wrapped phase can be determined using the standard arctan() formula that gives a range from $(-\pi/2, \pi/2]$, as shown in Figure 5.4. These wrapped phases have the discontinuous fringes at the domain walls, but the phase appears either continuous or has the appropriate π phase discontinuity expected from wrapped CGS phases in vertical strips, which implies that these phases could be unwrapped inside these vertical strips. The obvious first steps are to determine the ΔS for a stresses ferroelectric and then determine the intensity relationship for these interference patterns, because from first glance, interpreting these CGS images is nontrivial. Fortunately, the stress-related optical effects and other optical effects in these ferroelectrics are well characterized, so determination of the intensities is only a matter of careful analysis.

5.4 Conclusions

The future research for this CGS-photoelasticity experimental method pertains to two main avenues, improving the current method and then extending it to investigate fracture in crystalline materials. Errors related to misalignment of optics and to the non-polarizing beamsplitter may easily be mitigated by careful alignment procedures outlined above and by characterizing the quality of the optics. Also, a robust algorithm should be developed to reduce errors due to corrections to the wrapped isoclinic angle. To eliminate the inherent error in assuming that the CGS phase is related to the derivative of $\sigma_1 + \sigma_2$, the CGS phase is to be treated as a finite difference, and then the vertical and horizontal phase data are integrated using a new form of the discrete Poisson equation based on staggered grids. The extension of the experimental method to crystalline materials depends mainly on a detectable photoelastic effect from the crystal and on extensive analysis on the interference patterns in the individual experimental techniques. A preliminary investigation of the ferroelectric $BaTiO_3$ demonstrates that this crystal has a detectable photoelastic effect, but this effect is confounded by the spontaneous polarization; further analysis is required to determine the physical meaning of interference patterns from both photoelasticity and CGS for this ferroelectric.

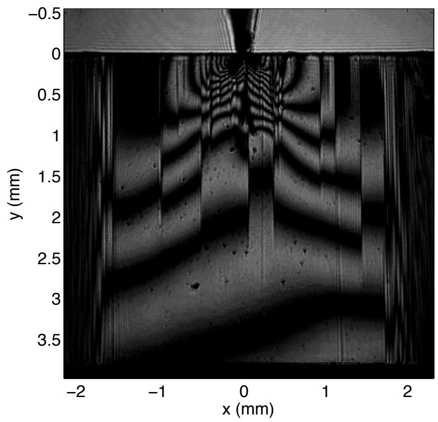

(a) I_1

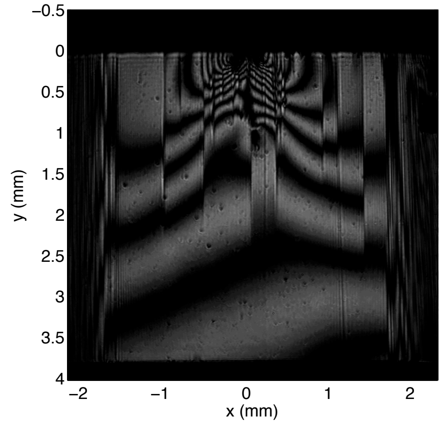

(b) I_2

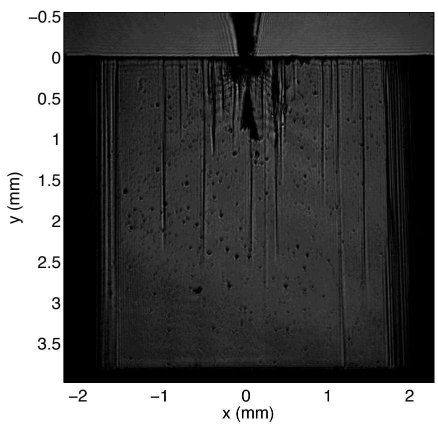

(c) I_3

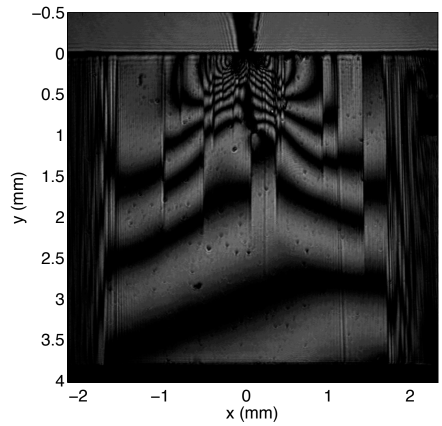

(d) I_4

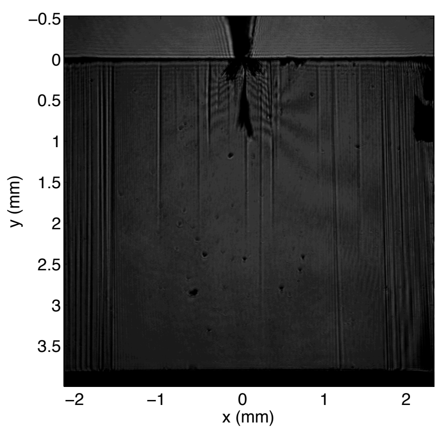

(e) I_5

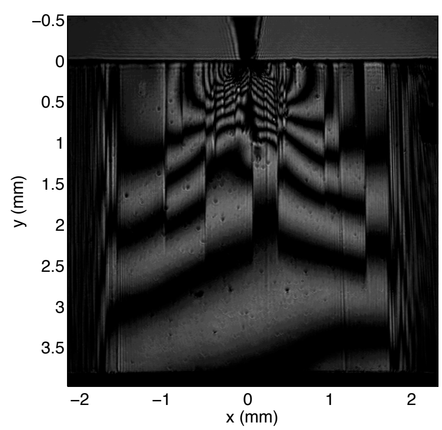

(f) I_6

Figure 5.1: Experimental images from six-step phase-shifting photoelasticity for a side-loaded $BaTiO_3$ single crystal

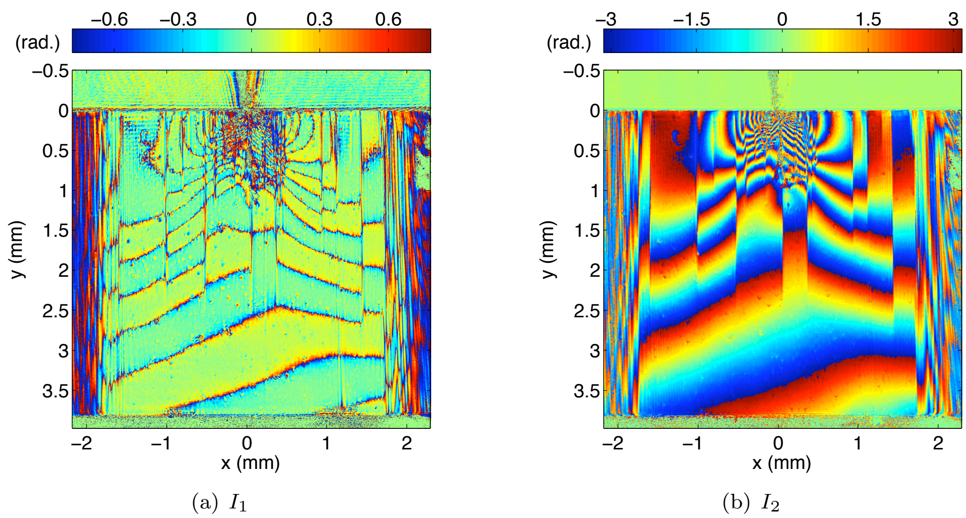

Figure 5.2: Experimental wrapped phases from six-step phase-shifting photoelasticity for a side-loaded $BaTiO_3$ single crystal

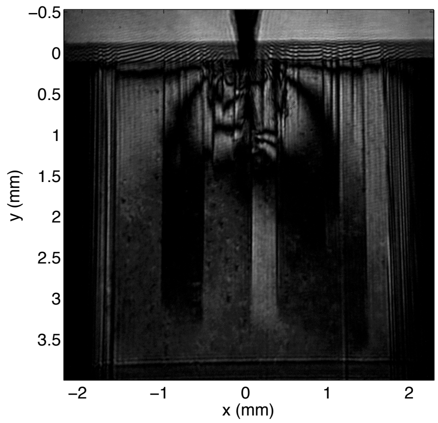

(a) Vertical I_1 from pure $E_x\hat{\imath}$

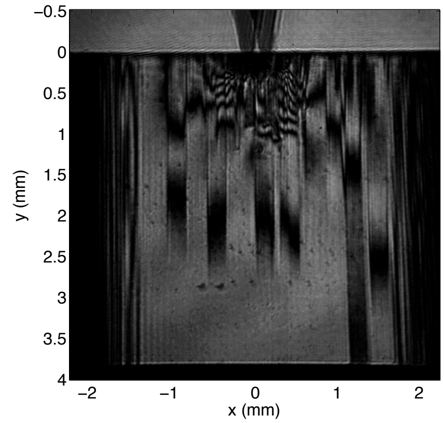

(b) Horizontal I_1 from pure $E_x\hat{\imath}$

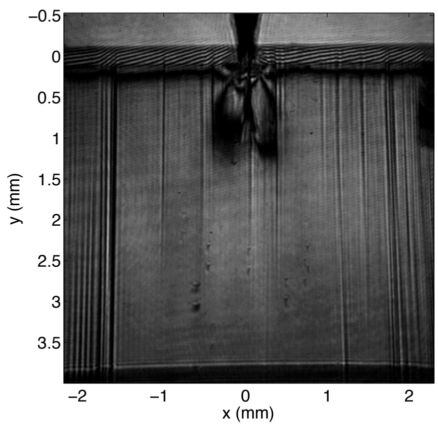

(c) Vertical I_1 from pure $E_y\hat{\jmath}$

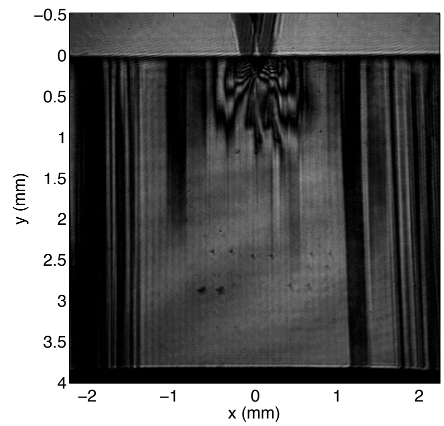

(d) Horizontal I_1 from pure $E_y\hat{\jmath}$

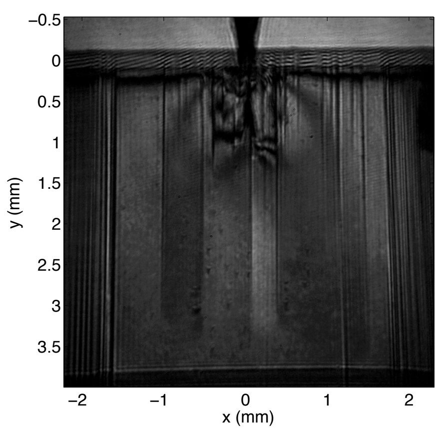

(e) Vertical I_1 from circular polarization

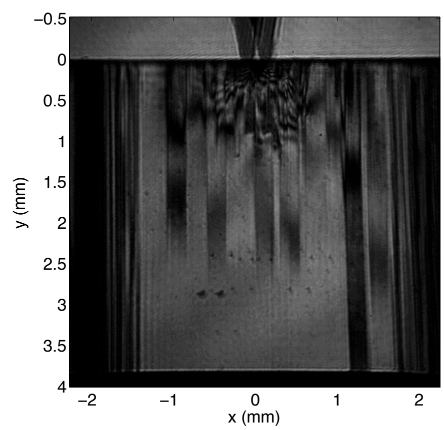

(f) Horizontal I_1 from circular polarization

Figure 5.3: Experimental images I_1 from the three polarization configurations for vertical and horizontal shearing directions for a side-loaded $BaTiO_3$ single crystal

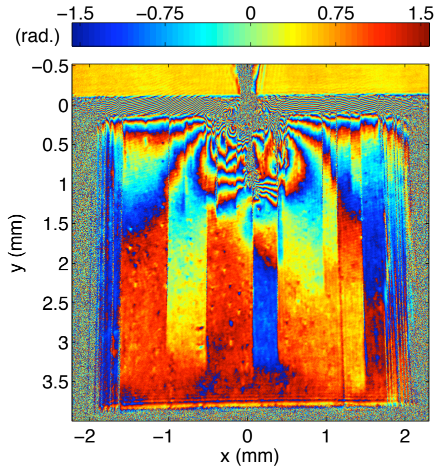

(a) Vertical I_1 from pure $E_x\hat{\imath}$

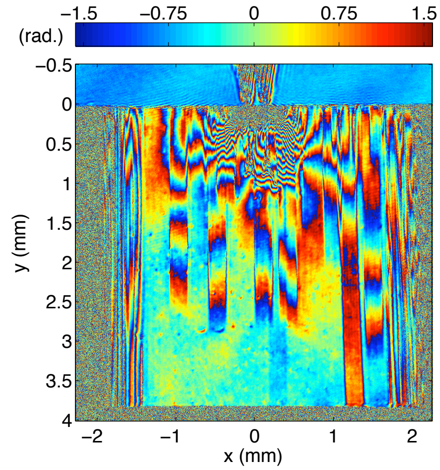

(b) Horizontal I_1 from pure $E_x\hat{\imath}$

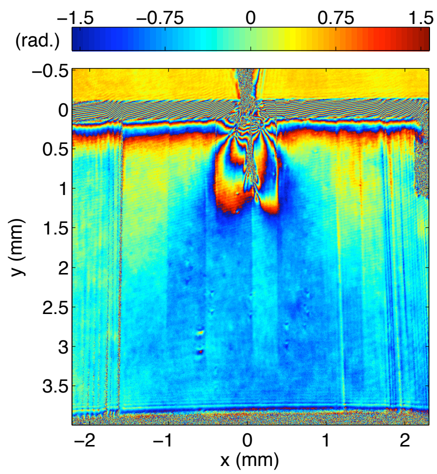

(c) Vertical I_1 from pure $E_y\hat{\jmath}$

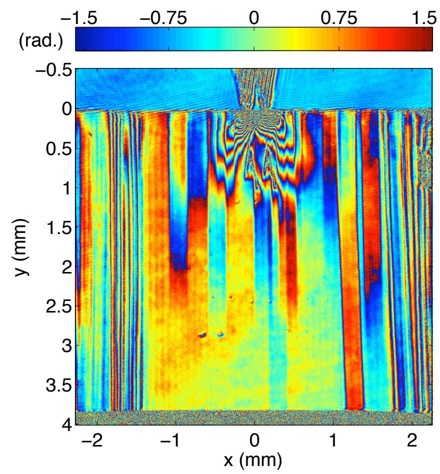

(d) Horizontal I_1 from pure $E_y\hat{\jmath}$

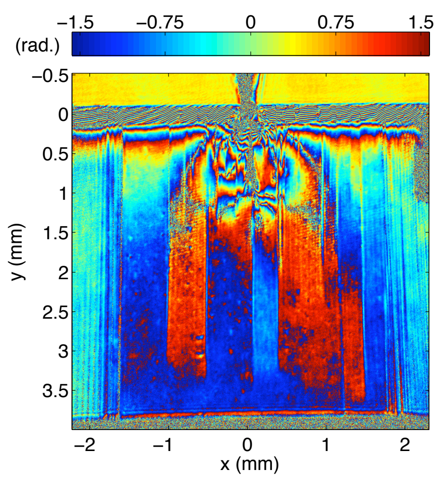

(e) Vertical I_1 from circular polarization

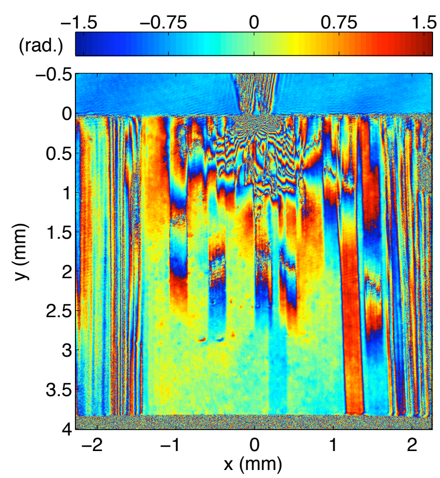

(f) Horizontal I_1 from circular polarization

Figure 5.4: Experimental wrapped phases from the three polarization configurations for vertical and horizontal shearing directions for a side-loaded $BaTiO_3$ single crystal

Chapter 6

Conclusions

This thesis has presented a hybrid full-field experimental method combining phase-shifting photoelasticity and transmission Coherent Gradient Sensing for in-plane tensorial stress determination for fracture studies. In order for this method to achieve its goals, a new analysis for transmission wavefront shearing interferometry applied to photoelastic materials has been developed and experimentally verified for the specific wavefront shearing interferometer Coherent Gradient Sensing. The hybrid experimental method has been developed and experimentally verified for photoelastic materials by good comparison between experimental and theoretical stress fields for a compressed polycarbonate plate with a side V-notch. The hybrid experimental method has also been validated for full-field tensorial stress determination around Mode I–dominant cracks in photoelastic materials, a study that is the first to achieve these goals, serving as the foundation for future research in extending this method for fracture studies in anisotropic materials.

The new analysis of transmission wavefront shearing interferometry for photoelastic materials derives an intensity expression I^{image} for the complicated interference pattern that, in general, is the sum of two interference patterns such that $I^{image} = I_o + I_{1o}\cos[\varphi_{sum} + \varphi_{diff}] + I_{2o}\cos[\varphi_{sum} - \varphi_{diff}]$ (Equation (2.16)); φ_{sum} is the phase related to $\sigma_1 + \sigma_2$ and is the only phase that results for these interferometers applied to optically isotropic materials, φ_{diff} is a phase related to $\sigma_1 - \sigma_2$, and I_{1o} and I_{2o} are coefficients determined by the polarization of the input electric field. The control of the input electric field polarization by polarization optics prior to the photoelastic specimen, in addition to phase-shifting techniques, allow for determination of the desired φ_{sum}. This analysis has been verified using a compressed polycarbonate plate with a side V-notch using CGS with the experimental phase maps comparing well with theory based on Williams (1952). This analysis serves as the governing theory for determination of x and y derivatives of $\sigma_1+\sigma_2$ for the hybrid experimental method presented in this thesis.

A six-step phase-shifting photoelasticity method has been presented utilizing different angles for the polarization optics in a circular polariscope to obtain six images related to $\sigma_1 - \sigma_2$ and the isoclinic angle, α, which is the angle between the Cartesian and principal coordinate systems. This method allows for full-field determination of $\sigma_1 - \sigma_2$ and α. Since the first two polarization optics of the circular polariscope, a polarizer and $\lambda/4$ plate set for circular polarization of the electric field prior to the specimen, are also useful for determination of φ_{sum} from CGS, then a non-polarizing beamsplitter or a translating mirror immediately after the sample allows for these two experimental techniques to be combined to investigate the same field of view of a specimen. The phase-shifting techniques produce "wrapped" phase fields that require unwrapping before the stress fields can be determined, a task achieved by a data-quality–guided unwrapping algorithm by Ghiglia and Romero (1994) based on preconditioned conjugate gradient (PCG) numerical methods used to solve discrete Poisson equations. A slightly modified version of the algorithm has been implemented for integration of the x and y derivatives of stress to determine $\sigma_1 + \sigma_2 + c_i$, where the constant of integration c_i is determined by a traction free boundary condition. The in-plane tensorial stress components can then be determined from full-field $\sigma_1 + \sigma_2$, $\sigma_1 - \sigma_2$, and α, as demonstrated for a compressed polycarbonate plate with a side V-notch. Some potential error sources have been identified as rotational misalignment of the polarization optics and transmission and reflectance coefficients of the non-polarizing beamsplitter, and mitigation techniques have been developed to minimize error, particularly in the isoclinic angle. Despite these error sources, the experimental and theoretical data have good agreement. This experimental verification of the hybrid experimental method is the basis for the application of the method for determination of the in-plane tensorial stress around a loaded crack in a photoelastic material.

The first study to experimentally determine full-field in-plane tensorial stress around a crack in a photoelastic material has been presented. The hybrid method has been applied to Mode I–dominant cracks in Homalite-100 for small fields of view, for a range of Mode I stress intensity factors from around one-quarter to just below the fracture toughness of Homalite-100, and for a small range of mode-mixity K_{II}/K_I from -0.010 to 0.020. The experimental stress fields show K-dominant behavior, allowing for excellent comparison to full-field theoretical data based on the 2D asymptotic crack solution using the experimentally calculated K_I and K_{II} values. These values have been calculated from stress fields incorporating both CGS and photoelasticity data and allow for global error less than 5% for most fields and no greater than 7.8%, showing that the two techniques work well together for stress determination around cracks. Common error sources identified in Chapter 3 are characterized for this application and can be mitigated with careful experimentation and with improved analysis algorithms. This study has successfully met the objective of this thesis: to apply a hybrid experimental method for full-field in-plane tensorial stress determination suitable for fracture studies in photoelastic materials with the ability to view local stresses around a crack for small (mm-scale) fields of view for small specimens. This study is the foundation for future research in extending this method for fracture studies in anisotropic materials.

Future research discussed in this thesis for the hybrid CGS-photoelasticity experimental method involves improvements to the current method and then extension of it for fracture studies in anisotropic materials, particularly crystalline materials. Errors associated with the rotational misalignment of the polarization optics and to the non-polarizing beamsplitter may be mitigated with careful alignment procedures and by characterizing the quality and tolerances of the optics. A robust algorithm should be developed to improve the user-correction of any remaining errors due to these sources in the isoclinic angle data. Since this experimental method ultimately uses the $\sigma_1+\sigma_2$ stress field data, then the derivative assumption relating the CGS phases to spatial derivatives of stresses and the error associated with this assumption may be eliminated by treating the phases as finite differences based on staggered grids. The vertical and horizontal phase data may be used in an algorithm, which requires future implementation, to solve a discrete Poisson equation to determine $\sigma_1+\sigma_2$. Extending the experimental method to crystalline materials requires (i) a detectable photoelastic effect from the crystal and (ii) extensive analysis of the interference patterns in the individual experimental techniques. A preliminary investigation of the ferroelectric $BaTiO_3$ has shown that this crystal has a detectable photoelastic effect, but this effect is confounded by the spontaneous polarization of the ferroelectric. Further analysis is required to determine the physical meaning of interference patterns from both photoelasticity and CGS for this ferroelectric. Established theories such as photoelasticity for crystals and the electro-optic effect serve as tools for new analyses that extend the CGS-photoelasticity experimental method to meet its ultimate goal of full-field stress determination for fracture criteria development for active anisotropic materials.

Appendix A

Stress in Principal, Cartesian, and Polar Coordinate Systems

A.1 Relations Between Stress Fields in Principal, Cartesian, and Polar Coordinate Systems

A.1.1 Principal and Cartesian Coordinate Systems

Transforming the 2D stress tensor $\boldsymbol{\sigma}$ from Cartesian to the principal coordinate system and vice versa requires the rotation matrix $\mathbf{R}_\alpha$, given in Equation (A.1), where α is the angle between the Cartesian and principal coordinate systems, as shown in Figure A.1. Equation (A.2) shows transforming $\boldsymbol{\sigma}$ from Cartesian to principal coordinates. Equation (A.3) shows transforming $\boldsymbol{\sigma}$ from principal to Cartesian coordinates in terms of the sum and differences of the principal stresses.

$$\mathbf{R}_\alpha = \begin{bmatrix} \cos(\alpha) & -\sin(\alpha) \\ \sin(\alpha) & \cos(\alpha) \end{bmatrix} \tag{A.1}$$

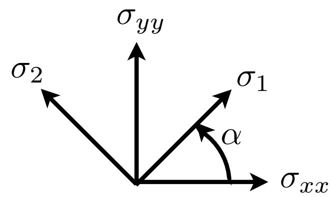

Figure A.1: Schematic of Cartesian and principal coordinate systems

$$
\begin{aligned}
\begin{bmatrix} \sigma_1 & 0 \\ 0 & \sigma_2 \end{bmatrix} &= \mathbf{R}_\alpha^{\mathbf{T}} \begin{bmatrix} \sigma_{xx} & \sigma_{xy} \\ \sigma_{xy} & \sigma_{yy} \end{bmatrix} \mathbf{R}_\alpha \\
&= \mathbf{R}_\alpha^{\mathbf{T}} \begin{bmatrix} \sigma_{xx}\cos(\alpha) + \sigma_{xy}\sin(\alpha) & -\sigma_{xx}\sin(\alpha) + \sigma_{xy}\cos(\alpha) \\ \sigma_{yy}\sin(\alpha) + \sigma_{xy}\cos(\alpha) & \sigma_{yy}\cos(\alpha) - \sigma_{xy}\sin(\alpha) \end{bmatrix} \\
&= \begin{bmatrix} [\sigma_{xx}\cos^2(\alpha) + \sigma_{yy}\sin^2(\alpha) & [(\sigma_{yy} - \sigma_{xx})\cos(\alpha)\sin(\alpha) \\ + 2\sigma_{xy}\cos(\alpha)\sin(\alpha)] & + \sigma_{xy}(\cos^2(\alpha) - \sin^2(\alpha))] \\ [(\sigma_{yy} - \sigma_{xx})\cos(\alpha)\sin(\alpha) & [\sigma_{xx} sin^2(\alpha) + \sigma_{yy}\cos^2(\alpha) \\ + \sigma_{xy}(\cos^2(\alpha) - \sin^2(\alpha))] & - 2\sigma_{xy}\cos(\alpha)\sin(\alpha)] \end{bmatrix} \\
&= \begin{bmatrix} [\sigma_{xx}\left(\frac{1+\cos(2\alpha)}{2}\right) & [(\sigma_{yy} - \sigma_{xx})\left(\frac{\sin(2\alpha)}{2}\right) \\ +\sigma_{yy}\left(\frac{1-\cos(2\alpha)}{2}\right) + \sigma_{xy}\sin(2\alpha)] & +\sigma_{xy}\cos(2\alpha)] \\ [(\sigma_{yy} - \sigma_{xx})\left(\frac{\sin(2\alpha)}{2}\right) & [\sigma_{xx}\left(\frac{1-\cos(2\alpha)}{2}\right) \\ +\sigma_{xy}\cos(2\alpha)] & +\sigma_{yy}\left(\frac{1+\cos(2\alpha)}{2}\right) - \sigma_{xy}\sin(2\alpha)] \end{bmatrix} \\
&= \begin{bmatrix} [\frac{1}{2}(\sigma_{xx} + \sigma_{yy}) + \frac{1}{2}(\sigma_{xx} - \sigma_{yy})\cos(2\alpha) & [-\frac{1}{2}(\sigma_{xx} - \sigma_{yy})\sin(2\alpha) \\ +\sigma_{xy}\sin(2\alpha)] & +\sigma_{xy}\cos(2\alpha)] \\ [-\frac{1}{2}(\sigma_{xx} - \sigma_{yy})\sin(2\alpha) & [\frac{1}{2}(\sigma_{xx} + \sigma_{yy}) - \frac{1}{2}(\sigma_{xx} - \sigma_{yy})\cos(2\alpha) \\ +\sigma_{xy}\cos(2\alpha)] & -\sigma_{xy}\sin(2\alpha)] \end{bmatrix}
\end{aligned}
\tag{A.2}
$$

$$
\begin{aligned}
\begin{bmatrix} \sigma_{xx} & \sigma_{xy} \\ \sigma_{xy} & \sigma_{yy} \end{bmatrix} &= \mathbf{R}_\alpha \begin{bmatrix} \sigma_1 & 0 \\ 0 & \sigma_2 \end{bmatrix} \mathbf{R}_\alpha^{\mathbf{T}} \\
&= \mathbf{R}_\alpha \begin{bmatrix} \sigma_1 \cos(\alpha) & \sigma_1 \sin(\alpha) \\ -\sigma_2 \sin(\alpha) & \sigma_2 \cos(\alpha) \end{bmatrix} \\
&= \begin{bmatrix} \sigma_1 \cos^2(\alpha) + \sigma_2 \sin^2(\alpha) & (\sigma_1 - \sigma_2) \cos(\alpha) \sin(\alpha) \\ (\sigma_1 - \sigma_2) \cos(\alpha) \sin(\alpha) & \sigma_1 \sin^2(\alpha) + \sigma_2 \cos^2(\alpha) \end{bmatrix} \\
&= \begin{bmatrix} \sigma_1 \left(\frac{1+\cos(2\alpha)}{2}\right) + \sigma_2 \left(\frac{1-\cos(2\alpha)}{2}\right) & (\sigma_1 - \sigma_2) \left(\frac{\sin(2\alpha)}{2}\right) \\ (\sigma_1 - \sigma_2) \left(\frac{\sin(2\alpha)}{2}\right) & \sigma_1 \left(\frac{1-\cos(2\alpha)}{2}\right) + \sigma_2 \left(\frac{1+\cos(2\alpha)}{2}\right) \end{bmatrix} \\
&= \begin{bmatrix} \frac{1}{2}(\sigma_1 + \sigma_2) + \frac{1}{2}(\sigma_1 - \sigma_2) \cos(2\alpha) & \frac{1}{2}(\sigma_1 - \sigma_2) \sin(2\alpha) \\ \frac{1}{2}(\sigma_1 - \sigma_2) \sin(2\alpha) & \frac{1}{2}(\sigma_1 + \sigma_2) - \frac{1}{2}(\sigma_1 - \sigma_2) \cos(2\alpha) \end{bmatrix}
\end{aligned} \tag{A.3}
$$

A.1.2 Polar and Cartesian Coordinate Systems

Transforming the 2D stress tensor $\boldsymbol{\sigma}$ from Cartesian to the polar coordinate system and vice versa requires the rotation matrix $\mathbf{R}_\theta$, given in Equation (A.4), where θ is the angle between the Cartesian x-axis and the radius vector. Equation (A.5) shows transforming $\boldsymbol{\sigma}$ from Cartesian to polar coordinates. Equation (A.6) shows transforming $\boldsymbol{\sigma}$ from polar to Cartesian coordinates. Since the simplifications are similar to the equations in Section (A.1.1), not all the steps are shown.

$$
\mathbf{R}_\theta = \begin{bmatrix} \cos(\theta) & -\sin(\theta) \\ \sin(\theta) & \cos(\theta) \end{bmatrix} \tag{A.4}
$$

$$\begin{bmatrix} \sigma_{rr} & \sigma_{r\theta} \\ \\ \sigma_{r\theta} & \sigma_{\theta\theta} \end{bmatrix} = \mathbf{R}_\theta^{\mathbf{T}} \begin{bmatrix} \sigma_{xx} & \sigma_{xy} \\ \\ \sigma_{xy} & \sigma_{yy} \end{bmatrix} \mathbf{R}_\theta$$

$$= \begin{bmatrix} [\sigma_{xx}\cos^2(\theta) + \sigma_{yy}\sin^2(\theta) & [-\frac{1}{2}(\sigma_{xx} - \sigma_{yy})\sin(2\theta) \\ +\sigma_{xy}\sin(2\theta)] & +\sigma_{xy}\cos(2\theta)] \\ [-\frac{1}{2}(\sigma_{xx} - \sigma_{yy})\sin(2\theta) & [\sigma_{xx}\sin^2(\theta) + \sigma_{yy}\cos^2(\theta) \\ +\sigma_{xy}\cos(2\theta)] & -\sigma_{xy}\sin(2\theta)] \end{bmatrix} \tag{A.5}$$

$$\begin{bmatrix} \sigma_{xx} & \sigma_{xy} \\ \\ \sigma_{xy} & \sigma_{yy} \end{bmatrix} = \mathbf{R}_\theta \begin{bmatrix} \sigma_{rr} & \sigma_{r\theta} \\ \\ \sigma_{r\theta} & \sigma_{\theta\theta} \end{bmatrix} \mathbf{R}_\theta^{\mathbf{T}}$$

$$= \begin{bmatrix} [\sigma_{rr}\cos^2(\theta) + \sigma_{\theta\theta}\sin^2(\theta) & [\frac{1}{2}(\sigma_{rr} - \sigma_{\theta\theta})\sin(2\theta) \\ -\sigma_{r\theta}\sin(2\theta)] & +\sigma_{r\theta}\cos(2\theta)] \\ [\frac{1}{2}(\sigma_{rr} - \sigma_{\theta\theta})\sin(2\theta) & [\sigma_{rr}\sin^2(\theta) + \sigma_{\theta\theta}\cos^2(\theta) \\ +\sigma_{r\theta}\cos(2\theta)] & +\sigma_{r\theta}\sin(2\theta)] \end{bmatrix} \tag{A.6}$$

A.1.3 Polar and Principal Coordinate Systems

The 2D stress tensor $\boldsymbol{\sigma}$ may be transformed from Cartesian to the Polar coordinate system and vice versa using the relations in Sections A.1.1–A.1.2. The stress components σ_{rr}, $\sigma_{r\theta}$, and $\sigma_{\theta\theta}$ are given in terms of the principal stresses, the principal direction (in terms of the angle α), and the angle θ, as given in Equations (A.7)–(A.9). The principal stress components are given in terms of the σ_{rr}, $\sigma_{r\theta}$, and $\sigma_{\theta\theta}$, the principal direction, and the angle θ, as given in Equation (A.10).

$$
\begin{aligned}
\sigma_{rr} &= [\tfrac{1}{2}(\sigma_1+\sigma_2) + \tfrac{1}{2}(\sigma_1-\sigma_2)\cos(2\alpha)]\cos^2(\theta) \\
&\quad + [\tfrac{1}{2}(\sigma_1+\sigma_2) - \tfrac{1}{2}(\sigma_1-\sigma_2)\cos(2\alpha)]\sin^2(\theta) + \tfrac{1}{2}(\sigma_1-\sigma_2)\sin(2\alpha)\sin(2\theta) \\
&= \tfrac{1}{2}(\sigma_1+\sigma_2) + \tfrac{1}{2}(\sigma_1-\sigma_2)\cos(2\alpha)[\cos^2(\theta)-\sin^2(\theta)] \\
&\quad + \tfrac{1}{2}(\sigma_1-\sigma_2)\sin(2\alpha)\sin(2\theta) \\
&= \tfrac{1}{2}(\sigma_1+\sigma_2) + \tfrac{1}{2}(\sigma_1-\sigma_2)[\cos(2\alpha)\cos(2\theta)+\sin(2\alpha)\sin(2\theta)] \\
&= \tfrac{1}{2}(\sigma_1+\sigma_2) + \tfrac{1}{2}(\sigma_1-\sigma_2)\cos(2\theta-2\alpha)
\end{aligned}
\tag{A.7}
$$

$$
\begin{aligned}
\sigma_{r\theta} &= \tfrac{1}{2}\{[\tfrac{1}{2}(\sigma_1+\sigma_2) - \tfrac{1}{2}(\sigma_1-\sigma_2)\cos(2\alpha)] \\
&\quad - [\tfrac{1}{2}(\sigma_1+\sigma_2) + \tfrac{1}{2}(\sigma_1-\sigma_2)\cos(2\alpha)]\}\sin(2\theta) + \tfrac{1}{2}(\sigma_1-\sigma_2)\sin(2\alpha)\cos(2\theta) \\
&= -\tfrac{1}{2}(\sigma_1-\sigma_2)\cos(2\alpha)\sin(2\theta) + \tfrac{1}{2}(\sigma_1-\sigma_2)\sin(2\alpha)\cos(2\theta) \\
&= -\tfrac{1}{2}(\sigma_1-\sigma_2)[\sin(2\theta)\cos(2\alpha)-\cos(2\theta)\sin(2\alpha)] \\
&= -\tfrac{1}{2}(\sigma_1-\sigma_2)\sin(2\theta-2\alpha)
\end{aligned}
\tag{A.8}
$$

$$
\begin{aligned}
\sigma_{\theta\theta} &= [\tfrac{1}{2}(\sigma_1+\sigma_2) + \tfrac{1}{2}(\sigma_1-\sigma_2)\cos(2\alpha)]\sin^2(\theta) \\
&\quad + [\tfrac{1}{2}(\sigma_1+\sigma_2) - \tfrac{1}{2}(\sigma_1-\sigma_2)\cos(2\alpha)]\cos^2(\theta) - \tfrac{1}{2}(\sigma_1-\sigma_2)\sin(2\alpha)\sin(2\theta) \\
&= \tfrac{1}{2}(\sigma_1+\sigma_2) - \tfrac{1}{2}(\sigma_1-\sigma_2)\cos(2\alpha)[\cos^2(\theta)-\sin^2(\theta)] \\
&\quad - \tfrac{1}{2}(\sigma_1-\sigma_2)\sin(2\alpha)\sin(2\theta) \\
&= \tfrac{1}{2}(\sigma_1+\sigma_2) - \tfrac{1}{2}(\sigma_1-\sigma_2)[\cos(2\alpha)\cos(2\theta)+\sin(2\alpha)\sin(2\theta)] \\
&= \tfrac{1}{2}(\sigma_1+\sigma_2) - \tfrac{1}{2}(\sigma_1-\sigma_2)\cos(2\theta-2\alpha)
\end{aligned}
\tag{A.9}
$$

$$
\begin{aligned}
\sigma_{1,2} = \tfrac{1}{2}\{&[\sigma_{rr}\cos^2(\theta) + \sigma_{\theta\theta}\sin^2(\theta) - \sigma_{r\theta}\sin(2\theta)] \\
&\quad + [\sigma_{rr}\sin^2(\theta) + \sigma_{\theta\theta}\cos^2(\theta) + \sigma_{r\theta}\sin(2\theta)]\} \\
&\pm \tfrac{1}{2}\{[\sigma_{rr}\cos^2(\theta) + \sigma_{\theta\theta}\sin^2(\theta) - \sigma_{r\theta}\sin(2\theta)] \\
&\quad - [\sigma_{rr}\sin^2(\theta) + \sigma_{\theta\theta}\cos^2(\theta) + \sigma_{r\theta}\sin(2\theta)]\}\cos(2\alpha) \\
&\pm [\tfrac{1}{2}(\sigma_{rr} - \sigma_{\theta\theta})\sin(2\theta) + \sigma_{r\theta}\cos(2\theta)]\sin(2\alpha) \\
= &\tfrac{1}{2}(\sigma_{rr} + \sigma_{\theta\theta}) \pm \tfrac{1}{2}(\sigma_{rr} - \sigma_{\theta\theta})[\cos^2(\theta) - \sin^2(\theta)]\cos(2\alpha) - \sigma_{r\theta}\sin(2\theta)\cos(2\alpha) \\
&\pm \tfrac{1}{2}(\sigma_{rr} - \sigma_{\theta\theta})\sin(2\theta)\sin(2\alpha) \pm \sigma_{r\theta}\cos(2\theta)\sin(2\alpha) \\
= &\tfrac{1}{2}(\sigma_{rr} + \sigma_{\theta\theta}) \pm \tfrac{1}{2}(\sigma_{rr} - \sigma_{\theta\theta})[\cos(2\alpha)\cos(2\theta) + \sin(2\alpha)\sin(2\theta)] \\
&\mp \sigma_{r\theta}[\sin(2\theta)\cos(2\alpha) - \cos(2\theta)\sin(2\alpha)] \\
= &\tfrac{1}{2}(\sigma_{rr} + \sigma_{\theta\theta}) \pm \tfrac{1}{2}(\sigma_{rr} - \sigma_{\theta\theta})\cos(2\theta - 2\alpha) \mp \sigma_{r\theta}\sin(2\theta - 2\alpha)
\end{aligned}
\tag{A.10}
$$

A.2 Important Stress Terms and Derivatives

A.2.1 Terms Involving the Sum of Principal Stresses

Coherent Gradient Sensing (CGS) involves the sum of principal stresses, so $\sigma_1 + \sigma_2$ and its derivatives must be developed in terms of Cartesian and polar coordinates. From Equations (A.3) and (A.10), the sum of principal stresses may be written as

$$\sigma_1 + \sigma_2 = \sigma_{xx} + \sigma_{yy} = \sigma_{rr} + \sigma_{\theta\theta}. \tag{A.11}$$

Given Equation (A.11), the derivatives of $\sigma_1 + \sigma_2$ with respect to r and θ may be written as

$$\frac{\partial\sigma_1 + \sigma_2}{\partial r} = \frac{\partial(\sigma_{xx} + \sigma_{yy})}{\partial r} = \frac{\partial(\sigma_{rr} + \sigma_{\theta\theta})}{\partial r}, \tag{A.12}$$

$$\frac{\partial\sigma_1 + \sigma_2}{\partial \theta} = \frac{\partial(\sigma_{xx} + \sigma_{yy})}{\partial \theta} = \frac{\partial(\sigma_{rr} + \sigma_{\theta\theta})}{\partial \theta}. \tag{A.13}$$

With Equations (A.11)–(A.13), the derivatives of $\sigma_1+\sigma_2$ with respect to x and y are

$$\begin{aligned}
\frac{\partial\sigma_1+\sigma_2}{\partial x} &= \frac{\partial r}{\partial x}\frac{\partial(\sigma_1+\sigma_2)}{\partial r}+\frac{\partial\theta}{\partial x}\frac{\partial(\sigma_1+\sigma_2)}{\partial\theta}\\
&=\cos(\theta)\frac{\partial(\sigma_1+\sigma_2)}{\partial r}-\frac{\sin(\theta)}{r}\frac{\partial(\sigma_1+\sigma_2)}{\partial\theta}\\
&=\cos(\theta)\frac{\partial(\sigma_{xx}+\sigma_{yy})}{\partial r}-\frac{\sin(\theta)}{r}\frac{\partial(\sigma_{xx}+\sigma_{yy})}{\partial\theta}\\
&=\cos(\theta)\frac{\partial(\sigma_{rr}+\sigma_{\theta\theta})}{\partial r}-\frac{\sin(\theta)}{r}\frac{\partial(\sigma_{rr}+\sigma_{\theta\theta})}{\partial\theta},
\end{aligned}\tag{A.14}$$

$$\begin{aligned}
\frac{\partial\sigma_1+\sigma_2}{\partial y} &= \frac{\partial r}{\partial y}\frac{\partial(\sigma_1+\sigma_2)}{\partial r}+\frac{\partial\theta}{\partial y}\frac{\partial(\sigma_1+\sigma_2)}{\partial\theta}\\
&=\sin(\theta)\frac{\partial(\sigma_1+\sigma_2)}{\partial r}+\frac{\cos(\theta)}{r}\frac{\partial(\sigma_1+\sigma_2)}{\partial\theta}\\
&=\sin(\theta)\frac{\partial(\sigma_{xx}+\sigma_{yy})}{\partial r}+\frac{\cos(\theta)}{r}\frac{\partial(\sigma_{xx}+\sigma_{yy})}{\partial\theta}\\
&=\sin(\theta)\frac{\partial(\sigma_{rr}+\sigma_{\theta\theta})}{\partial r}+\frac{\cos(\theta)}{r}\frac{\partial(\sigma_{rr}+\sigma_{\theta\theta})}{\partial\theta}.
\end{aligned}\tag{A.15}$$

A.2.2 Terms Involving the Difference of Principal Stresses and Directions

Both photoelasticity and CGS for photoelastic materials involve the difference of principal stresses; additionally, CGC for photoelastic materials involve the derivatives of $\sigma_1-\sigma_2$ and of α. These also must be written in terms of Cartesian and polar coordinates. The difference of principal stresses may be written in the following manner using Equation (A.3) and (A.10):

$$\begin{aligned}
\sigma_1-\sigma_2 &= (\sigma_{xx}-\sigma_{yy})\cos(2\alpha)+2\sigma_{xy}\sin(2\alpha)\\
&=(\sigma_{rr}-\sigma_{\theta\theta})\cos(2\theta-2\alpha)-2\sigma_{r\theta}\sin(2\theta-2\alpha).
\end{aligned}\tag{A.16}$$

Taking the r and θ derivatives of $\sigma_1-\sigma_2$ in terms of Cartesian coordinates produces equations that involve the r and θ derivatives of α, but using $\tan(2\alpha)=(2\sigma_{xy}/(\sigma_{xx}-\sigma_{yy}))$ can eliminate the terms involving the derivatives of α.

$$\begin{aligned}\frac{\partial(\sigma_1-\sigma_2)}{\partial r} &= \frac{\partial(\sigma_{xx}-\sigma_{yy})}{\partial r}\cos(2\alpha)+2\frac{\partial\sigma_{xy}}{\partial r}\sin(2\alpha)\\ &\quad +2\frac{\partial\alpha}{\partial r}[2\sigma_{xy}\cos(2\alpha)-(\sigma_{xx}-\sigma_{yy})\sin(2\alpha)]\\ &= \frac{\partial(\sigma_{xx}-\sigma_{yy})}{\partial r}\cos(2\alpha)+2\frac{\partial\sigma_{xy}}{\partial r}\sin(2\alpha)\\ &\quad +2\frac{\partial\alpha}{\partial r}[2\sigma_{xy}\cos(2\alpha)-2\sigma_{xy}\cos(2\alpha)]\\ &= \frac{\partial(\sigma_{xx}-\sigma_{yy})}{\partial r}\cos(2\alpha)+2\frac{\partial\sigma_{xy}}{\partial r}\sin(2\alpha)\end{aligned} \tag{A.17}$$

$$\begin{aligned}\frac{\partial(\sigma_1-\sigma_2)}{\partial \theta} &= \frac{\partial(\sigma_{xx}-\sigma_{yy})}{\partial \theta}\cos(2\alpha)+2\frac{\partial\sigma_{xy}}{\partial \theta}\sin(2\alpha)\\ &\quad +2\frac{\partial\alpha}{\partial \theta}[2\sigma_{xy}\cos(2\alpha)-(\sigma_{xx}-\sigma_{yy})\sin(2\alpha)]\\ &= \frac{\partial(\sigma_{xx}-\sigma_{yy})}{\partial \theta}\cos(2\alpha)+2\frac{\partial\sigma_{xy}}{\partial \theta}\sin(2\alpha)\\ &\quad +2\frac{\partial\alpha}{\partial \theta}[2\sigma_{xy}\cos(2\alpha)-2\sigma_{xy}\cos(2\alpha)]\\ &= \frac{\partial(\sigma_{xx}-\sigma_{yy})}{\partial \theta}\cos(2\alpha)+2\frac{\partial\sigma_{xy}}{\partial \theta}\sin(2\alpha)\end{aligned} \tag{A.18}$$

Writing these derivatives in terms of polar coordinates first requires determining r and θ derivatives of $\sigma_{xx}-\sigma_{yy}$ and σ_{xy}:

$$\begin{aligned}\sigma_{xx}-\sigma_{yy} &= \sigma_{rr}(\cos^2(\theta)-\sin^2(\theta))-\sigma_{\theta\theta}(\cos^2(\theta)-\sin^2(\theta))-2\sigma_{r\theta}\sin(2\theta)\\ &= (\sigma_{rr}-\sigma_{\theta\theta})\cos(2\theta)-2\sigma_{r\theta}\sin(2\theta)\end{aligned} \tag{A.19}$$

$$\frac{\partial(\sigma_{xx}-\sigma_{yy})}{\partial r} = \frac{\partial(\sigma_{rr}-\sigma_{\theta\theta})}{\partial r}\cos(2\theta)-2\frac{\partial\sigma_{r\theta}}{\partial r}\sin(2\theta) \tag{A.20}$$

$$\frac{\partial(\sigma_{xx}-\sigma_{yy})}{\partial \theta} =\Big[\frac{\partial(\sigma_{rr}-\sigma_{\theta\theta})}{\partial \theta}-4\sigma_{r\theta}\Big]\cos(2\theta)-2\Big[\frac{\partial\sigma_{r\theta}}{\partial\theta}+(\sigma_{rr}-\sigma_{\theta\theta})\Big]\sin(2\theta). \tag{A.21}$$

With Equations (A.17), (A.18), (A.20), and (A.21), the r and θ derivatives of $\sigma_1-\sigma_2$ may be written in terms of polar coordinates:

$$\frac{\partial(\sigma_1-\sigma_2)}{\partial r} = \frac{\partial(\sigma_{rr}-\sigma_{\theta\theta})}{\partial r}\cos(2\theta-2\alpha) - 2\frac{\partial\sigma_{r\theta}}{\partial r}\sin(2\theta-2\alpha) \tag{A.22}$$

$$\begin{aligned}\frac{\partial(\sigma_1-\sigma_2)}{\partial \theta} &= \frac{\partial(\sigma_{rr}-\sigma_{\theta\theta})}{\partial \theta}\cos(2\theta-2\alpha) - 2\frac{\partial\sigma_{r\theta}}{\partial \theta}\sin(2\theta-2\alpha) \\ &\quad - 2(\sigma_{rr}-\sigma_{\theta\theta})\sin(2\theta-2\alpha) - 4\sigma_{r\theta}\cos(2\theta-2\alpha).\end{aligned} \tag{A.23}$$

The x and y derivatives of $\sigma_1-\sigma_2$ in terms of Cartesian and polar coordinates are easily obtained from Equations (A.17), (A.18), (A.22), and (A.23).

$$\begin{aligned}\frac{\partial(\sigma_1-\sigma_2)}{\partial x} &= \cos(\theta)\frac{\partial(\sigma_1-\sigma_2)}{\partial r} - \frac{\sin(\theta)}{r}\frac{\partial(\sigma_1-\sigma_2)}{\partial \theta} \\ &= \left[\cos(\theta)\frac{\partial(\sigma_{xx}-\sigma_{yy})}{\partial r} - \frac{\sin(\theta)}{r}\frac{\partial(\sigma_{xx}-\sigma_{yy})}{\partial \theta}\right]\cos(2\alpha) \\ &\quad + 2\left[\cos(\theta)\frac{\partial\sigma_{xy}}{\partial r} - \frac{\sin(\theta)}{r}\frac{\partial\sigma_{xy}}{\partial \theta}\right]\sin(2\alpha)\end{aligned} \tag{A.24}$$

$$\begin{aligned}\frac{\partial(\sigma_1-\sigma_2)}{\partial y} &= \sin(\theta)\frac{\partial(\sigma_1-\sigma_2)}{\partial r} + \frac{\cos(\theta)}{r}\frac{\partial(\sigma_1-\sigma_2)}{\partial \theta} \\ &= \left[\sin(\theta)\frac{\partial(\sigma_{xx}-\sigma_{yy})}{\partial r} + \frac{\cos(\theta)}{r}\frac{\partial(\sigma_{xx}-\sigma_{yy})}{\partial \theta}\right]\cos(2\alpha) \\ &\quad + 2\left[\sin(\theta)\frac{\partial\sigma_{xy}}{\partial r} + \frac{\cos(\theta)}{r}\frac{\partial\sigma_{xy}}{\partial \theta}\right]\sin(2\alpha)\end{aligned} \tag{A.25}$$

$$\begin{aligned}\frac{\partial(\sigma_1-\sigma_2)}{\partial x} &= \cos(\theta)\frac{\partial(\sigma_1-\sigma_2)}{\partial r} - \frac{\sin(\theta)}{r}\frac{\partial(\sigma_1-\sigma_2)}{\partial \theta} \\ &= \left[\cos(\theta)\frac{\partial(\sigma_{rr}-\sigma_{\theta\theta})}{\partial r} - \frac{\sin(\theta)}{r}\left(\frac{\partial(\sigma_{rr}-\sigma_{\theta\theta})}{\partial \theta} - 4\sigma_{r\theta}\right)\right]\cos(2\theta-2\alpha) \\ &\quad - 2\left[\cos(\theta)\frac{\partial\sigma_{r\theta}}{\partial r} - \frac{\sin(\theta)}{r}\left(\frac{\partial\sigma_{r\theta}}{\partial \theta} + (\sigma_{rr}-\sigma_{\theta\theta})\right)\right]\sin(2\theta-2\alpha)\end{aligned} \tag{A.26}$$

$$\begin{aligned}\frac{\partial(\sigma_1-\sigma_2)}{\partial y} &= \sin(\theta)\frac{\partial(\sigma_1-\sigma_2)}{\partial r} + \frac{\cos(\theta)}{r}\frac{\partial(\sigma_1-\sigma_2)}{\partial \theta} \\ &= \left[\sin(\theta)\frac{\partial(\sigma_{rr}-\sigma_{\theta\theta})}{\partial r} + \frac{\cos(\theta)}{r}\left(\frac{\partial(\sigma_{rr}-\sigma_{\theta\theta})}{\partial \theta} - 4\sigma_{r\theta}\right)\right]\cos(2\theta-2\alpha) \\ &\quad - 2\left[\sin(\theta)\frac{\partial\sigma_{r\theta}}{\partial r} + \frac{\cos(\theta)}{r}\left(\frac{\partial\sigma_{r\theta}}{\partial \theta} + (\sigma_{rr}-\sigma_{\theta\theta})\right)\right]\sin(2\theta-2\alpha)\end{aligned} \tag{A.27}$$

The analysis for CGS for photoelastic materials requires determining the x and y derivatives of α; this first requires the r and θ derivatives of α, which come from taking the r and θ derivatives of $\tan(2\alpha) = 2\sigma_{xy}/(\sigma_{xx} - \sigma_{yy})$:

$$\begin{aligned}
\frac{\partial}{\partial r}[\tan(2\alpha)] &= \frac{\partial}{\partial r}\Big[\frac{2\sigma_{xy}}{\sigma_{xx}-\sigma_{yy}}\Big] \\
\frac{\partial \alpha}{\partial r}\frac{2}{\cos^2(2\alpha)} &= \frac{\partial \sigma_{xy}}{\partial r}\frac{2}{\sigma_{xx}-\sigma_{yy}} - \frac{\partial(\sigma_{xx}-\sigma_{yy})}{\partial r}\frac{2\sigma_{xy}}{(\sigma_{xx}-\sigma_{yy})^2} \\
\frac{\partial \alpha}{\partial r} &= \frac{\cos^2(2\alpha)}{\sigma_{xx}-\sigma_{yy}}\Big[\frac{\partial \sigma_{xy}}{\partial r} - \frac{\tan(2\alpha)}{2}\frac{\partial(\sigma_{xx}-\sigma_{yy})}{\partial r}\Big],
\end{aligned} \tag{A.28}$$

$$\begin{aligned}
\frac{\partial}{\partial \theta}[\tan(2\alpha)] &= \frac{\partial}{\partial \theta}\Big[\frac{2\sigma_{xy}}{\sigma_{xx}-\sigma_{yy}}\Big] \\
\frac{\partial \alpha}{\partial \theta}\frac{2}{\cos^2(2\alpha)} &= \frac{\partial \sigma_{xy}}{\partial \theta}\frac{2}{\sigma_{xx}-\sigma_{yy}} - \frac{\partial(\sigma_{xx}-\sigma_{yy})}{\partial \theta}\frac{2\sigma_{xy}}{(\sigma_{xx}-\sigma_{yy})^2} \\
\frac{\partial \alpha}{\partial \theta} &= \frac{\cos^2(2\alpha)}{\sigma_{xx}-\sigma_{yy}}\Big[\frac{\partial \sigma_{xy}}{\partial \theta} - \frac{\tan(2\alpha)}{2}\frac{\partial(\sigma_{xx}-\sigma_{yy})}{\partial \theta}\Big].
\end{aligned} \tag{A.29}$$

The x and y derivatives of α may be written as

$$\begin{aligned}
\frac{\partial \alpha}{\partial x} &= \cos(\theta)\frac{\partial \alpha}{\partial r} - \frac{\sin(\theta)}{r}\frac{\partial \alpha}{\partial \theta} \\
&= \frac{\cos^2(2\alpha)}{\sigma_{xx}-\sigma_{yy}}\Big\{\cos(\theta)\Big[\frac{\partial \sigma_{xy}}{\partial r} - \frac{\tan(2\alpha)}{2}\frac{\partial(\sigma_{xx}-\sigma_{yy})}{\partial r}\Big] \\
&\qquad - \frac{\sin(\theta)}{r}\Big[\frac{\partial \sigma_{xy}}{\partial \theta} - \frac{\tan(2\alpha)}{2}\frac{\partial(\sigma_{xx}-\sigma_{yy})}{\partial \theta}\Big]\Big\},
\end{aligned} \tag{A.30}$$

$$\begin{aligned}
\frac{\partial \alpha}{\partial y} &= \sin(\theta)\frac{\partial \alpha}{\partial r} + \frac{\cos(\theta)}{r}\frac{\partial \alpha}{\partial \theta} \\
&= \frac{\cos^2(2\alpha)}{\sigma_{xx}-\sigma_{yy}}\Big\{\sin(\theta)\Big[\frac{\partial \sigma_{xy}}{\partial r} - \frac{\tan(2\alpha)}{2}\frac{\partial(\sigma_{xx}-\sigma_{yy})}{\partial r}\Big] \\
&\qquad + \frac{\cos(\theta)}{r}\Big[\frac{\partial \sigma_{xy}}{\partial \theta} - \frac{\tan(2\alpha)}{2}\frac{\partial(\sigma_{xx}-\sigma_{yy})}{\partial \theta}\Big]\Big\}.
\end{aligned} \tag{A.31}$$

Appendix B

Derivation of Analytical Solutions for Various Loading Conditions

B.1 V-Notch Stress Field Derivation

Williams (1952) presented a derivation of the stress fields of a thin plate with an "angular corner" cut out of it under uniaxial tensile load with various boundary conditions. This derivation is most commonly utilized for the derivation of the stress field of a Mode-I crack, which is a corner of angle 0^o, in a plate. Here, the derivation is applied to a thin plate with a 60^o V-shaped notch under uniaxial compression, as shown in Figure B.1. β is the angle of the material about the notch tip at the origin; therefore here $\beta = 300^o = 5\pi/3$. The V-notch is symmetric about the x-axis, and the compressive load is applied along the y-axis. The free-free boundary conditions are for the edges of the corner and not the boundaries of the plate, since the solution is for an infinite plate: $\sigma_{r\theta} = \sigma_{\theta\theta} = 0$ at $\theta = \pm\beta/2$.

The 2D stress field for this configuration may be derived using the following Airy stress potential:

$$\phi(r, \theta) = r^{\lambda+1} F(\theta), \tag{B.1}$$

where $F(\theta)$ solves the differential equation

$$\left(\frac{d^2}{d\theta^2} + (\lambda+1)^2\right)\left(\frac{d^2}{d\theta^2} + (\lambda-1)^2\right)F(\theta) = 0. \tag{B.2}$$

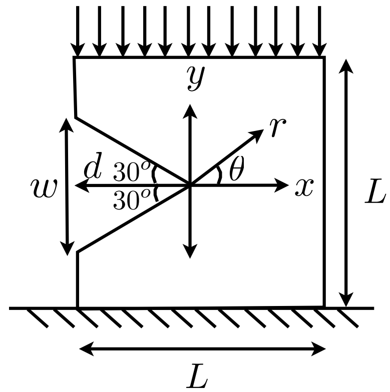

Figure B.1: Schematic of compressed plate with a side V-notch

The general solution to Equation (B.2) is

$$F(\theta) = A_1 \cos[(\lambda+1)\theta] + A_2 \sin[(\lambda+1)\theta] + A_3 \cos[(\lambda-1)\theta] + A_4 \sin[(\lambda-1)\theta]. \tag{B.3}$$

The 2D stress components are the following in terms of r, $F(\theta)$, and λ:

$$\begin{aligned}\begin{bmatrix} \sigma_{rr} & \sigma_{r\theta} \\ \sigma_{r\theta} & \sigma_{\theta\theta} \end{bmatrix} &= \begin{bmatrix} \frac{1}{r}\frac{\partial \phi}{\partial r} + \frac{1}{r^2}\frac{\partial^2 \phi}{\partial \theta} & \frac{\partial^2 \phi}{\partial r} \\ \frac{\partial^2 \phi}{\partial r} & -\frac{\partial}{\partial r}\left(\frac{1}{r}\frac{\partial \phi}{\partial \theta}\right) \end{bmatrix} \\ &= \begin{bmatrix} r^{\lambda-1}[F^{''}(\theta) + (\lambda+1)F(\theta)] & -\lambda r^{\lambda-1}F^{'}(\theta) \\ -\lambda r^{\lambda-1}F^{'}(\theta) & \lambda(\lambda+1)r^{\lambda+1}F(\theta) \end{bmatrix}.\end{aligned} \tag{B.4}$$

The $F^{'}(\theta)$ and $F^{''}(\theta)$ are

$$\begin{aligned} F^{'}(\theta) = &-(\lambda+1)A_1 \sin[(\lambda+1)\theta] + (\lambda+1)A_2 \cos[(\lambda+1)\theta] \\ &-(\lambda-1)A_3 \sin[(\lambda-1)\theta] + (\lambda-1)A_4 \cos[(\lambda-1)\theta] \end{aligned} \tag{B.5}$$

$$\begin{aligned} F^{''}(\theta) = &-(\lambda+1)^2 A_1 \cos[(\lambda+1)\theta] - (\lambda+1)^2 A_2 \sin[(\lambda+1)\theta] \\ &-(\lambda-1)^2 A_3 \cos[(\lambda-1)\theta] - (\lambda-1)^2 A_4 \sin[(\lambda-1)\theta]. \end{aligned} \tag{B.6}$$

In light of the traction-free boundary conditions at $\theta = \pm\beta/2$ and the above equations for stress, the following equations involving λ emerge:

$$\sigma_{\theta\theta}\Big|_{\theta=+\frac{\beta}{2}} = 0 = \lambda(\lambda+1)r^{\lambda-1}\{A_1\cos[(\lambda+1)\tfrac{\beta}{2}] + A_2\sin[(\lambda+1)\tfrac{\beta}{2}] + A_3\cos[(\lambda-1)\tfrac{\beta}{2}] + A_4\sin[(\lambda-1)\tfrac{\beta}{2}]\} \tag{B.7}$$

$$\sigma_{\theta\theta}\Big|_{\theta=-\frac{\beta}{2}} = 0 = \lambda(\lambda+1)r^{\lambda-1}\{A_1\cos[(\lambda+1)\tfrac{\beta}{2}] - A_2\sin[(\lambda+1)\tfrac{\beta}{2}] + A_3\cos[(\lambda-1)\tfrac{\beta}{2}] - A_4\sin[(\lambda-1)\tfrac{\beta}{2}]\} \tag{B.8}$$

$$\sigma_{r\theta}\Big|_{\theta=+\frac{\beta}{2}} = 0 = -\lambda r^{\lambda-1}\{-(\lambda+1)A_1\sin[(\lambda+1)\tfrac{\beta}{2}] + (\lambda+1)A_2\cos[(\lambda+1)\tfrac{\beta}{2}] - (\lambda-1)A_3\sin[(\lambda-1)\tfrac{\beta}{2}] + (\lambda-1)A_4\cos[(\lambda-1)\tfrac{\beta}{2}]\} \tag{B.9}$$

$$\sigma_{r\theta}\Big|_{\theta=-\frac{\beta}{2}} = 0 = -\lambda r^{\lambda-1}\{(\lambda+1)A_1\sin[(\lambda+1)\tfrac{\beta}{2}] + (\lambda+1)A_2\cos[(\lambda+1)\tfrac{\beta}{2}] + (\lambda-1)A_3\sin[(\lambda-1)\tfrac{\beta}{2}] + (\lambda-1)A_4\cos[(\lambda-1)\tfrac{\beta}{2}]\}. \tag{B.10}$$

Constants A_1–A_4 cannot be uniquely determined solely from the four boundary conditions because Equations (B.7)–(B.10) form a homogenous system of equations; therefore the determinant of this system must go to zero. Williams (1952) determined the eigen-equation for this free-free boundary condition:

$$\sin(\lambda\beta) = \pm\lambda\frac{\sin(\beta)}{\beta}. \tag{B.11}$$

Equation (B.11) determines the values of λ as a function of β. For continuity of displacements, $\lambda > 0$. The *min Re* λ such that $\lambda > 0$ is chosen, which results in unbounded stresses near the tip of the notch. For $\beta = 5\pi/3$, this λ is $\lambda_o = 0.512221$. Therefore, the Airy stress potential is Equation (B.12) in terms of A_1 and A_2:

$$\phi(r,\theta) = r^{\lambda_o+1}\Big[A_1\Big\{\cos[(\lambda_o+1)\theta] - \frac{\cos[(\lambda_o+1)\frac{\beta}{2}]}{\cos[(\lambda_o-1)\frac{\beta}{2}]}\cos[(\lambda_o-1)\theta]\Big\} A_2\Big\{\sin[(\lambda_o+1)\theta] - \frac{\sin[(\lambda_o+1)\frac{\beta}{2}]}{\sin[(\lambda_o-1)\frac{\beta}{2}]}\sin[(\lambda_o-1)\theta]\Big\}\Big]. \tag{B.12}$$

With uniaxial extension or compression along the y axis, only the symmetric portion of the Airy stress potential applies, as given in Equation (B.13).

$$\phi^{sym}(r,\theta) = A_1 r^{\lambda_o+1}\Big\{\cos[(\lambda_o+1)\theta] - \frac{\cos[(\lambda_o+1)\frac{\beta}{2}]}{\cos[(\lambda_o-1)\frac{\beta}{2}]}\cos[(\lambda_o-1)\theta]\Big\}. \tag{B.13}$$

With Equations (B.4) and (B.13), the 2D stresses may be written in terms of the constant A_1:

$$\sigma_{rr}(r,\theta) = \frac{A_1}{r^{1-\lambda_o}}\Big\{-\lambda_o(\lambda_o+1)\cos[(\lambda_o+1)\theta] + \lambda_o(\lambda_o-3)\frac{\cos[(\lambda_o+1)\frac{\beta}{2}]}{\cos[(\lambda_o-1)\frac{\beta}{2}]}\cos[(\lambda_o-1)\theta]\Big\} \tag{B.14}$$

$$\sigma_{\theta\theta}(r,\theta) = \frac{A_1\lambda_o(\lambda_o+1)}{r^{1-\lambda_o}}\Big\{\cos[(\lambda_o+1)\theta] - \frac{\cos[(\lambda_o+1)\frac{\beta}{2}]}{\cos[(\lambda_o-1)\frac{\beta}{2}]}\cos[(\lambda_o-1)\theta]\Big\} \tag{B.15}$$

$$\sigma_{r\theta}(r,\theta) = \frac{A_1\lambda_o}{r^{1-\lambda_o}}\Big\{(\lambda_o+1)\sin[(\lambda_o+1)\theta] - (\lambda_o-1)\frac{\cos[(\lambda_o+1)\frac{\beta}{2}]}{\cos[(\lambda_o-1)\frac{\beta}{2}]}\sin[(\lambda_o-1)\theta]\Big\}. \tag{B.16}$$

The constant A_1 is related to the applied stress in the far-field. Since the 2D stress field is in units of N/m^2, then A_1 is linearly related to applied stress, σ_{app}, and is related to the depth of the V-notch, d, to the power $1-\lambda_o$, such that

$$A_1 = C\sigma_{app}d^{1-\lambda_o}, \tag{B.17}$$

where C is a fitting constant depending on specimen geometry. With this factor, the 2D stresses become

$$\sigma_{rr}(r,\theta) = \frac{C\sigma_{app}d^{1-\lambda_o}}{(r)^{1-\lambda_o}}\Big\{-\lambda_o(\lambda_o+1)\cos[(\lambda_o+1)\theta] + \lambda_o(\lambda_o-3)\frac{\cos[(\lambda_o+1)\frac{\beta}{2}]}{\cos[(\lambda_o-1)\frac{\beta}{2}]}\cos[(\lambda_o-1)\theta]\Big\} \tag{B.18}$$

$$\sigma_{\theta\theta}(r,\theta) = \frac{C\sigma_{app}d^{1-\lambda_o}\lambda_o(\lambda_o+1)}{(r)^{1-\lambda_o}}\Big\{\cos[(\lambda_o+1)\theta] - \frac{\cos[(\lambda_o+1)\frac{\beta}{2}]}{\cos[(\lambda_o-1)\frac{\beta}{2}]}\cos[(\lambda_o-1)\theta]\Big\} \tag{B.19}$$

$$\sigma_{r\theta}(r,\theta) = \frac{C\sigma_{app}d^{1-\lambda_o}\lambda_o}{(r)^{1-\lambda_o}}\Big\{(\lambda_o+1)\sin[(\lambda_o+1)\theta] - (\lambda_o-1)\frac{\cos[(\lambda_o+1)\frac{\beta}{2}]}{\cos[(\lambda_o-1)\frac{\beta}{2}]}\sin[(\lambda_o-1)\theta]\Big\}. \tag{B.20}$$

Appendix C

Phase-Shifting Photoelasticity

Pockels developed a mathematical theory for photoelasticity in crystals known as Pockels' Phenomenological Theory (Narasimhamurty, 1981). This theory can be used to develop the well-known Stress Optic Law for photoelastic materials that are isotropic in structure and to develop stress-related equations for refractive index change in crystalline materials. The basics of this theory, based on (Narasimhamurty, 1981), are presented in this appendix, and the Stress Optic Law is derived.

A flexible and comprehensive method for analysis of a polariscope is by the use of matrices representing the action of each type of polarizing optic, i.e., using the matrix theory of photoelasticity. Theocaris and Gdoutos (1979) presented the matrices for Jones matrix algebra, which assumes that the incident light is polarized. The equations for the electric field after a polariscope result from Jones matrix algebra. The intensity of the interference pattern may then be calculated. Another, more general, method to determine the intensity of the images from a polariscope is Mueller calculus with Stokes vectors. This method does not require that the incoming light be polarized. A full treatment of Jones matrix algebra and Mueller calculus applied to the circular polariscope follows in this appendix.

By using appropriate configurations of the circular polariscope elements, different interference patterns related to the isoclinic angle and the isochromatic phase may be manipulated during analysis of the patterns to separate these two quantities of interest. This type of phase shifting is unlike the common methods that introduce a known phase shift, but capitalizes on the adaptability of the circular polariscope to achieve different trigonometric functions of the desired phases. The entire derivation of the six-step method used in this research is provided below.

C.1 Photoelasticity of Crystals: Pockels' Phenomenological Theory

The impermeability tensor $(1/K)_{ij}$ is given by $B_{ij} = 1/n_{ij}^2$. The triaxial ellipsoid surface called the optical index ellipsoid has the formula $B_{ij}x_ix_j = 1$. The optical properties of crystals are often expressed in terms of the principal refractive indicies, by way of the refractive index ellipsoid, given by

$$\frac{x^2}{n_x^2} + \frac{y^2}{n_y^2} + \frac{z^2}{n_z^2} = 1. \tag{C.1}$$

The assumptions used in this theory are the following:

1. In a homogeneously deformed solid, the effect of deformation is only to alter the optical parameters of the optical index ellipsoid.

2. When the strain is within the elastic limits, the change of an optical parameter (polarization constant) of the solid due to deformation can be expressed as a homogeneous linear function of the nine stress components, σ_{ij}, or nine strain components, ϵ_{ij}.

C.1.1 Mathematical Formulation in Terms of the Photoelastic Constants

An undeformed crystal has an index ellipsoid of $B_{ij}^o x_i x_j = 1$. A stressed crystal has an index ellipsoid of $B_{ij}x_ix_j = 1$. Using the second assumption about linearity of the stress (strain)-impermeability tensor, then

$$B_{ij} - B_{ij}^o = -q_{ijkl}\sigma_{kl} \tag{C.2}$$

$$B_{ij} - B_{ij}^o = p_{ijkl}\epsilon_{kl}. \tag{C.3}$$

The p_{ijkl} components are called the strain-optical or elasto-optic constants. The q_{ijkl} components are called the stress-optical or piezo-optic coefficients

Assuming the ΔB_{ij}, σ_{kl}, and ϵ_{kl} second-rank tensors are symmetric, then the 81 components of the q_{ijkl} fourth-rank tensor reduce to 36 independent components ($q_{ijkl} = q_{jikl}$ and $q_{ijkl} = q_{ijlk}$), and also the 81 components of the p_{ijkl} fourth-rank tensor reduce to 36 independent components ($p_{ijkl} = p_{jikl}$ and $p_{ijkl} = p_{ijlk}$). The p_{ijkl} and q_{ijkl} tensors can be related by the elastic stiffness constants, c_{ijkl}, and compliance constants, s_{ijkl}:

$$q_{ijkl} = p_{ijmn} s_{mnkl} \tag{C.4}$$

$$p_{ijmn} = q_{ijkl} c_{klmn}. \tag{C.5}$$

The common notation uses two suffixes. The impermeability tensor B_{ij} can be written as B_i with $i = 1-6$ ($B_{11} = B_1$, $B_{22} = B_2$, $B_{33} = B$, $B_{23} = B_4$, $B_{31} = B_5$, and $B_{12} = B_6$). The stress and strain tensors adopt the same corresponding notation as the impermeability tensor. The photoelastic coefficient tensors, p_{ijkl} and q_{ijkl}, are written as p_{ij} and q_{ij} with $i, j = 1-6$. The governing photoelastic equations Equation (C.2) and Equation (C.3) become

$$B_i - B_i^o = -q_{ij} \sigma_j \tag{C.6}$$

$$B_i - B_i^o = p_{ij} \epsilon_j. \tag{C.7}$$

With this two-suffix notation, the relationships between p_{ij} and q_{ij} are related by c_{ij} and s_{ij} with $i, j = 1-6$:

$$p_{ij} = q_{ik} c_{kj} \tag{C.8}$$

$$q_{ij} = p_{ik} s_{kj}. \tag{C.9}$$

C.1.2 Considering Crystal Symmetry

The above mathematics applies most generally to triclinic crystals. The photoelastic coefficients can be further simplified with higher crystal symmetry. The isotropic case reduces the photoelastic tensors to two independent coefficients each:

$$p^{isotropic} = \begin{bmatrix} p_{11} & p_{12} & p_{12} & 0 & 0 & 0 \\ p_{12} & p_{11} & p_{12} & 0 & 0 & 0 \\ p_{12} & p_{12} & p_{11} & 0 & 0 & 0 \\ 0 & 0 & 0 & \frac{1}{2}(p_{11}-p_{12}) & 0 & 0 \\ 0 & 0 & 0 & 0 & \frac{1}{2}(p_{11}-p_{12}) & 0 \\ 0 & 0 & 0 & 0 & 0 & \frac{1}{2}(p_{11}-p_{12}) \end{bmatrix} \tag{C.10}$$

$$q^{isotropic} = \begin{bmatrix} q_{11} & q_{12} & q_{12} & 0 & 0 & 0 \\ q_{12} & q_{11} & q_{12} & 0 & 0 & 0 \\ q_{12} & q_{12} & q_{11} & 0 & 0 & 0 \\ 0 & 0 & 0 & (q_{11}-q_{12}) & 0 & 0 \\ 0 & 0 & 0 & 0 & (q_{11}-q_{12}) & 0 \\ 0 & 0 & 0 & 0 & 0 & (q_{11}-q_{12}) \end{bmatrix}. \tag{C.11}$$

A cubic crystal systems in group 11, (T_d, O, O_h ($4\bar{3}m$, 43, $m3m$)), reduce to three constants;

magnesium oxide (MgO) has this symmetry.

$$p^{cubic-11} = \begin{bmatrix} p_{11} & p_{12} & p_{12} & 0 & 0 & 0 \\ p_{12} & p_{11} & p_{12} & 0 & 0 & 0 \\ p_{12} & p_{12} & p_{11} & 0 & 0 & 0 \\ 0 & 0 & 0 & p_{44} & 0 & 0 \\ 0 & 0 & 0 & 0 & p_{44} & 0 \\ 0 & 0 & 0 & 0 & 0 & p_{44} \end{bmatrix} \tag{C.12}$$

$$q^{cubic-11} = \begin{bmatrix} q_{11} & q_{12} & q_{12} & 0 & 0 & 0 \\ q_{12} & q_{11} & q_{12} & 0 & 0 & 0 \\ q_{12} & q_{12} & q_{11} & 0 & 0 & 0 \\ 0 & 0 & 0 & q_{44} & 0 & 0 \\ 0 & 0 & 0 & 0 & q_{44} & 0 \\ 0 & 0 & 0 & 0 & 0 & q_{44} \end{bmatrix}. \tag{C.13}$$

C.1.3 Connection to Linearized Theory

The isotropic case greatly simplifies the photoelastic equations:

$$B_1 - B_1^o = -(q_{11}\sigma_1 + q_{12}\sigma_2 + q_{12}\sigma_3) \tag{C.14}$$

$$B_2 - B_2^o = -(q_{12}\sigma_1 + q_{11}\sigma_2 + q_{12}\sigma_3) \tag{C.15}$$

$$B_3 - B_3^o = -(q_{12}\sigma_1 + q_{12}\sigma_2 + q_{11}\sigma_3) \tag{C.16}$$

$$B_4 - B_4^o = -(q_{11} - q_{12})\sigma_4 \tag{C.17}$$

$$B_5 - B_5^o = -(q_{11} - q_{12})\sigma_5 \tag{C.18}$$

$$B_6 - B_6^o = -(q_{11} - q_{12})\sigma_6. \tag{C.19}$$

For an isotropic material, $B_1^o = B_2^o = B_3^o = (1/(n_o^2))$, where n_o is the refractive index of the unstressed material; also, $B_4^o = B_5^o = B_6^o = 0$. By manipulating Equations (C.14)–C.16), the following equations result:

$$\frac{1}{n_1^2} - \frac{1}{n_2^2} = -(q_{11} - q_{12})(\sigma_1 - \sigma_2) \tag{C.20}$$

$$\frac{1}{n_1^2} - \frac{1}{n_3^2} = -(q_{11} - q_{12})(\sigma_1 - \sigma_3) \tag{C.21}$$

$$\frac{1}{n_2^2} - \frac{1}{n_3^2} = -(q_{11} - q_{12})(\sigma_2 - \sigma_3). \tag{C.22}$$

If the quadratic refractive index term is ignored, then $B_i - B_j$ terms can be simplified. For example,

$$\begin{aligned}\frac{1}{n_1^2} - \frac{1}{n_2^2} &= \frac{n_2^2 - n_1^2}{n_1^2 n_2^2} \\ &\simeq \frac{-(n_1 - n_2)(n_1 + n_2)}{n_o^4} \\ &\simeq \frac{-(n_1 - n_2)(2n_o)}{n_o^4} \\ &\simeq \frac{-(n_1 - n_2)}{n_o^3/2},\end{aligned} \tag{C.23}$$

assuming $n_1^2 n_2^2 \simeq n_o^4$ and $(n_1 + n_2) \simeq 2n_o$. Equations (C.20)–C.22) become the following:

$$n_1 - n_2 = \frac{n_o^3}{2}(q_{11} - q_{12})(\sigma_1 - \sigma_2) \tag{C.24}$$

$$n_1 - n_3 = \frac{n_o^3}{2}(q_{11} - q_{12})(\sigma_1 - \sigma_3) \tag{C.25}$$

$$n_2 - n_3 = \frac{n_o^3}{2}(q_{11} - q_{12})(\sigma_2 - \sigma_3) \tag{C.26}$$

The Maxwell equations for the photoelastic effect for isotropic materials are the above Equations (C.24)–C.26, given $(n_o^3/2)(q_{11} - q_{12}) = (C_1 - C_2) = C$, where C is the relative stress-optic coefficient. If the coordinate system is in the principal axes, then $\sigma_4 = \sigma_5 = \sigma_6 = 0$, and σ_1, σ_2, and σ_3 are the principal stresses.

The cubic equations with three constants result in the same relations as the isotropic case. In the plane stress case, σ_3 is zero. If the third principal axis is the optical axis, then only Equation (C.24) needs to be considered experimentally.

C.1.4 Stress Optic Law

A photoelastic plate under stress acts as a linear retarder plate for polarized light with linear retardation δ with a fast axis at angle α relative to the x axis. The change in refractive index in the plane perpendicular to the optical axis is related to δ by the thickness of the plate h and the wavelength λ,: $n_1 - n_2 = \delta\lambda/(2\pi h)$. Therefore, the governing equation, the Stress Optic Law, may be written as the following (Kobayashi, 1993; Narasimhamurty, 1981):

$$\sigma_1 - \sigma_2 = \frac{\delta\lambda}{2\pi c_o h} = \frac{N\lambda}{c_o h}, \tag{C.27}$$

where $N = \delta/2\pi$ is the "fringe order".

C.2 Matrix Theory of Photoelasticity and Circular Polariscopes

C.2.1 Jones Matrix Algebra

A circular polariscope includes an incident collimated beam of light, followed by a linear polarizer at angle ρ to the x axis, a 1/4 wave plate with fast axis at angle ξ to the x axis, a photoelastic material, another 1/4 wave plate with fast axis at angle ϕ to the x axis, and a second linear polarizer at angle ζ to the x axis, sometimes called the analyzer. Figure C.1 shows a schematic of the polariscope. Assuming that the collimated laser beam is polarized, then Jones matrix algebra may be used to analyze the electric field components incident to the sample (Theocaris and Gdoutos, 1979). Note: Theocaris and Gdoutos (1979) employs reference axes such that the x and y are perpendicular to the incident beam relative to the *front* of the optics. The reference axes x and y used in this research are perpendicular to the light beam, which is along the $+z$ axis, on the *back* of the optics, as shown

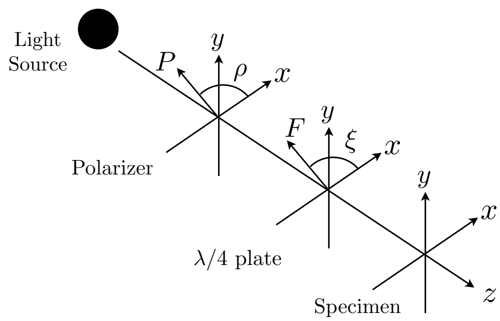

Figure C.1: Polarization optics before the transparent sample

in Figure C.1. The electric field prior to the polarizer is given in vector form by Equation (C.28):

$$\boldsymbol{E} = \begin{bmatrix} E_{ox} exp[j(kz - \omega t + \varphi_x)] \\ \\ E_{oy} exp[j(kz - \omega t + \varphi_y)] \end{bmatrix}. \tag{C.28}$$

The Jones vector, $\boldsymbol{a}$, represents the time-averaged x and y spatial amplitude and phase components of the electric field, a_x and a_y. Thus the Jones vector of the collimated light in Equation (C.28) is

$$\boldsymbol{a}^{collimated} = \begin{bmatrix} a_x \\ \\ a_y \end{bmatrix} = \begin{bmatrix} E_{ox} exp[j(kz + \varphi_x)] \\ \\ E_{oy} exp[j(kz + \varphi_y)] \end{bmatrix}. \tag{C.29}$$

After passing through a polarization optic, the electric field obviously changes, represented by the multiplication of the Jones matrix of the the polarization optic and the Jones vector of the incident electric field. Therefore, Jones matrix algebra is a compact way of determining the changes in an initially linearly polarized electric field due to polarization optics. The Jones matrices for a linear polarizer at angle ρ to the x axis and for a 1/4 wave plate with fast axis at angle ξ to the x

axis are as follows:

$$\mathbf{P}_{\rho} = \begin{bmatrix} \cos^2(\rho) & -cos(\rho)sin(\rho) \\ -cos(\rho)sin(\rho) & \sin^2(\rho) \end{bmatrix} \tag{C.30}$$

$$\mathbf{Q}_{\xi} = \begin{bmatrix} j\cos^2(\xi) + \sin^2(\xi) & (1-j)cos(\xi)sin(\xi) \\ (1-j)cos(\xi)sin(\xi) & j\sin^2(\xi) + \cos^2(\xi) \end{bmatrix}. \tag{C.31}$$

Generally, the electric field incident to the sample in Figure C.1 is given by Equation (C.32):

$$\boldsymbol{a}^{incident} = \mathbf{Q}_{\xi}\mathbf{P}_{\rho}\boldsymbol{a}^{\mathbf{collimated}}. \tag{C.32}$$

For example, if $\rho = \pi/2$ and $\xi = 3\pi/4$, then the electric field components have the same constant $A_o = \sqrt{2}E_{oy}/2$, as shown in Equation (C.33):

$$\begin{aligned} \boldsymbol{a}^{incident} = \mathbf{Q}_{\frac{3\pi}{4}}\mathbf{P}_{\frac{\pi}{2}}\boldsymbol{a}^{collimated} &= \frac{\sqrt{2}E_{oy}exp[j(kz+\varphi_y)]}{2}\begin{bmatrix} exp[j\frac{3\pi}{4}] \\ exp[j\frac{\pi}{4}] \end{bmatrix} \\ &= \begin{bmatrix} A_o exp[j(kz+\phi_x)] \\ A_o exp[j(kz+\phi_y)] \end{bmatrix}. \end{aligned} \tag{C.33}$$

A photoelastic material is modeled in terms of polarization optics as a linear retardation plate with retardation δ (the isochromatic phase) with fast axis at angle α (the isoclinic angle) to the x axis. The Jones matrix for such a linear retardation plate is as follows:

$$\mathbf{R}_{\delta,\alpha} = \begin{bmatrix} e^{j\delta}\cos^2(\alpha) + \sin^2(\alpha) & (1-e^{j\delta})cos(\alpha)sin(\alpha) \\ (1-e^{j\delta})cos(\alpha)sin(\alpha) & e^{j\delta}\sin^2(\alpha) + \cos^2(\alpha) \end{bmatrix}. \tag{C.34}$$

The general full expression for the electric field after a circular polariscope with all five elements is as follows:

$$\boldsymbol{E}^{out} = \mathbf{P}_{\zeta}\mathbf{Q}_{\phi}\mathbf{R}_{\delta,\alpha}\mathbf{Q}_{\xi}\mathbf{P}_{\rho}\boldsymbol{E}. \tag{C.35}$$

The intensity of the resulting image is a result of taking the dot product of the final electric field with its complex conjugate:

$$I^{image} = \boldsymbol{E}^{out} \cdot \tilde{\boldsymbol{E}}^{out} = E_x^{out}\tilde{E}_x^{out} + E_y^{out}\tilde{E}_y^{out}. \tag{C.36}$$

If $\rho = \pi/2$ and $\xi = 3\pi/4$, then the intensity of the image reduces to the following:

$$I^{image} = 2E_{oy}^2\{1 + \cos(\delta)\sin[2(\zeta - \phi)] - \sin(\delta)\cos[2(\zeta - \phi)]\sin[2(\alpha - \phi)]\}. \tag{C.37}$$

C.2.2 Mueller Calculus with Stokes Vectors

A Stokes vector, denoted $\boldsymbol{S}$ is another representation of the polarization of the electric field similar to the Jones vector except the Stokes vector has four time-averaged parameters, as shown in Equation (C.38), where $<>$ represents time averaging. The first Stokes parameter, s_o, is the intensity of the electric field, making it a convenient parameter to find the intensity of an image.

$$\boldsymbol{S} = \begin{bmatrix} s_o \\ s_1 \\ s_2 \\ s_3 \end{bmatrix} = \begin{bmatrix} < a_x\tilde{a}_x + a_y\tilde{a}_y > \\ < a_x\tilde{a}_x - a_y\tilde{a}_y > \\ < 2\Re\{a_x\tilde{a}_y\} > \\ < 2\Im\{a_x\tilde{a}_y\} > \end{bmatrix}. \tag{C.38}$$

Mueller matrices describe how the polarization changes after the light passes through a polarization optic, where the parameters of these matrices modify the Stokes vector representation of light polarization. The Mueller matrices, given the coordinate convention in Figure C.1, for a linear polarizer at angle ρ to the x axis and for a 1/4 wave plate with fast axis at angle ξ to the x axis are as follows:

$$\mathbf{P}_{\rho}^{\mathbf{M}} = \begin{bmatrix} 1 & \cos(2\rho) & -\sin(2\rho) & 0 \\ \cos(2\rho) & \cos^2(2\rho) & -\sin(2\rho)\cos(2\rho) & 0 \\ -\sin(2\rho) & -\sin(2\rho)\cos(2\rho) & \sin^2(2\rho) & 0 \\ 0 & 0 & 0 & 0 \end{bmatrix} \tag{C.39}$$

$$\mathbf{Q}_{\xi}^{\mathbf{M}} = \begin{bmatrix} 1 & 0 & 0 & 0 \\ 0 & \cos^2(2\xi) & -\sin(2\xi)\cos(2\xi) & \sin(2\xi) \\ 0 & -\sin(2\xi)\cos(2\xi) & \sin^2(2\xi) & \cos(2\xi) \\ 0 & -\sin(2\xi) & -\cos(2\xi) & 0 \end{bmatrix}. \tag{C.40}$$

The Mueller matrix of a linear retarder with retardation δ and fast axis α, the model for a photoelastic material, is

$$\mathbf{R}_{\delta,\alpha}^{\mathbf{M}} = \begin{bmatrix} 1 & 0 & 0 & 0 \\ 0 & \cos^2(2\alpha) + \sin^2(2\alpha)\cos(\delta) & -\sin(2\alpha)\cos(2\alpha)(1-\cos(\delta)) & \sin(2\alpha)\sin(\delta) \\ 0 & -\sin(2\alpha)\cos(2\alpha)(1-\cos(\delta)) & \sin^2(2\alpha) + \cos^2(2\alpha)\cos(\delta) & \cos(2\alpha)\sin(\delta) \\ 0 & -\sin(2\alpha)\sin(\delta) & -\cos(2\alpha)\sin(\delta) & \cos(\delta) \end{bmatrix}. \tag{C.41}$$

The Stokes vector of a general circular polariscope, with two polarizers, two 1/4 wave plates, and a photoelastic material, is the multiplication of the incident Stokes vector and the Mueller matrices of all the elements. The Stokes vector of the incident electric field is

$$\boldsymbol{S}^{incident} = \begin{bmatrix} E_{ox}^2 + E_{oy}^2 \\ \\ E_{ox}^2 - E_{oy}^2 \\ \\ 2E_{ox}E_{oy}\cos(\varphi_x - \varphi_y) \\ \\ 2E_{ox}E_{oy}\sin(\varphi_x - \varphi_y) \end{bmatrix}. \tag{C.42}$$

The general form of the Stokes vector for a circular polariscope is

$$\boldsymbol{S}^{out} = \mathbf{P}_{\zeta}^{\mathbf{M}}\mathbf{Q}_{\phi}^{\mathbf{M}}\mathbf{R}_{\delta,\alpha}^{\mathbf{M}}\mathbf{Q}_{\xi}^{\mathbf{M}}\mathbf{P}_{\rho}^{\mathbf{M}}\boldsymbol{S}^{\mathbf{incident}}. \tag{C.43}$$

Given a circular polariscope with the first polarizer at angle $\rho = \pi/2$, the first 1/4 wave plate at angle $\xi = 3\pi/4$, from Equation (C.43), the first Stokes parameter, the intensity of the electric field, may be reduced to

$$I_{image} = s_o^{out} = 2E_{oy}^2\{1 + \cos(\delta)\sin[2(\zeta - \phi)] - \sin(\delta)\cos[2(\zeta - \phi)]\sin[2(\alpha - \phi)]\}, \tag{C.44}$$

which is the same as the intensity determined by Jones matrix algebra in Equation (C.37).

C.3 Six-Step Phase Shifting

With the flexibility of the polariscope optics, many different combinations of intensities involving the isoclinic angle and isochromatic phase are possible. Choosing a certain set of these intensities allows for the separation of these two phases. The set of six images chosen for this research are given in Table C.1, where the first two elements do not change angle ($\rho = \pi/2$ and $\xi = 3\pi/4$) and the second 1/4 wave plate and second polarizer are at angles ϕ and ζ, respectively. The intensities for these images come from Equation (C.44).

Image	ϕ	ζ
$I_1 = 2E_{oy}(1 + \cos(\delta))$	$\pi/2$	$3\pi/4$
$I_2 = 2E_{oy}(1 - \cos(\delta))$	$\pi/2$	$\pi/4$
$I_3 = 2E_{oy}(1 - \sin(\delta)\sin(2\theta))$	π	π
$I_4 = 2E_{oy}(1 + \sin(\delta)\cos(2\theta))$	$\pi/4$	$\pi/4$
$I_5 = 2E_{oy}(1 + \sin(\delta)\sin(2\theta))$	$\pi/2$	$\pi/2$
$I_6 = 2E_{oy}(1 - \sin(\delta)\cos(2\theta))$	$3\pi/4$	$3\pi/4$

Table C.1: Photoelasticity phase shifting: Angles refer to fast axis of optics

Bibliography

Anderson, T. L., 2005. *Fracture Mechanics: Fundamentals and Applications*. CRC Press, 3rd edition.

Ashokan, K. and Ramesh, K., 2006. A novel approach for ambiguity removal in isochromatic phasemap in digital photoelasticity. *Meas. Sci. Tech.*, 17:2891–2896.

Azhdari, A. and Nemat-Nasser, S., 1996. Energy release rate and crack kinking in anisotropic brittle solids. *J. Mech. Phys. Solids*, 44(6):929–951.

Azhdari, A. and Nemat-Nasser, S., 1998. Experimental and computational study of fracturing in an anisotropic brittle solid. *Mech. Mater.*, 28:247–262.

Azhdari, A., Nemat-Nasser, S., and Rome, J., 1998. Experimental observations and computational modeling of fracturing in an anisotropic brittle crystal (sapphire). *Int. J. Fracture*, 94:251–266.

Baldi, A., Bertolino, F., and Ginesu, F., 2002. On the performance of some unwrapping algorithms. *Opt. Laser Eng.*, 37:313–330.

Barone, S. and Patterson, E. A., 1996. Full-field separation of principal stresses by combined thermo- and photoelasticity. *Exp. Mech.*, 36(4):318–324.

Barone, S. and Patterson, E. A., 1998. Polymer coating as a strain witness in thermoelasticity. *J. Strain Anal. Eng.*, 33(3):223–232.

Berghaus, D., 1991. Combining photoelasticity and finite-element methods for stress analysis using least squares. *Exp. Mech.*, 31(1):36–41.

Bradley, W. B. and Kobayashi, A. S., 1971. Fracture dynamics—a photoelastic investigation. *Engr. Fracture Mech.*, 3(3):317–332.

Bruck, H. A. and Rosakis, A. J., 1992. On the sensitivity of coherent gradient sensing: part I—a theoretical investigation of accuracy in fracture mechanics applications. *Opt. Laser Eng.*, 17:83–101.

Bruck, H. A. and Rosakis, A. J., 1993. On the sensitivity of coherent gradient sensing: part II—an experimental investigation of accuracy in fracture mechanics applications. *Opt. Laser Eng.*, 18:25–51.

Coker, E. G. and Filon, L. N. G., 1993. *A Treatise on Photo-elasticity.* Cambridge Univeristy Press.

Cotterell, B. and Rice, J. R., 1980. Slightly curved or kinked cracks. *Int. J. Fracture*, 16(2):155–169.

Dally, J. W., 1979. Dynamic photo-elastic studies of fracture. *Exp. Mech.*, 19(10):349–361.

Ekman, M. J. and Nurse, A. D., 1998. Completely automated determination of two-dimensional photoelastic parameters using load stepping. *Opt. Eng.*, 37(6):1845–1851.

Frocht, M. M., 1941. *Photoelasticity*, volume 1. John Wiley and Sons.

Ghiglia, D. C. and Romero, L. A., 1994. Robust two-dimensional weighted and unweighted phase unwrapping that uses fast transforms and iterative methods. *J. Opt. Soc. Am. A*, 11(1):107–117.

Goldstein, R. V. and Salganik, R. L., 1974. Brittle-fracture of solids with arbitrary cracks. *Int. J. Fracture*, 10(4):507–523.

Greene, R. J., Clarke, A. B., Turner, S., and Patterson, E. A., 2007. Some applications of combined thermoelastic-photoelastic stress analysis. *J. Strain Anal. Eng.*, 42:173–182.

Haake, S. J., Patterson, E. A., and Wang, Z. F., 1996. 2D and 3D separation of stresses using automated photoelasticity. *Exp. Mech.*, 36(3):269–276.

Hecht, E., 2002. *Optics.* Pearson Education, Inc., 4th edition.

Hodgdon, J. and Sethna, J. P., 1993. Derivation of a general 3-dimensional crack-proparation law—a generalization of the principle of local symmetry. *Phys. Rev. B*, 47(9):4831–4840.

Huang, Y. M., Mohsen, H. H. A., and Rowlands, R. E., 1990a. Determination of individual stresses thermoelastically. *Exp. Mech.*, 30(1):88–94.

Huang, Y. M., Rowlands, R. E., and Lesniak, J. R., 1990b. Simultaneous stress separation, smoothing of measured thermoelastic isopachic information and enhanced boundary data. *Exp. Mech.*, 30(4):398–403.

Irwin, G. R., Dally, J. W., Kobayashi, T., Fourney, W. L., Etheridge, M. J., and Rossmanith, H. P., 1979. Determination of the A-K relationship for birefringent polymers. *Exp. Mech.*, 19(4):121–128.

Jona, F. and Shirane, G., 1993. *Ferroelectric Crystals*. Dover Publications, Inc.

Kobayashi, A. S., editor, 1993. *Handbook of Experimental Mechanics*. Wiley.

Kramer, S. L. B., Mello, M., Ravichandran, G., and Bhattacharya, K., 2009a. Phase shifting full-field interferometric methods for determination of in-plane tensorial stress. *Exp. Mech.*, 49(2):303–315.

Kramer, S. L. B., Ravichandran, G., and Bhattacharya, K., 2009b. Transmission wavefront shearing interferometry for photoelastic materials. *Appl. Opt.*, 48(13):2450–2460.

Krishnaswamy, S., 2000. *Photomechanics*, volume 77 of *Topics in Applied Physics*, chapter Techniques for Non-Birefringnet Objects: Coherent Shearing Interferometry and Caustics, pages 295–321. Springer-Verlag Berlin Heidelberg.

Krishnaswamy, S., Rosakis, A. J., and Ravichandran, G., 1991. On the extent of dominance of asymptotic elastodynamic crack-tip fields, part ii: A numerical investigation of three-dimensional and transient effects. *J. Appl. Mech.*, 58(1):95–103.

Lee, H., Rosakis, A. J., and Freund, L. B., 2001. Full-field optical measurement of curvatures in unltra-thin-film-substrate systems in the range of geometrically nonlinear deformations. *J. Appl. Phys.*, 89(11):6116–6129.

Liu, C., Rosakis, A. J., Ellis, R. W., and Stout, M. G., 1998. A study of the fracture behavior of unidirectional fiber-reinforces composites using coherent gradient sensing (CGS) interferometry. *Int. J. Fracture*, 90:355–382.

Mason, J. J., Lambros, J., and Rosakis, A. J., 1992. On the use of coherent gradient sensing in dynamic mixed-mode fracture mechancis experiments. *J. Mech. Phys. Solids*, 40(3):641–661.

Murty, M. V. R., 1964. Use of single plane parallel plate as lateral shearing interferometer with visible gas laser source. *Appl. Opt.*, 3(4):531.

Narasimhamurty, T. S., 1981. *Photoelastic and Electro-optic Properties of Crystals*. Plenum Press.

Papdopoulos, G. A., 1993. *Fracture Mechanics: The Experimental Method of Caustics and the Det. Criterion of Fracture*. Springer-Verlag.

Park, T. S., Suresh, S., Rosakis, A. J., and Ryu, J., 2003. Measurement of full-field curvatue and geometrical instability of thin film-substrate systems through CGS interferometry. *J. Mech. Phys. Solids*, 51:2191–2211.

Patterson, E. A., Ji, W., and Wang, Z. F., 1997. On image analysis for birefringence measurements in photoelasticity. *Opt. Laser Eng.*, 28:17–36.

Patterson, E. A. and Wang, Z. F., 1998. Simultaneous observation of phase-stepped images for automated photoelasticity. *J. Strain Anal. Eng.*, 33(1):1–15.

Ramesh, K., 2009. Photelasticity. In W. Sharpe, editor, *Springer Handbook of Experimental Solid Mechanics*. Springer-Verlag.

Ramesh, K. and Tamrakar, D. K., 2000. Improved determination of retardation in digital photoelasticity by load stepping. *Opt. Laser Eng.*, 33(6):387–400.

RaviChandar, K., 1982. An experimental investigation into the mechanics of dynamic fracture. Ph.D. thesis, California Institute of Technology.

Rosakis, A. J., 1993. *Experimental Techniques in Fracture*, chapter Two Optical Techniques Sensitive to Gradients of Optical Path Difference: The Method of Caustics and the Coherent Gradient Sensor (CGS), pages 327–425. Society of Experimental Mechanics.

Rosakis, A. J., Krishnaswamy, S., and Tippur, H. V., 1990. On the application of the optical methods of caustics to the investigation of transient elastodynamic crack problems: Limitations of the clasical interpretation. *Opt. Laser Eng.*, 13:183–210.

Sakagami, T., Kubo, S., Fujinami, Y., and Kojima, Y., 2004. Experimental stress separation technique using thermoelasticity and photoelasticity and its applciation to fracture mechanics. *JSME Int. J. A*, 17(3):298–304.

Sanford, R. J. and Dally, J. W., 1979. A general method for determining mixed-mode stress intensity factors from isochromatic fringe patterns. *Engr. Fracture Mech.*, 11:621–633.

Shimizu, K., Suetsugu, M., Nakamura, T., and Takahashi, S., 1998. Evaluation of concentrated load by caustics and its application in the measurement of optical constant. *JSME Int. J.*, 41(1):134–141.

Siegmann, P., Backman, D., and Patterson, E. A., 2005. A robust approach to demodulating and unwrapping phase-stepped photoelastic data. *Exp. Mech.*, 45(3):278–289.

Smith, C. W. and Olaosebikan, O., 1984. Use of mixed-mode stress-intensity algorithms for photoelastic data. *Exp. Mech.*, 24(4):300–207.

Smith, D. G. and Smith, C. W., 1972. Photoelastic determination of mixed mode stress intensity factors. *Engr. Fracture Mech.*, 4:357–366.

Theocaris, P. S. and Gdoutos, E. E., 1979. *Matrix Theory of Photoelasticity*. Springer-Verlag.

Tippur, H. V., Krishnaswamy, S., and Rosakis, A. J., 1991a. A coherent gradient sensor for crack tip deformation measurements: analysis and experimental results. *Int. J. Fracture*, 48:193–204.

Tippur, H. V., Krishnaswamy, S., and Rosakis, A. J., 1991b. Optical mapping of crack tip deformations using the methods of trasmission and reflection coherent gradient sensing: a study of crack tip K-dominance. *Int. J. Fracture*, 52(91-117).

Williams, M. L., 1952. Stress singularities resulting from various boundary conditions in angular corners of plates in extension. *J. Appl. Mech.*, pages 526–528.

Yariv, A. and Yeh, P., 2007. *Photonics: Optical Electronics in Modern Communications*. Oxford University Press, 6th edition.

Yoneyama, S., Morimoto, Y., and Kawamura, M., 2005. Two-dimensional stress separation using phase-stepping interferometric photoelasticity. *Meas. Sci. Tech.*, 16:1329–1334.